Local dynamics and deformation of glass-forming polymers : modelling and atomistic simulations

Citation for published version (APA):
Vorselaars, B. (2008). *Local dynamics and deformation of glass-forming polymers : modelling and atomistic simulations*. [Phd Thesis 1 (Research TU/e / Graduation TU/e), Applied Physics and Science Education]. Technische Universiteit Eindhoven. https://doi.org/10.6100/IR633231

DOI:
10.6100/IR633231

Document status and date:
Published: 01/01/2008

Document Version:
Publisher's PDF, also known as Version of Record (includes final page, issue and volume numbers)

Please check the document version of this publication:

• A submitted manuscript is the version of the article upon submission and before peer-review. There can be important differences between the submitted version and the official published version of record. People interested in the research are advised to contact the author for the final version of the publication, or visit the DOI to the publisher's website.
• The final author version and the galley proof are versions of the publication after peer review.
• The final published version features the final layout of the paper including the volume, issue and page numbers.

Link to publication

General rights
Copyright and moral rights for the publications made accessible in the public portal are retained by the authors and/or other copyright owners and it is a condition of accessing publications that users recognise and abide by the legal requirements associated with these rights.

- Users may download and print one copy of any publication from the public portal for the purpose of private study or research.
- You may not further distribute the material or use it for any profit-making activity or commercial gain
- You may freely distribute the URL identifying the publication in the public portal.

If the publication is distributed under the terms of Article 25fa of the Dutch Copyright Act, indicated by the "Taverne" license above, please follow below link for the End User Agreement:

www.tue.nl/taverne

Take down policy
If you believe that this document breaches copyright please contact us at:

openaccess@tue.nl

providing details and we will investigate your claim.

Download date: 08. Feb. 2024

Local dynamics and deformation of glass-forming polymers:

modelling and atomistic simulations

PROEFSCHRIFT

ter verkrijging van de graad van doctor
aan de Technische Universiteit Eindhoven,
op gezag van de Rector Magnificus,
prof.dr.ir. C.J. van Duijn,
voor een commissie aangewezen door het College
voor Promoties in het openbaar te verdedigen
op donderdag 20 maart 2008 om 16.00 uur

door

Bart Vorselaars

geboren te Goirle

Dit proefschrift is goedgekeurd door de promotor:

prof.dr. M.A.J. Michels

Copromotor:
dr. A.V. Lyulin

CIP-DATA LIBRARY TECHNISCHE UNIVERSITEIT EINDHOVEN

Vorselaars, B.

Local dynamics and deformation of glass-forming polymers: modelling and atomistic simulations
Technische Universiteit Eindhoven, Eindhoven, the Netherlands (2008) - Proefschrift.
ISBN 978-90-386-1224-9
NUR 925
Trefwoorden: glasachtige polymeren / glas / moleculaire dynamica / computersimulatie / vervorming / polystyreen / mechanische eigenschappen
Subject headings: polymers / glass dynamics / molecular relaxation / glass transition / strain hardening / deformation / polystyrene / polycarbonate / molecular dynamics method / stress-strain relations

A full-colour electronic copy of this thesis is available at the website of the library of the Technische Universiteit Eindhoven (www.tue.nl/en/services/library).

Voor het gebruik van supercomputerfaciliteiten bij dit onderzoek is subsidie verleend door de Stichting Nationale Computer Faciliteiten (NCF), met financiële steun van de Nederlandse Organisatie voor Wetenschappelijk Onderzoek (NWO).

This work is financially also partly supported by the Dutch nanotechnology network NanoNed.

Druk: Universiteitsdrukkerij Technische Universiteit Eindhoven
Omslag: Een deels uitgerekte polycarbonaatketen in een glas t.g.v. uniaxiale extensie
Omslagontwerp: Full Frame (www.full-frame.nl)

Copyright © 2008 Bart Vorselaars

Contents

Contents **iii**

1 General introduction **1**
- 1.1 Technological relevance of polymers . . . 2
- 1.2 Glasses and their dynamics . . . 3
  - 1.2.1 Definition and existence of glasses . . . 3
  - 1.2.2 Glassy materials and models . . . 5
  - 1.2.3 Dynamical phenomena . . . 6
  - 1.2.4 Glass-transition theories . . . 13
- 1.3 Mechanical properties of vitrified polymers . . . 16
  - 1.3.1 Stress response . . . 16
  - 1.3.2 Brittle vs. tough response . . . 19
  - 1.3.3 Theoretical considerations on yield and strain hardening . . . 21
- 1.4 Simulation techniques . . . 24
- 1.5 Research goals and outline . . . 26

2 Simulation method and polymer models under study **29**
- 2.1 Molecular-dynamics method . . . 29
- 2.2 Interaction types . . . 31
- 2.3 Polystyrene model . . . 34
- 2.4 Polycarbonate model . . . 36
- 2.5 Sample preparation . . . 40

3 Non-Gaussian behaviour of glassy dynamics **41**
- 3.1 Introduction . . . 42
- 3.2 Model . . . 43
- 3.3 Comparison with simulation results . . . 51
- 3.4 Summary and conclusions . . . 53
- 3.A Random walk . . . 53

4 Heterogeneity in phenyl-ring-flip motions **55**
- 4.1 Introduction . . . 57
- 4.2 System description and simulation details . . . 59

4.3 Results and discussion 60
4.3.1 Free-energy barrier 61
4.3.2 Time correlation functions 63
4.3.3 Activation energy from relaxation times 68
4.3.4 Heterogeneity 69
4.3.5 Van Hove function 72
4.3.6 Two-state analysis 74
4.4 Summary, conclusions, and outlook 80

5 Deformation of polystyrene: atomistic simulations 83
5.1 Introduction 84
5.2 Simulation details 85
5.3 Results and discussion 87
5.3.1 Stress development during deformation 88
5.3.2 Energetics 96
5.3.3 Stress partitioning 108
5.4 Conclusions and outlook 112

6 Microscopic mechanisms of strain hardening in glassy polymers 117
6.1 Introduction 118
6.2 Simulation details 121
6.3 Chain structure 121
6.3.1 Fully extended chain 122
6.3.2 Intrachain length scales of vitrified polymer chains 124
6.4 Deformation and strain hardening 130
6.5 The role of non-affinity 131
6.5.1 Principle of non-affine displacements 131
6.5.2 Isotropic vs. deformed non-affine bead displacements 134
6.5.3 Non-affine bead displacements for various strains 137
6.5.4 Non-affine deformation of polymer-chain shape 139
6.5.5 Effective chain stiffness during deformation 143
6.6 Conclusions 149

7 Conclusions and outlook 151

Bibliography 157

Author index 178

Summary 183

Samenvatting 187

List of publications 191

Dankwoord **193**

Curriculum Vitae **195**

Chapter 1

General introduction

Window glass is often the first association people have when talking about glasses. It is a hard brittle transparent material, of which the structure at a microscopic level is disordered. The atoms are lined up in an irregular way, as opposed to, for example, a regular chess-board pattern or tiling. Other materials do have a regular pattern and are called crystalline. In physics the term glass serves to describe not only SiO_2-based materials (such as window glass), but disordered solids in general.

A specific class of glassy materials is the one made of polymers. Polymers are giant molecules composed of many connected building blocks, monomers. For applications for which transparency and toughness are required polymer glasses form a good alternative to the SiO_2-based materials; they are much lighter and less brittle. Products such as eyeglasses and vandal-proof glazing are therefore nowadays made of polymeric glasses. Moreover, they are applicable for many more products, in which flexibility, complex shapes and/or biocompatibility are needed.

Despite the many applications, some physical mechanisms causing the toughness of polymeric materials are still a mystery. This lack of understanding prevents one from having a clear design strategy in improving and optimizing toughness of polymer glasses to the one of desire: polymer glasses with extreme ultimate properties.

Insufficient knowledge can also lead to disastrous effects upon the application of the materials. One striking example is the following. In the eighties the American space shuttle Challenger exploded shortly after lift-off because a part of it turned into the glassy state due to the cold environment. The part was a rubber O-ring (of the shape of a torus) and served to join other material parts together, thereby preventing leakage of a liquid or gas. Under normal circumstances a small dilatation of the surrounding material parts will not result in leakage due to the expansion of the initially compressed resilient rubber. Below the glass-transition temperature this changes; then the material is solid and to a great extent the resilience is lost. As a consequence, a flare from the rocket booster could eventually reach the fuel tank, thereby causing the disaster.

Not only the mechanical properties of glassy polymers are poorly understood; also the properties of simpler low-molecular weight glasses are badly comprehended. Upon vitrification of a supercooled liquid into the glassy state its viscosity dramatically increases without large changes in its local structure. How this can happen is still an open question. Understanding the physics of the glassy state is considered one of biggest knowledge gaps in science [1].

The aim of the research presented in this thesis is to contribute to the knowledge necessary for solving these problems in the context of polymers. This is accomplished by the study of local dynamics and deformation of glass-forming polymers, both by means of a modelling approach and by atomistic simulations.

The goal of the present chapter is to give the necessary introduction into these fields: polymers, glasses, mechanical properties and simulation methods. Furthermore, the present chapter serves to enlighten some of the more specific subproblems these fields are coping with. The chapter concludes with an outline of the remaining thesis.

1.1 Technological relevance of polymers

A polymer chain can be compared with a pearl necklace, a lengthy string of beads. Just as a necklace, a polymer chain can be very flexible and fully extended or coiled up in a heap. Another analogy of a polymer chain is that of spaghetti. A pan filled with (over)cooked spaghetti is in some sense similar to an amorphous polymer melt; the strings are intertwined and possibly entangled and the structure is aperiodic.

Polymers can be found in nature, but they can also be synthesized artificially. Examples of natural polymers, so-called biopolymers, are natural rubber, DNA and spider silk. Typical synthesized polymers are Bakelite (the first polymer ever synthesized, for which a patent was granted in the year 1909), nylon, Teflon, polyethylene, polystyrene and polycarbonate. However, more and more biopolymers can be synthesized nowadays as well.

Polymeric materials form a major part of nowadays products. What circumstances are responsible for this? In contrast to steel, polymer thermoplastics melt already at quite low temperatures, typically around 100 °C, as opposed to about 1500 °C for steel. It is therefore much less demanding to process polymeric materials. They can be easily shaped in various forms. There even exist 3D printers capable of producing three-dimensional structures from polymeric materials. Another advantage is that they are relatively lightweight. The density of typical polymers is about a factor of 5 lower than that of steel, thereby reducing the overall weight of products with accompanying transport costs, etc. Yet another usefulness of polymeric-based materials is that they can be adjusted in many ways: the type of monomer unit can be changed, the topology of the molecules is modifiable (the size, the degree of crosslinking and branching), multi-components are possible to synthesize (block copolymers, functionalized hyperbranched polymers). This adjustability allows one to optimize the material for a wide number of applications. A polymer material can be made very flexible, or very tough. Some polymeric materials have strengths per unit of mass far exceeding that of steel. This makes them ideal materials for the aviation industry, or for applications such as bullet-proof vests.

A polymeric glass is a very specific type of polymeric material. Polymer glasses such as polycarbonate, poly(methyl methacrylate) and polystyrene have important applications in situations where transparency is demanded. Glassy polymers are often used because they have a high yield modulus in combination with some elasticity. Amorphous thermoplastics are not chemically crosslinked, but only physically entangled or crosslinked and are therefore both easy to process and easy to reuse.

1.2 Glasses and their dynamics

Many phenomena of glasses produced by the vitrification of a melt of polymer chains are a result of the fact that they are glasses, irrespective of their long-chain connectivity. Therefore the comprehension of glasses in itself is important and an introduction into this class of material will be given in this section.

1.2.1 Definition and existence of glasses

So what exactly is a glass? It is an amorphous solid material, see also fig. 1.1. The idea of a glass becomes more apparent if one compares it with other disordered material phases. To differentiate a glass from a liquid the glass is often defined as having a viscosity larger than about 10^{13} Pa s [18, 68]. This roughly corresponds to a relaxation time of 100 s. So the state of a material changes into a glass when the internal relaxation time of the material exceeds the typical time of a laboratory experiment. This state is usually reached by cooling down a material from its liquid state. Another disordered material is a quasi-crystal. Nevertheless, a quasi-crystal such as the Penrose tiling [135] can be obtained from a lattice in a higher dimension and could be regarded as being in a (degenerate) ground state. This is not the case for glasses. As time progresses, the glassy material 'ages' and a relevant energy usually decreases. A rubber, although disordered as well, also differs from a glass. A rubber can be defined as a huge molecular network which is formed when a polymeric liquid is irreversibly cross-linked by chemical bonds. Upon heating a rubber the chain segments between the crosslink points will deteriorate as well. A glass, on the contrary, has a reversible transition to the liquid state. Yet another amorphous system is a gel. A gel, however, consists of a diluted solid part (although this solid part forms a

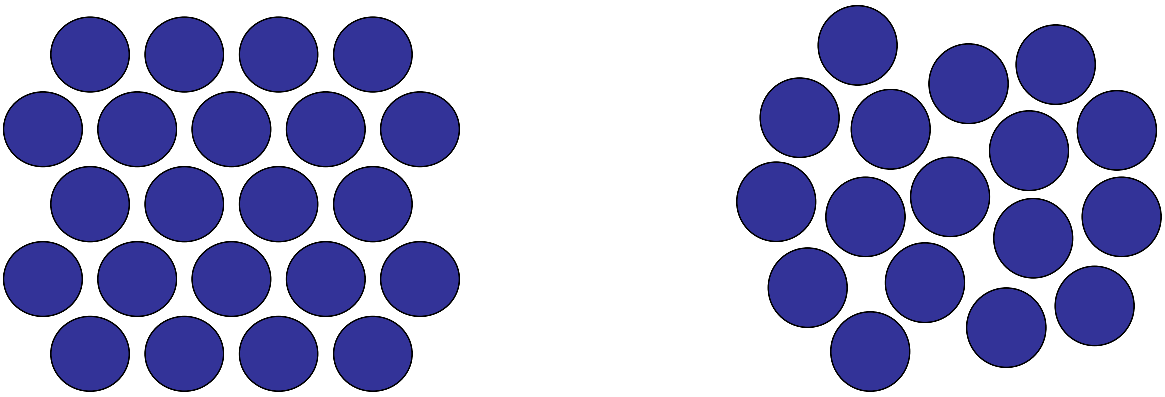

Figure 1.1: An example of a part of a two-dimensional crystalline (left) and a glassy (right) morphology.

percolating cluster throughout the whole system), while a glass consists of an undiluted solid (possibly prepared from a melt at higher temperature).

How is a glass prepared? Next to the usual method of cooling down a material from its liquid state, many other methods exist [7]. One example is to modify the pressure or density. By compressing a liquid or a crystal one can induce the glass transition. Decompressing a high-pressure stable crystal can induce the glass transition as well. In addition, shock, irradiation or intense grinding of a crystal can transform the material into a glassy state. The shear rate can be enhanced or reduced to vitrify a liquid into a glass. The temperature can even be increased to force the material to be in a glassy state [66, 201, 235].

What is the reason that a glass exists for a crystallisable material? Kauzmann's paradox [52] sheds light on this matter. A liquid can be cooled below the crystallization temperature without crystallizing, if the cooling happens fast enough. The reason for this is that a free-energy barrier prevents spontaneous crystallization below the crystallization temperature. In general, the liquid has a higher heat capacity c_P than its crystalline counterpart, which can be understood classically by the more degrees of freedom of the liquid. Therefore the entropy S of the supercooled liquid decreases faster than that of the crystal with decreasing temperature T (as $c_P = T\left(\frac{\partial S}{\partial T}\right)_P$). Upon extrapolation towards lower temperatures the entropy of the supercooled liquid would eventually be below that of the solid. The temperature at which the entropy of the two different states would cross each other by means of linear extrapolation is called the Kauzmann temperature T_K. Carrying out this extrapolation suggest that for many glass-forming materials $T_K > 0$ [52]. Thermodynamically such a crossing at positive temperatures would not be a problem [52]. However, upon linearly extrapolating the entropy of the undercooled liquid further towards $T = 0$ this would result in a lower value of the entropy of the supercooled liquid than that of the crystal. The entropy of the crystal at $T = 0$, if it is assumed to be perfect, would be zero. This implies that the entropy of the undercooled liquid would be negative at $T = 0$, so that it would violate Boltzmann's formula of the entropy $S = k_B \ln \Omega$ (with $\Omega \geq 1$ the number of quantum states corresponding to a certain energy, volume and mass). This is known as Kauzmann's paradox. A way to escape from this reasoning is that some degrees of freedom have to freeze in, so that the heat capacity of the supercooled liquid decreases. In this way the linear extrapolation fails and the entropy crisis can be circumvented. The point at which the degrees of freedom freeze in can then be associated with the glass transition and should be above T_K. Another way, of course, is that the material undergoes spontaneous crystallization. The ability of a material to form a glass is quantified by the critical cooling rate. Below this cooling rate the material has enough time to crystallize.

1.2.2 Glassy materials and models

What kind of materials are glasses? Polymer glasses, of current interest, are well-known glasses. They are widely used in for example DVD's, coffee cups, contact lenses, vandal-proof windows, toys, packaging and encapsulation parts such as computer housings. Partly because of the complexity in the backbone structure of some polymers, the crystallization of these polymers is easily prevented by moderate cooling rates. Even when crystallization does occur, it is often only partial, while amorphous regions are still present. Another possibility is that the polymer is intrinsically disordered (such as atactic chains, see also chapter 2) so that a crystalline state does not exist. Other typical glassy substances are ortho-terphenyl [100], metallic glasses [105] and SiO_2 (i.e., window glass). However, almost every material can turn into a glass, as long as the cooling rate is fast enough. Even water can vitrify [185].

To acquire a more fundamental understanding of glasses, model systems are studied. One of the simplest systems capable of vitrification is a monatomic system, consisting of spherical particles. An example showing some glassy phenomena such as metastable states is the five-disc-in-a-box [31] or even the two-disc-in-a-rhomboidal-box [243] system. A larger two-dimensional system is a soft-disc liquid [127]. Three-dimensional examples are a hard-sphere system [216] and a monatomic Lennard-Jones liquid [178, 195]. However, often these systems tend to crystallize after some period of time. Binary liquids are often employed to prevent this relatively fast crystallization; here the atomic radii and/or energy parameters are chosen different from each other in such a way as to prevent crystallization. Examples are a binary two-dimensional hard-disc system [84, 152] and a binary three-dimensional Lennard-Jones liquid [150]. Another glass-forming system is a polydisperse liquid [57] of which the polydispersity is accomplished by a variation in the radius among particles. This variation in radius is now not bidisperse as in the binary-liquid case, but described by a (piece-wise) continuous probability distribution function, so that the possible number of different particles is infinite. Moreover, there is an ideal-gas model showing glassy behaviour [264]. That system is made of infinitely thin Onsager-like crosses (a cross consists of three perpendicular line segments rigidly joined together at their midpoints), occupying thus zero volume. Upon increasing the number density dynamic localization effects are observed.

Yet a different class of glass-like systems is that of lattice glasses, such as spin glasses [26]. For a normal magnetic model system 'spins' are placed on lattice sites. Usually each spin will interact with neighbouring spins. The contribution to the total energy depends on the relative orientation of a spin with its surroundings. One possibility is that if neighbouring spins are parallel, then there is a negative contribution to the energy and opposite if they are antiparallel. A variant of a magnetic system is one with random interactions, showing thereby glassy behaviour. Here specific arrangements of spin orientations are favoured randomly: Some spin pairs prefer a parallel arrangement, while other spin pairs prefer an anti-parallel ordering. Due to this frozen-in disorder no long-range order is present.

An important group in spin-glass models is that consisting of kinetically constrained models [218]. In this case the interactions are usually very simple, without any disorder. However, for these kinetically constrained systems more attention is paid to the dynamics of the spins. An example of a possible constraint is that a spin can only flip if a certain minimum number of neighbours are in the upward state. It turns out that then the dynamics can become highly non-trivial and cooperative. This cooperativity manifest itself in the temperature dependence of some relaxation time: deviations from normal Arrhenius-like behaviour. As we will see in §1.2.3, that behaviour is typical for supercooled liquids approaching the glass-transition temperature from above. The benefit of some kinetically constrained models is that this temperature-dependence can be obtained analytically. An example is the one-dimensional East model [133, 218]. The relaxation time τ as a function of temperature T for this model in the low-temperature limit shows marked non-Arrhenius behaviour: the logarithm of the relaxation time is proportional to the square of the inverse temperature, $\log_{10}(\tau) \sim T^{-2}$ [26, 218].

1.2.3 Dynamical phenomena

Why are the dynamics of glasses interesting? To answer this, we should first answer a related question: what are the key properties of glasses? Properties which are both of technological and fundamental interest are optical properties (transparency, index of refraction, etc.), thermal expansion, conductivity, density and the glass-transition temperature. In addition to this, mechanical properties are of major interest. It is these properties that we focus on in the thesis. Many mechanical properties, such as the shear modulus, are ultimately linked to various relaxation times. Understanding the relaxation processes in the vicinity of the glass transition is thus of prime importance.

The dynamical phenomena present in glasses are linked to the motion of the constituent particles. Studying the trajectory of particles will thus give more insight into this. A specific particle trajectory $\mathbf{r}(t)$ is afflicted with thermal noise. We therefore look at quantities averaged over many particles. For an isotropic sample the average displacement of particles is zero. The first non-zero moment is the mean-square displacement (MSD)

$$\langle \Delta\mathbf{r}(t)^2 \rangle = \langle |\mathbf{r}(t_0 + t) - \mathbf{r}(t_0)|^2 \rangle. \tag{1.1}$$

Here $\langle \cdots \rangle$ denotes ensemble averaging.

Before we turn to the glassy dynamics, we first treat the ordinary classical simple gas. For this situation the MSD has two distinct regimes. For times much smaller than the typical time between collisions a particle move ballistically. Then the mean-square velocity of a particle of mass m equals the thermal velocity $v_{\mathrm{th}} = \sqrt{\frac{dk_BT}{m}}$ and $\langle \Delta\mathbf{r}(t)^2 \rangle = v_{\mathrm{th}}^2 t^2$ [17]. Here d is the spatial dimension. The second regime is visible for times much larger than the typical time between collisions. Then the motion of a particle can be regarded as a random walk and becomes diffusive. In this case $\langle \Delta\mathbf{r}(t)^2 \rangle = 2dDt$ with D the diffusion coefficient.

Upon vitrification the dynamics of a glass former becomes extremely sluggish. This will also show up in the MSD. In a glass a particle is surrounded by other particles. A collision with a neighbour particle causes the direction of the particle to change. However, it will collide again with other neighbour particles; the particle is therefore trapped within a cage (see also fig. 1.1). Only after many collisions a rearrangement is able to occur. Such a rearrangement is often of a collective nature involving the cooperative motion of many particles. Stringlike motions in large clusters of mobile particles have been observed [62]. For a binary liquid the degree of cooperativity is found to increase upon approaching the glass-transition temperature from above [21]. It was shown that this result also applies to polymeric liquids [5]. After the rearrangement the particle has moved into a new cage. The cage around the particle thus causes a temporal localization of the particle inside the trap and is responsible for a dramatic decrease of the long-time diffusion coefficient. Due to the localization a new regime in the MSD appears: a plateau is arising between the small-time ballistic and the large-time diffusive region.

The dramatic decrease of the diffusion coefficient upon cooling down only a few degrees is characteristic for glasses. The diffusion coefficient can be written as $D = \frac{\sigma^2}{2d\tau}$ with σ a typical length scale such as the diameter of the particle and τ the time it takes to diffuse the distance σ. So the decrease of the diffusion coefficient is accompanied by an increase in a relaxation time and is ultimately linked to an increase in the viscosity η. So if this dramatic increase lasts till $\eta = 10^{13}$ Pa s, the material has by definition (§1.2.1) vitrified into a glass.

A viewpoint which at first hand seems to be different from the MSD is to look at dynamic density-density correlation functions, quantified by the Van Hove function [262]

$$G(\mathbf{r}, t) = \frac{1}{\rho} \langle \rho(\mathbf{r}_0 + \mathbf{r}, t_0 + t) \rho(\mathbf{r}, t) \rangle. \tag{1.2}$$

It is a measure for the correlation of the density ρ at the position $\mathbf{r}_0 + \mathbf{r}$ and time $t_0 + t$ with the density $\rho(\mathbf{r}_0, t_0)$. For a disordered material no long-range order exists and the Van

Hove function $G(\mathbf{r},t)$ approaches ρ for $|\mathbf{r}| \to \infty$. It also approaches ρ for $t \to \infty$ because of relaxation processes such as diffusion.

The Van Hove function actually is related to the MSD. This can be seen from the following. As in the current discussion we treat particles as point-like, an enhanced correlation in the Van Hove function can arise either because the particle originally at $\mathbf{r}_0$ at t_0 displaces towards $\mathbf{r}_0 + \mathbf{r}$ at $t_0 + t$ (self correlation) or that a different particle appears at $\mathbf{r}_0 + \mathbf{r}$ at $t_0 + t$. From this it is clear that the Van Hove function can be partitioned in a self and a distinct part

$$G(\mathbf{r},t) = G_s(\mathbf{r},t) + G_d(\mathbf{r},t) \tag{1.3}$$

with the self part

$$G_s(\mathbf{r},t) = \langle \delta\left(\mathbf{r} - (\mathbf{r}_i(t_0+t) - \mathbf{r}_i(t_0))\right)\rangle \tag{1.4}$$

and the distinct part

$$G_d(\mathbf{r},t) = \frac{1}{N}\left\langle \sum_{i=1}^{N}\sum_{j\neq i}^{N} \delta\left(\mathbf{r} - (\mathbf{r}_j(t_0+t) - \mathbf{r}_i(t_0))\right)\right\rangle . \tag{1.5}$$

Here N is the number of particles in the system. The self part of the Van Hove function is a measure for the probability of a certain displacement $\mathbf{r}$ of a particle i after a time t. The MSD is then just the second spatial moment of $G_s(\mathbf{r},t)$.

A quantity related to $G(\mathbf{r},t)$ is commonly measured in experiments: the dynamic structure factor $S(\mathbf{q},\omega)$, depending on the wavevector $\mathbf{q}$ and frequency ω. This is the spatial as well as temporal Fourier transform of the Van Hove function. As with the Van Hove function, there is also a self part of the dynamic structure factor, called the incoherent dynamic structure factor $S_{\text{inc}}(\mathbf{q},\omega)$. This can be determined by a spatio-temporal Fourier transform of $G_s(\mathbf{r},t)$ [110]. Both the dynamic structure factor and the incoherent dynamic structure factor are measurable by neutron scattering, i.e., by bombarding neutrons onto the sample.

The intermediate scattering function $F_{\mathbf{q}}(t)$ is the density-density correlation function in the reciprocal space

$$F_{\mathbf{q}}(t) = N^{-1}\langle \rho_{\mathbf{q}}(t)\rho_{-\mathbf{q}}(0)\rangle, \tag{1.6}$$

and is determined alternatively by performing the temporal Fourier transform of $S(\mathbf{q},\omega)$ or spatial Fourier transform of $G(\mathbf{r},t)$. The Fourier component $\mathbf{q}$ of the density ρ as being used in eq. 1.6 is given by

$$\rho_{\mathbf{q}} = \sum_{j=1}^{N} \exp\left(-i\mathbf{q}\cdot\mathbf{r}_j\right), \tag{1.7}$$

with $\mathbf{r}_j$ the position of particle j and $i^2 = -1$.

Based on the intermediate scattering function we can construct a normalized function $\Phi_{\mathbf{q}}(t) = F_{\mathbf{q}}(t)/F_{\mathbf{q}}(0)$. It acts as a correlation function, as it measures the degree of correlation of the material with itself but at some later time. For a liquid it decays to zero for $t \rightarrow \infty$, as all memory will be lost. For a solid material in which the shape is fixed, $\Phi_{\mathbf{q}}(t)$ does not decay to zero, but towards a finite value $f_{\mathbf{q}}$. This value is also known as the Debye-Waller factor. $\Phi_{\mathbf{q}}(t)$ is a frequent object of study for some glass-transition theories, as will be discussed in §1.2.4.

The study of these extra correlation functions reveals more information about glasses than solely the second moment of the self part of the Van Hove function, the MSD. One example is the observance of non-Gaussian displacements. Around the time at which the localization-plateau regime as visible in the MSD ends, the functional form of $G_s(\mathbf{r}, t)$ shows pronounced deviations from a Gaussian shape. The effect can be quantified by a single characteristic, the non-Gaussian parameter. This non-Gaussian nature of displacements is typical for glasses [140] and has been measured both by means of experiments and simulations. A compelling theoretical explanation is still lacking. The focus point of chapter 3 of this thesis will be these deviations from Gaussianity.

The normalized correlator $\Phi_{\mathbf{q}}(t)$ also shows another characteristic of glass-forming materials: heterogeneous dynamics. This is elucidated by the following. Just as with the MSD, there is also a plateau present in the time dependence of $\Phi_{\mathbf{q}}(t)$, reminiscent of temporary localization within the cage. After this plateau regime the correlator $\Phi_{\mathbf{q}}(t)$ of a vitrifying material decays further again towards zero. This decay is called the main or α relaxation, as all correlation is lost afterwards. The functional form of it is known to be closely described by the Kohlrausch-Williams-Watts (KWW) law [26, 52, 273]. It is a stretched exponential function

$$c \exp\left(-\left(\frac{t}{\tau}\right)^{\beta}\right), \tag{1.8}$$

with τ a typical time of relaxation, β a measure for the stretch and c a pre-factor. The stretch parameter β for a glass-forming material is commonly between 0 and 1. It is a generalization of normal, Debye-like relaxation, which is just single-exponential, i.e., $\beta = 1$. An example of single-exponential behaviour is normal diffusion in the hydrodynamic limit [17, 110], for which the self part of the density autocorrelation function is related to the MSD

$$F_{s,\mathbf{q}}(t) = \exp\left(-\frac{1}{2d}\langle\Delta\mathbf{r}(t)^2\rangle q^2\right) = \exp\left(-Dq^2t\right). \tag{1.9}$$

The observation that the stretch parameter β is less than 1 has been associated with heterogeneous dynamics [215, 273]. It is observed that upon approaching the glass-transition point from the supercooled liquid the relaxation becomes more wide, i.e., the stretch parameter β decreases. It has been put forward that two different scenarios could be the cause of this [215]. One is that spatially separated subsystems all relax single-exponentially, but with a spectrum of relaxation times τ. This makes the overall relaxation non-exponential. Each of these subsystems is ought to be of a certain size. The second possibility is that all subsystems relax in an intrinsically non-exponential matter, i.e., each bead, and hence the self-part of the density autocorrelation function, relaxes non-exponentially. Examples of this intrinsic non-exponential decay are Rouse dynamics [56] and single-file diffusion [214]. No general consensus has been made so far regarding the right scenario. Also other issues related to the time and length scales of these heterogeneities are subject of much discussions [67]. By using simple models some progress has been achieved [239], although many controversies are still unresolved [239]. The focus of chapter 4 of this thesis will be mainly on the matter of heterogeneous dynamics in vitrifiable forming systems.

Next to being heterogeneous this α-relaxation time shows a highly non-trivial temperature dependence near the glass transition. Many thermally activated processes can be well described by the Arrhenius law, stating that their relaxation time increases exponentially with the inverse temperature [273, 282]

$$\tau = \tau_0 \exp\left(\frac{E}{k_B T}\right), \tag{1.10}$$

with E the activation energy and τ_0 a pre-factor that only weakly depends on temperature. However, for glassy materials this is generally not the case. Then the temperature dependence of the α-relaxation time is usually super-Arrhenius, meaning that upon cooling down the relaxation time increases faster than expected from the Arrhenius law.

A quite successful functional form of the temperature dependence of the α relaxation is the Vogel-Fulcher-Tammann (VFT) law [52, 273]

$$\tau = \tau_0 \exp\left(\frac{A}{k_B (T - T_0)}\right), \tag{1.11}$$

with τ_0, A and T_0 fit parameters. Note that the relaxation time diverges for T approaching T_0 from above, $T \downarrow T_0$. In §1.2.4 it will be shown that one of the outcomes of some theories of the glass transition is exactly the VFT law.

Another phenomenological law for the temperature dependence of a relaxation time is the Ferry or Bässler form [26, 77, 273]

$$\tau = \tau_0 \exp\left(\frac{B}{(k_B T)^2}\right), \tag{1.12}$$

in which τ_0 and B are fit constants. This exponential inverse temperature square (EITS) law is noteworthy because it is the exact solution for a model glass in the low-temperature limit: the one-dimensional kinetically constrained East model, as mentioned in §1.2.2.

The temperature dependence of the main relaxation time can act as a classification criterion for glassy materials. To see this, we first extract an effective temperature-dependent activation energy from the τ-T relation. One way is fitting the $\log_{10} \tau$ vs. $(k_B T)^{-1}$ relation with a tangent line. The accompanying slope is

$$E(T)/\ln(10) = \frac{\partial \log_{10} \tau(T)}{\partial 1/(k_B T)}. \tag{1.13}$$

The so-determined effective activation energy $E(T)$ is at $T = T_g$ related to the well-known steepness or fragility index [28]

$$m = \frac{E(T_g)}{k_B T_g \ln{(10)}}. \tag{1.14}$$

And it is the fragility index that is used to classify glasses. For a pure Arrhenius-like process the energy barrier is independent of temperature and we can make an estimation of the value of m in this case. Assuming that $\tau_0 = 0.1$ ps [64] and $\tau = 100$ s (the typical relaxation time at the glass-transition point), then a process adhering to the Arrhenius law would have an activation energy of $E = 15 k_B T_g \ln{(10)}$, so that $m = 15$.

Materials having a low value of m are called strong glass formers ($m \approx 25$), while materials with a high value of m ($m \approx 150$ [64]) are fragile. Very few glass formers have a fragility index lower than 25. Examples of fragile materials are *o*-terphenyl, toluene, chlorobenzene and to a lesser extent glycerol. Examples of strong glass-forming materials are the network oxides SiO_2 and GeO_2 [52]. It is observed that for polymers the fragility index is usually higher than for small molecules [41] and that the fragility index for longer chains is higher than for shorter ones [224]. This last observation seems to be connected with the chain-length dependence of the glass-transition temperature; shorter chains have a lower glass-transition temperature because of a higher relative contribution of chain ends, which are freer.

The fragility has been connected to the structure of a material. A fragile material looses its structure more rapidly upon heating than a strong material. Recently it has been shown that the fragility of a material is related to the Poisson ratio (which is a measure for the ratio of instantaneous shear modulus G to bulk dilatation modulus B) [196]. Here it was observed that the more fragile a material is, the smaller the ratio $\frac{G}{B}$. This implies that the structure of these materials is more vulnerable to shear deformation than to dilatation (as compared to strong materials).

In general the relaxation of a fragile material is departing more from simple exponential decay than that of a strong material [9, 41]. These materials with a high value of m have, obviously, a high apparent activation energy. This energy can easily exceed the molecular heat of vaporation (for *o*-terphenyl a factor of 5) implying that the viscous flow is highly cooperative [8]. To sum up, by means of the fragility index a connection between the dynamics and the structure of a glass-forming liquid can be made.

In addition to the main relaxation process (the α relaxation), numerous other processes are frequently observed in glassy materials. For very high temperatures in the liquid phase particles are flowing along each other and other local processes (such as a rotational motion or a permutation of particles) have a negligible contribution to the overall relaxation. Another possibility is that the local relaxation at high temperature is occurring so fast, that it falls out of the experimentally measurable time window. However, as the α-relaxation time increases in a super-Arrhenius way, local, more Arrhenius-like relaxation mechanisms will be able to contribute to the overall relaxation. Many of these processes can be detected by experimental techniques such as dielectric spectroscopy or dynamic mechanical analysis. In the last case these secondary relaxations show up as extra peaks in the frequency-dependent shear loss modulus below some bifurcation temperature; they are called β, γ, ... relaxations in order of appearance after the α relaxation for increasing frequency or decreasing temperature. The variation of the peak positions with temperature give information about the activation energies of these secondary processes.

The relaxation times are ultimately linked to other intrinsic properties, such as the shear modulus and viscosity [26, 182]. Although basic 'laws' can be used to show this connection for liquids, glasses often do not adhere to these laws. As an example we consider the connection with viscosity η. According to Stokes' law a non-slipping sphere of radius R moving with velocity v in a viscous medium experiences a drag force $F = 6\pi R\eta v$, so that the friction coefficient equals $\zeta = \frac{F}{v} = 6\pi R\eta$. Although Stokes' law is derived from macroscopic considerations, it also provides a good correlation of experimental data on simple liquids [110]. According to the Einstein equation the friction coefficient, in turn, is related to the diffusion coefficient D [56, 110]

$$D\zeta = k_B T, \tag{1.15}$$

with T the temperature and k_B the Boltzmann constant. Assuming that this diffusion coefficient is the same as the self-diffusion coefficient, D can be determined by measuring the averaged mean-square displacement of a particle $D = \lim_{t\to\infty} \frac{1}{6t}\langle|\mathbf{r}(t_0+t) - \mathbf{r}(t_0)|^2\rangle$. As the diffusion coefficient can be written as $D = \frac{L^2}{6\tau}$ (with τ the time it takes to diffuse a distance L) the connection between viscosity and τ is

$$\eta = \frac{k_B T}{\pi R L^2}\tau, \tag{1.16}$$

This result is derived from the combined Stokes-Einstein relation $D = \frac{k_B T}{6\pi\eta R}$ [17]. However, in glassy materials these basic laws do not suffice: the Stokes-Einstein relation is found to be violated. In the glassy state particles are caged and an apparent activation energy is needed for the particles to flow. It seems that below the glass-transition temperature the activation energy of the process probed by the measurement of the single-particle diffusion coefficient differs from the activation energy of the process probed by the measurement of the viscosity constant. The inequality between those activation energies is likely causing the breakdown of the Stokes-Einstein relation.

An important consequence of the increase in time scales upon cooling down is that eventually the system cannot relax within the time of observation. This is also qualified by the Deborah number $De = \frac{\tau}{t}$, with τ a typical relaxation time and t the time of observation [213]. If $De \gg 1$ then relaxation cannot take place. Partly due to the disordered structure of the material, the ideal equilibrium structure is different at each temperature (if no underlying crystal structure would be present). An example of a temperature-dependent structural property can be found with atactic polystyrene (see next chapter); an atactic polystyrene chain tends to be more stretched upon cooling down (see chapters 5 and 6).

As the stretching of a polymer chain as a whole is associated with large relaxation times, an out-of-equilibrium state easily occurs. In such a non-equilibrium situation the cooling rate starts to play a role. Also structural properties will be dependent on the deviation from equilibrium, so that aging effects can be observed. Mechanical properties can be very susceptible to the age of a material, as we will see in §1.3.2.

1.2.4 Glass-transition theories

Various theories exist to explain the glassy phenomena discussed in §1.2.3 and the most important ones will be discussed here. Although no well-accepted theory of the glass transition is available at the moment, these important theories each have an important physical picture accompanied with it and it is likely that the ultimate theory will contain traces of each picture.

One of the first, and still a popular one, is the free-volume theory [26, 52, 273]. In its basic form as developed by Cohen and Turnbull vitrification occurs when there is not enough free volume V_f available for translational molecular motions. If there is no energy penalty or correlation associated with the redistribution of free volume over particles, then after maximizing the number of possible free-volume configurations the free-volume distribution $\rho(V_f)$ is of Poisson form

$$\rho(V_f) = \frac{1}{\langle V_f \rangle} \exp\left(-\frac{V_f}{\langle V_f \rangle}\right) \tag{1.17}$$

with $\langle V_f \rangle$ the average free volume. As assumed, diffusion can only occur if a minimum amount of free volume $V_{f,\mathrm{min}}$ for a particle is available, so near the glassy state

$$D \sim \exp\left(\frac{-V_{f,\mathrm{min}}}{\langle V_f \rangle}\right). \tag{1.18}$$

Upon supposing that the free volume is linearly dependent on temperature the VFT-law for the temperature dependence of the viscosity near the glass-transition temperature (eq. 1.11) is recovered. Although intuitively appealing, the free-volume theory is highly disputed nowadays. One of the main criticisms is that the pressure dependence of the glass-transition temperature is not well described by the free-volume theory [26, 52, 225].

Another approach is the Adam-Gibbs theory [3, 18, 26, 52]. It is based on the assumption that many particles are involved for a non-trivial motion in the system. In order for such motion to occur these particles need to move collectively; this cluster of moving particles is called a cooperatively rearranging region (CRR). The entropy of the whole system is partitioned in a vibrational and a configurational part. The configurational entropy for a subsystem should be sufficiently large to allow for at least two configurations. Assuming that the subsystems are statistically independent, the number of subsystems is equal to the total number of particles divided by the (minimum) critical size of a CRR. The total configurational entropy S_c is then of the order of the number of subsystems and thus inversely proportional to the critical size of a subsystem. It is also assumed that the configurational entropy S_c vanishes at the Kauzmann temperature T_K. The result of these assumptions is that the VFT law (eq. 1.11, $\tau = \tau_0 \exp(-A/(T - T_0))$ is recovered with $T_0 = T_K$.

However, the predictions of the Adam-Gibbs theory sometimes fail. The stated equivalence between T_0 and T_K is found to be invalid for some systems. The (extrapolated) Kauzmann temperature T_K is found to be lower than the (extrapolated) VFT temperature T_0 [26, 52]. Also the definition of a CRR is not a stringent one, making it hard to identify CRRs in experiments or simulations.

A dynamical viewpoint on glassy behaviour is the mode-coupling theory (MCT). It describes the evolution of the normalized density-density correlation function $\Phi_{\mathbf{q}}(t) = F_{\mathbf{q}}(t)/F_{\mathbf{q}}(0)$ for supercooled atomic liquids. The basic form of MCT is described by an integro-differential equation for $\Phi_{\mathbf{q}}(t)$ [48, 50, 52, 101, 273]

$$\ddot{\Phi}_{\mathbf{q}}(t) + \nu_0 \dot{\Phi}_{\mathbf{q}}(t) + \Omega_{\mathbf{q}}^2 \left(\Phi_{\mathbf{q}}(t) + \int_0^t \Gamma_{\mathbf{q}}(t-t') \dot{\Phi}_{\mathbf{q}}(t') dt' \right) = 0. \tag{1.19}$$

Here ν_0 is a damping constant, $\Omega_{\mathbf{q}} = (\mathbf{q} v_{\mathrm{th}})^2 (F_{\mathbf{q}}(0))^{-1}$ the vibration frequency of modes with wavevector $\mathbf{q}$ (with the thermal velocity $v_{\mathrm{th}} = \sqrt{\frac{k_B T}{M}}$), M the mass of a molecule and $\Gamma_{\mathbf{q}}(t)$ a memory function, determined by the equation

$$\Gamma_{\mathbf{q}}(t) = \sum_{m=1}^{m_0} \frac{1}{m!} \sum_{\mathbf{q}_1, \ldots, \mathbf{q}_m} V^{(m)}(\mathbf{q}, \mathbf{q}_1, \ldots, \mathbf{q}_m) \Phi_{\mathbf{q}_1}(t) \cdots \Phi_{\mathbf{q}_m}(t), \tag{1.20}$$

where $V^{(m)}$ are the vertex functions or coupling constants depending on the static structure factor $F_{\mathbf{q}}(0)$. The memory function generalizes the Newtonian friction coefficient to a frequency-dependent function and couples different modes, hence the name of the theory. The difficulty partly lies in the form of the vertex functions $V^{(m)}$ acting as a closure for eq. 1.19. Various expressions for the vertex functions are in use. If chosen, the MCT thus predicts the time evolution of $\Phi_{\mathbf{q}}(t)$ with only the static structure factor and density at given temperature as an input [52]. Next to the MCT for monatomic liquids, a version of MCT has also been developed for dense polymeric systems assuming Gaussian chains [43]. In that version Rouse-like dynamics is resolved after the cage plateau.

The ideal MCT predicts a power-law divergence of the main relaxation time near the critical MCT temperature T_c

$$\tau = \tau_0 (T/T_c - 1)^{-\gamma}. \tag{1.21}$$

Here τ_0 is a prefactor and γ an exponent deducible from MCT. Measured values for the exponent γ are typically within the range 1.5–2.5 for simple fluids [8], while for a couple of glass-forming polymers higher values are found [177, 270]. Measured values of T_c generally are above the out-of-equilibrium temperature T_g, leading to an overestimation of the relaxation times near T_c.

Using the MCT proved to be successful in several cases. The mode-coupling theory describes the relaxation of the normalized density-density correlation function for a few systems qualitatively and sometimes even quantitatively [273]. Also MCT has predicted novel relaxation patterns correctly (such as that the addition of an attractive part to the hard-sphere potential could melt a hard-sphere glass [212]). MCT works better for fragile liquids [273], probably because ideal MCT predicts a power-law divergence of the main relaxation time near T_c and fragile glass-forming liquids are behaving in a super-Arrhenius way tending more to divergence-like behaviour than strong materials do.

Nevertheless, MCT also suffers from some serious flaws. A good description of relaxation data is only obtained in a limited temperature range above T_g, as the predicted divergence of time scales is not observed near the glass-transition temperature [27]. Due to this limitation for the temperature range and time scale, ideal MCT is considered not to be a theory of the glass transition [53]; additional relaxation mechanisms such as activated hopping motions are neglected. Extended versions of the 'ideal' MCT have been developed in order to include such hopping mechanisms [52]. Nevertheless, the extended version still does not perform well with characteristic glassy phenomena such as the non-Gaussian behaviour of particle displacements [80].

A framework different from MCT for studying the glass transition is the energy-landscape picture [53, 273], which has been put forward by Goldstein [99] and popularized by Stillinger [245]. Although no general theory has emerged from it, various glassy phenomena can be understood within this picture such as the decoupling of the α and the β relaxation [53]. Some models are built from this picture, such as the trap model inside a random free-energy landscape by Bouchaud [30] or the evolution of the energy-probability density function [65]. Concepts such as inherent dynamics in which the dynamics has been separated in vibrations around inherent structures and transitions between inherent structures [246] also find their origin in this framework, although similar nomenclature is also present in the Adam-Gibbs point of view.

Many other theories exist, which are often a combination of the aforementioned theoretical concepts with other approaches: free-volume theory in combination with percolation [170, 242], density-functional theory with the energy-landscape picture [146] or dynamic density-functional theory in combination with the nonlinear feedback mechanism of MCT [85, 86].

Also much can be learned from models or theories which only describe some aspects of the glass transition, such as those associated with aging and out-of-equilibrium phenomena. Examples of this are the self-retarding model by Struik [248], the Kovacs-Aklonis-Hutchinson-Ramos (KAHR) model [154] and the Tool-Narayanaswamy-Moynihan (TNM) [189, 193, 258] model. These phenomenological models show that the state of the material depends on the magnitude of the departure from equilibrium and on the sign of the departure [97]. They are used for describing the volume, stress or strain recovery phenomena as a function of thermal history.

However up to now no comprehensive theory of the glass transition is accepted and one has to stick with phenomenological descriptions like the KWW and the VFT laws. As will be described in more detail in §1.5, the goals of the first part of the current research are connected with two types of badly understood glassy phenomena: the non-Gaussian behaviour of glassy dynamics and the heterogeneous nature of relaxation processes.

1.3 Mechanical properties of vitrified polymers

Understanding the mechanical properties of glassy polymers is important for their applicability. The unstressed glassy state already reveals much of the characteristics of glassy polymers. However, as will be discussed, additional phenomena are revealed when the material is subject to an imposed stress or strain. An introduction thereof will be presented here. Two polymers are prototypical in this sense, as they show totally opposite mechanical behaviour: polycarbonate (PC) is a very tough polymer, while atactic polystyrene (PS, also depicted in fig. 1.4) is extremely brittle. In this section it will be explained what the difference actually is and why such a difference is present, what kind of theories exist to explain this difference and what shortcomings are present in these theories, which serve as a basis for nowadays research.

1.3.1 Stress response

A uniaxial-compression test reveals much of the mechanical behaviour of a glassy polymer material, see also figures 1.2 and 1.3. For small strains a linear viscoelastic response is present, in which the force per unit area (the stress) needed to deform the material is approximately linear with the strain. The equilibrium structure determines the properties of this relatively well understood linear regime [76, 157]. It is followed by a nonlinear elastic regime. Subsequently yielding takes place; a yield peak σ_{peak} with associated drop in stress till σ_{min} is visible. The stress drop $\sigma_{\text{drop}} = \sigma_{\text{peak}} - \sigma_{\text{min}}$ is also called yield drop or strain softening. For a more aged sample there is usually both an increase in σ_{peak} and in σ_{drop}, while σ_{min} remains approximately constant. The peak is visible as a small overshoot in the stress and the effect is known as yield tooth or stress overshoot. After the drop in stress, strain hardening sets in, meaning that the stress to deform increases again. Finally fracture takes place, either due to the disentanglement of the chains or due to chain scission [156].

A deformation experiment can be done in various ways. One possibility is to do a uniaxial-stress compression test (with the two other axes of the stress free, i.e., at constant ambient pressure). Another way is to apply compression along one axis, fix another and measure the response of the third one (plane-strain compression). A shear experiment is also frequently carried out. All these deformation modes give rise to different stress components, showing that the tensorial behaviour of the stress is important and that one should consider the

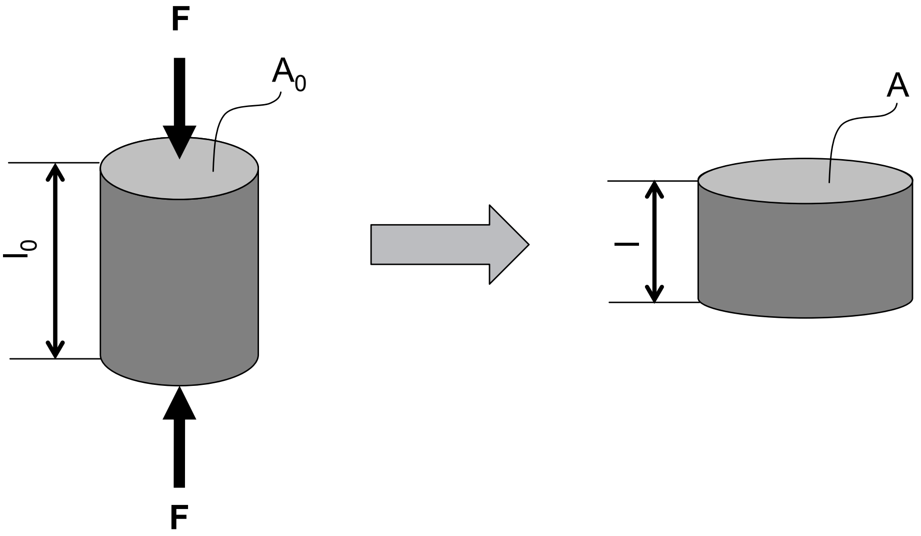

Figure 1.2: Uniaxial compression of a sample by applying an external force F. The length and cross-section area of the sample are l and A, respectively. The subscript 0 refers to the state prior to deformation. The engineering and true strain are $\varepsilon_{\mathrm{eng}} = \frac{l}{l_0} - 1$ and $\varepsilon_{\mathrm{true}} = \int_{l_0}^{l} \frac{dl'}{l'} = \ln(l/l_0)$, while the engineering (or nominal) stress and true stress are $\sigma_{\mathrm{eng}} = F/A_0$ and $\sigma_{\mathrm{true}} = F/A$. For small $\varepsilon_{\mathrm{eng}}$, $\varepsilon_{\mathrm{eng}} \approx \varepsilon_{\mathrm{true}}$ and the symbol ε will be used instead.

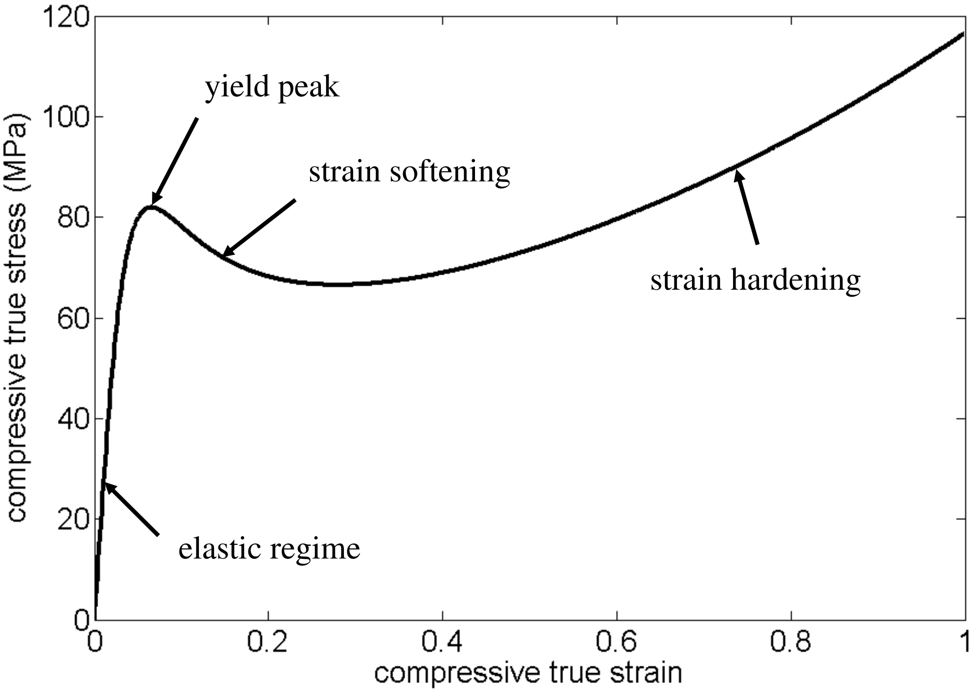

Figure 1.3: Typical stress response of a polymer glass under a uniaxial-stress compression test.

stress tensor $\bar{\bar{\sigma}}$ of rank 2. In order to circumvent studying all stress components, the von Mises stress σ_{vM} is often calculated, as it is apart from a constant factor equal to the second invariant of the stress tensor [164]

$$\sigma_{\mathrm{vM}} = \sqrt{\frac{3}{2}\mathrm{Tr}(\bar{\bar{\sigma}}^d \cdot \bar{\bar{\sigma}}^d)}, \tag{1.22}$$

in which $\bar{\bar{\sigma}}^d = \bar{\bar{\sigma}} + P\bar{\bar{I}}$ is the deviatoric part of the stress tensor $\bar{\bar{\sigma}}$ and Tr the trace. Here P is the pressure. Other names for the von Mises stress (with sometimes a deviation in the prefactor) are the octahedral [275] or deviatoric [226] stress. In the case of a symmetric stress tensor and with cartesian coordinates, eq. 1.22 is equal to

$$\sigma_{\mathrm{vM}}^2 = \frac{1}{2}\left((\sigma_x - \sigma_y)^2 + (\sigma_y - \sigma_z)^2 + (\sigma_z - \sigma_x)^2\right) + 3(\sigma_{xy}^2 + \sigma_{yz}^2 + \sigma_{zx}^2). \tag{1.23}$$

Eq. 1.23 can be simplified further in the case of a uniaxial-stress extension test along the x-axis (with $\sigma_x = \sigma_{\parallel}$) with the stress along the two perpendicular axes equal to a constant stress of $-P_{\perp} < 0$ and with zero off-diagonal elements of the stress tensor. Then the von Mises stress equals

$$\sigma_{\mathrm{vM}} = \sigma_{\parallel} + P_{\perp}. \tag{1.24}$$

The benefit of using the definition given by eq. 1.22 for the von Mises stress is that the latter is then equal to the tensile stress under uniaxial-stress extension or compression if the lateral sides are kept at zero stress.

1.3.2 Brittle vs. tough response

The interplay of the initial yield regime with the strain-hardening regime determines for a large part what kind of mechanical response is expected: brittle or tough. In brittle response the material already breaks within a few percent of extension [36]. A tough material absorbs more energy before fracture and is accompanied with much larger values of strain at failure. The difference between brittle and ductile behaviour can be explained by the localization of stress $\sigma = \frac{F}{A_0}$ (see fig. 1.2 and its caption text for nomenclature). Assume that a small part of the material, the weakest link, yields first upon uniaxial-stress extension. If the force F necessary to deform this part decreases upon further straining ($\frac{\partial F}{\partial \varepsilon} < 0$), the material at that point will be extended more, while the rest of the material remains before the yield peak. The deformation can be assumed to occur at approximately constant volume, therefore the cross-section of this weakest link will decrease and the local true stress intensifies. If it remains the weakest link, the true stress intensifies even further and localizes around this point up till fracture. This is called stress localization, as stress localizes within a small part. This stress localization results in a brittle fracture as only little energy is absorbed before breakage. If, on the other hand, the force necessary to further extend the weakest link increases, other parts of the material will start to yield. Therefore stress spreads over the whole material; this behaviour is known as stress delocalization and a tough response is expected.

So for a tough response to occur the true stress should increase sufficiently enough at larger strains to compensate for the decrease in cross-section. This behaviour is illustrated by means of the following stress-strain relation, which is known to often fit stress-strain relations after yielding under uniaxial-stress extension or compression well [114] and is inspired by rubber-elasticity theory (to be discussed in §1.3.3)

$$\sigma_{\text{true}} = \sigma_Y + G_h \left(\lambda^2 - \lambda^{-1}\right). \tag{1.25}$$

Here σ_Y is the offset yield value, G_h the strain-hardening modulus and $\lambda = 1+\varepsilon_{\text{eng}} = \frac{l}{l_0}$ the draw ratio. For simplicity a potential yield drop is neglected in this form of the stress-strain relation. As discussed above a decrease in the engineering stress, $\frac{\partial\sigma_{\text{eng}}}{\partial\varepsilon} < 0$, causes stress localization and necking. For small strains eq. 1.25 becomes $\sigma_{\text{true}} = \sigma_Y(1 + \frac{3G_h}{\sigma_Y}\varepsilon + \mathcal{O}(\varepsilon^2))$. With the constant-volume assumption, the engineering stress equals $\sigma_{\text{eng}} = \sigma_{\text{true}}/\lambda = \sigma_Y(1 + (\frac{3G_h}{\sigma_Y} - 1)\varepsilon + \mathcal{O}(\varepsilon^2))$. We see that σ_{eng} increases for $G_h > \sigma_Y/3$. This condition equals Considère's criterion for necking [114, 275]. The example thus illustrates that a brittle response can be circumvented by having a high strain-hardening modulus G_h as compared to the offset yield stress σ_Y.

In reality this picture is somewhat oversimplified for several reasons. One is that partly due to the stress drop necking occurs, making the problem multi-dimensional instead of one-dimensional. Also the deformation can induce a local heating of the material, changing the temperature-dependent material properties (such as yield stress). Nevertheless, Considère's construction gives a reasonable estimate of plastic instability [114]. This is illustrated by the comparison of σ_{peak} and G_h for polystyrene and polycarbonate. At room temperature PS has both a higher yield peak ($\sigma_{\text{peak}} = 100$ MPa vs. 70 MPa [103]) and a lower strain-hardening modulus (9 MPa [267] vs. 26 MPa [254]) than PC, making it more likely that PS breaks in a brittle manner (i.e., fractures within a few percent of length change during uniaxial extension) and PC in a ductile matter (i.e., fractures after tens of percent of length change). It is indeed observed that under uniaxial extension PS breaks at 2%, while PC breaks at around 100% under normal loading conditions [266].

It was shown recently by van Melick et al. [268] that mechanical preconditioning can drastically alter the properties of the material. Due to a prerolling treatment, a sample of atactic polystyrene was able to extend by 30%, an order of magnitude more than under normal conditions. The rolling causes a decrease of the yield tooth, and thereby the diminishing of stress localization. An appropriate thermal treatment can give similar results. Thermally quenching a polymeric material results in a lower yield tooth as well [112]. So also here the non-equilibrium nature of glassy materials plays a profound role.

Often one prefers the breakage of a material to occur in a ductile manner. This can thus be achieved by a decrease of the yield stress or by an increase of the strain-hardening modulus. Knowing the physical processes behind these values would allow one to tailor the ideal material in a much more goal-oriented way. Unfortunately there are no satisfactory physical theories available at the moment to guide this. Questions such as why polystyrene has a high yield tooth and why polycarbonate has not, and why polycarbonate hardens much more severely compared to polystyrene, remain unanswered.

1.3.3 Theoretical considerations on yield and strain hardening

In predicting the properties of polymer glasses constitutive laws are used. These include effects of external parameters such as temperature, pressure and strain rate on the mechanical properties. Also polymer-specific relations are incorporated such as the chain-length dependence of the glass-transition temperature (the Flory-Fox equation) or of the maximal draw ratio $\lambda_{\max}$. These relations are often physically well-funded. However, problems arise with the strain-hardening modulus. No compelling theory is available. Applying the theory of rubber elasticity to glassy polymers is troublesome. As we will see in eq. 1.29 it predicts an increase in the strain-hardening modulus with increasing temperature, in contradiction to what is observed experimentally; there it is found to actually decrease with temperature [102]. To shed more light on this matter we will first discuss the successful Eyring model of yielding and then the poorly-applicable rubber-elasticity network theory of hardening.

In order to surpass the energy barriers for changing the microstate, deformation can be thought of as a thermally activated process under the influence of a driving force. Then the well-known and still used Eyring model is applicable [275]. It states that a potential-energy barrier is present (of intra and/or intermolecular nature) for having a molecular event. In equilibrium flow events in all directions are equally probable, resulting in no net flow. An applied stress will result in a decrease of the effective energy barrier in the direction of the flow and in an increase in the backward direction. Therefore a net flow in the forward direction is present. If the strain rate $\dot{\varepsilon}$ is assumed to be linear with the number of flow events and if backward jumps are neglected, the temperature- and stress dependence of the strain rate is

$$\dot{\varepsilon} = \dot{\varepsilon}_0 \exp\left(-\frac{\Delta H - \sigma V'}{k_B T}\right). \tag{1.26}$$

Here ΔH is the potential-energy barrier height, σ the applied stress, V' the so-called activation volume and $\dot{\varepsilon}_0$ a constant pre-exponential factor.

Equation 1.26 is the basic form of Eyring's model. Modifications of it are usually applied in practice. It is found that an increase in hydrostatic pressure P results in a decrease of the strain rate, so that $\sigma V'$ has to be replaced with $\sigma V' - P\Omega$ with Ω the pressure activation volume. As discussed in §1.2.3 more relaxation processes are usually present below the glass transition; this requires a modification of eq. 1.26 by the inclusion of multiple energy barriers with accompanying multiple activation energies. Recently aging mechanisms have also been modelled within this framework [70] by using the TNM model [189, 193, 258], §1.2.4.

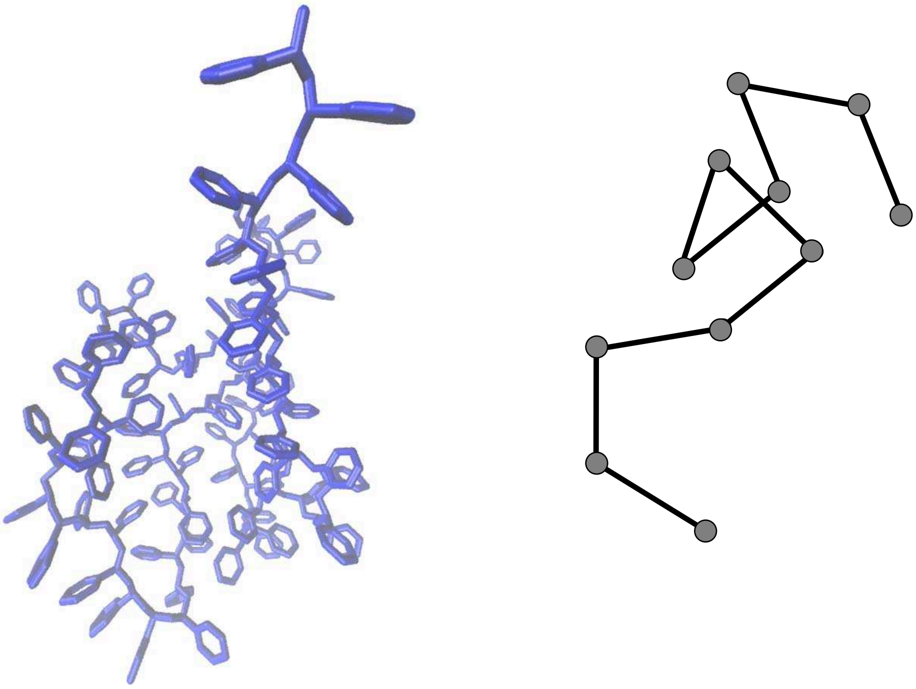

Figure 1.4: A polystyrene chain of 80 monomers (left) and a freely-jointed chain (right). The polystyrene chain is visualized by showing the covalent bonds between united-atoms as rods.

The polymer specifics are mostly visible in the phenomena associated with strain hardening, which is absent in simple supercooled glasses. So what would be the cause of this hardening? For temperatures well above the glass-transition temperature the theory of rubber elasticity is applicable [260, 275]. Upon straining a rubber-like material such as a chemically crosslinked polymer network or a highly entangled polymer melt the chains will be forced to be in a stretched state. Under unstrained conditions this would be an unlikely situation, as only a part of phase space corresponding to a stretched chain will be sampled. As the Boltzmann entropy is proportional to the logarithm of the number of available configurations Ω, this stretching leads to a decrease in entropy S. If it is assumed that the internal energy does not change upon straining, then the Helmholtz free energy $A = U - TS$ will increase by $-T\Delta S$.

The number of available configurations can be calculated analytically for some simple model chains. A particular one is the freely-jointed chain. Here rods (or bonds) of length l are connected with each other at their end points in a linear way, forming a continuous structure. An example together with a chemically realistic chain is depicted in fig. 1.4. The angle between two consecutive bonds is taken randomly, so that the total chain of N segments is analogous to a random walk of N steps. The end-to-end distance, a rough measure for the extent of the chain is thus in between 0 and Nl (for $N > 1$). In the limit $N \to \infty$ the distribution function of the end-to-end distances has a Gaussian shape, so that in this limit this model is regarded as a Gaussian chain. The limit to the Gaussian chain can also be achieved for other models, such as the freely rotating chain or the Rouse model [55, 56].

For a Gaussian chain the increase in the Helmholtz free energy upon straining is

$$\Delta A = -T\Delta S = \frac{N_{\mathrm{ch}} k_B T}{2V}\left(\lambda_x^2 + \lambda_y^2 + \lambda_z^2 - 3\right), \tag{1.27}$$

where λ_x is the draw ratio along the x-axis (similar for y and z), N_{ch} the number of subchains between junctions (or crosslinks) and V the volume. In case of a uniaxial-stress extension test, in which volume changes can be neglected the resulting stress is

$$\sigma = G_R\left(\lambda^2 - \lambda^{-1}\right), \tag{1.28}$$

with

$$G_R = N_{\mathrm{ch}} k_B T / V = \rho k_B T / M_{\mathrm{ch}} \tag{1.29}$$

the rubber modulus. Here ρ is the mass density and M_{ch} is the mean molecular mass of the chain segments between crosslinks or entanglements. Note that the rubber modulus derived in this way is linear with temperature and thus purely of entropic nature. Various extensions and refinements exist, such as taking into account a finite extensibility of a chain, or incorporating dangling chain ends [275].

However, for temperatures below the glass transition the entropy-based picture of rubber elasticity is not valid any more. Chains are frozen-in and the whole phase space cannot be sampled within the experimental time scales. In the framework of the energy-landscape picture (see §1.2.4) one could say that huge energy barriers separate the various microstates. Therefore the entropy argument breaks down and the rubber theory of elasticity is inapplicable; as mentioned before, it is indeed observed that below the glass-transition temperature the strain-hardening modulus G_h for amorphous polymers is decreasing with temperature [254, 266], instead of increasing as would be the case for a purely entropic phenomenon.

Another effect is that of pressure. The modified Eyring model takes into account a pressure effect in the yielding of a material; the yield stress increases under the influence of a high external pressure. The Eyring model also takes into account the decrease in yield for higher temperatures or for lower strain rates. These two last trends in the yield stress are also visible for the strain-hardening modulus. If rubber-elasticity theory would be valid, there would not be a direct influence of external pressure. Could the pressure have a similar effect on the strain-hardening modulus as on the yield stress below the glass-transition temperature?

From the above it is clear that a thermally and stress-activated approach should be applicable to the strain-hardening part as well. However, currently no theory of such exists yet. Another problem in the understanding of mechanical deformation of glassy polymers is related to the strain softening part. As mentioned in §1.3.2 it is experimentally observed that softening depends on both the mechanical and thermal history. Mechanical pre-rolling or thermally quenching a glassy material can result in a lower yield peak and hence less softening. Nevertheless, the exact microscopic origin of it in polymers such as polystyrene or polycarbonate is still unclear. A related open question is why the effect is much more visible in polystyrene.

For investigating mechanical properties a chemically-detailed simulation has proven to be an excellent method and mechanical characteristics can be reproduced. A simulation of mechanical deformation of a binary LJ glass by Utz et al. [261] demonstrated that aging and rejuvenation phenomena can be probed. For polymeric materials the simulated yielding and strain-hardening behaviour was also observed to act analogous to experimental behaviour; for atactic polystyrene (the polymer of investigation in the present research project) this was demonstrated by Lyulin et al. [176], although an insurmountable shift in time-scales is present with the atomistic simulations.

Also simulations of model systems give more insight. In the rugged energy-landscape model of Isner and Lacks [131] a yield tooth was observed and found to increase with more aged samples, demonstrating that this phenomenon is very generic. It was also found that deformation does not lead to the erasure of the thermal history; materials produced by a different thermal history gave different end states after mechanical deformation. This is also seen experimentally for polystyrene by means of positron-annihilation experiments [37]. McKechnie et al. [184] simulated a model polyethylene melt and showed that the chain conformation has a dramatic effect on the resulting strain-hardening modulus; artificially increasing the persistence length leads to stiffer polymer chains.

These observations demonstrate that simulations can be very valuable. However results are rather scarce as only recently enough computational power became available for the demanding task of simulating chemically realistic polymers. As a consequence, a functional theory about the strain hardening and the yield tooth has not arisen yet from these results. The focus of chapters 5 and 6 will be on these aspects of mechanical phenomena of glassy polymers. Next section deals with the role of simulation techniques and points out the method of usage for most of the results presented in this thesis.

1.4 Simulation techniques

Modelling the behaviour of polymers is an extensive task. One of the reasons for this is that there is a broad range in length scales, from smaller than the monomer unit to the whole object. Accompanying relaxation times form a broad spectrum as well. The dynamical properties of a polymer chain can therefore become quite elaborate. Moreover, a simple glassy material on its own already shows rich behaviour.

A successful approach for tackling this complexity is the usage of computer simulations. These simulations are carried out at different scales and at a different level of faithfulness, each with its own techniques. At the smallest scale quantum mechanics plays a role for studying the interactions between different atoms. These are mediated via, e.g., electron-electron interactions. Methods such as density-functional theory are used to determine the effective forces between atoms for a specific spatial arrangement. From these calculations a force field can be distilled taking into account the subatomic interactions. Subsequently such a force field is used as an input for classical molecular dynamics (or Monte Carlo) simulations, in which the electrons and the nucleus are combined into one particle, accompanied by effective interactions with other particles. In some circumstances groups of atoms are coarse-grained even further to a larger single coarsened particle [19].

Apart from chemically realistic polymers, more fundamental toy models are also simulated in polymer physics. These are similar to the more realistic systems, although now the force field is greatly simplified to a basic form, but in such a way that the essential physical phenomena one is interested in are still preserved. The omission of details will lead to faster calculations and less distractions of irrelevant aspects, thereby generating the opportunity to isolate the relevant characteristics for the property under study.

It is not necessary to adopt a coarse-grained description for all particles at the same level. Hybrid techniques are also used, in which the component one is interested in is explicitly simulated, while a much simpler description is adopted for the remaining parts. An example for such an object-varying level of coarse-graining is to simulate the atoms of a polymer chain explicitly, while modelling the solvent by random force kicks, as is done in Brownian dynamics. Another method in which the solvent is implicitly taken into account is dissipative particle dynamics [71, 120].

Next to the particles, the space and time can be coarse-grained as well. This is the case with lattice models, in which the lattice is a discretized version of the normal space. An example is the bond-fluctuation lattice model [40]. In this model each particle of the polymer chain resided on a point of a predefined lattice. The length of the bond connecting neighbouring beads is able to fluctuate between some discrete values. A similar strategy is employable for the time dimension. For a lattice model such as the bond-fluctuation model this is common practice, but also for continuum-space models exact dynamical particle trajectories are not always necessary to know. In this situation so-called Monte Carlo algorithms are often used. Then jumps in time or more generally in phase space can be achieved by performing complicated trial moves. One example of such a move is to displace a group of particles in a cooperative way. Another important example for simulating polymer chains is the class of moves which change the chain connectivity [83]. Yet a different technique, often used to study energy barriers, is energy minimization while constraining a certain coordinate [51].

At even larger scales continuum models are often used. Here the material is treated as a continuum with intrinsic properties. These properties are needed as an input and are parameters or functions such as the stress-strain relation. Usually these follow from experimental results. Theoretical models allow for powerful extrapolations. These continuum models are fairly successful in predicting the mechanical behaviour of an end product, as long as the relevant scales are not too small, although ongoing research is present to include more effects in the models (see, e.g., Klompen et al. [148]). Naturally, such continuum models do not give any insight in how the stress-strain relation follows from the chemical structure.

The interest of the current research is in dynamical and non-equilibrium phenomena (such as mechanical deformation) of glassy polymers and in seeking generic behaviour among chemically different polymer materials. The preferred simulation method is therefore the molecular-dynamics simulation technique applied at an atomistic scale. This method will be discussed in detail in chapter 2.

1.5 Research goals and outline

As can be concluded from the above discussions many aspects of the relaxational and mechanical behaviour of glassy polymers are still poorly understood. This is mainly a result of the absence of a well accepted theory of glasses in general and a theory of the mechanical deformation of polymer glasses in particular. The scope of the present project is on both parts. Here we will present in more detail what the research questions and goals are, specified for each chapter. Details about the simulation method and the polymer models used in those chapters will be presented first in chapter 2.

As discussed in §1.2.3 many glassy systems show non-Gaussian behaviour in the dynamics of particle displacements. The origin of these non-Gaussian effects is still fuzzy. The first goal is therefore to study the non-Gaussian behaviour of glassy dynamics, motivated by the observation that no glass-transition theory is able to describe such behaviour. To accomplish this, an effective one-particle diffusion model will be employed. The model and simulation results will be discussed in chapter 3. It will be shown that the generic diffusion model is capable of doing qualitative and sometimes even quantitative predictions about this behaviour for systems of different architecture.

A concept connected to non-Gaussian dynamics is the presence of heterogeneous dynamics in glasses, which is also an ill-understood problem. As stated before two different scenarios are in circulation for explaining heterogeneous dynamics. The second goal is to see how heterogeneous dynamics manifests itself in the polystyrene melt. A particular example of heterogeneous dynamics, the rotational motion of a chemical group in a glassy polymer melt (the phenyl ring in a melt of atactic polystyrene), is analyzed and discussed in terms of an energy-landscape-like picture in chapter 4. This rotational motion in polystyrene has been ascribed to the mechanical γ relaxation.

In §1.3.3 we saw that the strain-softening and hardening phenomena observed in strained polymer glasses are insufficiently understood. The goals related to these mechanical phenomena are firstly to see if experimental characteristic regimes in the stress-strain curve can be reproduced by appropriate simulations; secondly to determine in this way what kind of interactions (intrachain or interchain) are responsible for each of these regimes, as it is very hard to measure the separate interactions experimentally; and thirdly to see the influence of thermal history and pressure, as these will have a profound influence on the mechanical properties, yet are not taken into account by the theories as discussed in §1.3.3. To fulfil these goals extensive molecular-dynamics simulations are carried out for polystyrene under various conditions, and the measured stresses and energies are partitioned in intrachain and interchain contributions. This is the subject of chapter 5.

By using the basic knowledge acquired from the previous parts, the final goal is to explore the microscopic mechanisms behind the difference in strain hardening between PS and PC. Strain hardening is one of the major ingredients for determining the toughness of a material. Non-affine displacements of both polymers are being analyzed, together with the accompanying change in internal structure of the chains. A possible explanation of this strain-hardening difference is put forward in chapter 6.

The major conclusions resulting from the research presented in this thesis and an outlook are given in chapter 7. The thesis ends with a summary (both in English and in Dutch), list of publications, acknowledgements and a curriculum vitæ of the author.

Chapter 2

The molecular-dynamics simulation method and polymer models under study

The molecular-dynamics simulation method used in the subsequent chapters will be discussed. First the Newton equations of motion with accompanying types of forces and basic methods of MD simulations including deformation protocols are presented. Next some background information including the force field for both the two simulated polymers is given: atactic polystyrene (PS) and bisphenol-A polycarbonate (PC). These two polymers are typical in the sense that PS is a well characterized glass-forming polymer and is very brittle. PC, on the other hand, is known to behave very differently than PS; it is a tough and ductile material. Both these polymers have been successfully used for molecular simulations in the past [129, 187]. Finally, the sample-preparation and equilibration methods are being elucidated.

2.1 Molecular-dynamics method

The method of molecular-dynamics simulations at an atomistic level is effective for studying molecular processes of length and time scales up to about 100 nm and 1 μs [251], respectively. It is widely applied for studying molecular dynamics of liquids, solids and glassy materials. Many excellent textbooks are devoted to this method [6, 83, 108, 208]. In this section some of the basic ingredients of MD simulations will be discussed.

Classically the movement of particles is described by the equations of Newton. In its basic form it states that the time derivative of the momentum of a particle i equals the total force $\mathbf{F}_i$ acting on it

$$\frac{d\mathbf{p}_i}{dt} = \mathbf{F}_i, \tag{2.1}$$

with the momentum $\mathbf{p}_i$ of a particle i equal to its mass m_i times its velocity $\mathbf{v}_i$ (relativistic and quantum-mechanical effects can and will be neglected in our case). In our simulations the forces are conservative (except for the baro- and thermostat, to be discussed below) and thus follow from a (force field) potential U_{ff}

$$\mathbf{F}_i = -\nabla_i U_{ff}. \tag{2.2}$$

In §2.2 the various terms of the (force field) potential will be discussed.

In the present study a typical simulation consists of $N = 5000$–10000 particles. This means solving $3N$ coupled second-order nonlinear differential equations, a task which cannot be done analytically for a non-trivial case. Therefore these coupled equations are solved numerically, by discretizing the differential equations using velocity Verlet as the integration scheme [6]. The benefit of using a Verlet algorithm over a normal Taylor-like expansion of the differential equation is that the Verlet algorithm is symmetric with respect to time inversion. Therefore drifts in total energy are minimal. Simulations are carried out with an integration time step of $\Delta t = 4$ fs.

Periodic orthorhombic boundary conditions are used to remove any open boundary and to mimic the bulk material of interest. Another way to look at these boundary conditions is to interpret the geometry of the space as a three-dimensional torus.

Controlling the temperature is carried out by using the so-called collisional-dynamics method. Details can be found in the article of Lemak and Balabaev [165], but a brief description of the method is the following. The temperature is controlled by colliding 'virtual' particles with a certain mass m_0 with the 'normal' particles during a simulation run. Due to these collisions kinetic energy is redistributed. The velocity of each virtual particle is taken randomly from a Maxwell-Boltzmann distribution with the prescribed temperature. The time between subsequent collisions is also random and follows the Poisson distribution. The average collision frequency λ and the mass of the virtual particles are chosen small enough in order to not disturb the trajectory of a particle too much, typically $m_0 = 0.1$ Da and $\lambda_{\text{coll}} = 1$ ps^{-1}.

The pressure is controlled by means of the Berendsen barostat [6, 22]. The variant we use is based on rescaling the coordinates of all particles along each (μ) of the three primary axes (x, y, z) if the pressure in that direction P^μ deviates from the external pressure P^μ_{ext}. The correction is based on the difference $P^\mu - P^\mu_{\text{ext}}$. The three lengths L^μ of the orthorhombic box are propagated in time by using

$$L^\mu(t+\Delta t) = L^\mu(t)\left(1 + \frac{\Delta t\beta}{3\tau_P}(P^\mu(t) - P^\mu_{\text{ext}}) + \frac{1}{2}\left(\frac{\Delta t\beta}{3\tau_P}(P^\mu(t) - P^\mu_{\text{ext}})\right)^2\right), \tag{2.3}$$

in which Δt is the time step of integration and β/τ_P mediates the strength of the correction. Here β is the isothermal compressibility and τ_P a time constant. A typical value for this ratio in our simulations is $\tau_P/\beta = 0.011$ Pa s. To give a feeling for the associated time scale, a value of the compressibility coefficient is needed. For polystyrene at the glass-transition temperature (one of the polymers under current investigation) the compressibility coefficient is 4.9×10^{-5} bar^{-1} [181], corresponding to $\tau_P = 5.4$ ps. For room or for melt temperatures this coefficient changes by at most a factor of 2.

In using the Berendsen barostat, the instantaneous pressure needs to be determined. The stress tensor $\tau^{\mu\nu}$ and pressure $P^\mu = -\tau^{\mu\mu}$ (the Einstein summation convention should not be applied here) can be calculated by using the virial theorem of Clausius. The result is [255]

$$\tau^{\mu\nu} = \left\langle -\frac{1}{V} \sum_{i=1}^{N} \left(\frac{p_i^\mu p_i^\nu}{m_i} + r_i^\mu F_i^\nu \right) \right\rangle , \tag{2.4}$$

where the summation is over all N particles, with momentum p_i^ν, mass m_i, position r_i^ν and total force F_i^ν acting on the particle i. Here ensemble averaging is denoted by $\langle \cdots \rangle$ and the total volume by V.

The MD method will also be used to carry out simulations of deformation, such as uniaxial-stress compression (fig. 1.2) and extension. In these situations the strain in the uniaxial direction (this direction is denoted by $\|$) is imposed and can be accomplished by replacing eq. 2.3 by a predetermined relation. In case of constant-velocity deformation this is

$$L_\|(t) = L_\|(0) + \dot{L}_\| t \tag{2.5}$$

and for constant-rate deformation

$$L_\|(t) = L_\|(0) \exp\left(t/\tau_d\right) . \tag{2.6}$$

In these equations $L_\|(0)$ stands for the initial box size in the axial direction and $\dot{L}_\|$ and τ_d are the control parameters for adjusting the strain velocity and strain rate of the mechanical deformation. Results of these simulations are presented in chapters 5 and 6.

2.2 Interaction types

The potential U_{ff} defines the force in the Newton's equation for a particle (eq. 2.1 and eq. 2.2) and is equal to the sum of all interaction potentials of the particles. For the models we will consider these are two-body, three-body and four-body interactions. The interactions are split into bonded and nonbonded ones. Bonded interactions act only between pre-selected particles (these particles are as a result close to each other), while nonbonded interactions act between all particles (except between some particles which are already bonded, as will be discussed later).

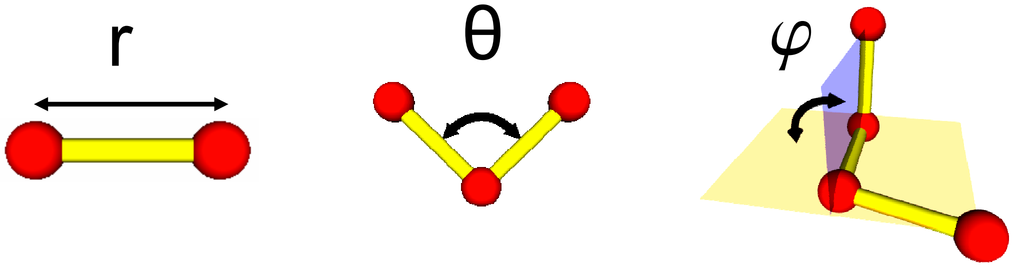

Figure 2.1: Bonded coordinates: covalent bond length (left), valence bond angle (middle) and torsion angle (right).

For the polymer models in use we have three types of bonded interactions, see also fig. 2.1: covalent bonds, valence-angle bonds and torsion bonds. The covalent bond is the only two-body bonded interaction. It arises from two neighbouring atoms i and j sharing their valence electrons (electrons from the outermost unfilled shell of an atom)

$$U_{l,ij} = k_l (r_{ij} - l_0)^2, \tag{2.7}$$

with r_{ij} the distance between the two particles, $2k_l$ the spring constant of this interaction and l_0 the equilibrium length of the bond. This is also the stiffest bond of the three types.

If an atom shares its valence electrons with more atoms, as is the case for the carbon atom, it has more covalent bonds. The valence angle θ between two covalent bonds (fig. 2.1) fluctuates around an equilibrium angle θ_0 with a certain stiffness represented by the constant k_θ. This can therefore be described by the following three-body interaction

$$U_{\theta,ijk} = k_\theta (\theta_{ijk} - \theta_0)^2. \tag{2.8}$$

The last bonded interaction included in the polymer force field is the four-body torsion interaction. In its original form it describes the rotation around a covalent bond. For polymers this rotation is not free, but hindered. The reason for this hinderance lies in the combined effect of electron-electron repulsions, electrostatic repulsions between nuclei and rotation-dependent polarization effects [81] and can be modelled by the following potential

$$U_{\varphi,ijkl} = k_\varphi \cos\left(n\varphi_{ijkl}\right), \tag{2.9}$$

with $2k_\varphi$ the energy barrier separating the minima. The torsion angle φ_{ijkl} is defined as the angle between two planes: that formed by the triplet ijk and that formed by the triplet jkl, see fig. 2.1. So some torsion angles are more preferred than others. For example, in the case of polyethylene (a linear polymer chain in which the backbone atoms are carbons and side groups are absent), the favourable positions are $\varphi = 0°$ (four subsequent carbon atoms lie in a plane and the first and last atom are on opposite side of the middle bond and thus maximally separated) and $\varphi = \pm 120°$. These three positions are named trans and gauche$^{\pm}$, respectively. The conformation $\varphi = \pm 180°$ (all four atoms in a plane but now the first and the last atom are on the same side of the bond and minimally separated) is called cis and is the most unfavourable conformation for polyethylene.

This form of the potential is also used to describe so-called improper-torsion interactions. They serve to keep an atom with its covalently bonded neighbours in a specific arrangement, such as in a planar configuration, as we will see later on. It is called improper, as there is no direct chemical (covalent) bond between the third (k) and fourth (l) atom defining the torsion angle φ_{ijkl}.

We have two types of nonbonded interactions, both of them of two-body type. They are not taken into account for particles which are separated by one or two covalent bonds. The first nonbonded interaction is of electrostatic nature, described by the Coulomb potential

$$U_{C,ij} = \frac{q_i q_j}{4\pi\epsilon_0 r_{ij}}, \tag{2.10}$$

with q_i and q_j the charges of particles i and j, r_{ij} the distance between them and ϵ_0 the permittivity in a vacuum. The other nonbonded interaction in use is due to the Lennard-Jones (LJ) potential that models the induced-dipole–induced-dipole attraction at large separations (van der Waals attraction) and the repulsive interaction due to the nonbonded overlap of electron clouds at short separations

$$U_{LJ,ij} = \epsilon_{ij}\left[\left(\sigma_{ij}/r_{ij}\right)^{12} - 2\left(\sigma_{ij}/r_{ij}\right)^{6}\right]. \tag{2.11}$$

Here $\epsilon_{ij} = \sqrt{\epsilon_i \epsilon_j}$ is a measure for the strength of the interaction and $\sigma_{ij} = \frac{1}{2}\left(\sigma_i + \sigma_j\right)$ a measure for the length scale of the interaction. Both are constants for a given type of particle. The LJ potential has a minimum at $r_{ij} = \sigma_{ij}$ with energy at this well equal to $-\epsilon_{ij}$. For large separations the potential decays much faster to zero than the electrostatic one, as the leading term $\sim r^{-6}$ goes faster to zero than r^{-1} for $r \to \infty$.

Because of the periodic boundary conditions a particle interacts with infinitely many other particles for the non-bonded forces. To deal with this long-range effect two methods are used. As stated before, the LJ interaction is relatively short-ranged. Common practice is therefore to smoothly cut off the potential at a certain distance R_{off}. As long as the cutoff distance is not too short, the dynamics will not be influenced much [6]. To accomplish this we make use of a switching function [205]. The LJ potential $U_{\text{LJ},ij}$ is then replaced by

$$U'_{\text{LJ},ij} = U_{\text{LJ},ij} W_{ij} \tag{2.12}$$

with the switching function

$$W_{ij} = \begin{cases} 1 & r_{ij} \le R_{\text{on}} \\ \frac{(R_{\text{off}}^2 - r_{ij}^2)^2 (R_{\text{off}}^2 - 3R_{\text{on}}^2 + 2r_{ij}^2)}{(R_{\text{off}}^2 - R_{\text{on}}^2)^3} & R_{\text{on}} < r_{ij} < R_{\text{off}} \\ 0 & r_{ij} \ge R_{\text{off}}. \end{cases} \tag{2.13}$$

We use $R_{\text{on}} = 2\sigma_{ij}$ and $R_{\text{off}} = 2.2\sigma_{ij}$. This is smaller than half the minimal length of the orthorhombic box. Note that this switching function only operates for $r_{ij} > R_{\text{on}}$. The smoothness of the function ensures that the first derivative is continuous so that it does not create any jumps in the resulting force.

The electrostatic interactions are long-ranged. To cope with them in combination with periodic boundary conditions, a so-called smooth particle mesh Ewald method is used [6, 72], in order to take into account systems with periodic boundary conditions. In this method a part of the Coulomb interaction is calculated in Fourier space in a form suitable for fast Fourier transformations.

All types of bonded and nonbonded interactions have been given now. To simulate a polymer system one just has to give the parameters of the interactions and pairs, triplets and quartets forming bonded interactions. However, then still freedom of choice remains in the configuration of some polymers, like polystyrene. Configurational isomers are molecules which have the same chemical bonds, but differ only from each other in the arrangements of their atoms and cannot be converted into each other by rotations around single bonds [69]. For example, some molecules exist in both a left-handed form and a right-handed one (just as one cannot rotate a left hand in three-dimensional space to let it superimpose onto the right hand). As we will see in §2.3 this configurational isomerism is also occurring with polystyrene.

Based on quantum-mechanical calculations it is known that cross terms (such as a potential term depending on both the bond length and bond angle) are in principle present as well. Also interaction which involves even more particles or more complicated expressions for the current potentials should give a better description of the studied material. Of course this is at the expense of computational power. However, the results acquired with the current level of description give already satisfactory results, as has been demonstrated thoroughly before in literature (and as we will see later on).

2.3 Polystyrene model

The monomer unit of polystyrene is depicted in fig. 2.2. It is made solely of carbon and hydrogen atoms. We use a united-atom model, meaning that there are no explicit hydrogen atoms present, but instead they are collapsed on the carbon atoms and treated as an effective particle. The motivation for using this model for polystyrene is that the speed-up of the calculations as compared to the all-atom model is a factor of about 10, while structural information is reproduced within the error of experimental data [187]. The monomer unit consists of a backbone (-CH-CH_2-) with a side group attached to it, the phenyl ring (-C_6H_5).

The monomer unit is not enough to describe the configurational structure of polystyrene.

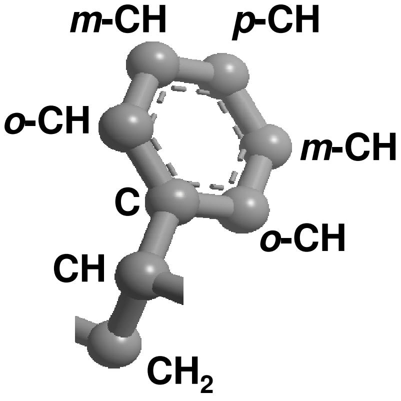

Figure 2.2: Monomer unit of the polystyrene model with the naming convention of the (united) atoms. Here o=ortho, m=meta and p=para [69]. The notation x-CH is used for any of the three possible positions of the CH group in the phenyl ring.

This is because two different types of dyads (a dyad consists of two neighbour monomer units) are possible: a meso and a racemic dyad. Both types are exemplified in fig. 2.3. In a meso dyad a plane of symmetry is present in between the two phenyl rings, while in a racemic dyad this mirror plane is absent. For an isotactic polystyrene chain only meso dyads are present, while a syndiotactic polystyrene chain contains solely racemic dyads. The system under present investigation consists of atactic chains, meaning that each chain is composed of a random sequence of meso and racemic dyads. The ratio of the number of meso to the number of racemic dyads is chosen to be near unity. Systems made of isotactic or syndiotactic chains of polystyrene are able to crystallize. The frozen-in disorder of the sequence of the dyads in atactic polystyrene prevents the system from crystallization.

The parameters for the currently used united-atom force field of polystyrene are based on those given by Mondello et al. [187] and used before by Lyulin et al. [176]. Since it has not documented in a complete form before, we will do so here. The force field of the present study differs from Mondello et al. [187] in some parts, namely that the bonds and the valence angles in the phenyl ring are now flexible, the planarity of the phenyl ring is accomplished as is done by Han and Boyd [109] and the tacticity of the chain is maintained by a different improper-torsion potential from that implemented by Mondello et al. [187].

The parameters for each type of atom are given in table 2.1. The parameters for the CH_3 united atoms positioned at the chain ends are the same as for CH_2. The mass m of each (united) atom is calculated using $m_C = 12$ Da and $m_H = 1$ Da. In this table X stands for the (united) atom having a chemical bond with the (united) atom next to it.

The improper torsion listed first in table 2.1 serves for keeping the o-CH, C and CH-group in a plane. The second one is used for maintaining the tacticity of the chain. The four

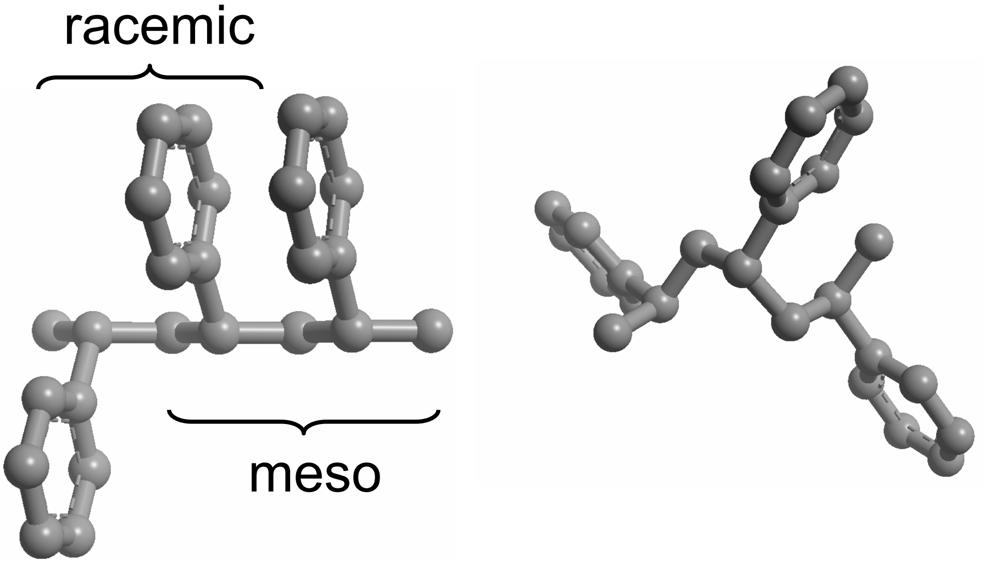

Figure 2.3: (left) An example of a pair of neighbouring monomers in a racemic dyad (left pair) and in a meso dyad (right pair) for a backbone in the planar trans state. (right) The same chain segment but now in a random sequence of gauche$^{\pm}$ states.

consecutive (united) atoms defining the improper torsion are for the (united) atoms around the CH-united atom (X–CH–X–X'): C–CH–CH$_2$–CH$_2$, CH$_2$–CH–CH$_2$–C and CH$_2$–CH–C–CH$_2$; and for the united atoms around the C atom (X–C–X–X'): x-CH–C–x-CH–CH, x-CH–C–CH–x-CH and CH–C–x-CH–x-CH.

2.4 Polycarbonate model

Polycarbonate (PC) is a prototypical material, in the sense that is the example of a very tough and ductile amorphous polymer glass as compared to polystyrene. In a uniaxial-stress elongation test PC breaks only after a 100% increase in length, while brittle PS already breaks within a few percent of length increase [266]. However, the molecular origin for this difference is still unknown. Polycarbonate is therefore the ideal material to study, in order to compare it with the mechanically oppositely behaving material made of polystyrene chains. The method of molecular-dynamics simulations is perfectly suited for this, because it gives insight at an atomistic level. The polycarbonate under investigation is a short name for bisphenol-A polycarbonate and its complete chemical name is 2,2-bis(4-hydroxyphenyl)propane polycarbonate [256], or 4,4'-isopropylidenediphenol polycarbonate [130]. Some commercial names are Makrolon (from Bayer) or Lexan (GE). Polycarbonate is, in contrast to polystyrene, a heterochain polymer, meaning that the backbone consists of multiple atom types. In the case of PC also oxygen atoms are present in the backbone. The monomer unit is depicted in fig. 2.4.

Table 2.1: The united-atom force field in use for atactic polystyrene. See text for details.

Force field
Non-bonded interactions (eq. 2.11)
$\epsilon = 0.377$ kJ mol^{-1}, σ=4.153 Å for CH
$\epsilon = 0.502$ kJ mol^{-1}, σ=4.321 Å for CH_2
$\epsilon = 0.502$ kJ mol^{-1}, σ=4.153 Å for C and x-CH
Bond stretching (eq. 2.7)
$k_l = 669$ kJ mol^{-1} Å^{-2}, $l_0 = 1.53$ Å for CH_2–CH
$k_l = 669$ kJ mol^{-1} Å^{-2}, $l_0 = 1.51$ Å for CH–C
$k_l = 669$ kJ mol^{-1} Å^{-2}, $l_0 = 1.40$ Å for C–x-CH
$k_l = 669$ kJ mol^{-1} Å^{-2}, $l_0 = 1.40$ Å for x-CH–x-CH
Bond angle (eq. 2.8)
$k_\theta = 251$ kJ mol^{-1} rad^{-2}, $\theta_0 = 109.5°$ for X–CH–X
$k_\theta = 264$ kJ mol^{-1} rad^{-2}, $\theta_0 = 109.5°$ for X–CH_2–X
$k_\theta = 293$ kJ mol^{-1} rad^{-2}, $\theta_0 = 120.0°$ for X–C–X and X–x-CH–X
Torsion (eq. 2.9)
$k_\varphi = -2.93$ kJ mol^{-1}, $n = 3$ for X–CH–CH_2–X
$k_\varphi = -2.09$ kJ mol^{-1}, $n = 2$ for X–CH–C–X
$k_\varphi = 27.2$ kJ mol^{-1}, $n = 2$ for X–C–x-CH–X
$k_\varphi = 54.4$ kJ mol^{-1}, $n = 2$ for X–x-CH–x-CH–X
Improper torsion (eq. 2.9)
$k_\varphi = 20.9$ kJ mol^{-1}, $n = 2$ for X–C–X–X'
$k_\varphi = 20.9$ kJ mol^{-1}, $n = 3$ for X–CH–X–X'

The force field for polycarbonate is the same as was used by Lyulin et al. [177] and is based on the force field by Hutnik et al. [128]. For the sake of completeness and because it is not documented in a complete form before, we will give the details here. Parameters are given in table 2.2. Differences from the force field by Hutnik et al. [128] are that the bonds and the valence angles are now flexible, the torsions have simpler potentials and the phenyl rings consist of united atoms. The covalent-bond force constants are equal to about half the value of a 'pure' C-C bond of the AMBER force field [278] (allowing for a larger integration time step while the effect on dynamical properties such as on transition rates is only small [119], and has been done before for other MD simulations of polymeric systems as well). The bond length parameter l_0 of the CH-united atom is as of Weiner et al. [278]. The same accounts for the valence angle force constant for O-$C_{C=O}$-O [278] (the constant for O-$C_{C=O}$-$O_{C=O}$ is equal to this one). The valence angle force constant for X-CT-X is the same as for CH_2-CH_2-CH_2 as given by Weiner et al. [278]. The valence angle force constants for the triplets X-C-X, X-C_+-X and X-CH-X are the same as for CH-C-CH_2 by Weiner et al. [278]. The planarity of the phenyl ring is accomplished as is done by Han and Boyd [109]. The mass m of each (united) atom is determined using $m_O = 16$ Da,

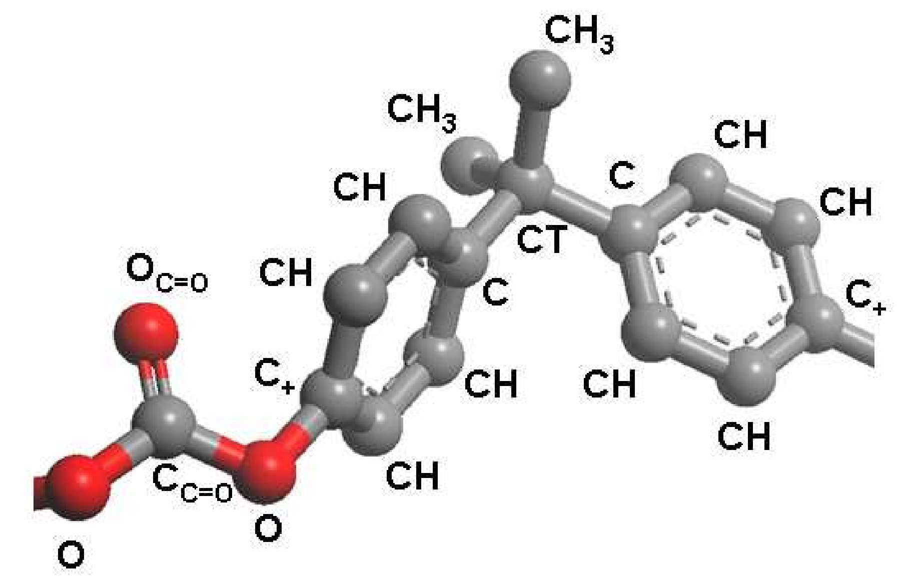

Figure 2.4: Monomer unit of the polycarbonate model with the naming convention of the (united) atoms. The naming of CT is after the AMBER force field [278], $C_{C=O}$ and $O_{C=O}$ for carbons having a double covalent bond and C_+ to distinguish it from C, as C_+ has a positive partial charge in this model (see table 2.2).

$m_C = 12$ Da and $m_H = 1$ Da. As with polystyrene the X stands for the (united) atom having a chemical bond with the (united) atom next to it.

The parameters for the LJ diameters and energies are equal to those given by Hutnik et al. [128], in which each LJ energy ϵ_i is calculated from the polarizability α_i and effective number of electrons $N_{e,i}$ by using the Slater-Kirkwood equation for it. This equation reads in atomic units $\epsilon_i = \frac{3\alpha_i^2}{8\sqrt{\alpha_i/N_{e,i}}\sigma^6}$ [98]. The radius for the united-atom CH is the same as used by Weiner et al. [278]. The values of the partial charges q' as given in table 2.2 are in units of the charge of one electron and are from Hutnik et al. [128] (the charge of CH is taken to be the sum of its two constituents).

As with polystyrene every sequence of three covalent bonds has an associated torsion-potential term. For example, around a specific C-CT bond six torsions are operational, while around a CH-CH bond only one is operational.

The improper torsions present in polycarbonate only serve to keep a triple-bonded atom with its three neighbours in a plane. These groups are the C atom with neighbours CH, CH and CT; the C_+ atom with neighbours CH, CH and O; and the $C_{C=O}$ atom with neighbours O, O and $O_{C=O}$. For each triple-bonded atom three torsion contributions are present. The four consecutive (united) atoms defining the improper-torsion angle around the C-united atom (X–C–X–X') are: CH–C–CT–CH, CT–C–CH–CH and CH–C–CH–CT;

Table 2.2: The united-atom force field in use for 4,4'- isopropylidenediphenol polycarbonate (bisphenol A polycarbonate). See text for details.

Force field
Nonbonded interactions (eqs 2.10 and 2.11)
$\epsilon = 0.748$ kJ mol^{-1}, σ=3.40 Å, $q' = 0.5$ for $C_{C=O}$
$\epsilon = 0.492$ kJ mol^{-1}, σ=3.40 Å, $q' = 0$ for CT
$\epsilon = 0.784$ kJ mol^{-1}, σ=3.80 Å, $q' = 0$ for CH_3
$\epsilon = 1.058$ kJ mol^{-1}, σ=3.00 Å, $q' = -0.3$ for $O_{C=O}$
$\epsilon = 0.805$ kJ mol^{-1}, σ=3.00 Å, $q' = -0.18$ for O
$\epsilon = 0.450$ kJ mol^{-1}, σ=3.70 Å, $q' = 0$ for C and CH
$\epsilon = 0.450$ kJ mol^{-1}, σ=3.70 Å, $q' = 0.08$ for C_+
Bond stretching (eq. 2.7)
$k_l = 669$ kJ mol^{-1} Å^{-2}, $l_0 = 1.53$ Å for CH_3–CT
$k_l = 669$ kJ mol^{-1} Å^{-2}, $l_0 = 1.54$ Å for C–CT
$k_l = 669$ kJ mol^{-1} Å^{-2}, $l_0 = 1.40$ Å for C–CH, C_+–CH and CH–CH
$k_l = 669$ kJ mol^{-1} Å^{-2}, $l_0 = 1.41$ Å for C_+–O
$k_l = 669$ kJ mol^{-1} Å^{-2}, $l_0 = 1.33$ Å for $C_{C=O}$–O
$k_l = 669$ kJ mol^{-1} Å^{-2}, $l_0 = 1.21$ Å for $C_{C=O}$–$O_{C=O}$
Bond angle (eq. 2.8)
$k_\theta = 335$ kJ mol^{-1} rad^{-2}, $\theta_0 = 125.5°$ for O–$C_{C=O}$–$O_{C=O}$
$k_\theta = 335$ kJ mol^{-1} rad^{-2}, $\theta_0 = 109.0°$ for O–$C_{C=O}$–O
$k_\theta = 264$ kJ mol^{-1} rad^{-2}, $\theta_0 = 109.5°$ for X–CT–X
$k_\theta = 293$ kJ mol^{-1} rad^{-2}, $\theta_0 = 124.0°$ for X–O–X
$k_\theta = 293$ kJ mol^{-1} rad^{-2}, $\theta_0 = 120.0°$ for X–C–X, X–C_+–X and X–CH–X
Torsion (eq. 2.9)
$k_\varphi = 5.23$ kJ mol^{-1}, $n = 2$ for X–$C_{C=O}$–O–X
$k_\varphi = 1.05$ kJ mol^{-1}, $n = 2$ for X–C_+–O–X
$k_\varphi = -1.05$ kJ mol^{-1}, $n = 4$ for X–C–CT–X
$k_\varphi = 27.2$ kJ mol^{-1}, $n = 2$ for X–C–CH–X and X–C_+–CH–X
$k_\varphi = 54.4$ kJ mol^{-1}, $n = 2$ for X–CH–CH–X
Improper torsion (eq. 2.9)
$k_\varphi = 20.9$ kJ mol^{-1}, $n = 2$ for X–C–X–X', X–C_+–X–X' and X–$C_{C=O}$–X–X'

around the C_+ atom (X–C_+–X–X'): CH–C_+–O–CH, O–C_+–CH–CH and CH–C_+–CH–O; and around the $C_{C=O}$ atom (X–$C_{C=O}$–X–X'): $O_{C=O}$–$C_{C=O}$–O–O, O–$C_{C=O}$–O–$O_{C=O}$ and O–$C_{C=O}$–$O_{C=O}$–O.

The ends of the chains are 2,2 diphenylpropane units. Other possibilities would be to end with the diphenylcarbonate units, as is done in Hutnik et al. [128] or Leon et al. [166]. For long chains, however, the ending units will have only a minor influence on the overall properties.

2.5 Sample preparation

The polymer samples are prepared by a procedure similar to that of Lyulin and Michels [171], starting with a one-chain system of the polymer chain in question (either a 80-monomer chain for polystyrene or a 10-monomer chain for polycarbonate). After the equilibration of this single chain, the orthorhombic box is doubled in all three directions in the case of polystyrene and quadrupled in all three directions in the case of polycarbonate, making the total number of chains per sample equal to 8 (PS) and 64 (PC). The resulting sample is equilibrated further for about 10 ns at $T = 540$ K for PS and at $T = 600$ K for PC. To correct for the potential cutoff and any other force-field deviations the pressure has been adjusted so that the density at these high melt temperatures equals the experimentally observed density at atmospheric pressure. For PS the experimental density at $T = 540$ K is determined by a linear extrapolation from lower temperatures [293], making the target density at this temperature equal to 0.916 $\mathrm{g\,cm^{-3}}$. For PC the target density is 1.05 $\mathrm{g\,cm^{-3}}$ [166]. At these pressure offsets the samples are subsequently cooled to the desired temperature, typically by 0.01 $\mathrm{K\,ps^{-1}}$. For both polymers this process is carried out for five independent samples, in order to increase statistics.

Chapter 3

Non-Gaussian behaviour of glassy dynamics by cage to cage motion

ABSTRACT

A model based on a single Brownian particle moving in a periodic effective field is used to understand the non-Gaussian dynamics in glassy systems of cage escape and subsequent recaging, often thought to be caused by a heterogeneous glass structure. The results are compared to molecular-dynamics simulations of systems with varying complexity: a quasi-two-dimensional colloid, atactic polystyrene, and a dendritic glass. The model nicely describes generic features of all three topologically different systems, in particular around the maximum of the non-Gaussian parameter. This maximum is a measure for the average distance between cages.

The contents of this chapter are for a large part published in Phys. Rev. E, **75**, 011504 (2007). Copyright 2007 by the American Physical Society.

3.1 Introduction

The most striking feature of glass-forming liquids is a rapid increase of their viscosity when temperature decreases. Usually, the glass-transition temperature is defined as the temperature at which the viscosity reaches 10^{12} Pa s for simple liquids, or at which the intrinsic relaxation time of the material exceeds the experimental time scale. Yet relaxation in liquids and glasses is still an unresolved problem in soft-matter physics [68].

Extensive research has been carried out to study the dynamic *heterogeneity* of the glassy state. Many interpretations exist for this concept of heterogeneous dynamics. A common one is that heterogeneous dynamics is applicable when individual relaxing units have site-specific relaxation times [215]. The size of a relaxing unit is typically a few nm for glasses such as ortho-terphenyl [215]. A conventional way to quantify this type of heterogeneity is the observation that the non-Gaussian parameter (NGP) [207]

$$\alpha_2(t) = \frac{\langle \Delta\mathbf{r}(t)^4 \rangle}{(1 + 2/d)\langle \Delta\mathbf{r}(t)^2 \rangle^2} - 1 \tag{3.1}$$

is nonzero. Here $\Delta\mathbf{r}(t) = \mathbf{r}(t_0 + t) - \mathbf{r}(t_0)$ is the displacement of a particle after a time interval t, d the spatial dimension and $\langle \cdots \rangle$ denotes ensemble averaging. For a system of identical particles described by the diffusion equation, the mean-square translational displacement (MSTD) of a particle increases linearly in time, and the Van Hove self-correlation function $\langle \delta(\mathbf{R} - \Delta\mathbf{r}(t)) \rangle$ [262] has a Gaussian shape. In this case the NGP is zero. For an ensemble of identical particles in the ballistic regime with a velocity given by the Maxwell-Boltzmann distribution the self part of the Van Hove function is also of a Gaussian shape and the NGP equals zero as well.

It is indeed observed that many simulations of monatomic [127, 207, 291] and binary systems [80, 151], polydisperse liquids [58], metallic glasses [149], salts [132], small molecules [236], glassy networks [121], and polymers [221] do show a non-zero value of the NGP. This behaviour is also observed in experiments on colloidlike particles using confocal microscopy [276] and on glassy polymer systems by means of neutron scattering [294]. A particular result is that the NGP peaks at a time t^*, corresponding to the crossover between the so-called cage regime and the diffusive regime of the MSTD. The cage escape is associated with complex dynamic behaviour, involving complicated clusters in space and correlated jumps in time. Typical values of the maximum of the NGP range from 0.1 to 10 but higher or lower values have been observed as well.

Nevertheless, the relation between deviations from Gaussian behaviour and dynamic heterogeneity in the sense of different relaxation units is not obvious. First note that many causes of non-Gaussian behaviour exist, also in glasses. A few possible sources are: averaging over intrinsically different types of particles, crossover from ballistic to diffusive motion [54], or anharmonic motion within a cage [294]. The focus of the present study is on non-Gaussian behaviour (NGB) occurring close to the glass transition, and related to cage-escape dynamics. Various models are in use, to shed some light on this type of NGB. One of the current models is the well-known mode-coupling theory (MCT) for the glass transition [87, 143]. Yet it predicts a time dependence of $\alpha_2(t)$ which differs significantly from simulation results and, moreover, may strongly underestimate (by about one order of magnitude) the deviations from Gaussian behaviour close to the glass transition [80]. The local-mobility model [127] connects the deviations from Gaussian behaviour with a fluctuating diffusion coefficient. However, it has the disadvantage that *a priori* it is not clear to what extent the concept of fluctuating mobilities is reasonable [58]. The trapping-diffusion model of Odagaki and Hiwatari [198] captures the glassy heterogeneity in a broad relaxation spectrum. It has some communalities with the model of the present study. However, as we will see, a major difference is that it is based on a totally different relaxation spectrum and it predicts that the average relaxation time diverges at the glass transition (as is also the case with the ideal MCT). This is usually not observed both in experiments and in simulations [52]. Yet another model [11] tries to describe non-Gaussian behaviour by assuming a wide distribution of jump lengths causing the heterogeneous dynamics. The most probable jump distance is then interpreted as a localization length. Each of the last three models assumes some distribution (either in time, jump lengths or diffusion coefficients) to capture a heterogeneous aspect and to explain the non-Gaussian behaviour. Still no consensus exists which process is dominating for the non-Gaussian behaviour around cage escape and how to quantify this.

The aim of the present study is to employ a simple model for capturing the main physical mechanism underlying the non-Gaussianity of glassy dynamics. The purpose of the model is not to express the glassy dynamics in its full detail (such as aging effects, backscattering, heterogeneity), but only the part which we think is the most relevant for the description of non-Gaussian behaviour. In particular it does not assume any heterogeneity in the sense of site-specific relaxation times. The analytical low-temperature results are found to describe quantitatively important features of the NGP acquired by molecular dynamics (MD) simulations of three different kinds of systems: a quasi-two-dimensional colloidlike system, atactic polystyrene and a dentritic glass, thereby suggesting that the model describes the main process creating non-Gaussian behaviour.

3.2 Model

A particle in a liquid is surrounded by neighbours which hinder its motion, and caging occurs. For example, if the interaction between particles is soft repulsive, the hindered particle needs to overcome an effective energy increase to get closer to the edge of the cage, as it approaches the neighbours. Therefore it is trapped in a local energy minimum. The flanking neighbour particles can lower the increase in energy by moving away and creating more vacancy, or by some other sort of collective rearrangement. After passing the flanking neighbours this particle is again in a local energy minimum if the particle previously at this

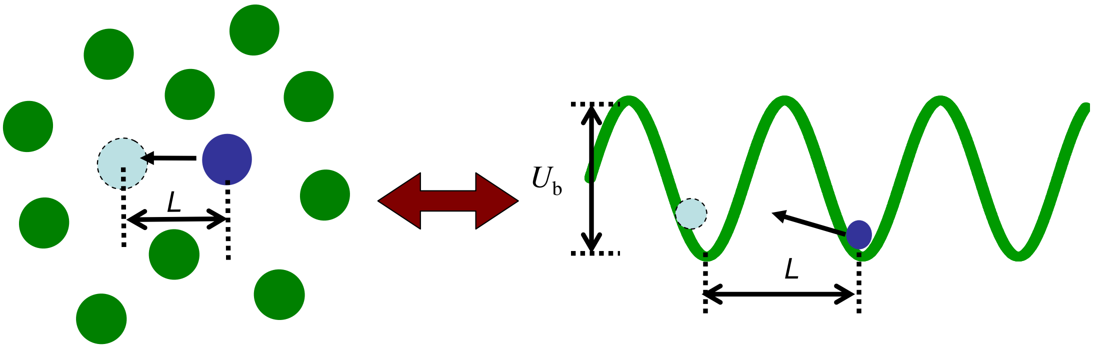

Figure 3.1: Schematic view of the effective neighbourhood model, in which the particle jumps from one cage to another.

position experiences a similar type of movement (thereby causing stringlike motion [62]), or if another cooperative mechanism has created enough space. So the particle passed an effective energetic barrier. In this new caged position the mechanism repeats itself.

This effect of caging and subsequent cage escape to a new cage can be modelled by the motion of a single particle in an effective field describing the interactions with the neighbour particles in the following way. The particle in question experiences frequent collisions with its neighbours. As the surrounding particles have zero velocity on average, the collision is harder if the velocity of the particle is higher. We describe these two effects by a friction force and a stochastic force acting on the particle. The energy barrier to be passed is modelled by an effective potential. This can be interpreted as a mean-field-like potential. To keep the model simple we restrict ourselves for the moment to the one-dimensional (periodic) sine function. Later on it will be shown that the resulting non-Gaussian parameter does not depend much on the precise shape of this potential, nor on its dimension.

Note that the actual potential is highly fluctuating in space and time, leading to strongly correlated processes at the short time scale. One example of such correlation is that easy local transitions are frequently reversed and repeated, leading to strong back-scattering sequences in the process. Such correlated processes can be resummed in a way as is done in the multiple-scattering theory for transport in disordered media [188, 269]. In this picture the atomistic diffusion process can be described quantitatively by a site-to-site hopping process with a large spread in transition probabilities. The resulting mobility, which has a similarity with the diffusion coefficient via the Einstein relation, can then be expressed in terms of effective site-to-site propagation probabilities. These probabilities are then expanded in a multiple-scattering perturbation series involving all other sites. To deal with the correlations the perturbation series is reordered into a renormalized self-avoiding-path expansion, in which closed-loop processes (in particular direct back-scattering events) are fully summed first. After making a closure in the expansion by uncorrelating at a higher level of approximation (e.g., via a T-matrix approximation), one then arrives at a description of the diffusion process on a coarse-grained effective level. When considered at a coarse-grained time scale, the diffusion coefficient contains the local correlated processes, while the effective time constant has the meaning of a dwelling time, i.e., the time after which the probability for a series of repeated local events equals the probability for an escape over a hard local barrier. These hops over a hard barrier have a very small probability of reversal, so that for times above the time scales associated with this process the dynamics can to a good approximation indeed be treated as uncorrelated. The present study is restricted to such a coarse-grained picture, with strong back-scattering events resummed. The surrounding cage potential of the particle in question is then also averaged, which justifies the use of the simple sinusoidal potential.

In the above picture, the dynamics of a particle inside an external field is captured in the Langevin equation (fig. 3.1)

$$m\frac{\partial^2 x(t)}{\partial t^2} + \zeta\frac{\partial x(t)}{\partial t} = -\frac{\partial U(x)}{\partial x} + \zeta f(t), \tag{3.2}$$

with m the mass of the particle, ζ the friction constant, $-\frac{\partial U(x)}{\partial x}$ the force acting on the particle due to the external potential $U(x) = \frac{1}{2}U_b \sin(\frac{2\pi x}{L})$ and $\zeta f(t)$ a random force, of which the first moment is zero and the second moment is $\langle f(t)f(t')\rangle = 2D_0\delta(t-t')$. Here $D_0 = \frac{k_BT}{\zeta}$ is the coarse-grained bare diffusion constant of the particle, U_b the height of the energy barrier, L the (effective) distance between cages and k_B Boltzmann's constant. We limit ourself to cases where the inertial term can be neglected, in which the long-time diffusion coefficient of the particle in the sine potential is given by $D = \frac{L^2}{2d\tau} = D_0\left(I_0(\frac{U_b}{2k_BT})\right)^{-2}$ [217], where I_0 is the modified Bessel function of the first kind and τ is the average time to travel a distance L under the influence of the potential; so τ is of the order of the dwelling time as discussed above.

The non-Gaussian parameter for the dynamics of the particle under the influence of the external potential can be calculated analytically for a sufficiently low temperature-to-barrier ratio, $\frac{k_BT}{U_b} \ll 1$. In this limit the minimum of the potential can be approximated by a parabola. For very small times the particle is diffusing freely, $\langle \Delta\mathbf{r}(t)^2\rangle = 2dD_0t$. After some time its dynamics is influenced by the potential and the particle becomes trapped; the MSTD reaches a constant value of $\langle \Delta\mathbf{r}(t)^2\rangle = \Delta^2$. Time scales up to the start of caging at $t = t_c = \Delta^2/(2dD_0)$ will be discarded in this calculation. For longer times the particle mostly vibrates in a potential minimum n and due to thermal excitation it occasionally jumps to neighbouring minima; the jumping part of the particle motion then obeys the master equation [263]

$$\frac{\partial \Psi_n(t)}{\partial t} = \frac{D}{L^2}\left(\Psi_{n-1}(t) + \Psi_{n+1}(t) - 2\Psi_n(t)\right), \tag{3.3}$$

with $\Psi_n(t)$ the probability that the particle is in a potential well n at time t. It is now straightforward to generalize this one-dimensional random-walk master equation to higher (spatial) dimensions to afford a better comparison to simulation results. The assumption that the MSTD inside a well is of Gaussian nature leads to (see Appendix 3.A)

$$\langle \Delta\mathbf{r}(t)^2 \rangle = \Delta^2(1 + t/t^*) = \Delta^2 + 2dDt, \tag{3.4}$$

and

$$\langle \Delta\mathbf{r}(t)^4 \rangle = (1 + 2/d)\langle \Delta\mathbf{r}(t)^2 \rangle^2 + 2dDtL^2, \tag{3.5}$$

with $t^* = \Delta^2/(2dD)$ and Δ^2 the MSTD within the cage (the plateau value, due to the rattling motion inside the cage). Substituting eqs 3.4 and 3.5 in eq. 3.1 yields the high-effective-barrier result

$$\begin{aligned} \alpha_2(t) &= \frac{L^2}{(1+2/d)\Delta^2}\frac{t/t^*}{(1+t/t^*)^2} \\ &= \frac{L^2}{(1+2/d)\Delta^2}\frac{2dDt/\Delta^2}{(1+2dDt/\Delta^2)^2}, \end{aligned} \tag{3.6}$$

with $d = 1$ for the random walk described by eqs 3.2 and 3.3. Equation 3.6 in this exact form is also valid for a broader class of random walks, which includes a random walk in random directions, and on regular triangular and cubic lattices (this last case is considered by Odagaki and Hiwatari [198]); also a distribution of jump lengths results in the same expression (then L represents an effective jump length).

As an additional outcome of the model the fraction of particles which have jumped at least once after some time t can be determined. In the high-effective-barrier limit this fraction is given by $\phi_j(t) = 1 - \exp(-\frac{2dDt}{L^2})$. At t^* this is expressible in terms of the maximum value of the NGP $\phi_j^* = 1 - \exp(-\frac{\Delta^2}{L^2}) = 1 - \exp(-\,(4(1+2/d)\alpha_2^*)^{-1})$. For a typical value of $\alpha_2^* = 2.0$, we have $\phi_j \approx 0.072$, which can be interpreted as the fraction of mobile particles at $t = t^*$.

We summarize our main claims as follows. First of all, a simple one-particle model is suggested which allows an analytical solution for the NGP. In the low temperature-to-barrier case the maximum of $\alpha_2(t)$ is determined by the ratio of the squared jump distance and the value of the MSTD in the cage,

$$\alpha_2^* = \alpha_2(t^*) = \frac{L^2}{4(1+2/d)\Delta^2}. \tag{3.7}$$

Finally, the time at which the NGP peaks, $t = t^*$, is when the rattling part of the MSTD (Δ^2 in eq. 3.4) equals the diffusive part ($2dDt^*$ in eq. 3.4). For higher ratios of $\frac{k_BT}{U_b}$, where the plateau region of the MSTD is not that pronounced (see fig. 3.2), eq. 3.6 is not applicable. In this case the model can be solved numerically and it is still possible to define the crossover time between caged motion and final diffusion as the point at which on a log-log plot for the MSTD vs. time the two tangent lines (to the cage regime and to the final diffusive regime) intersect. Again this time is close to t^* (fig. 3.2).

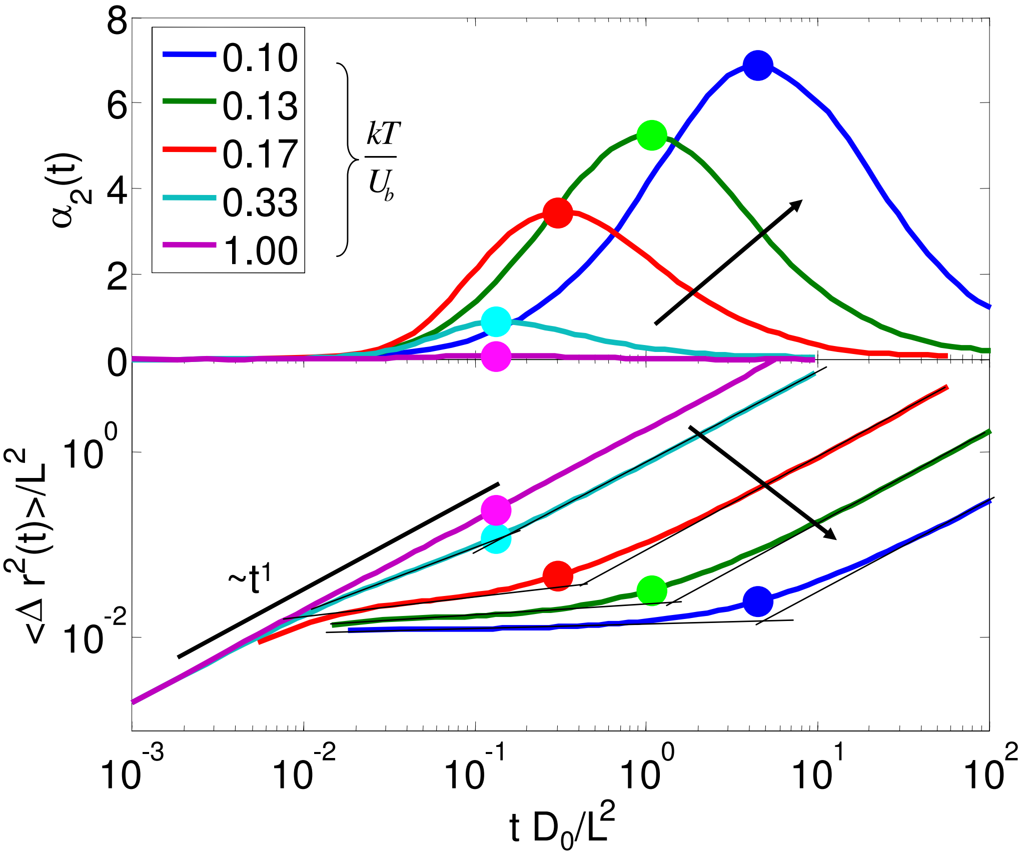

Figure 3.2: Predictions of the model for the NGP (upper panel) and the MSTD (lower panel) for various $\frac{k_B T}{U_b}$ ratios. The arrows point towards decreasing ratios. Results are obtained by numerically integrating eq. 3.2 [55, 217]. The time t^* at which $\alpha_2(t)$ peaks (indicated by bullets) agrees well with the crossover from the cage regime to the final diffusion (intersection of black solid lines).

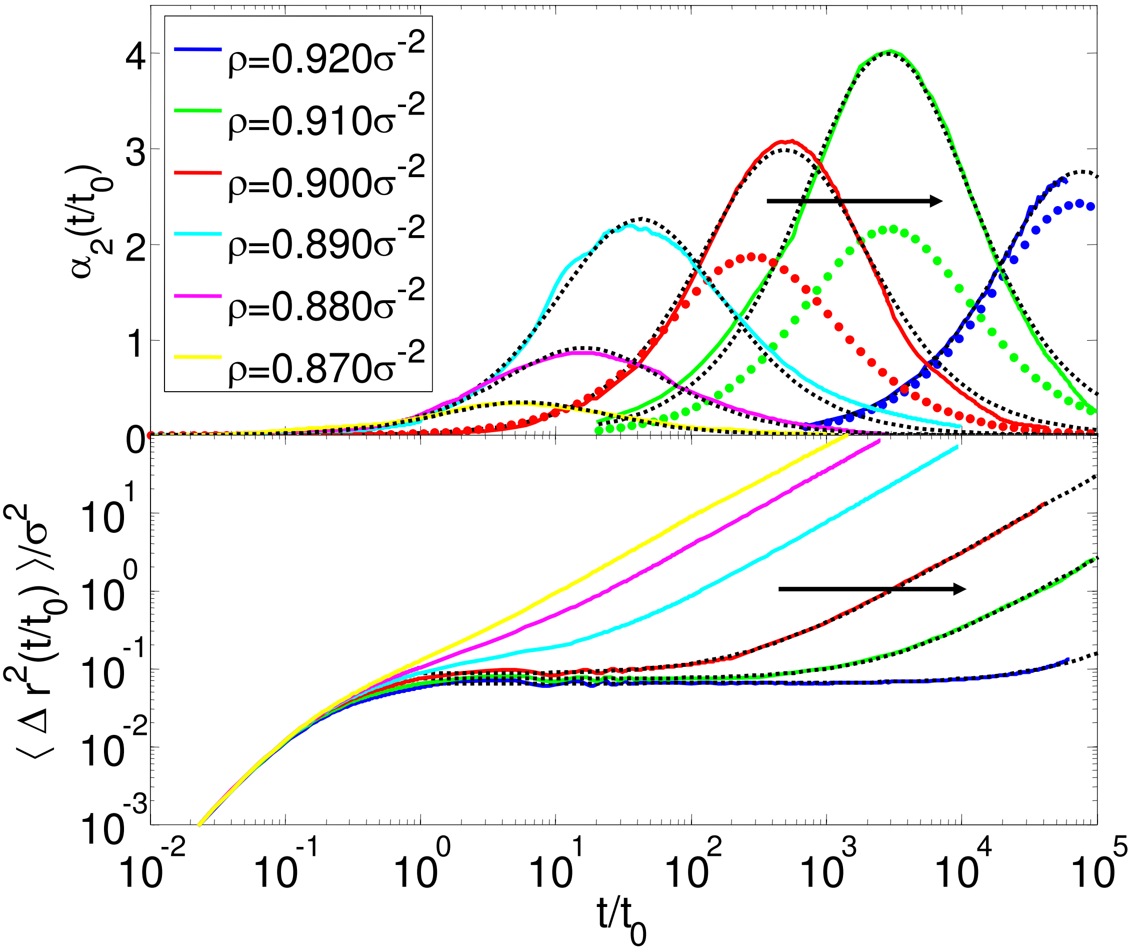

Figure 3.3: Predictions of the model and simulation results for the colloidlike system [291] for various densities ρ, for the NGP and MSTD parallel to the slab. The arrows point towards increasing densities. Here t_0 is the unit of time [291]. Black lines (small dots) are fits of the model (MSTD: eq. 3.4; NGP: eq. 3.6) to the simulation results (solid coloured lines). The coloured lines (large dots) for the NGP are predictions of the model by an independent set of parameters, see main text.

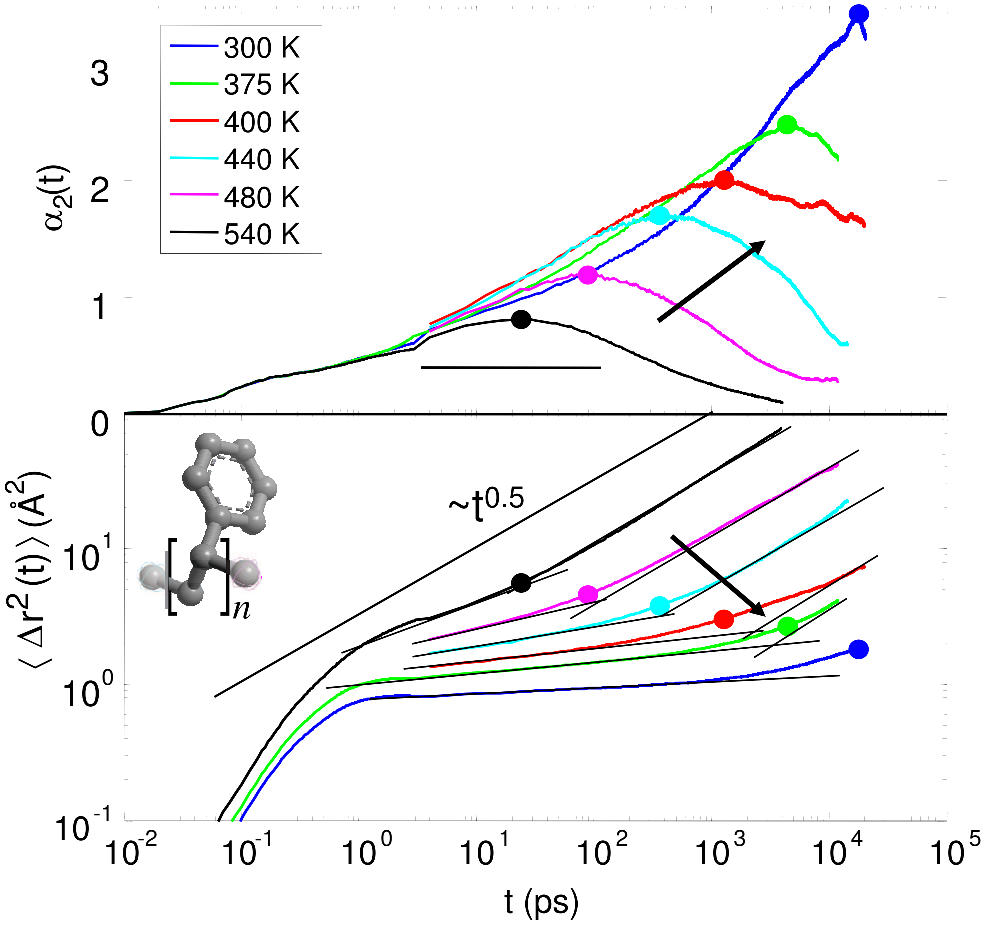

Figure 3.4: NPG and MSTD of atactic polystyrene (shown is the monomer unit) for various temperatures. The arrows point towards decreasing temperatures. The MSTD crossover time from caging to Rouse diffusion ($\langle \Delta \mathbf{r}(t)^2 \rangle \sim t^{0.5}$ [55]) is close to the time at which $\alpha_2(t)$ peaks. The horizontal bar indicates the FWHM of the NGP for a time-independent diffusion coefficient (see text).

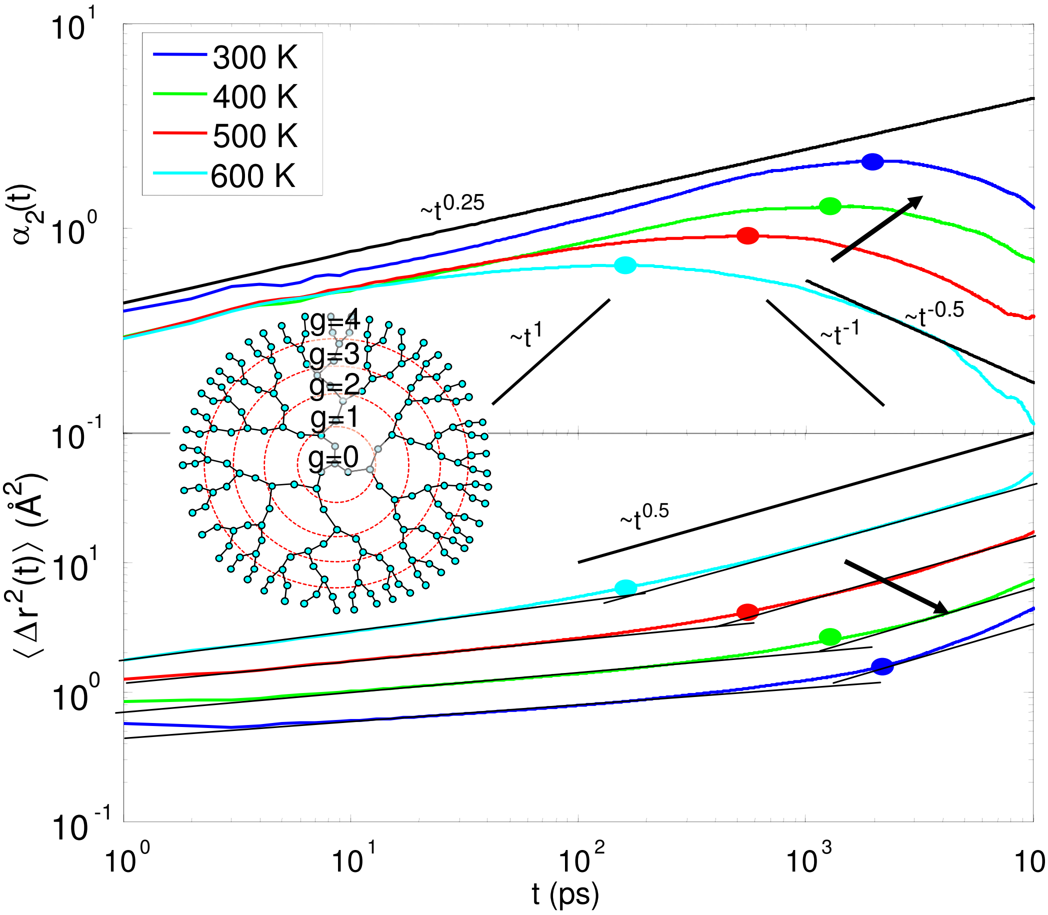

Figure 3.5: Same as fig. 3.4, but for the dendrimer melt, of which the architecture is shown.

3.3 Comparison with simulation results

We compare the predictions of the model to results from simulations of three distinctly different glassy systems. The quasi-two-dimensional colloidlike monatomic system simulated by Zangi and Rice [291] shows NGB. Here particles of diameter σ are confined to a slab with a width $W = 1.2\sigma$ and interact with each other via a purely repulsive potential. Simulation results of Zangi and Rice [291] for the in-plane MSTD and NGP are fitted with the model for various number densities ρ in two ways. First we use eq. 3.6 and treat $t^* = \Delta^2/(2dD)$ and the ratio L^2/Δ^2 as two adjustable parameters. In this case the full shape of the NGP is reproduced remarkably well (see the full coloured lines vs. black dotted lines in fig. 3.3), especially for high densities (i.e., high effective barriers). Note that the analytical expression for the NGP, eq. 3.6, implies that its full width at half maximum (FWHM) on a log scale is not adjustable but has the constant value of $w = \log_{10}(t_{\text{high}}/t_{\text{low}}) = \log_{10}(17 + 12\sqrt{2}) \approx 1.53$. Nevertheless it adequately describes the simulation results, $w = 1.43$ and 1.48 at $\rho = 0.900\sigma^{-2}$ and $0.910\sigma^{-2}$, respectively.

Alternatively, we can find the values of the model parameters for the NGP in an independent way, namely from the MSTD together with an estimate of the cage to cage distance. Fitting the simulated MSTD for the densities for which there exists a definite plateau ($\langle \Delta\mathbf{r}(t)^2 \rangle \sim t^0$) with eq. 3.4 renders the plateau value Δ^2 and a prediction for t^*. To determine the maximum value of the NGP, α_2^*, the effective jump length L is needed as well. Presuming that it corresponds to the distance between the nearest neighbours, L is calculated by assuming that the particles are placed on a triangular lattice, so that $L^{-2} = \frac{\sqrt{3}}{2}\rho$.

Two distinct aspects are observed when comparing this alternative fit to the simulation results (compare solid vs. large-dotted coloured lines, fig. 3.3). First, it can be seen that the cage-diffusion crossover time in the MSTD is equal to the time at which the NGP peaks, t^*, in accordance with the prediction of the model. Second, this parameter-free fit underestimates the maximum of the NGP by at most a factor of 2.

A higher peak value of the NGP can be interpreted as being due to a larger effective jump length than the nearest-neighbour distance. This suggests that also next-nearest-neighbour jumps as well as jumps of higher order could be important. It can be shown that when one takes into account these multiple jump lengths, only the effective jump length L of eq. 3.6 changes, while the functional form of $\alpha_2(t)$ remains invariant. Nevertheless, it seems that for the highest density this multiple-jump-length effect vanishes and the accordance with the model is better when assuming a single jump length.

In order to study polymer-specific effects of the non-Gaussian dynamics we have performed molecular-dynamics simulations of a melt of atactic polystyrene (PS), one of the most common polymer glass formers. Simulation details are the same as mentioned by Lyulin et al. [174]. The glass-transition temperature T_g for the PS melt of eight chains of 80 monomers each is around 370 K. The MSTD and the NGP, after averaging over all united atoms, are shown in fig. 3.4.

Some generic features of the one-particle model can also be seen for this polymer system. The peak time of the NGP, t^* is also situated at the crossover from the cage regime to Rouse-like diffusion. However, because of the different bonded interactions of the backbone and the phenyl-ring atoms, the jump distances, the cage sizes and the mobilities of these atoms are different as well. We therefore compare only the values of the MSTD and NGP for atoms in the backbone (including the first atom of the phenyl ring and excluding chain ends). We assume that the jump distance is now due to an internal torsion potential in the polymer chain; this potential favours specific positions of the atoms, corresponding to trans or gauche conformations. We also assume that these conformations are separated by a distance L between them of about 2.5 Å. At $T = 375$ K the plateau value of the MSTD is $\Delta^2 \approx 0.64$ Å^2. Using eq. 3.7 with these values of Δ^2 and L gives then $\alpha_2^* = 1.5$, which is remarkably close to the simulated value $\alpha_2^* = 1.3$.

The molecular-dynamics simulations also show that the shape of the NGP is similar to but much wider than the prediction of the one-particle model. The FWHM in case of a time-independent diffusion coefficient is shown in fig. 3.4 as a bar. This difference can be partly explained by the anomalous (nonlinear in time) Rouse diffusion of the segments in a polymer chain, $\langle \Delta\mathbf{r}(t)^2 \rangle \sim t^{1/2}$. Note that for a time-independent diffusion coefficient, a result of the model is that the NGP increases linearly in time for $t_c < t < t^*$, i.e., $\alpha_2(t) \sim t^1$ (eq. 3.6). A broader peak can be interpreted in terms of a lower effective scaling exponent of the NGP for $t_c < t < t^*$. Using the Rouse exponent 1/2 (so $D \sim t^{-1/2}$) in eq. 3.6 indeed results in a broader peak. Still, this anomalous diffusion cannot fully explain the broad shape of $\alpha_2(t)$ occurring with polystyrene (fig. 3.4). It is possible that due to disorder in the polymer structure close to the glass transition the packing is not ideal, and a varying environment is present. As a result low-energy pathways are preferential and single-file diffusion is enhanced. It is known that this type of diffusion is anomalous as well, $\langle \Delta\mathbf{r}(t)^2 \rangle \sim t^{1/2}$ [214]. The combination of Rouse-like and single-file diffusion (giving an effective exponent of 1/4 for $t < t^*$) could be the cause for this wider peak. Another possible cause is that the various united atoms are not identical, due to the different bonded interactions. This results in different dynamics and thereby promotes a wider relaxation distribution.

Finally, molecular-dynamics simulations have been performed of a perfectly branched dendritic melt (see the article of Karatasos [141] for details). The atom connectivity of this system has an even more complex structure than in the previous case. In the present study we only show results for the fourth-generation dendrimer melt, for which the glass transition occurs around $T_g \approx 550$ K, although results for other generations are similar. The MSTD and the NGP of the outer-generation atoms are given in fig. 3.5. As with the PS glass, the same main features of the model are observed for this system. Following the same analysis as for the polymer glass, the prediction of the model for $T = 500$ K (assuming a trans-gauche distance of 2.5 Å as the most dominant jump length L and using the plateau value of the MSTD, $\Delta^2 = 1.25$ Å^2) is $\alpha_2^* = 0.75$, compared to the simulation result of $\alpha_2^* = 0.92$. This similarity appears to indicate that the model indeed captures the dominant mechanism responsible for non-Gaussian behaviour. Similar to the PS case, the simulated NGP is broader than the calculated one. We assume that a similar reasoning as for the polystyrene system (Rouse-like and single-file dynamics) may be applied here as well to account for the extra broadening.

3.4 Summary and conclusions

In short, we have shown that some universal aspects of the non-Gaussian dynamics (observed for many systems [58, 80, 121, 127, 132, 149, 151, 221, 236, 276, 291, 294]) around the cage-diffusion transition can well be explained by a simple model, which does not assume *a priori* any heterogeneity of glassy dynamics (in the sense as mentioned in the introduction). For this model the maximum of the NGP occurs at the crossover between the caged plateau and the final diffusion, and the maximal height of the NGP is given by eq. 3.7. These statements are confirmed even within fair quantitative detail by simulation results for glass-forming systems with widely different topology — a quasi-two-dimensional colloidlike low-molecular-weight glass former, linear polystyrene glass, and a glass of perfectly branched dendrimers. It is important to emphasize that this model considers the motion at a coarse-grained time scale. It only assumes the existence of cages in which the cage to cage motion results in non-Gaussian behaviour. No further details of any explicit collective or heterogeneous glassy dynamics are required to understand the non-Gaussian behaviour in this sense.

In contrast to the low-molecular-weight liquids, additional intrachain (torsion) interactions in polymer melts make multiple jumps very unlikely, and the predictions of the model regarding the maximum of the NGP are found to be closer to the simulated results. On the other hand, the polymer connectivity introduces more complicated anomalous diffusion effects, which effectively broadens the simulated NGP peak.

3.A Random walk

We will show in this Appendix how one can determine the expressions for the mean-square translational displacement and the mean quartic translational displacement for a certain class of random walks (i.e., eqs. 3.4 and 3.5). First we will look at a discrete random walk, in which the particle makes a jump after each step i in some direction $\mathbf{x}_i$ with a certain probability distribution for the step vector $\rho(\mathbf{x}_i)$. Later on the time dependency is introduced.

We only consider random walks for which the probability distribution for a step $\mathbf{lj}$ fulfils

$\rho(\mathbf{L}) = \rho(-\mathbf{L})$, i.e., a walk of Pólya type [126, §I.3.3]. Then the MSTD for a n-step random walk is $\langle \Delta\mathbf{r}(n)^2 \rangle = nL^2$, with $\Delta\mathbf{r}(n) = \sum_{i=1}^{n} \mathbf{x}_i$, $L^2 = \langle \mathbf{x}_i \cdot \mathbf{x}_i \rangle = \langle \mathbf{x}_i^2 \rangle$ [126, §I.2.1] and $\langle \cdots \rangle$ denoting averaging over all possible step vectors.

The discrete mean quartic translational displacement (MQTD) is then

$$\langle \Delta\mathbf{r}(n)^4 \rangle = \sum_i \sum_j \sum_k \sum_l \langle (\mathbf{x}_i \cdot \mathbf{x}_j)(\mathbf{x}_k \cdot \mathbf{x}_l) \rangle \tag{3.8}$$

One can easily see that the only terms in the right hand side of eq. 3.8 which do not cancel to zero when averaging over all possible steps $\mathbf{L}$ are when $i = j = k = l$ (n terms), $i = j \neq k = l$, $i = k \neq j = l$ and $i = l \neq j = k$ (all $n(n-1)$ terms). Therefore the discrete MQTD is

$$\langle \Delta\mathbf{r}(n)^4 \rangle = n\langle \mathbf{x}_i^4 \rangle + n(n-1)L^4 + 2n(n-1)\langle (\mathbf{x}_i \cdot \mathbf{x}_j)^2 \rangle. \tag{3.9}$$

The time-dependent MSTD (and MQTD) is then acquired by observing that the chance for n jumps at time t is described by the Poisson distribution $\rho_n(t) = \exp(-t/\tau)\frac{(t/\tau)^n}{n!}$. Here τ is the average time it takes to make a jump. It is assumed that non-jumped particles already have a constant value of the MSTD Δ^2 within the cage. Then the time-dependent MSTD is

$$\begin{aligned} \langle \Delta\mathbf{r}(t)^2 \rangle &= \Delta^2 + \exp(-t/\tau) \sum_{n=0}^{\infty} \frac{(t/\tau)^n}{n!} \langle \Delta\mathbf{r}(n)^2 \rangle \\ &= \Delta^2 + L^2 t/\tau. \end{aligned} \tag{3.10}$$

We will further limit ourselves to random walks in which all steps are of equal length $|\mathbf{x}_i| = L$ (so $\langle \mathbf{x}_i^4 \rangle = L^4$), and obey $\langle (\mathbf{x}_i \cdot \mathbf{x}_j)^2 \rangle = L^4/d$. Random walks for which the steps adhere these two conditions are, for example, a d-dimensional isotropic random flight, or random walks on lattices such as on a two-dimensional triangular, on a three-dimensional body-centred cubic, and on a three-dimensional face-centred-cubic lattice. These relations can be checked for each type of random walk by straightforward calculations (i.e., averaging over all possible step vectors). Repeating the calculation for the time-dependent MQTD and assuming that the displacement within the cage obeys Gaussian statistics (i.e., $\Delta^4 = (1 + 2/d)(\Delta^2)^2$) results in

$$\langle \Delta\mathbf{r}(t)^4 \rangle = (1 + 2/d)\langle \Delta\mathbf{r}(t)^2 \rangle^2 + L^4 t/\tau, \tag{3.11}$$

which completes the determination of the two moments.

Chapter 4

Development of heterogeneity near the glass transition: Phenyl-ring-flip motions in polystyrene

ABSTRACT

Molecular-dynamics simulations are employed to study the phenyl-ring flip in polystyrene, thought to be the molecular origin of the γ relaxation. The results show that upon cooling the system towards the glass transition the motion of the phenyl ring becomes more heterogeneous, which seems to result from a distribution of local energy barriers in combination with slower transitions between states with these local energy barriers. The growing of the heterogeneity affects the determination of the effective energy barrier. In particular, the 'static' energy barrier (as determined from the distribution of the orientation of the phenyl ring with respect to the backbone) is found to be different from the 'dynamic' energy barrier, as determined from the temperature dependence of some relaxation time (i.e., the activation energy). However, below the glass-transition temperature it appears that the two methods render the same value for the height of the energy barrier, although the time scales differ approximately by a constant factor. It is shown that another relaxation time can be determined to characterize the ring-flip process, which seems not to be affected by the growth of heterogeneity and which closely follows the 'static' energy

---

The contents of this chapter are for a large part published in Macromolecules **40**, 6001 (2007). Reproduced in part with permission. Copyright 2007 American Chemical Society barrier. The effective barrier as determined in this way by the simulations is in fair agreement with experimental values for the γ relaxation.

4.1 Introduction

The mechanical properties of glassy polymers are complex functions of temperature and experimental time scales. Various relaxation processes determine the precise viscoelastic behaviour of a polymer glass, such as chain relaxation, segmental relaxation within a chain, and conformational transitions. The complex microstructure of a polymer material is responsible for the nature and time scales of these relaxation processes. Yet, some generic features are present, related to the physics of the glass transition. The main relaxation process, the α process, freezes in at the glass-transition temperature T_g. In general, the α process is a very collective process [52], which shows strongly non-Arrhenius behaviour. Below T_g only local rearrangements of chain segments within their cages formed by neighbouring segments are possible. In order of freezing-in upon cooling these sub-T_g processes are called β, γ, ... These faster processes are more Arrhenius-like and less collective in the glassy regime [52].

An attractive prototype glassy polymer to study experimentally and theoretically is atactic polystyrene (PS). The major reasons for this are that its properties are well documented, it is a common plastic, and its mechanical behaviour is still poorly understood, despite the extensive studies of the relaxation processes of PS. The temperature at which the α relaxation reaches 100 s (which can be used as the definition of the glass-transition temperature [52]) is $T_g \approx 374$ K; the exact value depends on cooling rate and molecular-weight distribution [232].

The β process (not to be confused with the β relaxation in the mode-coupling theory (MCT) of the glass transition, of which the time scale diverges near the critical temperature in the ideal-MCT framework [52]) appears for atactic polystyrene around a frequency of 110 Hz at $T = 320$ K; it has an activation energy of about 1.3×10^2 kJ mol^{-1} [287]. At high frequencies the peak of the β process will merge with the α-relaxation peak [287]. It is believed that the β process in PS originates from a local oscillation mode of the backbone chain [287]. If annealing conditions are varied, the barrier will also vary between ~ 90 and ~ 170 kJ mol^{-1} [272].

The γ process has a smaller activation energy and has been associated with a phenyl-ring flip. The activation energy obtained by mechanical experiments is 34–38 kJ mol^{-1} [104, 287]. Other experimental studies [211] lead to energy-barrier heights in the range 21–29 kJ mol^{-1}; in these studies the energy barrier was determined by a fit based on a rotator model, leading to a lower energy value than obtained from an Arrhenius fit.

As the ascribed molecular origin of the γ relaxation is conceptually simple, it has been subject of many theoretical studies. Early estimates for the energy barrier of a phenyl-ring flip are based on taking into account only intrachain interactions [107, 144, 211, 252, 257]. It was found that the potential-energy barrier depends on the conformation of the backbone chain and on tacticity [107, 252, 257]. The energy barrier is lower when the backbone torsions operate cooperatively with the phenyl-ring motion [144, 252].

However, in a melt the backbone dihedral angles cannot rotate freely, without hindering other chains as well. When other chains are also included (i.e., a phenyl-ring flip in its glassy neighbourhood), the mean energy-barrier height determined by an energy-minimization method turns out to be 116 kJ mol^{-1} [210]. The actual distribution of barrier heights was found to be very broad, in the range of 0.96–1115 kJ mol^{-1} (for the cases in which the energetic barrier was positive). Another study [145] also uses a form of energy minimization to determine energy barriers in the glassy structure. The result ranges from 19.2 to 133 kJ mol^{-1} for 10 different measurements of a phenyl-ring rotation (in which rotations in both directions have been considered, viz. clockwise and counterclockwise). These results show that the glassy structure has a tremendous effect on the actual barrier of the phenyl-ring flip. So the relaxation of the surrounding polymer matrix should be taken into account for studying the dynamical behaviour of the phenyl ring. Variations in molecular packing can cause a distribution of relaxation times, which in turn can cause heterogeneous dynamics [239].

The usage of molecular dynamics (MD) simulations is an effective method to study the dynamics of transitions of small chemical groups near the glass transition. The results of previous MD simulations for melts of other polymer systems have shown that there is a distribution of transition rates for the rotation of a side group (such as for the rotation of the methyl group in poly(methyl methacrylate) [194], in poly(vinyl methyl ether) (PVME) [230], and in polyisobutylene [142]) or for conformational transitions [136]. Also, a distribution of energy-barrier heights has been found for CH_3 rotations in PVME [24], or for conformational transitions [136]. MD simulations have been carried out before for polystyrene as well [14, 73, 88, 109, 111, 118, 153, 171, 172, 174, 175, 177, 187, 197, 222, 223, 249], and some of these simulation results have been used to look at typical relaxation times in the vicinity of the glassy state [118, 172, 174, 222]. However, no emphasis was given to the motion of a phenyl ring.

The aim of the present chapter is to study the flip of the side-group phenyl ring in a melt of atactic polystyrene and determine the accompanying energy-barrier landscape, typical relaxation time scales, and the Arrhenius activation energy by means of different methods. A special point of focus is to look at the influence of the glassy dynamics on the dynamical properties of this ring, which effectively makes the ring flip very heterogeneous (in terms of a wide distribution of relaxation times).

The current chapter is organized as follows. In the next section the polystyrene model is described and simulation details are explained. From MD simulation data the free-energy barrier for the phenyl-ring flip is then determined, by means of the distribution function of the orientation of the phenyl ring with respect to the backbone. Next the temperature dependencies of the relaxation times of autocorrelation functions are studied to yield a value for the activation energy. Van Hove functions are analyzed for studying the heterogeneity in the dynamical behaviour of the phenyl ring, leading to a kinetic model for ring flipping. Finally, some conclusions are stated.

4.2 System description and simulation details

The atactic-polystyrene melt in the simulation consists of eight chains of 80 monomers each. In the left panel of fig. 4.1 a monomer unit of polystyrene is depicted together with the nomenclature of the (united) atoms. The united-atom force field is described in table 2.1. Simulations are carried out in the constant-NPT ensemble (constant number of particles N, pressure P and temperature T), using velocity Verlet as the numerical integration scheme for the Newtonian equations of motion (with an integration time step of 4 fs), the Berendsen barostat ($\tau_P = 10$ ps [6]), and the collisional-dynamics method [165] as a thermostat ($\lambda_{\mathrm{coll}} = 1\ \mathrm{ps}^{-1}$, $m_0 = 0.1$ Da). Strictly speaking, when using the Berendsen barostat, the constant-NPT ensemble is not probed [6], but this effect is assumed to be of minor significance for the present study.

The sample is prepared by a procedure similar to that of Lyulin and Michels [171], starting with a one-chain melt of polystyrene. After the equilibration of this single chain, the orthorhombic box is doubled in all three directions, and the resulting sample is equilibrated further for another 10 ns at $T = 540$ K. To correct for the potential cutoff and any other force-field deviations, the pressure has been adjusted so that the density at $T = 540$ K equals the experimentally observed density at this temperature and at atmospheric pressure [293]. The sample is subsequently cooled to the desired temperature by $0.01\ \mathrm{K\,ps}^{-1}$. This process is done for five independent samples in order to increase statistics. For testing the proper temperature behaviour of some of the data, the temperature of one sample (first equilibrated at $T = 540$ K) has been set to 1000 K, followed by an additional 4 ns equilibration with an integration time step of 2 fs. To see what the influence of the glassy state is compared with the gas phase, another simulation has been carried out, in which only one chain has been simulated. This atactic polystyrene chain consists of 15 monomer units and is placed in a vacuum.

The glass-transition temperature T_g of this 8-chain model for atactic polystyrene is determined by plotting the specific volume vs. temperature and applying a linear fit to both low and high temperatures. The crossing point of these linear fits is then taken as the definition of the glass-transition temperature, with the result $T_g = 388$ K [175]. This is somewhat higher than the experimentally determined glass-transition temperature for approximately the same molecular weight, $T_g = 361$–363 K [232, 293]. The difference becomes smaller upon extrapolating the observed glass-transition temperature towards experimental cooling rates [175].

As the present study is mainly concerned with the rotational dynamics of the phenyl ring, the angle χ between the phenyl ring and the backbone is defined here in detail (see fig. 4.1). It is slightly different from that as given in Abe et al. [2], as now it is not assumed that the phenyl ring is strictly planar (in the case of an all-atom model of polystyrene a different convention is possible [219]). The plane P is defined by the normal vector C–CH connecting the phenyl ring to the backbone. The vector $\mathbf{v}_{ph}$ pointing from one o-CH to

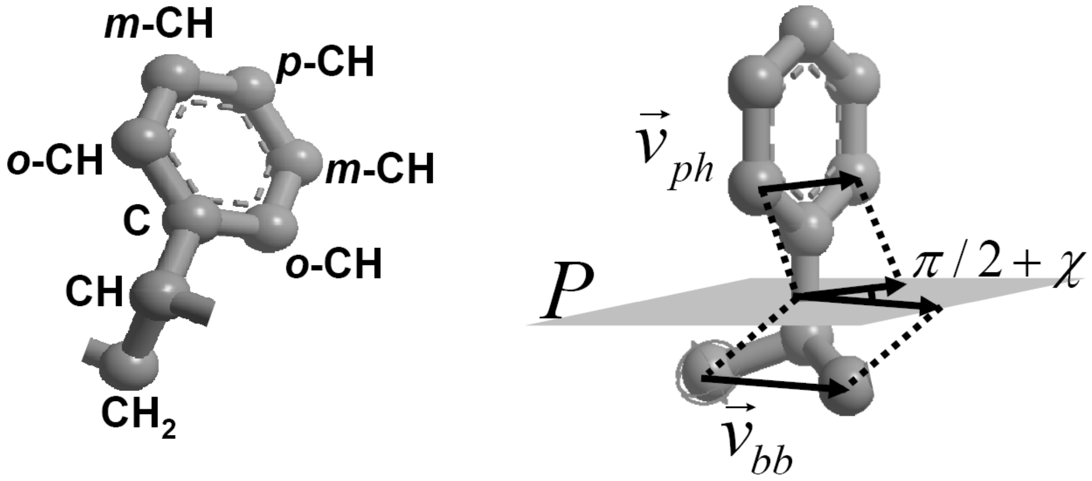

Figure 4.1: (left) Monomer unit of the polystyrene model with the naming convention of the (united) atoms. Here o=ortho, m=meta and p=para. The notation x-CH is used for any of the three possible positions of the CH group in the phenyl ring. (right) Illustration with the definition of the angle χ between the phenyl ring and the backbone. See text for details.

the other o-CH and the vector $\mathbf{v}_{bb}$ pointing from one CH_2 to the other CH_2 (two chemical bonds away) are projected onto this plane P. Then the angle χ is defined as the angle between these two projected vectors minus $\pi/2$. In this way the equilibrium position of the phenyl ring with respect to the backbone is around $\chi = 0$ and around $\chi = \pi$.

4.3 Results and discussion

The rotational dynamics of the phenyl ring can be studied in various ways. First the free-energy barrier height for rotation is determined from the probability distribution of χ (a measure for the orientation of the phenyl ring with respect to the backbone). As a second method, the time dependence of some autocorrelation functions associated with the phenyl ring is investigated; from this an activation energy can be distilled. The concept of heterogeneity is used to explain the difference between the two energies thus determined. To acquire more evidence for heterogeneous dynamics, some typical trajectories of the phenyl-ring angle with respect to the backbone are displayed, and the self-part of the Van Hove function is calculated. Based on this, a two-state model (χ around 0 vs. χ around π) is used to calculate in yet another way an activation energy. The various results give clear evidence for heterogeneity in the glassy dynamics.

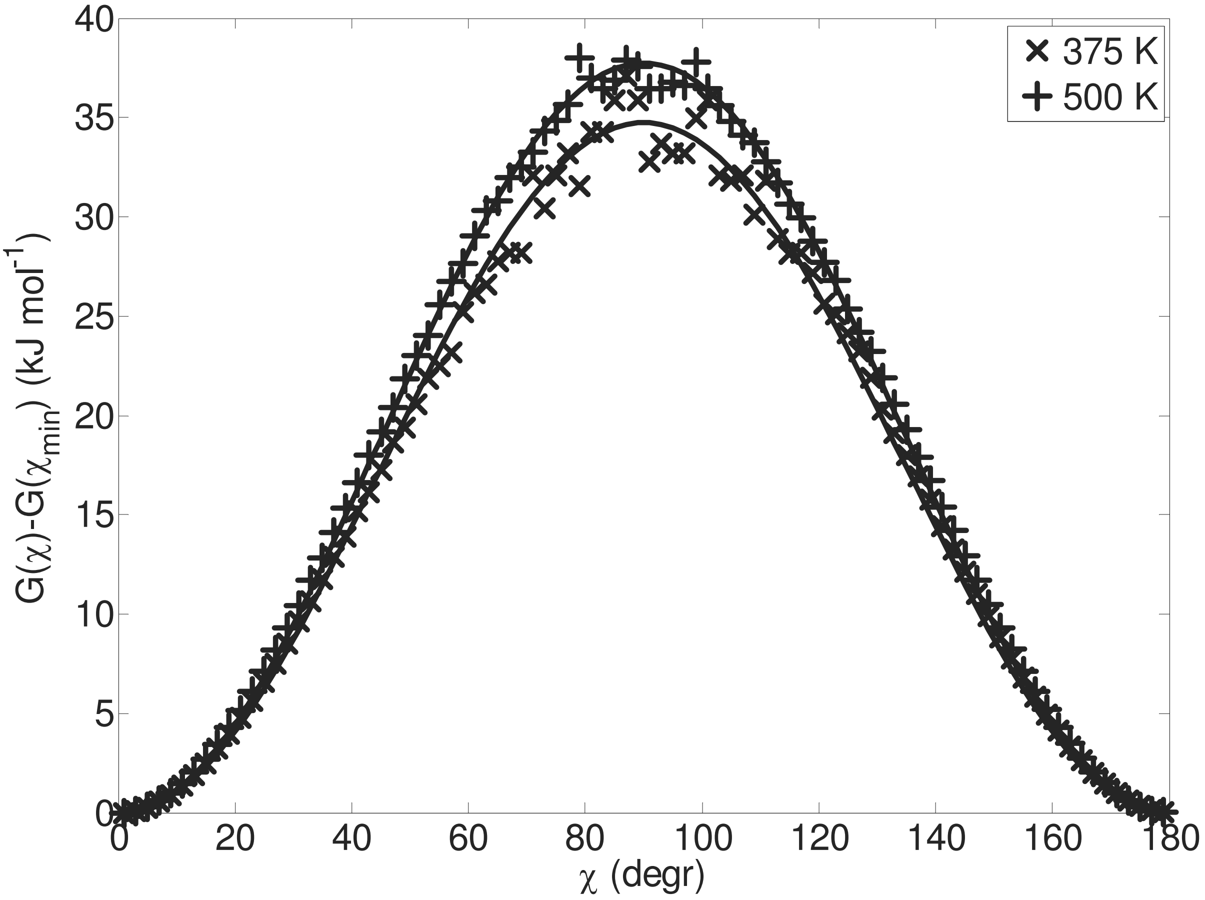

Figure 4.2: Free energy G for two different temperatures (around T_g and well above it) as a function of the angle χ of the phenyl ring with respect to the backbone, as calculated using eq. 4.1. Solid lines are fits to the simulation data (crosses and pluses) with the cosine function eq. 4.2.

4.3.1 Free-energy barrier

To see what energy barrier is associated with a phenyl flip in our constant-NPT simulation run, the distribution function $\rho(\chi)$ has been measured. From this the (Gibbs) free energy $G(\chi)$ can be calculated by using the Boltzmann distribution law [42]

$$\rho(\chi) = \rho(\chi_{\min}) \exp\left[-\frac{G(\chi) - G(\chi_{\min})}{k_B T}\right], \tag{4.1}$$

with k_B Boltzmann's constant. The reference value $\chi_{\min}$ is taken to be the value of χ at which the free energy is at its minimum. A similar analysis has also been carried out in Berthet et al. [24]. The result is shown in fig. 4.2 for two different temperatures. Data for other temperatures are similar. The shape of this effective potential (potential of mean

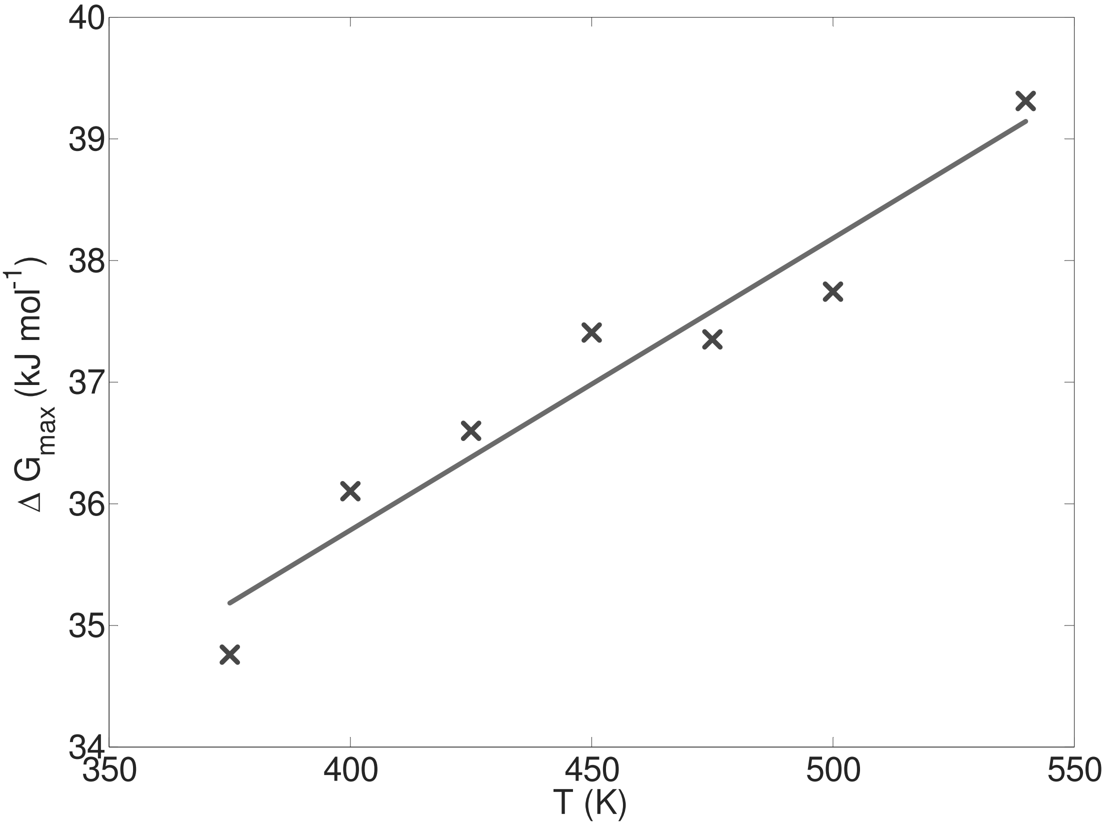

Figure 4.3: Free-energy barrier height as a function of the temperature, extracted from the distribution function of χ, eq. 4.1. Solid line is a fit to the simulation data (crosses) with eq. 4.3.

force) is well described by a simple cosine function

$$G(\chi) - G(\chi_{\min}) = \frac{1}{2}\Delta G_{\max}(1 - \cos(\chi)), \tag{4.2}$$

with $\Delta G_{\max}$ the free-energy barrier height. This barrier height $\Delta G_{\max}$ as acquired by fitting $G(\chi) - G(\chi_{\min})$ by eq. 4.2 is plotted in fig. 4.3 as a function of temperature.

The entropic part of the free-energy barrier height can be determined by fitting the data with the linear relation

$$\Delta G_{\max}(T) = \Delta H_{\max} - T\Delta S_{\max}, \tag{4.3}$$

when one assumes that the enthalpy difference $\Delta H_{\max}$ and the entropy difference $\Delta S_{\max}$ are independent of temperature. The contribution $P\Delta V_{\max}$ to the free-energy barrier could also be determined by varying the pressure, but it is assumed that this contribution is temperature-independent as well and therefore it is discarded in this study. In this way $\Delta H_{\max}$ could be interpreted as some kind of activation enthalpy, in the case of a single barrier (see, e.g., Witten and Pincus [282]). The outcome of the fit is $\Delta H_{\max} = 26$ kJ mol^{-1} and $\Delta S_{\max} = -0.024$ kJ mol^{-1} K^{-1} (fig. 4.3). The free-energy barrier height is seen to increase with increasing temperature. This could be interpreted that it is entropically unfavourable to be at the unstable maximum position ($\chi_{\max} = \pi/2$), compared to the stable minimum position ($\chi_{\min} = 0$).

The entropic contribution to the free-energy barrier height is higher than found from an energy-minimization technique [145]. From our simulation results the contribution $T\Delta S_{\max}$ to the free-energy barrier at $T = 300$ K is estimated to be about 20%. The contribution $T\Delta S_{\max}$ obtained from the energy minimization, in which the entropy is acquired by applying a quadratic approximation for the potential-energy surface near the transition state for a phenyl-ring flip, was less than 10% [145].

Another way to determine the energetic barrier is by looking at the temperature dependence of the relaxation times. In the next section relaxation times associated with a phenyl-ring flip are calculated; afterwards activation energies corresponding to some of these times are determined.

4.3.2 Time correlation functions

The dynamics of the phenyl ring is examined by looking at the vector connecting the two united carbon atoms in the ortho position, *o*-CH (see fig. 4.1). The rotational behaviour of this vector $\mathbf{v}_{ph}$ can be studied by considering ensemble-averaged Legendre polynomials $P_l(x)$ of the inner product of the unit vector $\hat{\mathbf{v}}_{ph} \equiv \mathbf{v}_{ph}/|\mathbf{v}_{ph}|$ at time t_0 with itself at time $t_0 + t$, i.e., the autocorrelation function

$$C_l(t) = \langle P_l\left[\hat{\mathbf{v}}_{ph}(t_0) \cdot \hat{\mathbf{v}}_{ph}(t_0 + t)\right]\rangle. \tag{4.4}$$

One of the reasons to look at this quantity is that some of these autocorrelation functions can be measured experimentally. In particular, when instead a $C-H$-vector is considered, then the correlation time (also called an average relaxation time [52])

$$\tau_c \equiv \int_0^\infty ACF(t)dt \tag{4.5}$$

is measurable by NMR experiments, if $ACF(t) = C_2(t)$. Reasonable agreement was observed when comparing the result of this kind of NMR experiments to the results of MD simulations [118].

It is quite common when studying glassy materials to fit such autocorrelation functions by a Kohlrausch-Williams-Watts (KWW) stretched-exponential function [52]

$$A\exp\left[-(t/\tau_{\mathrm{KWW}})^\beta\right] \tag{4.6}$$

in which τ_{KWW} is a typical time scale of relaxation, β the stretch exponent, and A a pre-exponential factor to account for other relaxation processes at shorter time scales (such as librating motion, which usually occurs at time scales below 4 ps, the interval at which trajectories are saved in this study). Integrating eq. 4.6 [169] then results in the correlation time τ_c (eq. 4.5)

$$\tau_c = \frac{\tau_{\mathrm{KWW}}}{\beta}\Gamma(\beta^{-1}), \tag{4.7}$$

with $\Gamma(x)$ the (complete) gamma function. So for $1 \geq \beta \geq 1/2$ the correlation time τ_c is at most a factor of 2 larger than τ_{KWW}. The KWW function can be considered as arising from a specific superposition of exponentials

$$\exp\left[-(t/\tau_{\mathrm{KWW}})^\beta\right] = \int_0^\infty \rho_{\mathrm{KWW}}(\tau)\exp\left(-\frac{t}{\tau}\right)d\tau \tag{4.8}$$

with the KWW distribution function $\rho_{\mathrm{KWW}}(\tau)$. The width of $\rho_{\mathrm{KWW}}(\tau)$ is then determined by the exponent β, a lower value of β meaning a wider distribution [169].

One should be cautious in interpreting the fitting parameters of the KWW function. A limited time window for the relaxation function (due to limitations in simulation time) can result in a lower value for the fitted τ_{KWW} [241]. Also, in the case of glasses the interference of the start of the α relaxation with the end of the cage plateau can result in lower values of β [167].

The results for

$$C_1(t) = \langle \hat{\mathbf{v}}_{ph}(t_0)\cdot\hat{\mathbf{v}}_{ph}(t_0+t)\rangle \tag{4.9}$$

and

$$C_2(t) = \frac{3}{2}\langle[\hat{\mathbf{v}}_{ph}(t_0)\cdot\hat{\mathbf{v}}_{ph}(t_0+t)]^2\rangle - \frac{1}{2} \tag{4.10}$$

describing the reorientation of the normalized *o*-CH–*o*-CH vector are shown in fig. 4.4. It is seen that the three-parameter KWW function is able to describe the data well.

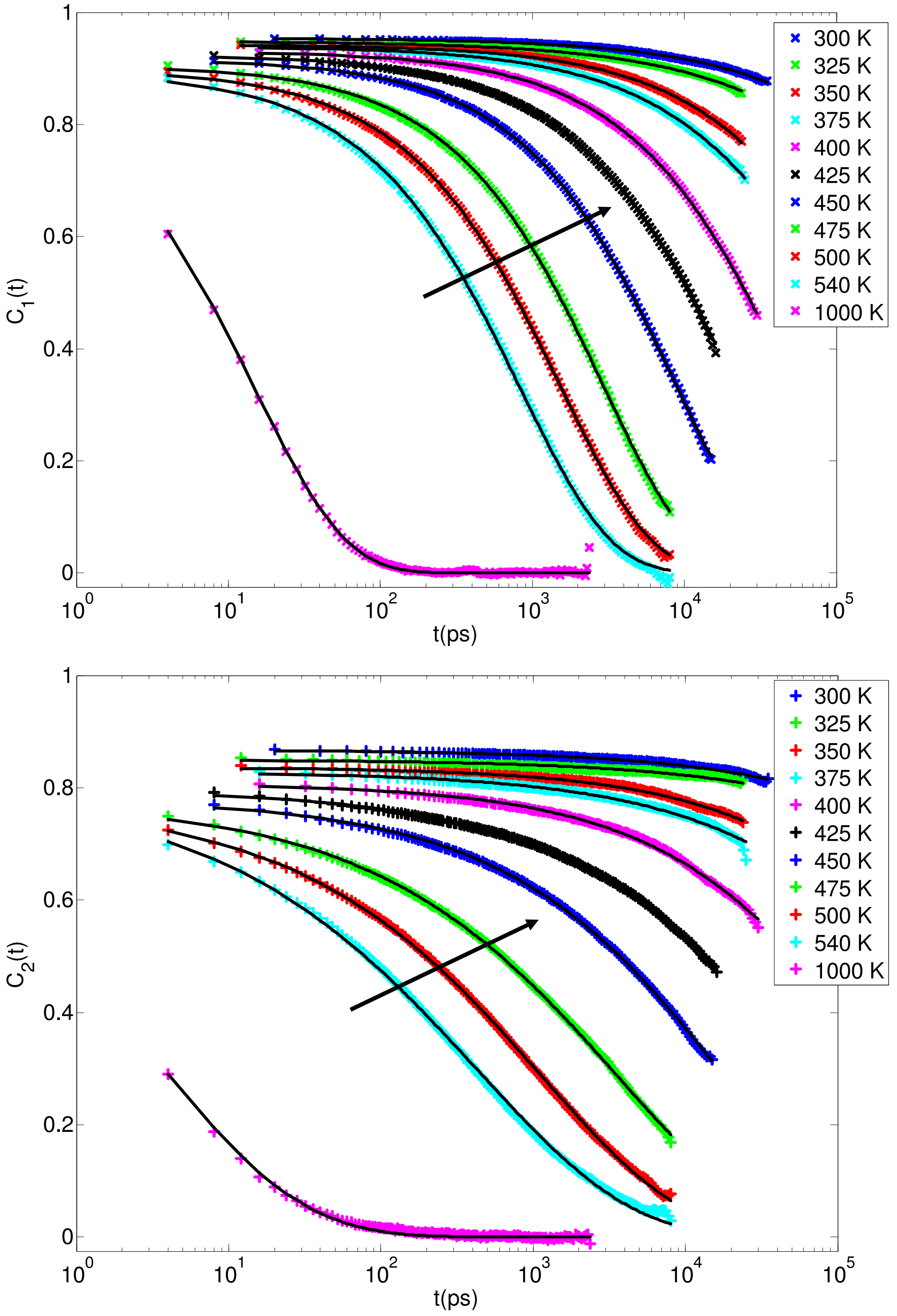

Figure 4.4: $C_1(t)$ and $C_2(t)$ for the vector $\mathbf{v}_{ph}$ pointing from one *o*-CH-atom to the other one within a phenyl ring for various temperatures. Solid lines are fits to the simulation data by a stretched exponential, eq. 4.6. Arrows point towards relaxation curves of decreasing temperature.

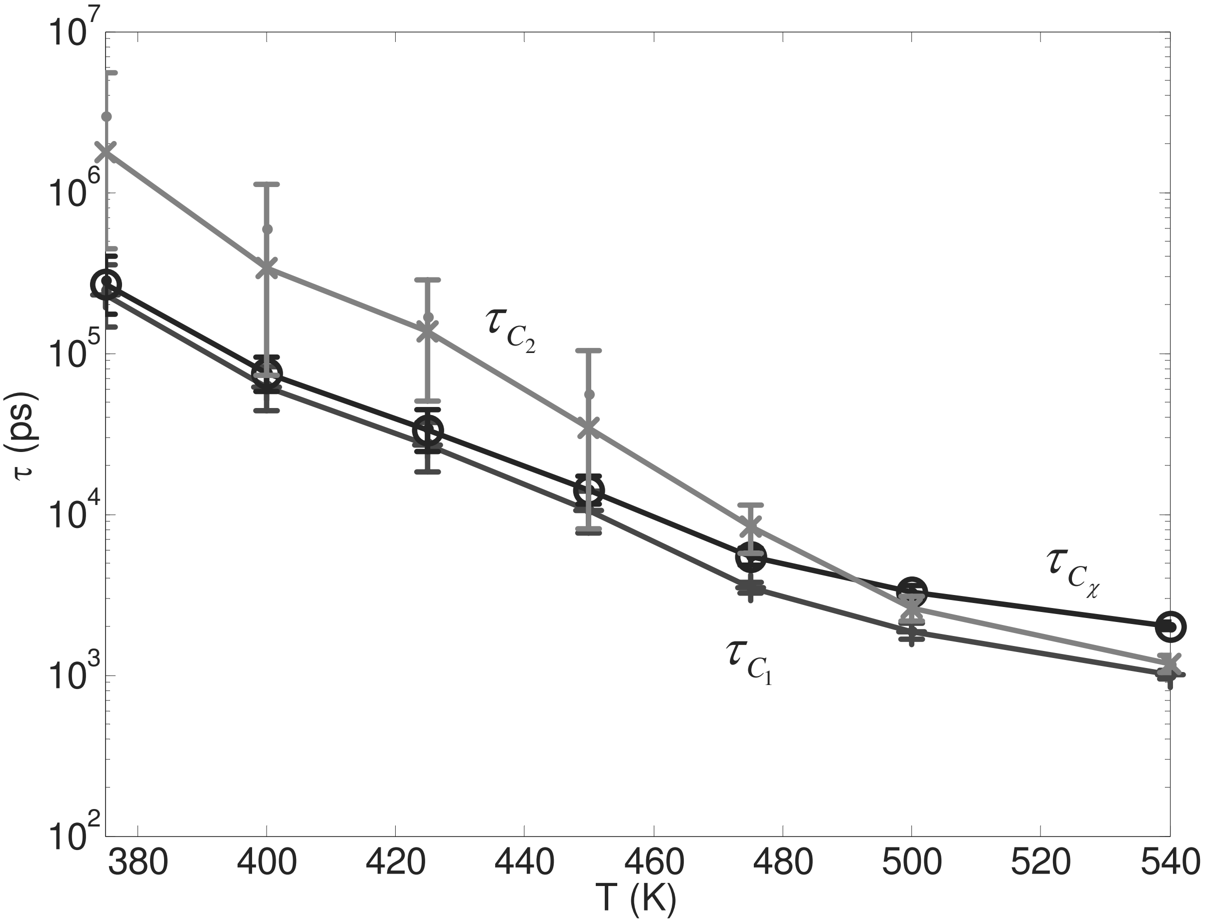

Figure 4.5: Correlation relaxation times as a function of temperature for the vector within the phenyl ring (τ_{C_1} (pluses) as determined by fitting $C_1(t)$ and τ_{C_2} (crosses) by fitting $C_2(t)$ depicted in fig. 4.4 by eq. 4.6) and for the χ-angle (τ_{C_χ} (circles) by fitting $C_\chi(t)$ (eq. 4.11) by eq. 4.6). All KWW times are rewritten in correlation times by using eq. 4.7. Solid lines serve as a guide to the eye.

Some important differences can be observed when comparing the $C_1(t)$ and $C_2(t)$ autocorrelation functions for the *o*-CH–*o*-CH phenyl vector. In fig. 4.5 the correlation time (deduced from eqs 4.6 and 4.7) is plotted as a function of temperature. The relaxation time of $C_2(t)$, τ_{C_2}, rises more quickly than that of $C_1(t)$, τ_{C_1}, upon decreasing temperature. This is because $C_2(t)$ is invariant under a phenyl-ring flip. So a flip contributes to the relaxation of $C_1(t)$, but not of $C_2(t)$. Nevertheless, $C_2(t)$ still relaxes at low temperatures. This means that main-chain reorientation and/or the flapping motion of the phenyl ring around the backbone still are active relaxation modes at low temperatures, although much slower than the motion of the phenyl-ring flip itself.

To isolate the pure effect of the phenyl-ring reorientation with respect to the backbone we consider the relaxation of the autocorrelation function of the cosine of the accompanying angle χ (fig. 4.1)

$$C_\chi(t) = \langle \cos[\chi(t) - \chi(0)] \rangle. \tag{4.11}$$

This autocorrelation function would be identical to $C_1(t)$ (eq. 4.9), if the backbone would be frozen and the phenyl ring could only move by rotating around the chemical bond joining it to the backbone. It turns out that this is almost the case for low temperatures, where the two autocorrelation functions are close to each other. The time dependence of $C_\chi(t)$ is also well-described by a stretched-exponential function, eq. 4.6. The temperature dependence of the corresponding correlation time τ_{C_χ} is shown in fig. 4.5. At high temperature this relaxation is rather slow, slower than both $C_1(t)$ and $C_2(t)$. This is because both $C_1(t)$ and $C_2(t)$ are able to relax by the motion of the backbone, while $C_\chi(t)$ can only relax via the relative motion of the phenyl ring with respect to the backbone. However, upon decreasing the temperature, this behaviour changes. The flip-relaxation channel becomes the dominant one for temperatures of about 440 K and lower, as then the relaxation time of $C_1(t)$ almost equals that of $C_\chi(t)$, τ_{C_χ}. So the difference between $C_1(t)$ and $C_2(t)$ is due to the (obvious) anisotropy of the relaxation; for low temperatures it is for example easier for the phenyl ring to make a π-flip motion around its axis, than to end up with a $\pi/2$ rotation around the same axis (not rotation invariant in χ), or to rotate around a different axis (anisotropic in the orientation of the axis). Anisotropic relaxations have been studied before for other polymer systems as well [49, 89].

Despite the dominance of the flip-relaxation channel at lower temperatures, it seems that for temperatures below about 420 K the three different relaxation times show approximately the same temperature dependence (see fig. 4.5). This observation could be an indication of a coupling between the backbone conformation and the rotation of the phenyl ring. An analogous coupling was also found for a different polymer system [142]. Tonelli [257] showed that the energy barrier for a phenyl-ring flip can exceed 400 kJ mol^{-1} for some accompanying backbone conformations. A change to a new backbone conformation with a lower energy barrier for the phenyl-ring flip would allow these phenyl rings to flip much earlier. As $C_2(t)$ is invariant under a phenyl-ring flip, its long-time behaviour is mostly sensitive to backbone relaxations. Therefore, a plausible explanation for the observation that the temperature dependencies of the different relaxations times are about equal for low temperatures is that the relaxation of the phenyl rings which have a high-barrier conformation for a flip have to wait for the relaxation of the backbone.

4.3.3 Activation energy from relaxation times

In section 4.3.1 the free-energy barrier height for a phenyl-ring flip was determined by considering the distribution function of the angle χ, fig. 4.3. Alternatively, one can determine the activation barrier (i.e., the barrier to activate the motion of the process), by assuming that the relaxation time of $C_\chi(t)$ follows activated kinetics (Arrhenius-like behaviour)

$$\tau = \tau_0 \exp\left(\frac{\Delta H}{k_B T}\right) \tag{4.12}$$

in which the inverse of the pre-exponential factor τ_0^{-1} is a measure for the attempt rate [282] and ΔH is the activation enthalpy. The choice of activated behaviour might be motivated by the experimental observation that secondary relaxations are usually well described by such a law [52], including the γ relaxation of polystyrene [287]. This in contrast with the main α relaxation, which is usually described by the Vogel-Fulcher-Tammann-equation [52]. The Arrhenius fit of the relaxation times of $C_\chi(t)$ results in an activation enthalpy of 50 $\mathrm{kJ\,mol^{-1}}$ for the temperature range of 375–540 K. However, fitting the results for the temperature range below the glass-transition temperature, 300–375 K, results in a lower activation enthalpy, 35 $\mathrm{kJ\,mol^{-1}}$.

So the activation enthalpy as acquired by an Arrhenius plot of τ_{C_χ} for T in the range 375–540 K is almost twice the enthalpy-barrier height as determined from the distribution function $\rho(\chi)$, which was $\Delta H_{\mathrm{max}} = 26\ \mathrm{kJ\,mol^{-1}}$. From one point of view a different value is what one would expect. The decorrelation of $C_\chi(t)$ is described by a stretched-exponential fit, with the temperature-dependent KWW exponent β_{C_χ} found to be smaller than 1. As discussed, this implies a distribution of relaxation times $\rho(\tau) \approx \rho_{\mathrm{KWW}}(\tau)$ rather than a single transition time. Another way of interpreting this is that there exists a distribution of energy-barrier heights, which obviously determines the average energy barrier. One reason for this fluctuating barrier height could be the cooperative nature of the flip transition, as shown by energy-minimization methods [144, 145, 252]. The energy barriers for some conformations are much lower than for other ones. Also, the local barrier heavily depends on the nonbonded local environment, i.e., on the interchain interactions [145, 210].

In fig. 4.6 the KWW exponent β of various autocorrelation functions is plotted as a function of temperature. At relatively high temperatures $\beta_{C_\chi} \approx 1$. This is what one would expect for a relaxation mechanism which only involves a single energy barrier. So this indicates that at these temperatures the phenyl-ring flip might be approximately described by a single barrier, too.

At lower temperatures β_{C_χ} decreases. One way of interpreting this is that the distribution of energy barriers becomes broader upon lowering the temperature. However, then the question remains regarding the origin of the broadening of this distribution. A more appealing interpretation is that a set of states with a diversity in energy barriers exists both at low and at high temperatures. Only now the difference is that upon lowering the temperature the residence time at each state (with accompanying energy barrier) increases, making it harder to find the lowest energy barrier within the typical time of a transition. This state is likely to be largely characterized by the backbone conformation, which mainly determines the potential-energy barrier of a phenyl-ring flip (as is discussed before). The relaxation of the backbone is then indicative of the residence time at each state. This interpretation is supported by the simulation result of the atactic chain of polystyrene in a vacuum at $T = 375$ K. For this simulation we find that $\beta_{C_\chi} = 1$ (compared to $\beta_{C_\chi} = 0.7$ for the glassy system at the same temperature). In a vacuum conformational transitions are not hindered by the presence of other chains, leading (in this picture) to faster transitions between the various local energy barriers, and thereby the phenyl ring with its surroundings (apparently) finds the lower energy barrier within the transition time accompanied by this energy barrier.

A decrease of the stretch parameter β for decreasing temperature has been observed for other glassy materials as well, such as for the autocorrelation function of the torsion angle in polyethylene [137].

In contrast to β_{C_χ}, β_{C_2} is approximately independent of temperature (although a small drift towards higher values upon cooling is visible, which possibly originates from the limited time window available for fitting; it is known that in some situations this could lead to an increase in the fitted stretch parameter β [47]) and approximately equal to 0.4–0.6. This value is typical for simulation results of polymers. It has been observed in other MD simulations of polystyrene [118], and also for other polymers, such as poly(ethylene oxide) [89].

4.3.4 Heterogeneity

A distribution of energy-barrier heights generally would imply heterogeneous dynamics. This can indeed be seen from trajectories of the χ-angle. Some typical trajectories are shown in fig. 4.7. For $T = 300$ K it is observed that out of a total number of 560 phenyl rings (the five phenyl rings near each chain end are discarded in view of the known increase in mobility around the ends of a polymer chain [55, 171]) 548 phenyl rings (98%) did not flip at all during a 24 ns simulation run. However it turns out that of the remaining phenyl rings eight flipped once, two flipped twice and two flipped more than 10 times, illustrating the nonhomogeneous dynamics during this time window.

It is also observed that, while the averaged equilibrium position of the χ angle is at 0 (and at π), some phenyl rings seem to prefer other (temporarily) quasi-equilibrium positions (such as seen in fig. 4.7b and fig. 4.7c) and that infrequent transitions are possible between these quasi-equilibrium positions (fig. 4.7c). Note also that a phenyl-ring flip not necessarily

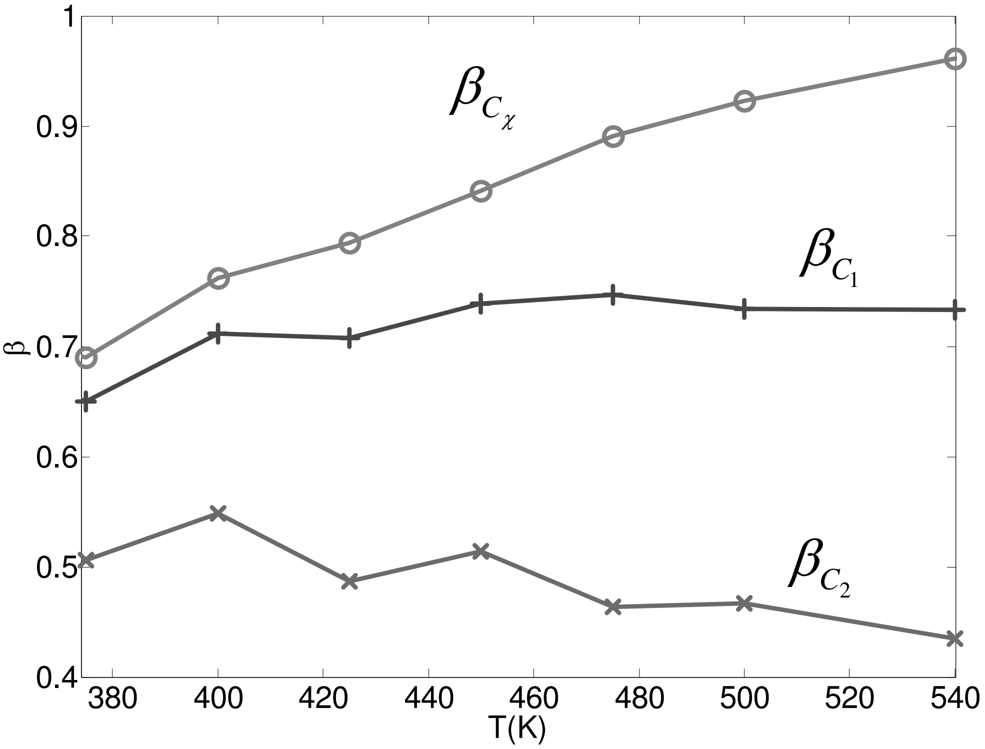

Figure 4.6: Fitted KWW exponent β as a function of temperature for $+$: the relaxation of the *o*-CH–*o*-CH vector within the phenyl as probed by $C_1(t)$, $\times$: same, now as probed by $C_2(t)$, $\circ$: the relaxation of the χ-angle as probed by the accompanying angle-based $C_\chi(t)$. Solid lines serve as a guide to the eye.

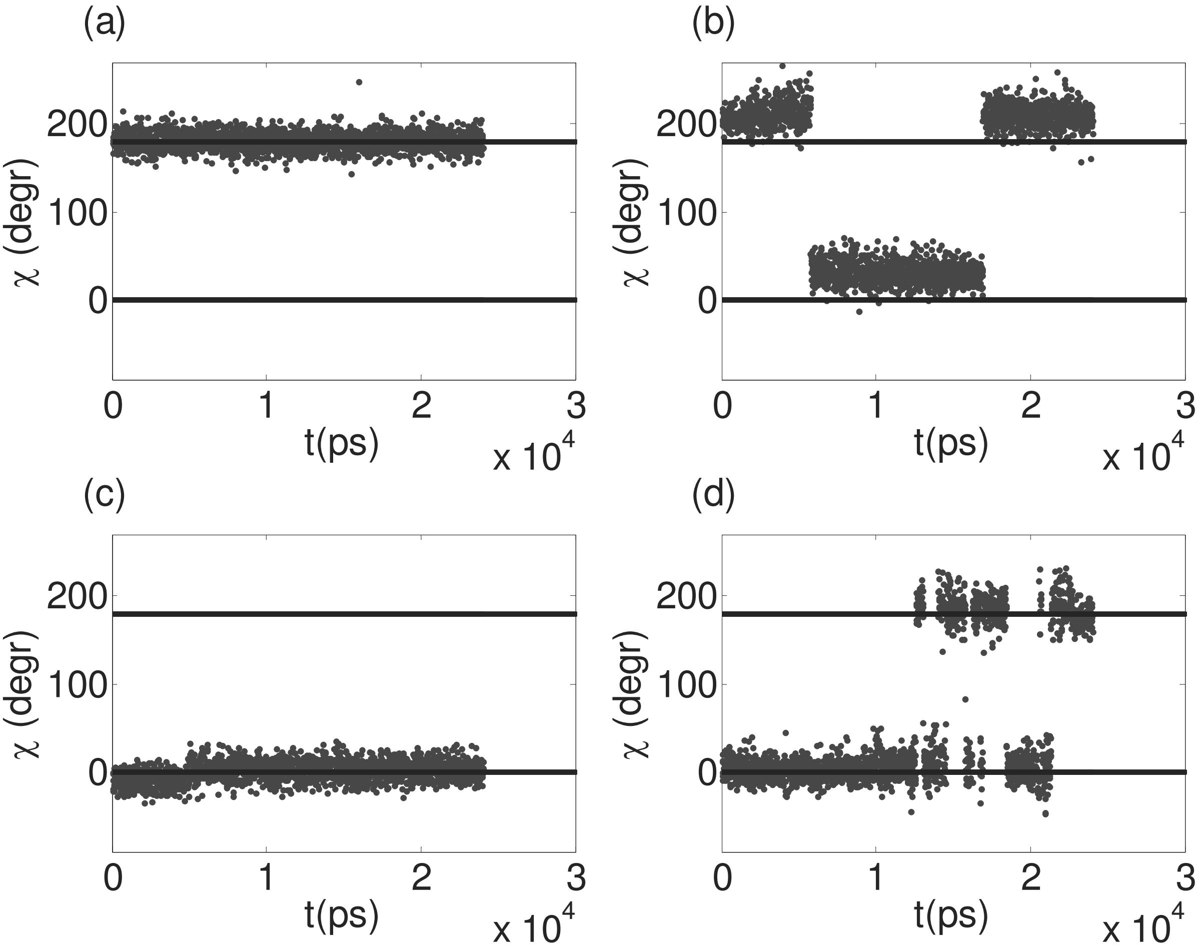

Figure 4.7: Typical trajectories for the χ angle at $T = 300$ K during a 24 ns simulation run. χ-values are plotted every 12 ps. (a) no jumps, (b) two jumps, (c) jump within cage around 5 ns, (d) many jumps. Solid lines denote the equilibrium values $\chi_{\text{min}} = 0,\, \pi$.

forces the quasi-equilibrium position to change (fig. 4.7b). So next to the heterogeneity in energy-barrier heights, there also exists heterogeneity in the value of $\chi_{\rm min}$, i.e., in the angle χ at which the energy is at its minimum. Yet another type of heterogeneity is in the width of the energy minimum. The fluctuations around the local minimum in fig. 4.7(b) are significantly larger than for example those in fig. 4.7(a). These small-scale heterogeneities can be seen more quantitatively by looking at the Van Hove function, which is carried out in the next section.

As was concluded from the behaviour of the time correlation functions, the reason for these heterogeneities must be sought in a combination of inter- and intrachain interactions. For example, a shift of the equilibrium position to a new quasi-equilibrium position could arise because of these interactions, which could effectively hinder the phenyl ring to be around the usual equilibrium position, as has been illustrated in Bicerano [25]. Of course, some types of heterogeneities already exists in the sample. The polystyrene chains are atactic; three different triads for a phenyl ring are present in the simulation run (meso, racemic, and hetero). Also, the presence of chain ends near a phenyl ring could be a reason for a variation in the environment. The two most active phenyl rings in this particular trajectory (which turn out to be well separated from each other, namely about 30 Å) are in a different type of triad, and the closest chain ends have a minimal separation of about 3.2 and 7.5 Å for these phenyl rings. Moreover, all three types of triads are among the phenyl rings which flip two or more times. On the basis of these results, no definite conclusions can be drawn whether or not the dynamical heterogeneities of the phenyl-ring flip are mainly caused by the presence of chain ends or due to variations in tacticity.

As mentioned before, a plausible cause of the heterogeneity is that below the glass-transition temperature the motion of the main chain is nearly frozen in, so is the backbone conformation near a phenyl ring. It has been shown [107, 252, 257] that some backbone conformations (depending on the type of triad) result in a lower energy barrier for the phenyl-ring flip than other backbone conformations. At sufficiently low temperature some phenyl rings can therefore be stuck in these low-energy-barrier conformations, while others are stuck in the high-energy-barrier conformations. From this one could conclude that the length scale associated with the most active phenyl rings is limited to one phenyl ring only, as each phenyl ring is surrounded by its own backbone conformation. It would be interesting to have a future study investigating the correlations between active phenyl rings and specific backbone conformations by means of molecular-dynamics simulations, as is, e.g., done in the study of methyl-group rotations in polyisobutylene [142].

4.3.5 Van Hove function

The self-part of the Van Hove function [110] can be examined to give more insight into the distribution of angular displacements over a time interval t of the angle χ_i describing the orientation of a phenyl ring i with respect to the backbone. As χ is a periodic coordinate,

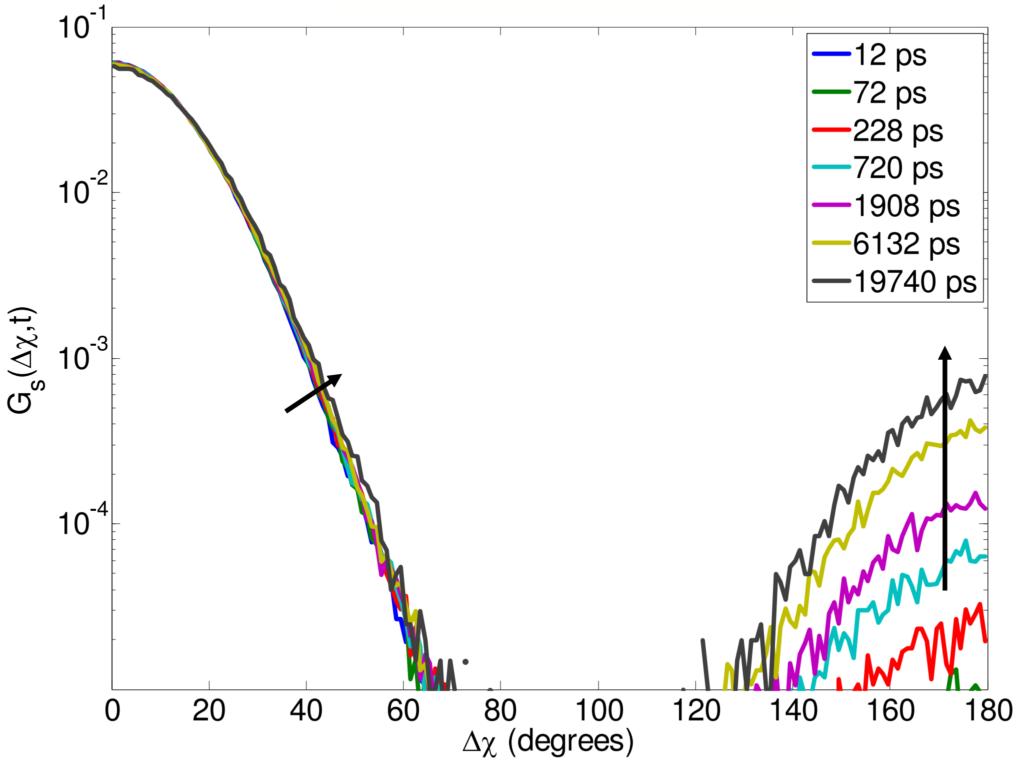

Figure 4.8: Self part of the Van Hove function $G_s(\Delta\chi, t)$ (eq. 4.13) for the absolute value of the boxed angular displacement $\Delta\chi$ for various instances of time at $T = 300$ K. Arrows point towards increasing time.

the periodic, 'boxed' Van Hove function

$$G_s(\Delta\chi, t) \equiv \langle \delta \left\{ \Delta\chi - |f[\chi_i(t_0 + t) - \chi_i(t_0)]| \right\} \rangle \qquad (4.13)$$

is calculated. Here the averaging $\langle \cdots \rangle$ is done over every phenyl ring i as well as over all available time origins t_0. To handle the periodicity of the χ angle, the difference $\chi_i(t_0+t) - \chi_i(t_0)$ is first boxed (as is also common in calculations of spatial coordinates in combination with periodic boundary conditions [6]), by using the function $f(\chi) \equiv \chi - 2\pi \cdot \text{anint}(\frac{1}{2\pi}\chi)$, in which the function $\text{anint}(x)$ rounds x towards the nearest integer. The absolute value symbols, $| \cdots |$, serve to acquire only positive displacements. So the self-part of the Van Hove function $G_s(\Delta\chi, t)$ is a measure for the probability of a certain angular displacement $\Delta\chi$ after a period of time t.

The simulation data of $G_s(\Delta\chi, t)$ for $T = 300$ K are displayed in fig. 4.8. The first bump at angle differences smaller than about $\pi/2$ is relatively constant over the investigated time interval. This means that the surrounding of the local minimum is already mostly explored within 12 ps. Nevertheless, there is a small increase in the displacement up until about $\Delta\chi = \pi/2$. Probably this has its origin in processes responsible for the small-scale heterogeneity in the value of $\chi_{\min}$ and in the magnitude of fluctuations around this value. If a phenyl ring makes for example a small-scale jump to a new quasi-equilibrium position (such as the one visible in the trajectory displayed in fig. 4.7c), then the effective angular displacement within the first cage will increase.

The second bump is representative for the fraction of phenyl rings which made a flip motion. Note that it is steadily increasing in time. The next section will be devoted to the time dependence of this fraction.

4.3.6 Two-state analysis

To isolate the fraction of jumped phenyl rings in a more quantitative way, we divide the phenyl rings into two states, $\uparrow$ and $\downarrow$, in which the boundary between the two states is taken to be at $\chi = 90$ degrees. If a π flip occurs, the phenyl ring will go from one to the other state. A similar analysis for transitions between the trans, gauche$^+$, and gauche$^-$ conformations has been carried out before [33, 230].

The $\uparrow$ state is defined so that at $t = 0$ all phenyl rings are in this state. The fraction of phenyl rings at time t in the $\uparrow$ state is denoted by $\phi_\uparrow(t)$. The initial conditions are $\phi_\uparrow(0) = 1$ and $\phi_\downarrow(0) = 0$, and it is expected that $\lim_{t\to\infty} \phi_\uparrow(t) = \lim_{t\to\infty} \phi_\downarrow(t) = \phi_{eq} = \frac{1}{2}$, since the two states are completely symmetric. If there would be only one energy barrier and if inertial effects can be neglected, then at sufficiently low temperatures this process can be modelled by a simple master equation [217]

$$\begin{aligned} \dot{\phi}_\uparrow(t) &= -k\phi_\uparrow(t) + k\phi_\downarrow(t) \\ \dot{\phi}_\downarrow(t) &= -k\phi_\downarrow(t) + k\phi_\uparrow(t), \end{aligned} \tag{4.14}$$

with the solution

$$\begin{aligned} \phi_\uparrow(t) &= \frac{1}{2}(1 + e^{-2kt}) \\ \phi_\downarrow(t) &= \frac{1}{2}(1 - e^{-2kt}), \end{aligned} \tag{4.15}$$

with k the transition rate, and with the dot denoting differentiation with respect to time. As the two fractions are simply related via $\phi_\uparrow(t) + \phi_\downarrow(t) = 1$, we will from now on only focus on the fraction of jumped particles $\phi_E(t) = \phi_\downarrow(t)$, with $E \equiv -k_B T \ln(k/k_0)$ and k_0 a measure for the attempt rate. Here the subscript E stands for the activation energy of the process and has been added to differentiate $\phi_E(t)$ from the jump fraction $\phi(t)$ as measured during the MD simulation (as $\phi(t)$ does not necessarily stem from one energy barrier).

From the fraction of jumped particles we can construct the normalized autocorrelation function [56]

$$\begin{aligned} C_\phi(t) &= \frac{\langle \Delta\phi(t)\Delta\phi(0)\rangle}{\langle \Delta\phi(0)\Delta\phi(0)\rangle} \\ &= \frac{\langle [\phi_i(t) - \phi_{eq}]\,[\phi_i(0) - \phi_{eq}]\rangle}{\langle [\phi_i(0) - \phi_{eq}]\,[\phi_i(0) - \phi_{eq}]\rangle} \\ &= 1 - 2\langle \phi_i(t)\rangle \\ &= 1 - 2\phi(t), \end{aligned} \tag{4.16}$$

in which the equalities $\phi_{eq} = \frac{1}{2}$ and $\phi(0) = 0$ have been used. The average $\langle \cdots \rangle$ is taken over all phenyl rings i. So in the case of a single transition rate eq. 4.16 simplifies to $C_\phi(t) = C_{\phi_E}(t) = e^{-t/\tau}$, with $\tau = \frac{1}{2k}$.

Note that $C_\phi(t)$ is very similar to $C_\chi(t)$. In fact, if the librating motion within the local minimum would be negligible and all rings would be either at the position $\chi = \pi$ or $\chi = 0$, then $\cos[\Delta\chi(t)] = -1$ if the phenyl ring has flipped and $\cos[\Delta\chi(t)] = 1$ if it did not flip. In this case $\phi(t) = \frac{1}{2}\langle 1 - \cos[\Delta\chi(t)]\rangle$ and hence $C_\chi(t) = C_\phi(t)$. The simulation results indicate that these two functions indeed show approximately the same long-time behaviour. Fitting both $C_\chi(t)$ and $C_\phi(t)$ by a stretched exponential (eq. 4.6) results in almost the same values for β and τ_c; the difference is less than 3% for β and 9% for τ_c for $T > T_g$. However, the short-time behaviour is very different, because in this regime the librating motion cannot be neglected for $C_\chi(t)$. As is shown below, the short-time response of $C_\phi(t)$ is interesting to study in more detail.

On the basis of the non-exponential decay of $C_\chi(t)$, we expect to have a distribution of local free-energy barriers E with a distribution function $g(E)$. Therefore the expression for $C_{\phi_E}(t)$ needs to be averaged over all possible energy barriers, i.e.

$$C_\phi(t) = \langle C_{\phi_E}(t)\rangle = \int C_{\phi_E}(t) g(E) dE. \tag{4.17}$$

It is now easy to see that in general $\langle C_{\phi_E}(t)\rangle$ is not a single-exponential function. By Taylor expansion the average of $C_{\phi_E}(t) = \exp(-t/\tau_E)$ over the energy distribution function, $C_\phi(t)$ can be written as a linear combination of negative moments $\langle \tau^{-n}\rangle$ of the distribution function of relaxation times $\rho(\tau)$ (this distribution follows from $g(E)$ via $\tau_E = \frac{1}{2k_E}$). It would be much more desirable to use a simpler invariant of the energy distribution function, such as a single moment of $\rho(\tau)$. This can be done by concentrating on the short-time behaviour of $\phi(t) = \frac{1}{2}[1 - C_\phi(t)]$ and the associated first moment $\langle \tau^{-1}\rangle$ by only taking the leading part of the Taylor expansion

$$\phi(t) = \langle \phi_E(t)\rangle = \frac{1}{2} t\langle 1/\tau\rangle + \langle O(t/\tau)^2\rangle. \tag{4.18}$$

In fig. 4.9 the simulation results for $\phi(t)$ are shown for various temperatures. For sufficiently high temperatures we indeed see that $\phi(t)$ saturates towards the expected equilibrium value

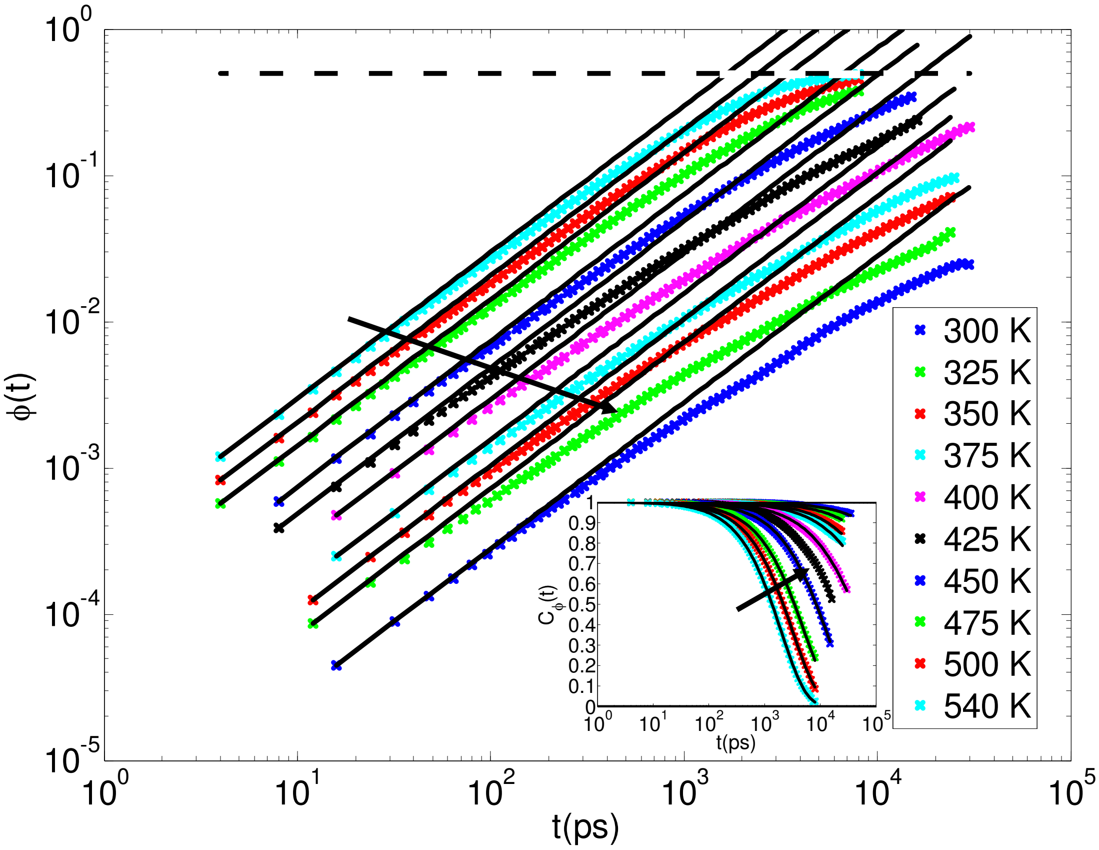

Figure 4.9: Fraction of phenyl rings that flipped with respect to the initial ($t = 0$) orientation. Solid lines are linear fits to the short-time behaviour of the simulation data (crosses). The long-time equilibrium value $\phi_{eq} = \frac{1}{2}$ is shown as a dashed line. The inset shows $C_\phi(t) = 1 - 2\phi(t)$, with solid lines fits to the simulation data by a stretched exponential, eq. 4.6, with $A = 1$. The arrows point towards decreasing temperature.

$\phi_{eq} = \frac{1}{2}$ for high values of t. For small time scales $\phi(t)$ is fitted by the linear function $\frac{t}{2\tau}$. One can observe that the deviation from linearity is only small for these time scales, suggesting that we indeed mostly probe the moment $\langle \tau^{-1} \rangle$.

Plotting $\tau_{-1} \equiv \langle \tau^{-1} \rangle^{-1}$ as a function of inverse temperature results in fig. 4.10. Also shown are the correlation relaxation times of $C_\phi(t)$, τ_{C_ϕ} (as determined by fitting $C_\phi(t)$ by a stretched exponential, eq. 4.6, but now with the prefactor fixed to $A = 1$). From the differences between the curves it is clear that the method of determining the relaxation time is very important for the exact temperature dependence of this time. For $T \approx 540$ K the two times as determined from the two different methods are about the same. However, for lower temperatures they start to deviate significantly from each other. A similar splitting of relaxation times upon cooling down has also been found experimentally (see, e.g., the review [67] for a discussion on this splitting for the small molecule *o*-terphenyl). For these low temperatures in which the two time scales differ significantly from each other, the relaxation time of $C_2(t)$ becomes larger than either τ_{-1} or τ_{C_ϕ} (see fig. 4.5). Since $C_2(t)$ is insensitive to a phenyl-ring flip, τ_{C_2} can be regarded as a measure for the time it takes for the phenyl ring to change to a new environment. So it appears that the dynamics of the phenyl-ring flip become heterogeneous because this time τ_{C_2} exceeds the typical transition time of a phenyl-ring flip. Around T_g the relaxation times τ_{-1} and τ_{C_ϕ} differ from each other by almost 1 order of magnitude. Despite this difference, they show approximately the same temperature dependence below T_g.

The observation that $\tau_{-1} \leq \tau_{C_\phi}$ can also be rationalized from the existence of a distribution of energy barriers. Phenyl rings having a low local free-energy barrier will relax first (i.e., at short times), and the phenyl rings with a higher local free-energy barrier will relax later. The short-time behaviour of $C_\phi(t)$ (as measured by τ_{-1}) is therefore representative for these low-energy barriers, while the long-time behaviour (as measured by τ_{C_ϕ}, arising from the stretched-exponential-function fit of $C_\phi(t)$) is more sensitive to the higher energy barriers. So the splitting of the two relaxation times upon cooling down can also be interpreted as a slowing down of transitions between states of different energy barriers, thereby promoting heterogeneous dynamics.

Fitting the relaxation times τ_{-1} by an Arrhenius law results in an activation enthalpy of $\Delta H_{\tau_{-1}} = 27\,\mathrm{kJ\,mol^{-1}}$. Note that this enthalpy $\Delta H_{\tau_{-1}}$ is much lower than the value acquired by fitting the relaxation times of $C_\phi(t)$, 47 kJ mol^{-1} (in which the temperature range for the fit was 375–540 K), but it is remarkably close to the enthalpy barrier as determined from the temperature dependence of the distribution function of χ, viz. $\Delta H_{\max} = 26$ kJ mol^{-1}(fig. 4.3). Note also that the activation enthalpy for $C_\phi(t)$ for temperatures below the glass-transition temperature (i.e., 300–375 K), $\Delta H_{C_\phi} = 25\,\mathrm{kJ\,mol^{-1}}$, is close as well to the enthalpy barrier $\Delta H_{\max}$.

The observed similarity between $\Delta H_{\tau_{-1}}$ and $\Delta H_{\max}$ can also be explained by assuming a distribution of energy barriers. The free-energy barrier height as determined from the distribution function is calculated using the ratio $\rho(\chi_{\max})/\rho(\chi_{\min})$, i.e., $\Delta G_{\max} =$

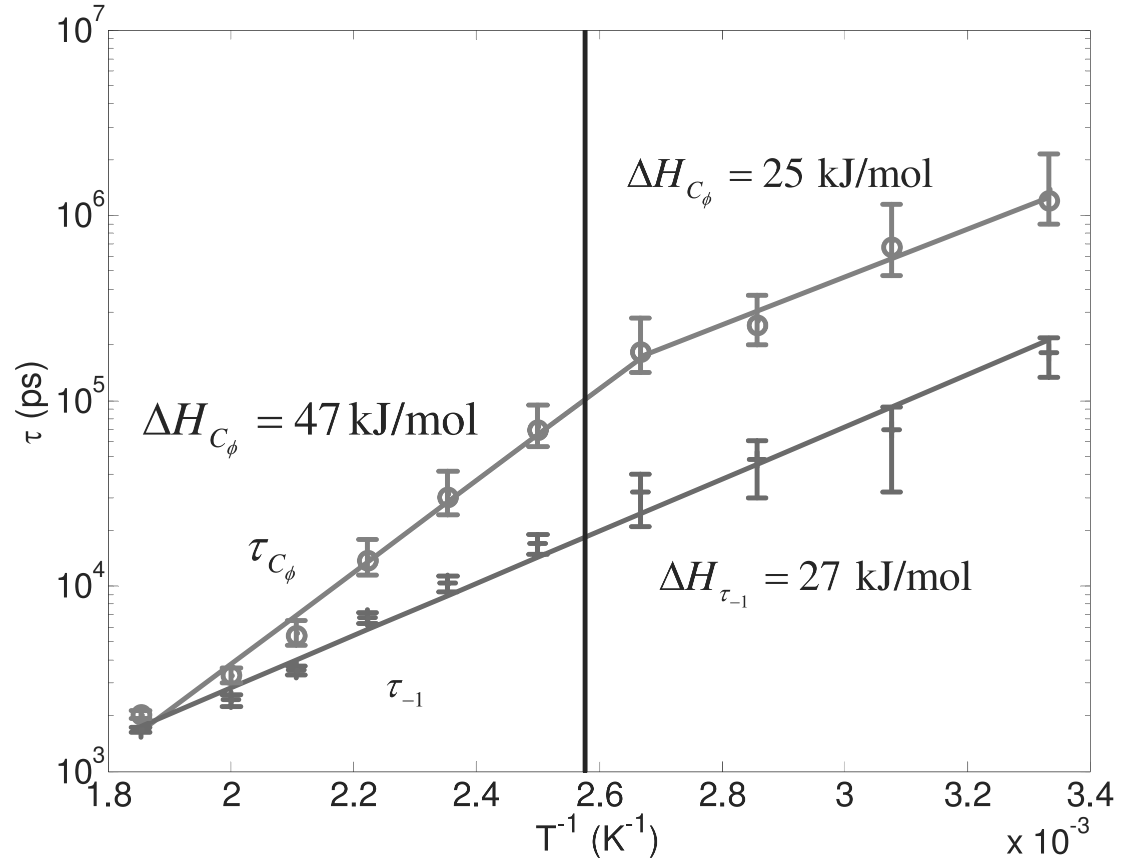

Figure 4.10: Typical time scales of a phenyl-ring flip as a function of the inverse temperature. +: determined from the initial time behaviour of the fraction of flipped phenyl rings $\phi(t)$. ∘: determined from the correlation time of the autocorrelation function $C_\phi(t)$ (by fitting it with a stretched exponential, eq. 4.6). The solid vertical line indicates $T_g = 388$ K. The three other solid straight lines are Arrhenius fits (eq. 4.12); the resulting activation enthalpies are 47 kJ mol^{-1} (∘, $T \geq 375$ K), 25 kJ mol^{-1} (∘, $T \leq 375$ K) and 27 kJ mol^{-1} (+). The remaining solid lines are a guide to the eye. The splitting of the two time scales τ_{-1} and τ_{C_ϕ} for lower temperatures is indicative of the broadening of the distribution of relaxation times.

$-k_BT\ln\left[\frac{\rho(\chi_{\max})}{\rho(\chi_{\min})}\right]$. What is measured during a simulation run is the number of phenyl rings $n(\chi)$ which have an angle between χ and $\chi + d\chi$. Call the total number of phenyl rings N. With $n(\chi) = \frac{1}{N}\rho(\chi)d\chi$ it follows that $n(\chi) = \langle n_E(\chi)\rangle = N\langle\rho_E(\chi)\rangle d\chi = N\rho(\chi)d\chi$. For $\chi_{\max}$ we can write

$$\begin{aligned}\rho(\chi_{\max}) &= \langle\rho_E(\chi_{\max})\rangle \\ &= \left\langle \rho(\chi_{\min})e^{-\frac{E(\chi_{\max})-E(\chi_{\min})}{k_BT}}\right\rangle \\ &= \rho(\chi_{\min})\left\langle e^{-\frac{E(\chi_{\max})-E(\chi_{\min})}{k_BT}}\right\rangle \qquad (4.19)\end{aligned}$$

in which it has been assumed that $\rho(\chi_{\min})$ is approximately independent of the local energy barrier. Therefore

$$\Delta G_{\max} = -k_BT\ln\left(\left\langle e^{-\frac{E(\chi_{\max})-E(\chi_{\min})}{k_BT}}\right\rangle\right). \qquad (4.20)$$

Similarly, averaging the inverse transition time (given by eq. 4.12) over the distribution of energy barriers, while assuming that $\tau_0' = \tau_0\exp\left(\frac{\Delta S_{\max}}{k_B}\right)$ is approximately independent of the local energy barrier, gives

$$\begin{aligned}\left\langle\tau^{-1}\right\rangle &= \left\langle \tau_0'^{-1}e^{-\frac{\Delta E}{k_BT}}\right\rangle \\ &= \tau_0'^{-1}\left\langle e^{-\frac{E(\chi_{\max})-E(\chi_{\min})}{k_BT}}\right\rangle. \qquad (4.21)\end{aligned}$$

In other words, if the assumptions are met, $\langle\tau^{-1}\rangle$ and $\Delta G_{\max}$ (and therefore also $\Delta H_{\max}$, by the usage of eq. 4.3) probe the same invariant of the energy distribution function, and as a result they yield the same enthalpy-barrier height.

The correspondence between ΔH_{C_ϕ} and $\Delta H_{\max}$ for $T < T_g$ could be due to the supposed fact that the width of the distribution of energy barriers is not changing much anymore in this temperature range. A similar result has been observed before by MD simulations [230], in which the spread of activation energies for a methyl-group rotation in poly(vinyl methyl ether) remains constant below the glass-transition temperature; this was also seen in experimental data on the same system. However, another reason could be the limited time window of the autocorrelation function $C_\phi(t)$. Fitting this with a stretched exponential function then effectively favours the short time scales over the long time scales, so that it becomes more sensitive to the lower energy barriers. Upon cooling further, this effect becomes even stronger.

The method of determining the time scale by means of the fraction of escaped particles at short times gives thus a relaxation time of about 30 ns at $T = 375$ K. This is consistent with NMR experiments [244], which find that the correlation time of the π jump is in the range of 10–100 ns at $T = 373$ K.

4.4 Summary, conclusions, and outlook

It has been shown that the effective energy barrier associated with a phenyl-ring flip of polystyrene is very dependent on the physical quantity under study. This is a result of the growth of dynamical heterogeneity upon cooling down, as confirmed by various methods. For relatively high temperatures the effect is small, but close to the glass transition heterogeneity plays an important role. For temperatures just above the glass transition the activation enthalpy of one relaxation time of the phenyl-ring flip (probing the long-time behaviour) is almost a factor of 2 higher than that of another relaxation time of the same process (but probing the short-time behaviour), as is shown in fig. 4.10. Nevertheless, the fraction of flipped phenyl rings for very small times gives an estimate for the average transition rate, and it turns out that the temperature dependence of this transition rate is similar to one that would be expected from the effective energy barrier based on the probability distribution function of the orientation of the phenyl ring, despite the presence of heterogeneous dynamics.

A possible reason for the observed apparent widening of the distribution of local energy barriers upon cooling down could be given by the following picture. It is known that the effective phenyl-ring barrier depends on the local environment, in particular on the backbone conformation. The flip barrier associated with some conformations can easily exceed the α-relaxation time. A phenyl ring in such a state will be able to flip faster by changing its state (by means of a change in the nearby backbone conformation) to another one with a low flip barrier. So the total time it takes to flip for such phenyl rings is on the scale of the sum of the relaxation time of the environment and the low-barrier flip time. For high temperatures the local environment relaxes much faster than the low-barrier flip time. In this case the flip time for the phenyl rings with a high flip barrier is almost the same as the flip time for phenyl rings with a low flip barrier, so that the heterogeneity in the flipping dynamics is practically absent. However, for lower temperatures the environment of the phenyl rings becomes more sluggish, and eventually the relaxation time of the environment will be much larger than the low-barrier flip time. In this case the phenyl rings with a high flip barrier will flip on a much slower time scale than the low-barrier phenyl rings. This encompasses a spread in relaxation times and therefore heterogeneous dynamics.

In contrast to temperatures above the glass transition, it turns out that for the sub-T_g regime the two different definitions of relaxation time (from a KWW fit and from the short-time analysis) render about the same effective energy barrier. This could be either due to the limited time window of the relaxation function (so that one effectively only probes these short-time scales) or because of that the width of the energy distribution stays approximately constant. This energy barrier for the phenyl-ring flip is shown to be in accordance with the energy barrier for the γ relaxation as is deduced from experimental results. Of course, this does not rigorously imply that the γ relaxation is the result of the phenyl-ring flip. It is also possible that the phenyl-ring flip acts as an indicator for the γ relaxation, but that it does not participate in the mechanical relaxation, as is also speculated for the π-flip in polycarbonate [277]. Another possibility is that the γ relaxation is due to the backbone relaxation, as preliminary results show that the free energy barrier between some conformations is of about the same magnitude as the free-energy barrier of a phenyl-ring flip. A more stringent test would be to carry out a simulation in which the γ relaxation is identified, such as with an oscillatory shear experiment. The persistence or disappearance of the γ relaxation upon artificially increasing the phenyl-ring-flip barrier would then show whether this is the true molecular origin of the γ relaxation.

Chapter 5

Deformation of polystyrene: atomistic simulations

ABSTRACT

To gain more insight at an atomistic level into yielding, strain softening and strain hardening in glassy polymers, molecular-dynamics simulations of atactic polystyrene under the influence of active deformation have been carried out. In these simulations it is observed that the yield peak is mainly connected with interchain and the strain hardening mainly with intrachain interactions. The deformation does not lead to complete erasure of the thermal history. The strain-hardening modulus increases with increasing external pressure, an observation that can not be explained by the entanglement picture.

5.1 Introduction

Glassy polymeric materials show a rich behaviour under deformation. During a compression test an initial elastic regime is followed by yield after which the material softens (strain softening, with a noticeable drop in stress). Upon compressing even further the strain-hardening regime is entered; then the stress needed to deform the material grows. This is quantified by the strain hardening modulus, defined as the slope of the stress as function of Gaussian strain [114].

The relative magnitudes of these regimes have a dramatic effect on the resulting mechanical behaviour of the polymer during a tensile test. For example, if the yield drop is high and the strain hardening is low, the material will be very brittle during uniaxial-stress extension. This is the case for the well-known atactic polystyrene glass. Here stress localization plays a role. If the weakest link of a material with a high yield drop yields, the stress necessary to strain that part further will be lower than the stress to yield other parts of the material. Therefore, the weakest link will be strained further. If the strain hardening is insufficient to strengthen the weakest link this will ultimately break. As in this case the strain is limited to only a small part of the material the macroscopic sample shows an almost instantaneous fracture (i.e., within a few percent of extension). However, a minor change in the mechanical characteristics results in a totally different behaviour. A slight decrease in yield drop or more strain hardening can result in a material which can easily be extended by one order of magnitude more before breakage.

The toughness is a variable which depends both on the polymer structure and on the combined thermal and mechanical history of the polymer material. Glassy polymers such as polyvinylchloride, polycarbonate and polymethyl-methacrylate [102, 114] are more tough than polystyrene, because they have a higher strain-hardening modulus. Brittle polystyrene itself can also be made tougher, as was shown recently by Govaert et al. [103]. Such toughening can be reached by mechanical preconditioning or by thermal quenching of a polymer glass.

The thermal and mechanical history is therefore of prime importance in predicting the mechanical behaviour of the polymer glass. Unfortunately a satisfying theory about the stress drop and the strain hardening of polymeric glasses is lacking. It is unknown what the exact reason is for the high yield tooth (peak and subsequential drop of the stress) observed in polystyrene. The other serious knowledge gap is the physical original of strain hardening. Rubber-elasticity theory, based on the entropic picture of a polymer chain, predicts a strain-hardening modulus two orders of magnitude lower than what is measured experimentally [155, 266].

Understanding what is happening at the microscopic scale would be useful for developing new theories. Despite the vast literature of experimental results on the mechanical properties of polystyrene [20, 35, 37, 59, 61, 96, 103, 106, 112, 114, 147, 159, 160, 186, 199, 202–

204, 238, 240, 266–268, 279, 285], studies at the molecular level are rather scarce as it is experimentally very hard to measure changes at this level.

The method of molecular-dynamics simulations has proven to be a successful alternative to study the mechanical properties of glassy polymers as various parameters can be changed rather easily and physical details of all atoms are available. Numerous studies applied this method before on various polymer models, such as on bead-spring models [91–94, 226, 227, 229, 274] and on bead-spring with bond-angle-potential models [90, 123–125]. More chemically realistic MD simulations of polymers have been carried out on amorphous polyethylene [34, 38, 39, 46, 184, 286], polystyrene [173, 176, 177, 237] and polycarbonate [82, 173, 177, 237]. Also other simulation techniques are applied to study the deformation of polymers, such as Monte Carlo algorithms or energy-minimization-alike methods for polypropylene [12, 13], PMMA [44], poly(oxypropylene) [134], polycarbonate [74, 75, 130] and polyethylene [168, 191].

These simulations show that trends seen in experimental studies on mechanical properties as a function of external parameters are reproducible. Examples are the behaviour of the Young modulus, the yield peak and the strain-hardening modulus as a function of control parameters such as temperature and strain rate. As the simulation studies are limited to only small time and length scales, numerical agreement is often only possible by means of extrapolation over orders of magnitude. The importance of mechanical history is recently also observed in simulations.

Despite all these findings no new theory has emerged and the two questions raised above about the physical origins of strain hardening and the yield tooth are still open.

The goal of the current chapter is to acquire more physical insight in these two phenomena of deformation of glassy polymers. This is done by looking at the partitioning of energy and stress to see which interactions are dominant for the yield and the strain-hardening regime. The simulations are on a chemically realistic atactic-polystyrene melt under various conditions: extension vs. compression, quenched vs. annealed, and as a function of external pressure. A chemically realistic model allows one to compare the simulation results with experiments, although extrapolations are necessary. Before showing the results, the details of the simulation method are explained first.

5.2 Simulation details

Simulations are carried out by using the molecular-dynamics program *puma* developed by Balabaev [15] and Mazo [183]. Variants of this program have been used before [165]. The program has been modified slightly to distinguish intrachain Lennard-Jones (LJ) interactions from interchain LJ interactions.

The used force field for atactic polystyrene can be found in [271] and chapter 2. The density of the sample is set to the experimental density at $T = 540$ K and atmospheric pressure. As no data were available at this temperature and pressure, the density at this point is determined by a linear extrapolation from lower temperatures [293] at atmospheric pressure, with the result 0.916 $\mathrm{g\,cm^{-3}}$. After an equilibration of several ns, the internal pressure at this density is measured and is found to be equal to 42 MPa. A possible reason for this deviation from atmospheric pressure could be deviations in the force field; an example is that the LJ potentials have a finite cut off. As the experimentally observed bulk compression modulus of polystyrene is about 3 GPa at room temperature [181], the pressure offset of 42 MPa roughly corresponds to a small volume decrease of 1.4%. Unless stated otherwise, simulations are carried out at this pressure. The influence of a pressure change on the mechanical moduli is also subject of study in the present chapter.

Five independent samples are prepared at $T = 540$ K by the procedure as is described in §2.5. To study the effect of cooling rate these samples are cooled to $T = 300$ K by two velocities: 0.01 K ps^{-1} ('slowly' cooled or computationally annealed) and 0.1 K ps^{-1} ('fast' cooled or computationally quenched). If not specified, results are for the slowly cooled samples.

The simulations are carried out at uniaxial-stress extension or uniaxial-stress compression. The strain in the active deformation direction is changed by resizing the periodic orthorhombic box in that direction. The lateral sides are kept at a constant stress value by using the Berendsen barostat [6] with a ratio of the time constant to the compressibility $\tau_P/\beta = 0.011$ Pa s. Temperature is controlled by using the so-called collisional-dynamics method [165], in which the particles collide with 'virtual' particles of mass $m_0 = 0.1$ Da and with times between collisions described by a Poisson process with average frequency $\lambda_{\mathrm{coll}} = 20\ \mathrm{ps}^{-1}$.

To increase statistics the deformation is carried out three times for each sample (along each axis once), making the total number of runs equal to 15 for each set of external conditions (if unspecified).

Some simulations are carried out at $T = 300$ K, but at pressures different from the offset value. This is established by taking the slowly cooled samples at 300 K and setting the external pressure to the desired value. This is followed by an equilibration of 0.5 ns. These samples then either serve as an input for the deformation run or for the unstrained production run.

The initial box sizes are around $L(0) = 50$ Å. The coordinate system is taken in such a way, so that active extension or compression is in the x-direction. The engineering strain is then $\varepsilon_{\mathrm{eng}} = \frac{L_x(t)-L_x(0)}{L_x(0)}$. Other symbols which will be used throughout this chapter are the true strain, $\varepsilon_{\mathrm{true}} = \ln(1 + \varepsilon_{\mathrm{eng}})$ and the draw ratio, $\lambda = 1 + \varepsilon_{\mathrm{eng}}$. For small strains $\varepsilon_{\mathrm{eng}} \approx \varepsilon_{\mathrm{true}}$ and then the strain is simply written as ε.

All uniaxial-stress extension simulations are carried out at a constant velocity of 0.01 Å ps^{-1}, corresponding to a deformation rate of $\dot{\varepsilon}_{\mathrm{eng}} \approx 2 \times 10^8\ \mathrm{s}^{-1}$ (here the dot means differentiation with respect to time). The compression simulations are done at a constant deformation rate of $\dot{\varepsilon}_{\text{true}} = -10^8\ \text{s}^{-1}$. Some constant-rate extension simulations with $\dot{\varepsilon}_{\text{true}} = 10^8\ \text{s}^{-1}$ are also realized. However, a direct comparison with the constant-velocity extension simulations shows that the difference in the resulting stress-strain relation is below the statistical fluctuations and therefore we restrict ourselves from now one to the extension results with constant velocity.

In the current study relatively short chains are used; the number of monomers per chain equals 80. This is below the monomer entanglement length N_e of polystyrene ($N_e = 83$ [249, simulations, $T = 450$ K], $N_e = 128$ [78, experiments, $T = 413$ K], $N_e = 139$ [79, experiments, $T = 490$ K], determined via $M_e = \frac{4}{5}\rho RT/G_N$, with M_e the molecular weight between entanglements, R the universal gas constant and G_N the rubber-plateau modulus). Usually deformation would be affine for large length scales; for very long chains the ends do not feel immediately the connectivity constraint of each other as they are separated by many segments. For short chains this is not the case, and deformation becomes more non-affine; the end-to-end distance does not change in the same way as the box sizes. This could have an effect on the determination of the strain hardening. However, even short chains of length equal to about N_e show strain-hardening moduli comparable to longer chains for the typical strain rates in use up till about 100% extension [177]. Other evidence for substantial strain hardening for short chains was given by Hoy and Robbins [124]. Their study showed that the change in the end-to-end distance for a (short) chain of length $N \approx N_e$ was more than 80% of the affine value (here 0% is taken to be if the chains do not change in size at all) at $|\lambda^2 - \lambda^{-1}| = 2.6$ ($|\varepsilon_{\text{true}}| \approx 1$) under uniaxial compression, and that the resulting strain-hardening modulus for these short chains was nearly the same as for the much longer chains. In summary, we feel that the present short-chain simulations should give relevant insight into strain hardening in general.

5.3 Results and discussion

This result section is divided in three parts. First, the global stress-strain relation will be presented for various conditions: extension vs. compression, for different thermal histories, and as a function of external pressure. In the second part the results will be analyzed in terms of energetic contributions. This comprises the work, energy partitioning, the effect of thermal history and a connection with density and cage escape. In the third part the different contributions to the total stress are analyzed for the various situations. The consistent picture arising from these results is given in the conclusion section at the end of this chapter.

5.3.1 Stress development during deformation

In this part of the results section we will look at the stress development of polystyrene during deformation under various conditions. At first, we compare compression and extension simulations with each other and with the literature, in order to see if the simulations show some resemblance with experimental results.

The second condition to vary is the thermal history, as it is known that the yield tooth is highly influenced by this. It therefore gives more insight in this phenomenon. The final external factor of interest is the pressure, which greatly affects the strain-hardening modulus.

Compression and extension

During uniaxial-stress extension and compression tests the stress tensor is monitored. Instead of looking at all components of the stress tensor it is customary to study the von Mises equivalent true stress [164], which is a measure of the second invariant of the stress tensor (see also §1.3.1). The measured von Mises stress as a function of the applied strain during a uniaxial-stress extension and a uniaxial-stress compression simulation is depicted in fig. 5.1. Results are very similar if the true stress in the axial direction is plotted instead of the von Mises true stress (not shown). Each marker in fig. 5.1 represents an average of the measured stress during a period of time corresponding to the separation between two subsequent markers. In addition to this, the stress is averaged over 15 runs. The standard deviation of the average stress near the yield peak is about 4 MPa and increases slightly for larger strains (near $|\varepsilon_{\mathrm{true}}| = 0.7$ it is about 7 MPa).

It can be seen in fig. 5.1 that the stress both at the yield peak and near the yield drop after the peak are higher under compression than under tension. For extension the maximal stress value near initial yield is $\sigma_{\mathrm{peak}} = 117$ MPa and for compression $\sigma_{\mathrm{peak}} = 143$ MPa. The reason for the higher yield stresses under compression is that in this case the hydrostatic pressure is higher than under tension, and it is known that the stress for yielding amorphous polymers usually increases with increasing pressure [275, §11.5.3]. Molecular-mechanics simulations of a different polymer, atactic poly(oxypropylene) [134], also show that the yield stress under compression is higher than under extension.

Experimental values at room temperature are $\sigma_{\mathrm{peak}} = 100$ MPa [103, $\dot{\varepsilon}_{\mathrm{true}} = -10^{-2}$ s^{-1}], $\sigma_{\mathrm{peak}} = 87$ MPa [267, $\dot{\varepsilon}_{\mathrm{true}} = -10^{-3}$ s^{-1}], $\sigma_{\mathrm{peak}} = 72$ MPa [112, $\dot{\varepsilon}_{\mathrm{true}} = -10^{-3}$ s^{-1}, 'quenched'], $\sigma_{\mathrm{peak}} = 92$ MPa [112, $\dot{\varepsilon}_{\mathrm{true}} = -10^{-3}$ s^{-1}, annealed, cooling velocity in the order of mK s^{-1}]. The experimental values of σ_{peak} are all under uniaxial-stress compression and are a bit lower than in our simulations. The reason for this is that the deformation conditions are not the same. The experiments have a much slower strain rate (thereby lowering the yield stress; experimentally it is observed that the yield stress has a logarithmic dependence on the strain rate [267]), slower cooling rate (resulting in a higher yield stress

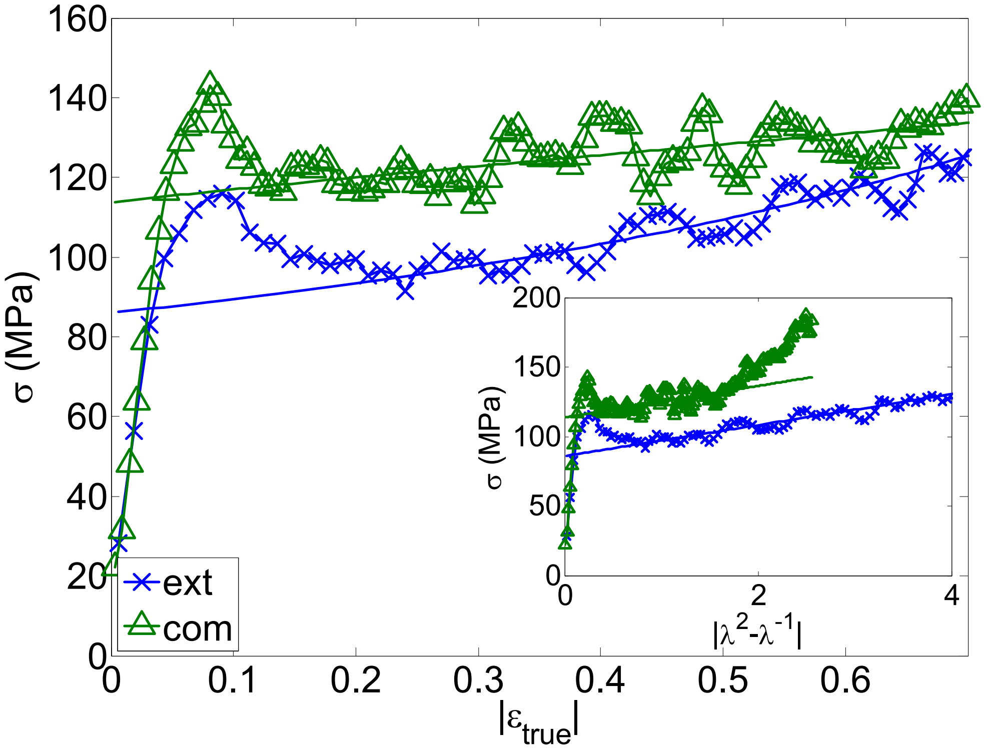

Figure 5.1: Von Mises true stress vs. absolute true strain for atactic polystyrene during extension ($\dot{\varepsilon}_{\text{eng}} = 2 \times 10^8$ s^{-1}, 'ext') and compression ($\dot{\varepsilon}_{\text{true}} = -10^8$ s^{-1}, 'com'). Inset shows the von Mises stress as a function of $|\lambda^2 - \lambda^{-1}|$, thereby showing a wider range for the compression data. Fitting the data in the inset by eq. 5.1 in the range $|\varepsilon_{\text{true}}| = 0.2$–$0.6$ gives for extension $\sigma_Y = 86$ MPa and $G_h = 11$ MPa, and for compression $\sigma_Y = 114$ MPa and $G_h = 11$ MPa.

[112]), and longer chain lengths (increasing the yield stress due to the slower relaxation of the middle of the chain compared to the chain ends [285]). Nevertheless, despite these differences, the results show qualitatively the same behaviour.

A simple constitutive relation between the (true) stress σ and the strain after yielding is the Gaussian-based equation [115, 117, §5.6.1]

$$\sigma = \sigma_Y + G_h(\lambda^2 - \lambda^{-1}) \tag{5.1}$$

with G_h the strain-hardening modulus, and σ_Y the offset yield stress (which is lower than the yield peak value, σ_{peak}).

To determine the strain-hardening modulus the stress-strain curves in fig. 5.1 are fitted with eq. 5.1. For extensions the fit range is $|\varepsilon_{\mathrm{true}}| = 0.25$–$0.6$ (as for $\varepsilon_{\mathrm{true}} > 0.6$ samples break) and to allow for a better comparison the fit range for compression is restricted to the same range in terms of the absolute value of the true engineering strain. The so-determined mechanical moduli are $G_h = 11$ MPa for extension, with an offset yield value of $\sigma_Y = 86$ MPa and $G_h = 11$ MPa for compression, with $\sigma_Y = 114$ MPa. In eq. 5.1 the stress is linear with the Gaussian strain $\lambda^2 - \lambda^{-1}$, both for extension and for compression. To check this, the stress is also plotted as a function of the absolute value of the Gaussian strain, see inset in fig. 5.1. The tension test shows indeed a linear regime after initial yield. The compression data deviate from this fit for large strains; extending the fit range to include all data points at large strains would result in a much larger apparent strain-hardening modulus, $G_h = 37$ MPa. We will come back to this point later on in this chapter in §5.3.3, as there the stress will be partitioned into smaller parts to isolate which interaction is responsible for this effect.

The experimental values for the strain-hardening modulus for room-temperature polystyrene under compression are around the values as found by the present compression and extension simulations; $G_h = 9$ MPa [279, $\dot{\varepsilon}_{\mathrm{true}} = -10^{-3}$ s^{-1}], $G_h = 11$ MPa [267, $\dot{\varepsilon}_{\mathrm{true}} = -10^{-3}$ s^{-1}], $G_h = 13$ MPa [266, $\dot{\varepsilon}_{\mathrm{true}} = -10^{-2}$ s^{-1}]. During an extension experiment it is difficult to measure the strain-hardening modulus as then a polystyrene sample usually breaks. However, a study of crazes of polystyrene under extension [113] gave $G_h = 2.2$ MPa.

It is known that the strain-hardening modulus of polymeric materials increases with increasing strain rate; examples are high-density polyethylene [113], and polyurea [233]. However, for other polymers the increase is very small or nearly absent, such as for polycarbonate [192]. It could very well be the case that the strain-hardening modulus of polystyrene also hardly changes with strain rate. This could explain the observed quantitative similarity between the simulation and the experimental results.

In spite of the obvious differences in deformation conditions, we can conclude that the simulated polymer system shows the same qualitative behaviour as polymers do in experimental studies. Hence the polystyrene model in use is quite realistic in terms of reproducing some mechanical properties.

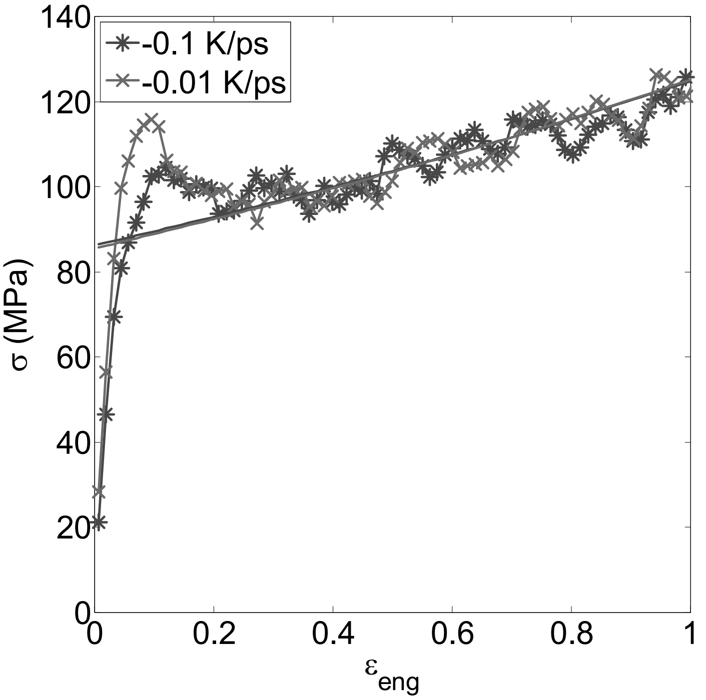

Figure 5.2: Von Mises equivalent true stress vs. strain for atactic polystyrene for two different cooling rates. Solid lines are fits of eq. 5.1. There is no difference for the strain-hardening modulus and the extrapolated yield value: for both $G_h = 11$ MPa and $\sigma_Y = 86$ MPa. However, the initial yield peak is higher for the slowly cooled sample ($\sigma_{\text{peak}} = 117$ MPa vs. $\sigma_{\text{peak}} = 104$ MPa). Also there is a small difference in the strain at which the yield peak occurs: $\varepsilon_{\text{eng}} = 9\%$ (slow) vs. $\varepsilon_{\text{eng}} = 12\%$ (fast).

Quenched vs. annealed samples

The properties of a glassy material are much affected by the thermal history of the sample, i.e., the initial thermal treatment before deformation starts. In particular is the mechanical behaviour affected, as can be seen in the two simulated stress-strain curves in fig. 5.2. Two different scenarios are compared: samples cooled down by 0.1 K ps^{-1} ('fast' cooled) and samples cooled down by 0.01 K ps^{-1} ('slowly' cooled).

Observe that for the faster-cooled sample (more quenched) the yield peak is lower than for the slower-cooled sample, 104 ± 4 vs. 117 ± 4 MPa. As discussed this tendency is confirmed by experimental results on polystyrene under compression; $\sigma_{\text{peak}} = 72$ MPa [112, $\dot{\varepsilon}_{\text{true}} = -10^{-3}$ s^{-1}, 'fast' cooled], $\sigma_{\text{peak}} = 92$ MPa [112, $\dot{\varepsilon}_{\text{true}} = -10^{-3}$ s^{-1}, 'slowly' cooled, cooling velocity in the order of mK s^{-1}].

The strain at the yield peak is around 9% for the slowly cooled sample, and 12% for the

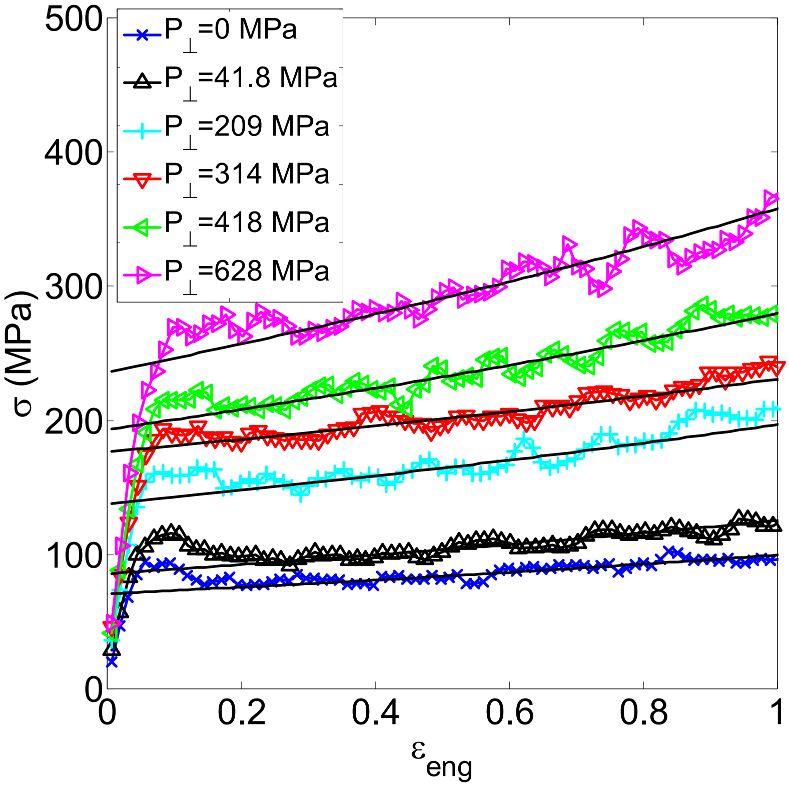

Figure 5.3: Von Mises stress vs. strain during uniaxial-stress extension for different external pressures at $T = 300$ K. Solid lines are fits to the simulation data as is done in fig. 5.1. Observe that both the yield peak and the strain-hardening modulus turn out to increase with increasing external pressure.

faster-cooled sample. Experimental results show a smaller strain value at yield (7%, Hasan and Boyce [112]). However, the trend is the same; also experimentally the quenched sample has a slightly higher strain value at yield as compared to the annealed sample [112].

Within statistical error the strain-hardening modulus is not altered by a different thermal history, the strain-hardening modulus is $G_h = 11$ MPa for both cooling scenarios.

Influence of external pressure

The behaviour of σ_Y as a function of external factors such as temperature T and pressure P is relatively well known. The effects of these external factors are described by the Eyring equation [275]. Even so, much less understanding is available for G_h. If rubber theory [117, 259] would be valid for glassy polymers, G_h equals $\frac{k_B T \rho}{M_e}$. Here ρ is the mass density and M_e the molecular weight between entanglements. Note that the predicted strain-hardening modulus does not depend explicitly on external pressure and it increases linearly with temperature. Experimentally the trend is, however, opposite; it is found that the strain-hardening modulus is decreasing with temperature (see for example Tervoort and Govaert [254]).

A different way of reasoning is that the strain-hardening modulus actually depends in the same way as the yield stress on external factors such as temperature and strain rate. Regarding the temperature dependence it indeed has been found experimentally that the ratio σ_Y/G_h is fairly constant over a range of temperatures [114, 117]. Simulations have shown that also the dependence on strain rate is about the same for both σ_Y and G_h [123].

What about the influence of external pressure? Based on the observed communalities between yielding and strain hardening with respect to temperature and strain rate, one would expect that pressure would also play a role during strain hardening. It is known that the yield stress rises with increasing pressure. Would the same be true for the strain-hardening modulus?

Simulations have been carried out at various external pressures to test this. In fig. 5.3 the von Mises stress is plotted as a function of strain for six imposed lateral pressures (number of simulation runs per pressure point is at least 10). Conform experimental data the simulation results show that the yield stress increases with external pressure. Note that the strain-hardening modulus also increases with increasing external pressure. As just stated, this is in contrast to what one would expect on the basis of the rubber theory [117], in which the strain-hardening modulus $G_h = \frac{k_B T \rho}{M_e}$ does not explicitly depend on the external pressure.

First we will study the pressure dependence of the yield stress, see fig. 5.4. Both the von Mises yield stress $\sigma_{\mathrm{vM},Y}$ and the yield stress in the extension direction $\sigma_{\parallel,Y}$ are plotted in this figure. That $\sigma_{\parallel,Y}$ is decreasing with external pressure is because it is taken as the absolute stress and not as the deviatoric stress.

These yield stresses are determined by fitting eq. 5.1 to the accompanying stress-strain curves. For the abscissa the pressure near the start of yielding, $P_Y = \frac{2}{3}P_\perp - \frac{1}{3}\sigma_{\parallel,Y}$, is used. Various other definitions of a yield stress exist [275], but the currently used one is chosen as it is not so susceptible to noise.

The data in fig. 5.4 are fitted by the straight lines

$$\sigma_{\parallel,Y}(P) = \sigma_{\parallel,Y,P_Y=0} + \mu'_Y P_Y \tag{5.2}$$

and

$$\sigma_{\mathrm{vM},Y}(P) = \sigma_{\mathrm{vM},Y,P_Y=0} + \sqrt{3}\mu_Y P_Y. \tag{5.3}$$

Here $\sigma_{\parallel,Y,P_Y=0}$, $\sigma_{\mathrm{vM},Y,P_Y=0}$, μ'_Y and μ_Y are fit coefficients. μ_Y is known as the pressure coefficient for yielding a material (the same convention has been adopted as by, e.g., van Melick et al. [267], hence the factor $\sqrt{3}$). The constant μ_Y can be interpreted as some

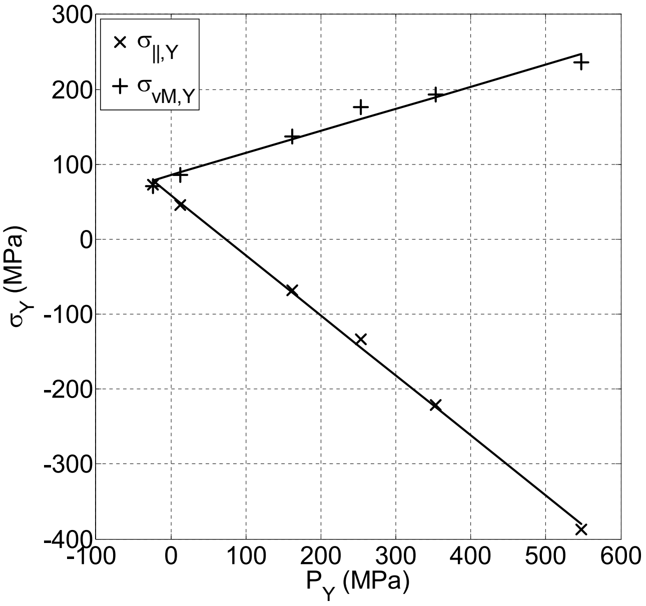

Figure 5.4: True yield stress in the extension direction and von Mises true yield stress vs. pressure near the yield point. Lines are fits to eqs 5.2 and 5.3.

kind of internal friction coefficient [226], in analogy with the proportionality constant in the Amontons-Coulomb law, which relates the friction force to the normal force for sliding two materials over each other under the influence of this normal force [164].

A least-squares fit results in $\sigma_{\mathrm{vM},Y,P_Y=0} = 86$ MPa and $\mu_Y = 0.17$; $\sigma_{\|,Y,P_Y=0} = 59$ MPa and $\mu'_Y = -0.80$. The parameters for $\sigma_{\|,Y}(P)$ and $\sigma_{\mathrm{vM},Y}(P)$ are obviously related and this can be used as a consistency check. If off-diagonal elements of the stress tensor are zero and a uniaxial-stress extension in the x-direction $\sigma_x = \sigma_\|$ is applied in which the perpendicular directions are kept at a constant stress of $-P_\perp < 0$, then the von Mises stress equals $\sigma_{\mathrm{vM},Y} = \sigma_\| + P_\perp$. Combining this expression with eqs 5.2 and 5.3 gives $\sigma_{\|,Y,P_Y=0} = \frac{2}{3}\sigma_{\mathrm{vM},Y,P_Y=0}$ and $\mu'_Y = \frac{2}{3}\sqrt{3}\mu_Y - 1$. A manual check shows indeed that the fit values fulfil these relations between the two set of coefficients present in eqs 5.2 and 5.3 well.

The experimental values for μ_Y of atactic polystyrene are around the simulation results; $\mu_Y = 0.14$ [267], and $\mu_Y = 0.22$ [204]. The value depends on the exact method of extracting a yield-stress value [226].

As is common for the pressure dependence of the von Mises yield stress, one can also try to use a similar 'law' for the pressure dependence of the strain-hardening modulus G_h

$$G_h = G_{h,P_Y=0} + \mu_h P_Y, \tag{5.4}$$

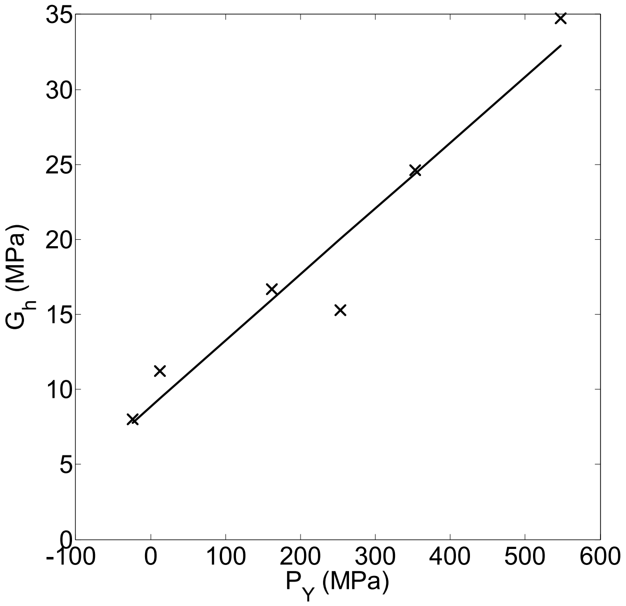

Figure 5.5: Strain-hardening modulus vs. pressure near yield.

with $G_{h,P_Y=0}$ the strain-hardening modulus for the case that the pressure at yield is equal to zero and μ_h the pressure-dependency-factor of the strain-hardening modulus. We find $\mu_h = 0.045$ and $G_{h,P_Y=0} = 8.6$ MPa.

In literature it has been proposed that σ_Y and G_h are coupled, i.e., eq. 5.1 is written as (see Hoy and Robbins [123])

$$\sigma = \sigma_Y(T, P, \dot{\varepsilon})F(\lambda) \tag{5.5}$$

in which only σ_Y is influenced by temperature, pressure and deformation rate, while $F(\lambda) = \left(1 + \frac{G_h}{\sigma_Y}(\lambda^2 - \lambda^{-1})\right)$ and thus $\frac{G_h}{\sigma_Y}$ depends on other intrinsic polymer-specific properties. Our simulation results with various values of the external pressure do not exclude this multiplicative form of the stress-strain relation, see fig. 5.6. In fact, it favours this type of stress-strain-relation over the type in which the strain-hardening modulus is independent of the external pressure.

One could think that the material becomes tougher upon an increase in the strain-hardening modulus. However, according to Considère's construction it is the ratio G_h/σ_Y which determines the toughness of the material [114]. Therefore, the Considère limit for necking $G_h/\sigma_Y = \frac{1}{3}$ is also shown in fig. 5.6. So despite the increase in the strain-hardening modulus, the polymer will not become much tougher upon applying an external pressure.

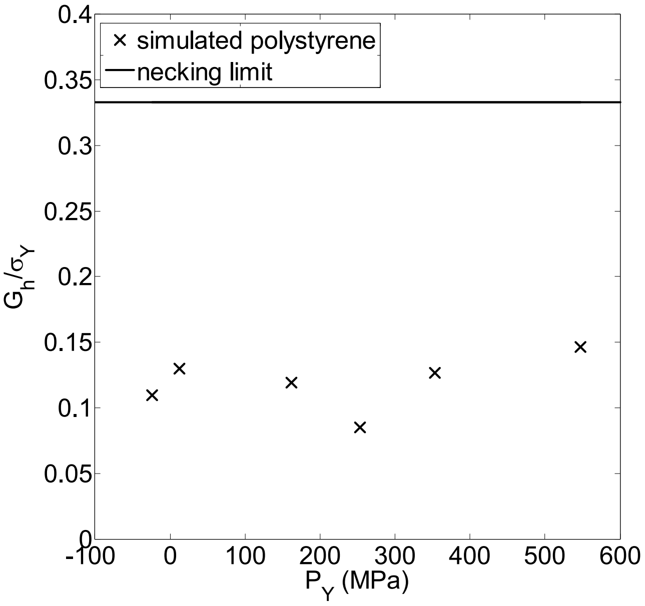

Figure 5.6: The ratio of strain-hardening modulus to von Mises true yield stress vs. yield pressure. For comparison, Considère's limit for necking, $G_h/\sigma_Y = 1/3$, is also shown.

5.3.2 Energetics

Work and dissipation

Work is needed to stress a sample. Part of this energy is stored in the material (elastic response) and another part will be dissipated (viscous response). In what way is this energy stored? And how much of the energy is dissipated? To answer these questions we first look at the evolution of the work and total internal energy and then look at the further partitioning of this internal energy into smaller components.

The amount of work W done on the sample is determined by calculating the product of the net force on a side of the orthorhombic box and the displacement of that side for all three perpendicular directions of the box during deformation [206], as the off-diagonal elements of the strain tensor are zero for the chosen coordinate system [161]

$$\begin{aligned} dW &= F_x \mathrm{d}L_x + F_y \mathrm{d}L_y + F_z \mathrm{d}L_z \\ &= \sigma_x L_y L_z \mathrm{d}L_x + \sigma_y L_z L_x \mathrm{d}L_y + \sigma_z L_x L_y \mathrm{d}L_z \\ &= V(\sigma_x \mathrm{d}\varepsilon_x + \sigma_y \mathrm{d}\varepsilon_y + \sigma_z \mathrm{d}\varepsilon_z), \end{aligned} \tag{5.6}$$

where ε_x equals $\frac{1}{L_x} dL_x$, σ_x the true-stress component along the x-axis, and similar for the y and z components. The total work done onto the sample during deformation is the integral

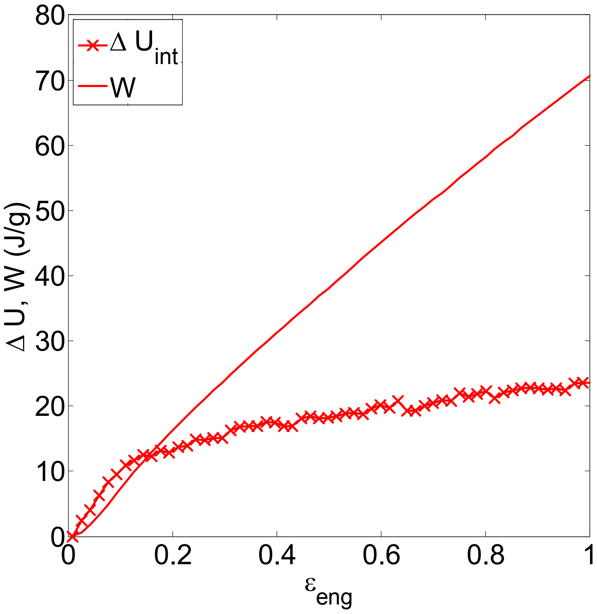

Figure 5.7: Applied work W and increase in internal energy $\Delta U_{\rm int}$ vs. strain.

$W = \int_0^\varepsilon dW$ where the integration has to be carried out from the initial undeformed state to the final deformed state.

The work done on the polystyrene sample and the increase of the internal energy $\Delta U_{\rm int}$ as a function of engineering strain $\varepsilon_{\rm eng}$ is shown in fig. 5.7. Up to about 15% strain all work done on the sample is converted into internal energy. The internal energy even rises faster than the amount of work done on the sample. This is a well-known effect under small extensions (see, e.g., Haward and Young [117] or Haward [116]). Under these small extensions the temperature of the material usually drops: the Joule-Thomson effect. But as our sample is immersed in a heat bath (the thermostat), there is a net heat flow into the sample, nullifying the temperature drop.

For larger strains the internal energy keeps increasing, but most of the work is now converted into heat. This means that during the flow of the material almost all energy is dissipated. Only a fraction of the work is converted into internal energy. This is in accordance with experimental results for polystyrene; the percentage of work which is converted into internal energy decreases after the initial yielding [238]. An MD simulation of a toy-model polymer [124] renders similar results. Also here most of the work in the strain-hardening regime is converted into heat (but there it was expressed in terms of the dissipative stress).

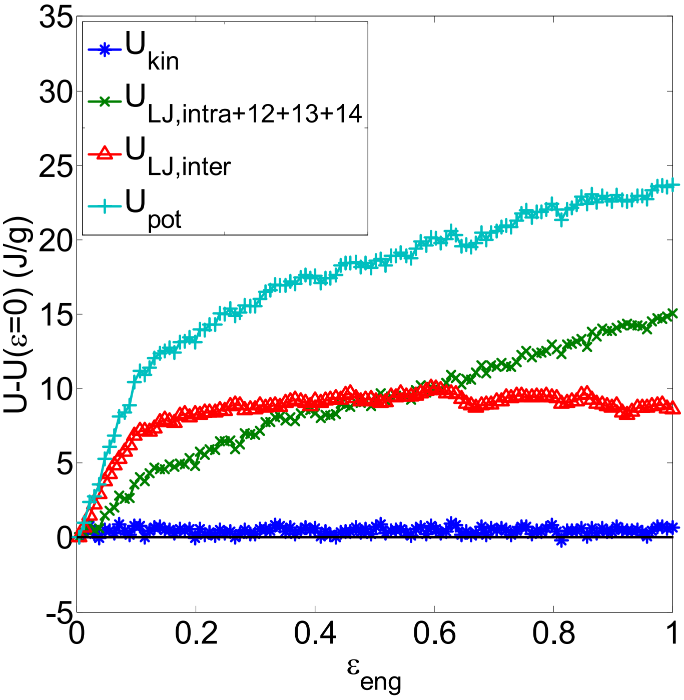

Figure 5.8: Various contributions to the internal energy as a function of strain during uniaxial-stress extension.

Internal-energy partitioning

To see where this extra internal energy is stored, the components of it are monitored during deformation, see fig. 5.8. The internal energy U_{int} is composed of a kinetic part U_{kin} and a potential part U_{pot}. The potential energy is further partitioned into interchain energy $U_{\mathrm{LJ,inter}}$ and intrachain energy $U_{\mathrm{LJ,intra+12+13+14}}$. The interchain energy consists only of LJ interactions and the intrachain energy $U_{\mathrm{LJ,intra+12+13+14}}$ is made of intrachain LJ, 2-particle covalent-bond (12), 3-particle covalent-angle (13) and 4-particle torsion (14) interactions. Up to about 10% extension the main increase is in the interchain Lennard-Jones interactions. After initial yielding only the intrachain energy contribution continues to rise, while the interchain contributions saturate to a value of almost 10 $\mathrm{J\,g^{-1}}$. The kinetic-energy term stays approximately constant (due to the thermostat).

Possible causes of the increase in intrachain energy could be the following. Upon extending the sample the chains become more extended as well. The covalent bonds will be extended first. However, as they impose an opposite force they will drag other particles along with it to relax the stress. Then other mechanisms for making the chain more extended will become active (such as bending the valence angles and changing conformations from gauche to trans states). Nevertheless, the opposite force of the covalent bond will increase the energetic contribution of that interaction. So is the case for other interactions, such as for bond-angle bending interactions and torsion interactions. Also the energy from the intrachain LJ interactions is likely to increase, for the following reason. In a trans configuration the two phenyl rings of a meso dyad repel each other because of their close distance; they feel a repulsive LJ interaction. An extended chain has more trans configurations and therefore this could lead to an increase in the intrachain LJ energy.

The reason for the initial increase in interchain LJ energy and saturation afterwards can be understood from the breaking of LJ bonds upon flowing. With a LJ bond between two particles it is understood that the separation between the particles is small enough so that the energy necessary to separate the two particles is more than about 10% of the well depth of the LJ interaction. The breaking of LJ bonds upon flowing will be treated later on in more detail when the samples of different thermal history will be discussed.

Similar trends in energy contributions have been found in a Monte Carlo simulation of a uniaxially compressed network [44]. Also here the intermolecular potential energy increases a lot up to yield and hardly increases after yield. Furthermore, the intramolecular energies continue to increase as well after yield. This suggests that the observed behaviour is rather general.

In molecular-mechanics simulations of atactic poly(oxypropylene) [134] the dominant change in the energy near the initial yield point was also ascribed to the van der Waals energy, although no distinction was made between intrachain and interchain energy.

Results of the simulation of amorphous polyethylene [288] differ from the present work;

the change in intermolecular energy is almost negligible as compared to changes in the other energetic contributions. A possible reason for this difference could be that there the deformation rate is 5×10^{11} s^{-1}, i.e., 2500 times faster than the present deformation rate near $\varepsilon = 0$. As is discussed by Rottler and Robbins [228] it could be that for such high deformation rates a different (deformation) regime is entered. Another reason could be that the equilibration time for their structure is relatively short, 3 ps (opposed to more than 10 ns for our simulation), so that the sample does not have enough time to form Lennard-Jones bonds.

Influence of thermal history

We saw in fig. 5.2 that the thermal history has a large effect on the yield peak. Contrary to this is the behaviour of the strain-hardening modulus. This is not affected by the cooling rate: both cooling scenarios gave the same value of $G_h = 11$ MPa. Here we want to focus on two questions. The first question is what interaction types are responsible for the difference in yield peak. The second question is related to mechanical rejuvenation. From the identical behaviour of the two thermally different materials after yield it was proposed that the aging history is erased completely from this point [117] and that deformed annealed samples are behaving similar as quenched samples (hence the term mechanically-induced rejuvenation). However, only one property has been compared, the stress. Are other properties of the material also equivalent after initial yielding?

Let us take a look again at the development of energy upon deformation for samples with different cooling history. As was shown, the potential energy U_{pot} plays a large role for initial yield. The difference between the fast and the slower-cooled sample in terms of this energy is depicted in fig. 5.9.

Prior to deformation U_{pot} is lower for the slower-cooled sample, as is typical for glassy materials [273], and is understandable by the following argument. Upon cooling down the polymer melt vitrifies and falls out of equilibrium. The slower-cooled sample, however, has more time to equilibrate and falls out of equilibrium at a lower temperature. It is therefore closer to the equilibrium state, of lower energy. Another useful picture of understanding this is that the slower-cooled sample has more time to find deeper minima of the energy landscape. The decrease in energy towards the equilibrium value is sometimes also interpreted as an increase in local ordering, as then the difference from the underlying crystalline structure (if any) is smaller (in terms of the total energy).

During deformation the difference in potential energy between the two samples of varying cooling scenario changes. For strains up to about 10% the potential-energy difference decreases and for larger strains the difference saturates to an approximately constant value. Note that the energy difference does not vanish entirely, illustrating that the deformation of a sample does not completely erase the aging history. A similar observation has been made

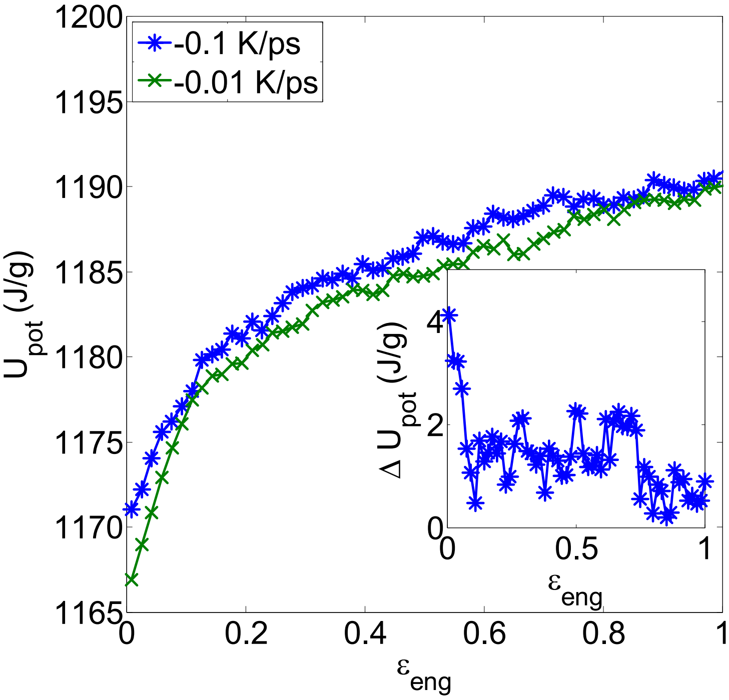

Figure 5.9: Total potential energy vs. engineering strain for atactic polystyrene produced with two different cooling rates. Inset shows the difference. The initial difference in potential energy does not vanish entirely upon deformation. The main decrease occurs up till shortly after the yield point ($\varepsilon_{\mathrm{eng}} \approx 0.1$). In the strain-hardening regime the difference stays approximately the same.

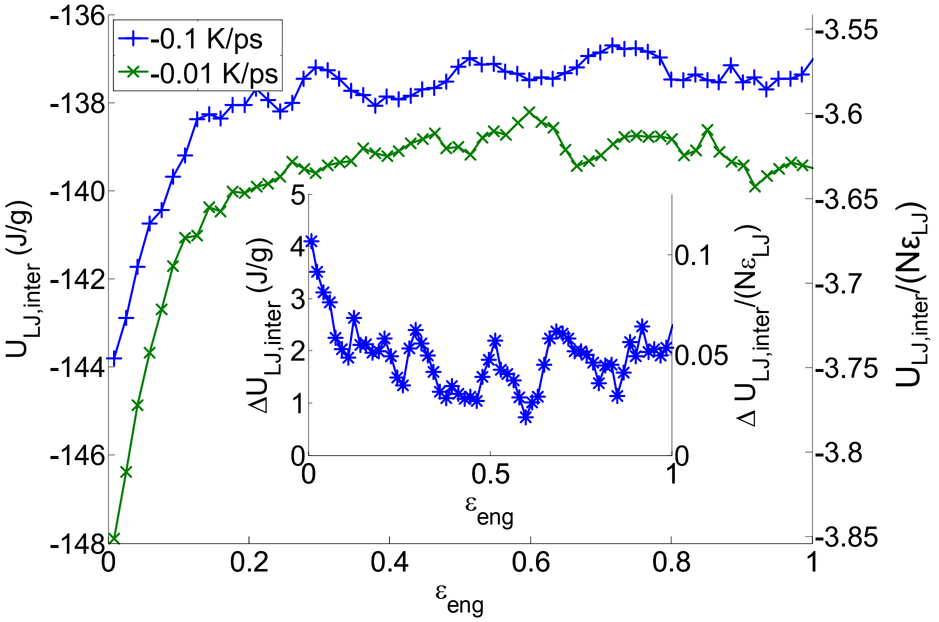

Figure 5.10: Total interchain energy vs. strain for atactic polystyrene for two different cooling rates, both in units of J g^{-1} and ϵ_{LJ} (see text). Inset shows the difference. The initial difference in potential energy does not vanish entirely upon deformation. The main decrease occurs after initial yield. In the strain-hardening regime the difference stays the same.

before for smaller strain values [173]. Despite this incomplete erasure, the strain-hardening modulus is apparently not affected (fig. 5.2).

Most of the difference in potential energy between the two cooling scenarios can be ascribed to the interchain Lennard-Jones energy, being recognized by comparison of the insets in fig. 5.10 and fig. 5.9. We could also expect this, as the slowly and faster-cooled samples differ mainly in the initial yield region, and the main contribution to the increase in potential energy near initial yield is due to interchain interactions.

In a prior study of atactic polystyrene [173] it was seen that the difference between quenched and annealed samples was more evenly distributed among the various interactions (bond stretching, bond bending, torsion and total LJ energy). However, in the present study we partition the LJ energy further into an intrachain and an interchain part. These two observations can be reconciled, because it turns out that the intrachain LJ energy for the faster-cooled sample is even lower than for the slower cooled one, thereby making the total contribution of the LJ energy less significant. An explanation for the observed increase in intrachain LJ energy for the older sample will be given in §5.3.3, when the stress is partitioned as well.

The interchain energy shown in fig. 5.10 is displayed both in units of $\mathrm{J\,g^{-1}}$ and in units of ϵ_{LJ}, where ϵ_{LJ} equals the minimal energy of the LJ potential of all united atoms except the CH atoms, which is smaller by a fraction of 0.75. Here one can see that before deformation a united atom has on average about $-3.85\epsilon_{\mathrm{LJ}}$ interchain energy for the slowly cooled sample. As this is smaller than the minimum of the LJ potential, each united atom has on average multiple interchain bonds (i.e., a LJ-bond coordination number which is at least larger than 3). A plausible cause could be phenyl-phenyl ring interactions.

The difference between the slower and the faster-cooled sample is that the interchain energy per united-atom particle is on average approximately $0.1\epsilon_{\mathrm{LJ}}$ lower for the slower-cooled sample prior to deformation. During deformation the difference does not vanish entirely; a plausible reason for this observation will be given on page 107.

To yield the slowly cooled sample an increase in the interchain LJ energy is necessary: On average $0.2\epsilon_{\mathrm{LJ}}$ per (united atom) particle. For the faster-cooled sample the binding energy is less, so also less bonds need to be broken to yield the material, suggesting that this is the reason that less force is needed to yield the younger material. The same effect could explain mechanical rejuvenation; if weak LJ bonds are already broken in the mechanical pretreatment by for example rolling [267], then these bonds need not to be broken in the tension test and it would be likely that the resulting stress-strain curve would then show a much less pronounced or even absent yield tooth. Note that it takes time to reform and equilibrate the broken LJ bonds; as a consequence the total interchain LJ energy effectively becomes less negative during the initial straining region of net bond breaking.

Connection with density

So we saw that for the more aged sample more interchain LJ bonds are present and that it is therefore logical that this leads to an increase in a yield-tooth stress. In this part this view is further supported by the evolution of density.

The evolution of the density during deformation (fig. 5.11) is similar to the evolution of the interchain LJ energy (fig. 5.10). Upon straining the density quickly decreases. This dilation is quantified by the Poisson ratio, the ratio of the strain in one of the perpendicular directions $\varepsilon_{\perp}$ to the strain in the extension direction $\varepsilon_{\parallel}$ in the limit of infinitely small strain $\nu = -\lim_{\varepsilon\to 0} \frac{\varepsilon_{\perp}}{\varepsilon_{\parallel}}$. Experimental values for polystyrene are $\nu = 0.33$ [36], $\nu = 0.37$–0.38 [265]. These values are in accordance with the values of the present and previous [176] simulation results of $\nu = 0.35 \pm 0.02$. Another way of expressing this is that the Young modulus E is not negligible with respect to the bulk modulus K, as $\nu = \frac{3K-E}{6K}$ [265]. This was also observed in a simulation of a polyethylene-like model [34]. For larger strains ($\varepsilon_{\mathrm{eng}} > 0.1$), the density decreases only weakly and the difference between the annealed

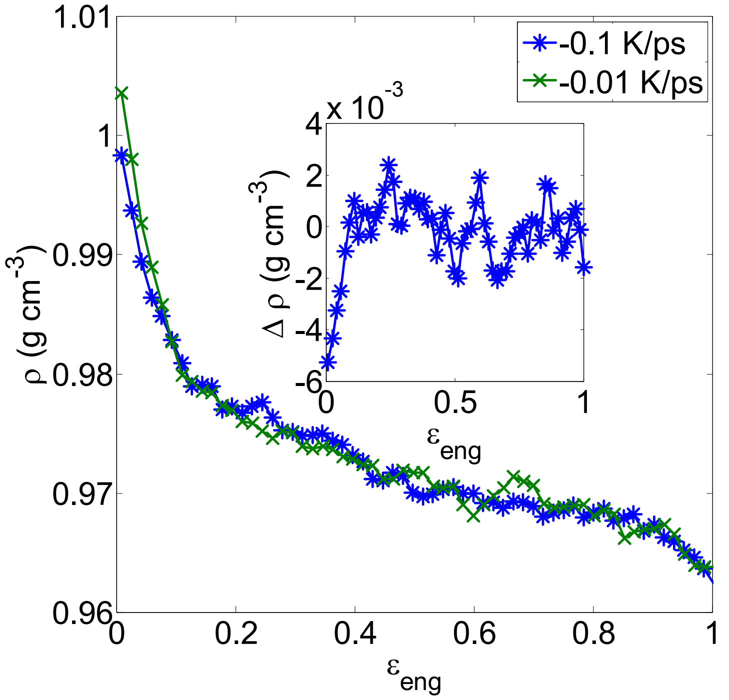

Figure 5.11: Density vs. strain for atactic polystyrene for two different cooling rates during uniaxial-stress extension. Inset shows the difference. The initial difference in density disappears after yield.

and the quenched samples has disappeared. To sum up, the quenched and the annealed samples show next to a similar stress response also a similar density response for large strains.

The relation with out-of-cage escape

We found that under deformation yielding is associated with breaking of LJ bonds. This means that particles are forced to depart from their original cages. In chapter 3 we have shown that the cage in an undeformed glassy substance manifests itself in the root-mean-square translational displacement (RMSTD) of particles as a plateau. After the plateau there is an increase in the RMSTD associated with cage escape. Deformation should therefore lead to an early increase in the RMSTD. Would the effect of thermal history or varying pressure also be visible in the RMSTD?

This is indeed so. In fig. 5.12 the RMSTD $\langle \Delta \mathbf{r}(t)^2 \rangle^{1/2} = \langle (\mathbf{r}(t_0+t) - \mathbf{r}(t_0))^2 \rangle^{1/2}$ of all united-atom particles in polystyrene is plotted as a function of time t both for the deformed and the undeformed case. For the deformed case the trivial convective velocity is removed as described in more detail by Lyulin et al. [177] and in chapter 6. The resulting RMSTD will be also called the root-mean-square non-affine displacement or simply non-affine displacement. In the case of deformation there is no translational invariance in time present and we therefore take t_0 as the time when the sample is unstrained, i.e., at $\varepsilon = 0$. Later times $t_0 + t$ will correspond to a strained sample at a strain value as given by the additional axis in fig. 5.12. The results are plotted for three situations: the annealed sample, the quenched sample and the sample under a high external pressure ($P_\perp = 628$ MPa).

The RMSTD is associated with two basic phenomena: the temporary localization plateau and the cage to cage motion. The first thing we study is the plateau. The value of the localization plateau of the RMSTD is, as shown in chapter 3, a measure for the space within the cage. If particles are closer to each other, we expect that the space within the cage is smaller. A higher density therefore implies a lower plateau value. Prior to deformation the fast-cooled sample has $\rho = 1.001$ g cm^{-3} (fig. 5.11, the slowly cooled sample $\rho = 1.006$ g cm^{-3} and the high-pressure sample $\rho = 1.11$ g cm^{-3}. This order in density is consistent with the observed order in plateau values in fig. 5.12.

Note that an aging effect is also visible in the high-pressure plateau. When preparing the high-pressure sample a 0.5 ns equilibration at that pressure preceded the unstrained, isotropic production run (as mentioned in §5.2). This equilibration time is even visible in the RMSTD plateau: while the two other samples (slowly and fast cooled) show a minor steady increase for the plateau value for larger time scales, the high-pressure sample shows a slight step near 0.5 ns, reminiscent of the continuing aging.

The second point to observe in fig. 5.12 is the early cage escape during deformation. This looks quite similar for all three different situations. Only there seems to be a trend that

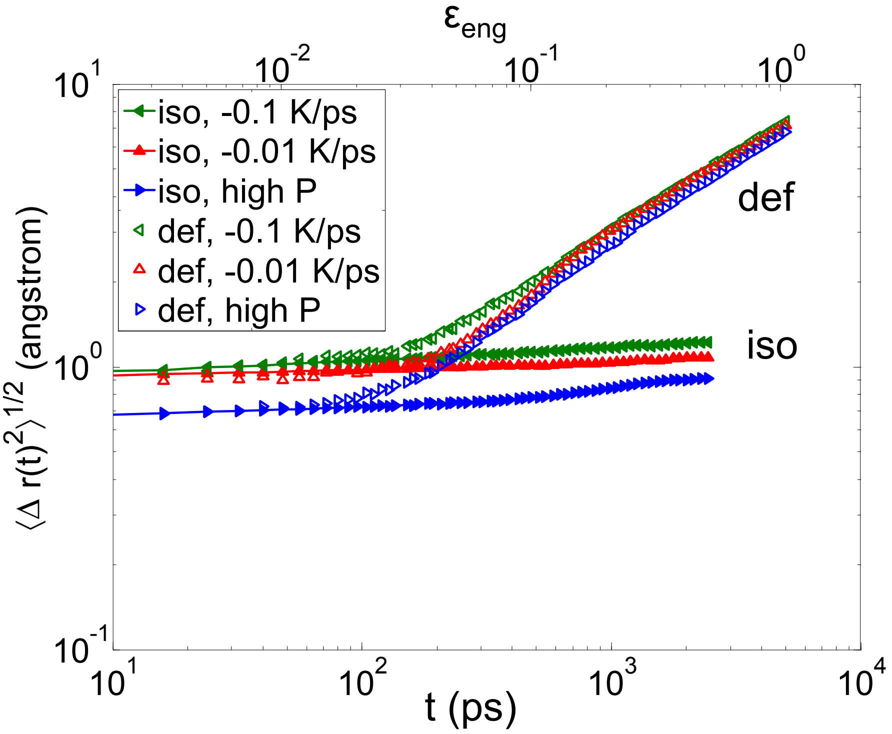

Figure 5.12: Root-mean-square displacement of all particles for the slowly cooled, fast-cooled and high-pressure ($P = 628$ MPa) samples in the undeformed ('iso', closed markers) and the deformed ('def', open markers) cases as a function of strain (for the deformed samples) and time.

the more bound cases (i.e., the cases with the lowest RMSTD plateau values) also have a smaller non-affine displacement after cage escape. This could be simply caused by the following. Assume that the position of a particle $\mathbf{r}(\varepsilon_{\text{eng}})$ at $\varepsilon_{\text{eng}} = 0$ can be written as $\mathbf{r}(0) = \mathbf{r}_{\text{min}}(0) + \Delta\mathbf{r}_{\text{rat}}$, in which $\mathbf{r}_{\text{min}}(0)$ is the quasi-equilibrium position of the particle in the unstrained glass, along where rattling takes place in the direction $\Delta\mathbf{r}_{\text{rat}}$. Then

$$\langle(\mathbf{r}(\varepsilon_{\text{eng}}) - \mathbf{r}(0))^2\rangle = \langle(\mathbf{r}(\varepsilon_{\text{eng}}) - \mathbf{r}_{\text{min}}(0))^2\rangle + \langle\Delta\mathbf{r}_{\text{rat}}^2\rangle + \langle(\mathbf{r}(\varepsilon_{\text{eng}}) - \mathbf{r}_{\text{min}}(0))(\Delta\mathbf{r}_{\text{rat}})\rangle. \quad (5.7)$$

Assuming that the rattling motion is uncorrelated with $\mathbf{r}(\varepsilon_{\text{eng}}) - \mathbf{r}_{\text{min}}(0)$, the last term in eq. 5.7 vanishes. Therefore the more bound states (i.e., with a lower $\langle\Delta\mathbf{r}_{\text{rat}}^2\rangle$) have a lower total RMSTD $\langle(\mathbf{r}(\varepsilon_{\text{eng}}) - \mathbf{r}(0))^2\rangle^{1/2}$.

Mechanical erasure?

Although some properties become independent of the thermal history after straining, differences still last for other properties. From our point of view this behaviour is to be expected. A small strain will obviously change the local structure. However, the erasing effect on much larger scales will be much less. For example, the end-to-end distance of a long polymer chain will approximately be transformed affinely for such small strains. The characteristic ratio, a measure for the end-to-end distance, is temperature dependent for polystyrene [209], and as it has a very long relaxation time, it will vary between the two differently cooled samples (as both samples fall out of equilibrium in a different way). Therefore, this difference in characteristic ratio and hence in the end-to-end distance will not be erased after initial yielding. We think that this even applies for experimental results, as in a glass phase the relaxation time of chain diffusion can easily exceed the duration of a typical experiment.

This temperature dependence of the chain structure can also explain the lasting difference in inter-chain energy between the two samples. As the characteristic ratio for polystyrene increases with lowering temperature (directly [290], and indirectly, see also §6.3.2) it is likely that the characteristic ratio of the slower-cooled sample has a higher value (as it had more time to adjust at a certain temperature). It turns out that this is indeed the case in our simulation results. This means that the 'older' chain is more extended (and thus penetrating more in overlap regions with other chains). Hence it is more likely that the annealed chain has more LJ interactions with other chains. This argument explains why the slowly cooled sample has a lower total interchain LJ energy, even after yielding, as was shown in fig. 5.10.

Note that this is not in contradiction with the simulation of a binary LJ glass, in which the deformation did induce complete erasure [261]. In this simple glass the structure at scales larger than about two atom diameters looked identical in terms of the pair distribution function $g(r)$ for samples of different thermal history, so that the no thermal-history-dependent ordening was visible for large length scales.

The chain shape depends on its conformation, such as the trans and gauche parameters, and these probabilities are temperature dependent. Moreover, the chain has a spectrum of length scales with accompanying relaxation times. Depending on the exact thermal history, each length scale can fall out-of-equilibrium at a different temperature. Therefore, many ordening parameters describing the non-equilibrium state of polystyrene would be necessary (in the language of the Kovacs-Aklonis-Hutchinson-Ramos (KAHR) model [154]).

Our observed discrepancy from mechanical erasure of the thermal history is in line with other results. In the random-landscape model by Isner and Lacks [131], in which the state of the material is given by a position in this energy landscape and strain is simply associated with a displacement in the energy landscape, the non-equilibrium state is also not only defined by one thermal and/or mechanical history-dependent variable and therefore also needs more ordening parameters. It seems thus that it has some long-range structure, too. Experimental studies of polystyrene by means of positron-annihilation lifetime spectroscopy [37] revealed as well that mechanical rejuvenation is a too simple picture.

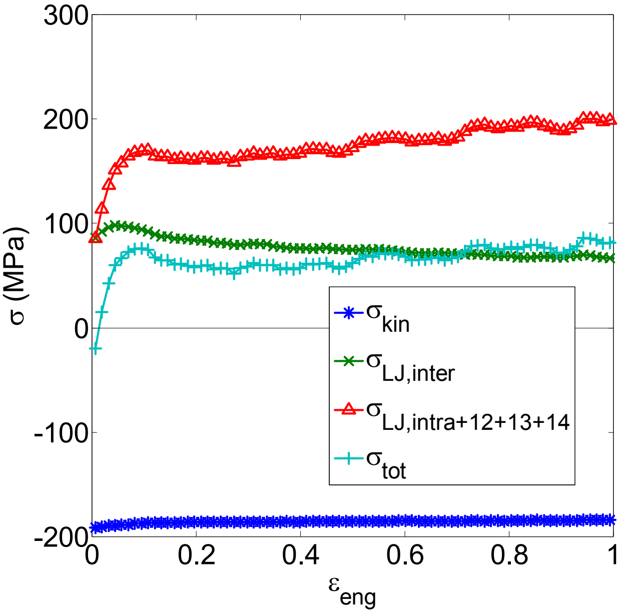

Figure 5.13: True stress in the extension direction vs. strain during uniaxial-stress extension, for different stress contributions. The hardening is mainly due to intrachain interactions. Interchain stress decreases after the yield peak, likely caused by the simultaneous decrease in density after yield. The yield tooth (peak and further softening) is caused by a combination of intrachain and interchain interactions.

5.3.3 Stress partitioning

From the study of the changes in energetic contributions during uniaxial extension deformation it was observed that interchain interactions were most prominent near yield, while intrachain interactions dominate the strain-hardening regime. In this part we want to see if this is consistent with the stress interactions. Again we will use partitioning. First we focus on the unstrained, isotropic situation ($\varepsilon = 0$). Although the total stress is simply connected to the pressure, the values of the various stress contributions are not. This analysis is followed by a discussion around the yield point for the deforming polymer. Finally, the stress partitioning in the strain-hardening regime is discussed. The stress-partitioning in this last regime gives more insight in the observed difference between compression and extension (fig. 5.1).

Undeformed state

We first concentrate on the undeformed case, $\varepsilon = 0$. In fig. 5.13 the absolute true stresses along the uniaxial-stress extension direction are plotted as a function of (future) strain. The total stress has been partitioned into several terms: the kinetic stress σ_{kin}, the intrachain stress $\sigma_{\text{intra}} = \sigma_{\text{LJ,intra+12+13+14}}$ (using the same notation as for the energy partitioning), and the interchain stress $\sigma_{\text{LJ,inter}}$.

The kinetic stress is $\sigma_{\text{kin}} = -P_{\text{kin}} = -\rho_N k_B T \approx -200$ MPa with ρ_N the (united atom) particle density. For the normal pressure simulations the imposed pressure is the offset pressure $P_\perp = 42$ MPa (due to the density correction, §5.2), which is lower than P_{kin}. The negative kinetic stress term, naturally, is an expanding term to the total stress (i.e., due to the kinetic term particles repel each other). It is counterbalanced by the positive interchain and intrachain stress terms, which lead to contracting contributions. At $\varepsilon = 0$ the intrachain stress and the interchain stress are of the same magnitude.

In contrast to the present results a negative total LJ stress was found in a polymeric network [44]. However, in that work this total LJ stress was not split into a intrachain and interchain contribution. Then the LJ interaction present between atoms separated by minimally three covalent bonds within the chain is also part of this total LJ stress. The LJ interactions between atoms that are separated by exactly three covalent bonds could cause repulsion. An example is the conformation for which equilibrium values for the bond length and valence angle are taken and where the torsion is in the gauche state, $\phi = 120$ degrees. Then the separation of these two atoms is smaller than the distance at which the LJ interaction is at its minimum for their used LJ parameters [44]. Upon lowering the ratio of the LJ radius to the covalent-bond length the LJ stress did become less negative; however, it stayed negative [44].

Nevertheless, a similar result (i.e., a negative LJ stress) is present in our simulations. We can see this if the intrachain stress is partitioned further. This intrachain stress is composed of the stress due to covalent bonds σ_{12}, the stress due to the valence-angle interaction σ_{13}, the stress due to both the proper and improper-torsion interactions σ_{14}, and the stress due to intrachain LJ interactions $\sigma_{\text{LJ,intra}}$. The $\sigma_{\text{LJ,intra}}$ of polystyrene turns out to be negative as well and the effect is even stronger than for the polyethylene model: at $\varepsilon = 0$ the stress $\sigma_{\text{LJ,intra}}$ is approximately equal to -4 GPa, about one order of magnitude larger than for the polyethylene-like network model [44]. This can be understood by the following argument. Different from a linear united-atom polyethylene chain, polystyrene has side groups. In case of an all-trans configuration, the two C atoms of a meso dyad would be very close to each other (see fig. 2.3), well below the distance at which the LJ potential is at its minimum. As they are separated by four chemical bonds they will exert in the currently adopted force field a LJ interaction, which would be very repulsive in this situation, making the associated $\sigma_{\text{LJ,intra}}$ negative. As a reaction, the bonds in between will be extended, causing an attractive stress contribution (i.e., the bond wants to contract). From the simulation results it follows that there is indeed a big attractive intrachain stress contribution; also σ_{12} has a very large value at $\varepsilon = 0$, over 4 GPa. As expected, these high intrachain stress values almost cancel each other; the sum of σ_{12} and $\sigma_{\text{LJ,intra}}$ is less than 100 MPa.

Yield regime

Now let us take a closer look in what way these stress contributions in fig. 5.13 change upon straining the material. We concentrate first on the regime near the yield point. The polystyrene yield peak present in the true stress is caused both by intrachain and interchain contributions. Each shows a yield tooth (peak with subsequent drop) in the stress, at around 5–10% extension, although that of interchain nature occurs at a slightly smaller strain value.

The dominant contribution to the total increase in the true stress from $\varepsilon = 0$ till yield can be ascribed to the intrachain stress, in contrast to what was found for a melt of a freely-rotating chain, in which the interchain nonbonded-stress difference is the dominant contribution [92]. It is not clear what the reason is for this difference, although the force fields differ a lot from each other.

It is instructive to also compare the stress partitioning of the two samples with different thermal histories, because we observed that the slower-cooled sample has a higher yield peak than the faster-cooled sample (fig. 5.2). Both intrachain and interchain stresses are responsible for this difference in yield peak, see fig. 5.14.

Can we understand these observations and are they reconcilable with the energy-partitioning results? Yes. The outcome of the energy-partitioning examination was that the main difference between the two samples lies in the interchain energy. For the slower-cooled sample the interchain LJ interactions have a lower energy, i.e., a strong bond. To break this LJ bond a larger force is thus needed. If certain particles are dragged out of the LJ well, then neighbouring covalently bonded particles will be moved along. Therefore, both the stress associated with the covalent bond and the stress associated with the LJ interaction need to be higher for the slower-cooled sample, in agreement with the present simulation results.

Strain-hardening regime

In the strain-hardening regime two facts are apparent from the stress partitioning (fig. 5.13). First, the intrachain interactions give rise to a positive contribution to the strain-hardening modulus. Second, the interchain interactions lead to a negative contribution.

A probable cause of the latter is that there is a simultaneous decrease in density in this region (fig. 5.11), making it likely that interchain LJ bonds become weaker or are even broken. The total stress support that all interchain bonds can sustain obviously decreases or vanishes (in case they are broken) during extension. The value of σ_{kin} also increases slightly due to the decrease in density upon the uniaxial-stress extension. Under compression, however, there is no decrease in density after yield. We indeed find that in this case

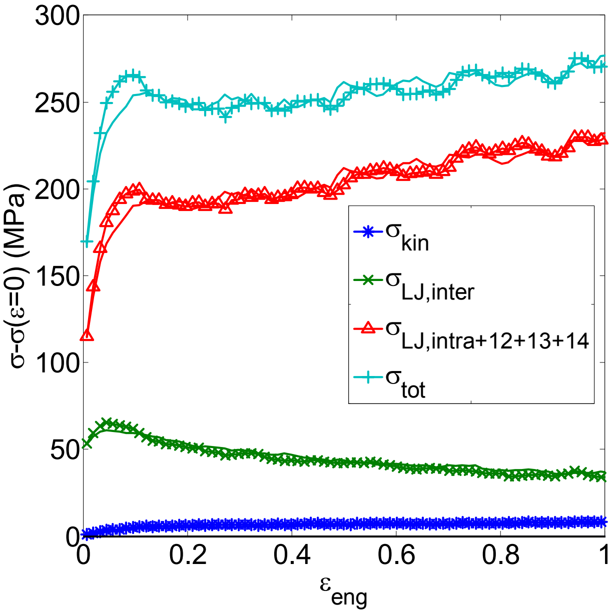

Figure 5.14: True stress in the direction of uniaxial extension vs. strain for different stress contributions for the slowly (with markers, upper curve near yield) and the fast-cooled (without markers, lower curve near yield) sample. The stress at $\varepsilon = 0$ is subtracted and a separation of 50 MPa between the different contributions is added for clarity. One can see that both the interchain and intrachain stress is higher for the slowly cooled sample.

the interchain stress does not decrease upon compression, see the results of partitioning the stress in case of a uniaxial-stress compression simulation in fig. 5.15.

The first observation, meaning that the positiveness of the strain-hardening modulus stems from intrachain interactions implies that the strain hardening is mainly carried by intrachain stresses. From one point of view this behaviour seems logical, as the interchain bonds are broken during yielding (apart from entanglements), while the intrachain bonds are much stiffer and can withstand more stress before breaking (in our simulations the covalent bonds are even not allowed to break).

Can we also understand the observed difference in the strain-hardening modulus between the compression and the extension result for large strains (fig. 5.1)? The reason that we would expect similar moduli stems from assuming a simple strain-energy function U of quadratic form $U(\lambda_1, \lambda_2, \lambda_3) = C(\lambda_1^2 + \lambda_2^2 + \lambda_3^2 - 3)$ (with C a positive constant and λ_1, λ_2 and λ_3 the chain stretches along the three principal axes [275]), so that the state of minimal energy is the unstrained chain. If the material behaves incompressible, then the outcome of such a strain-energy function is that the strain-hardening modulus under compression is the same as under extension. The density is, as just discussed, not constant but decreasing during extension. One consequence of this density decrease is that it is accompanied by a net breaking of interchain LJ bonds. If we exclude this interchain LJ stress but only take into account the intrachain stress, and fit σ_{intra} by eq. 5.1, then the result is $G_h = 26$ MPa for compression and 17 MPa for extension, fig. 5.16. Note that these values are much closer to each other than when the strain-hardening moduli are determined by fitting the total stress (compression: $G_h = 37$, extension: $G_h = 11$ MPa, fig. 5.1). Still a difference remains between the compression and the extension data, possibly caused by other consequences of the decrease in density during extension and the slight increase in density during compression. To sum up, the observed difference in strain hardening moduli is mainly due to the decrease in interchain stress for large strains under extension.

5.4 Conclusions and outlook

The major difference between polystyrene chains with a different thermal history lies in the interchain LJ energy. A more annealed sample has more effective LJ bonds, which should be broken in order to yield the material. Therefore, the yield stress is higher for the more aged sample. After some LJ bonds have been broken, the stress needed to deform decreases (strain softening). This breaking of bonds disturbs the thermal history at local scales and therefore both quenched and annealed samples soften to approximately the same yield minimum. However, differences in structure at large scales persist. Upon straining further the major contribution to final hardening is due to intrachain interactions. This conclusion is valid for uniaxial-stress compression as well as extension.

There is also an influence of pressure on the behaviour at large strains. It is seen that the

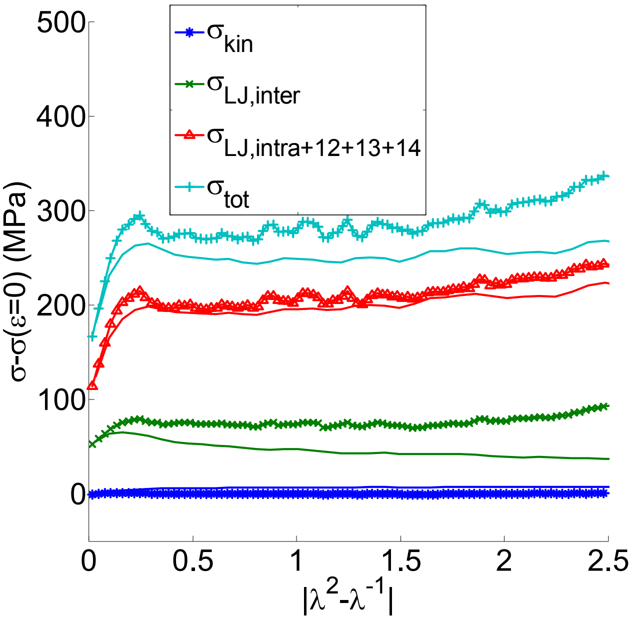

Figure 5.15: True stress in the active direction vs. absolute Gaussian strain $|\lambda^2 - \lambda^{-1}|$ for different stress contributions under compression (with markers) and extension (without markers). The stress at $\varepsilon = 0$ is subtracted and an offset of 50 MPa between the curves is added for the sake of clarity. For compression the stresses have been multiplied by -1 to allow for a better comparison with extension. While for extension the interchain stress decreases after initial yielding, it is for compression fairly constant in the displayed range after initial yielding.

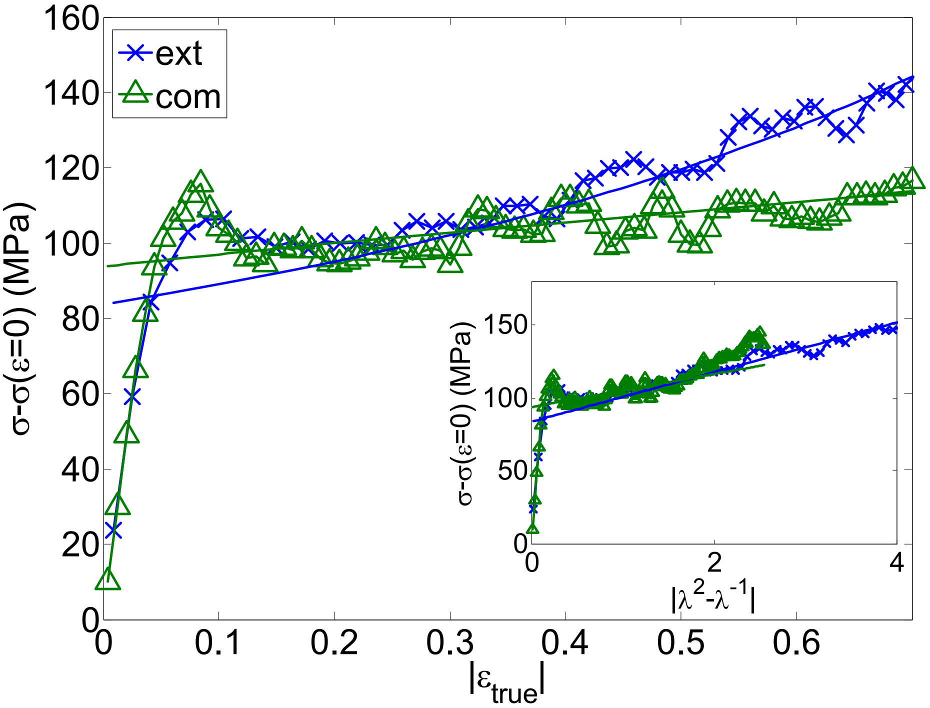

Figure 5.16: True intrachain stress in the active direction vs. absolute true strain for (△) compression and (×) extension. The stress at $\varepsilon = 0$ is subtracted. For compression the stresses have been multiplied by -1 to allow for a better comparison with extension. Inset shows the same as a function of $|\lambda^2 - \lambda^{-1}|$. Results of fitting the data by the Gaussian-based constitutive equation 5.1 are that $G_h = 26$ MPa (compression) and $G_h = 17$ MPa (extension).

strain-hardening modulus increases with increasing pressure, which is in contradiction to the classical entropy-based rubber-elasticity picture. In the strain-hardening regime most of the applied work is dissipated. As the yield stress also increases with increasing external pressure, and the toughness of the material is characterized by the ratio of the strain-hardening modulus to the yield stress (according to Considère's construction), a higher external pressure does not lead to a significant increase in toughness.

A real understanding of the origin of strain hardening needs more insight at the microscopic level. Therefore, the focus of the next chapter is at that level.

Chapter 6

Microscopic mechanisms of strain hardening in glassy polymers

ABSTRACT

The mechanisms underlying the increase in stress for large mechanical strains, quantified by the strain-hardening modulus, are still poorly understood. In this chapter molecular-dynamics simulations of two polymers with very different strain-hardening moduli (polycarbonate and polystyrene) have been carried out. It is seen that the amount of non-affine displacement increases faster for polycarbonate, which has the higher strain-hardening modulus. This is connected to the observation that also more non-affine chain stretching is present for polycarbonate. The inner distances of a deformed chain can be well described by the inner distances of the worm-like chain, but with an increase of the effective stiffness length (equal to the Kuhn length for an infinite worm-like chain) during deformation. In this way the increase in non-affine displacement can be understood as resulting from an increase in the effective stiffness length of the perturbed chain during deformation, so that at larger strains more plastic flow in terms of non-affine displacement is necessary, causing in turn the strain hardening.

6.1 Introduction

Glassy polymeric materials harden for large strains, i.e., the stress needed to deform the material increases upon straining at large deformations. This is quantified by the strain-hardening modulus, which is the gradient of the line describing the relation between the stress and the Gaussian strain [117]. If the strain-hardening effect is large enough, it can lead to a tough response of the polymeric material; the material breaks only after a significant plastic strain, as is the case for polycarbonate. For polystyrene, the strain-hardening effect is usually too weak and consequently it breaks within a few percent of extension. Understanding the origin of the strain-hardening effect provides a strategy for tailor-made polymeric materials.

Unfortunately no well-accepted theory is available for the strain-hardening effect in the glassy state. The entropy-based rubber theory of elasticity does describe some features of the strain-hardening effect (such as the functional dependence on strain), but drastically fails in predicting the absolute magnitude. For example, its prediction for polystyrene is short by two orders of magnitude [155, 266].

The failure of rubber-elasticity theory is caused by the following difference between a rubber and a glassy state. In a rubbery material the various conformations of a polymer-chain part between cross-link points are easily accessible. These cross-link points can be either of a chemical nature (such as covalent bonds) or a physical nature (such as entanglements). In a glassy material, in contrast, a chain is surrounded by a glassy matrix and has a frozen-in conformation, because of energetic barriers between the various states. At rest it is trapped in a local energy minimum and when the sample is stretched and released afterwards the strained state will not immediately relax towards the equilibrium state. Moreover, to deform the glassy material the energetic barriers need to be surpassed and energy dissipation takes place. The work needed for this irreversible energy dissipation is delivered by a dissipative stress. This stress of dissipative nature is not present in the rubber-elasticity theory.

The dissipative nature of deforming a glassy polymer is confirmed by experiments and simulations. Experimentally it is found that for large strains ($> 15\%$ for polycarbonate and $> 30\%$ for polystyrene [117, 199, 231]) more work is converted into heat (i.e., dissipated) than into internal energy. Recent simulations of polymer toy models confirmed that most of the stress at large strains is due to dissipation [124, 125].

One way of dealing with the dissipative nature of the deformation is to model the stress-strain relation in the strain-hardening regime by two contributions. The first part is a constant dissipative stress σ_Y, due to the presence of energy barriers. The second is the strain-dependent part, which is thought to be described by rubber-elasticity theory and represents the strain-hardening effect. In this description the strain-hardening modulus is not affected by thermally activated processes.

However, experiments demonstrate that such a description for the strain-hardening part is invalid; also the strain-hardening modulus has characteristics of a thermally-activated process. One observation is that the strain-hardening modulus decreases for higher temperatures [102]. This is in line with what one would expect for thermal activation. Another observation is that a higher strain rate leads to an increase in the strain-hardening modulus [233], although for some polymers the dependency on strain rate is almost absent [32]. Also this can be interpreted within the barrier-crossing picture. For higher deformation rates less particles are able to overtake energetic barriers by a sufficient thermal fluctuation and therefore more particles need to be mechanically forced for crossing their barrier. Next to temperature and strain rate, the external pressure affects the strain-hardening modulus as well. A higher external pressure can lead to an increase in the strain-hardening modulus (see previous chapter). Again, this behaviour is typical for thermally-activated processes. All these three observations on the strain-hardening modulus are not present within the classical rubber theory.

The increase in stress for larger strains in combination with the dissipative nature of the stress in the strain-hardening regime suggest that there is an increase in the rate of energy dissipation, i.e., more energy per unit of strain is needed for more stretched samples. This picture is confirmed by Hoy and Robbins [124] in a simulation study of a polymeric material. They observed that the dissipative stress increases with larger strain and that at zero temperature the stress was directly correlated to the rate of changes in Lennard-Jones (LJ) binding.

What is the polymer-specific part of the strain-hardening modulus? Experiments [266] and simulations [123] show that this modulus is positively correlated with the entanglement density, and polymers with a larger Kuhn or persistence length often have a higher strain-hardening modulus [114]. It was even shown by molecular-dynamics (MD) simulations that if the persistence length of a polyethylene-like polymer is artificially increased by changing the trans-to-gauche ratio, the strain-hardening modulus of the resulting material increases as well [184]. That example illustrates that the strain-hardening modulus depends on the conformation of the chain, which is frozen in the glassy state.

Strain-hardening effects are already visible for relatively short chains. Although MD simulations are usually carried out at much higher deformation rates than experimental ones, the observed strain-hardening phenomena are similar to experimental results. In previous MD simulations of polystyrene [177] strain hardening was already observed for chain lengths of 80 monomers, below the experimentally observed entanglement length of about 128–139 monomers [78, 79]. Simulations of a toy-polymer glass [124] demonstrated that there is a gradual increase in the strain-hardening modulus as a function of chain length for chains up to about the entanglement length. For longer chains saturation occurs in the modulus. In this last study it was also observed that the strain hardening is more correlated with the change in the end-to-end distance of the polymer chains than with the change in the global sample size [124]. For example, if the sample size is decreasing while the end-to-end distance does not, then the stress does not increase as well. Nevertheless, the same is probably also true for physically entangled rubbers.

Despite these findings, there is not a definite answer on the question why the energy-dissipation rate is increasing with increasing strain (leading ultimately to an increase in the strain-hardening modulus). In this chapter the aim is to shed light on this problem, by simulating two glassy polymers, viz. polycarbonate (PC) and polystyrene (PS), and studying their behaviour. These two polymers vary greatly in their strain-hardening moduli; that of polycarbonate is more than a factor of two higher than that of polystyrene [267]. Previous molecular-dynamics simulations [176, 177] have reproduced these experimental findings qualitatively, with a strain-hardening modulus of polystyrene that is much lower than that of polycarbonate. Such simulations open ways to look at the molecular level beyond the limitations of the currently available experimental techniques.

Next to benefits of using MD simulations, one should also bear in mind the limitations of it. An obvious but important one is the limited range of length and time scales. For this reason equilibration times, cooling times, deformation times and chain lengths are all relatively short. A consequence of those short times is that motions appear to be frozen on the time scale accessible for simulations. However, in the present chapter we are dealing with polymers at room temperature, which is well below their experimental glass-transition temperature (PS: 373 K; PC: 423 K [181]). Segmental relaxation times for these polymers are around 100 s at the glass-transition temperature [10] and increasing for even lower temperature. Motions at these length scales and above till the scale of a whole chain appear to be frozen as well in common experimental circumstances at room temperature. Therefore, many non-equilibrium phenomena associated with the glassy state present in simulations can also be observed in experiments (and vice versa).

The next sections of this chapter are organized in the following manner. Details of the simulations are given in §6.2. This is followed by a discussion of the structural properties of the polymer chains (PS and PC) in terms of characteristic ratio and Kuhn length (§6.3), with three main purposes: to check the simulation models, to compare PS with PC, and to use this information later on for understanding the deformation process. In §6.4 the stress-strain relation for both polymers is presented and a difference in strain-hardening effect is observed, the effect being larger for PC. In §6.5 the role of non-affinity is discussed. It is shown in §6.5.2 that also the average non-affine particle displacement, a measure for the amount of plasticity, is larger for PC. However, more evidence is needed to ascribe strain hardening to it. This is done in §6.5.3, where the rate of non-affine displacements is calculated. It is found that this rate increases with larger strain, and that the increase is larger for PC. The non-affine displacements of particles are due to restrictions and hindrances, in particular from covalent and steric interactions. It is demonstrated in §6.5.4 that, along with non-affine self displacements of particles, the inner length scales of a chain also change in a non-affine way. This is because at the scale of the Kuhn length a chain cannot be stretched any further. However, due to the stretching of the chain at larger strains, the effective stiffness length of a perturbed chain increases, §6.5.5. As a result, the rate of non-affine particle displacement increases at larger strains, causing more energy dissipation and hence a larger stress, i.e., strain hardening. The conclusions based on these results are given in §6.6.

6.2 Simulation details

The united-atom force fields in use for the two polymers under investigation, polystyrene (PS) and polycarbonate (PC), are given in chapter 2 and have been used before in previous studies [177]. The systems consist of 8 chains of 80 monomers each for polystyrene and 64 chains of 10 monomers each for polycarbonate. The total amount of united atoms per sample is therefore 5128 for polystyrene and 11904 for polycarbonate. The equilibration procedure for the two polymer melts is described in chapter 2. The results to be presented for polystyrene are based on samples which are cooled from $T = 540$ K with a velocity of -0.01 K ps^{-1} till about room temperature, $T = 300$ K. Apart from the initial yield peak (see chapter 5) the results based on these samples are very similar to those of the samples cooled with a temperature ramp of -0.1 K ps^{-1}. The polycarbonate samples have been cooled towards $T = 300$ K with a velocity of -0.05 K ps^{-1}. Initial densities at $T = 300$ K prior to deformation are 1.01 g cm^{-3} for polystyrene and 1.36 g cm^{-3} for polycarbonate. The deformation protocol is the same as in chapter 5. Here we study only the uniaxial-stress extension simulations, in which the boxsize in the extension direction increases with a velocity of $\dot{L}_{\|} = 0.01$ Å/ps. Simulations with a constant deformation rate of 10^8 s^{-1} have been carried out as well, but they do not lead to different conclusions and are not presented in this chapter. The stress in the two other directions are controlled by the Berendsen barostat, in which the ratio of the relaxation time to the isothermal compressibility is taken to be $\tau_P/\beta = 0.011$ Pa s.

For the simulated atactic-polystyrene system the glass-transition temperature is found to be around 380 K and for polycarbonate around 433 K [177], so that both polymer systems are deep in the glassy state around room temperature. The results presented in this chapter are averaged over 15 samples for polystyrene and 5 samples for polycarbonate.

6.3 Chain structure

First we will study the inner length scales of the two chemically-detailed model polymers of PS and PC. We will do this for two situations; for a polymer chain in the melt and for an extended polymer chain. The purpose of this is to check the quality of our simulations for these polymers; to determine the stiffness or the extensibility of a polymer chain, which will turn out to be an important characteristic during deformation; and to be able to compare polystyrene to polycarbonate.

Many methods exist to determine the chain stiffness. One of these methods, fitting the root-mean-square end-to-end distance by the worm-like chain model (to be discussed in §6.3.2), requires information about the extended state. We will first determine this state.

6.3.1 Fully extended chain

Two methods will be employed to determine the state in which the chain is fully extended. The first one is to give a rough estimate of it by a simple calculation based on an all-trans configuration. In the second method the chain is forced to an extended state by means of molecular-dynamics simulations. This will serve as a check for the calculations.

Fully-extended all-trans chain

For polystyrene we can estimate the maximal extension by the following. The length of a backbone bond vector is on average approximately $l_{bb} = l_{\mathrm{CH_2-CH}} = 1.53$ Å and the angle between subsequent backbone vectors equals $\theta_v = 180° - \theta_{\mathrm{CH-CH_2-CH}} = 180° - \theta_{\mathrm{CH_2-CH-CH_2}} = 70.5°$ [187]. Hence the distance between two neighbouring backbone CH units is $2l_{bb}\cos(\theta_v/2) = 2.5$ Å. If we assume that all backbone torsion angles are in the trans state (i.e., three subsequent bond vectors lie in a plane and are maximally separated), then $r_{n,\mathrm{max,PS}} = 1.25n$ Å (for an even number of backbone bonds n). However, this is only an approximation, as due to the phenyl-ring side group the stable trans state deviates from a planar configuration of three subsequent backbone bond vectors. The exact value of the trans state also depends on the type of dyad. These considerations render the maximally extended state slightly smaller in reality.

For polycarbonate a similar calculation for the length of the maximally extended chain can be carried out. If the carbonate group is in the (extended) trans state, then the monomer unit can be regarded as consisting of one long virtual bond of length $l_{vb} = 12.63$ Å [250]. The accompanying angle between two subsequent virtual-bond vectors is $\theta_v = 24.5°$. This makes the length of the cord vector connecting the centres of two adjacent virtual bonds equal to $l_{vb}\cos(\theta_v/2) = 12.3$ Å. Since a virtual bond consists of 12 backbone bonds, the maximal distance between two segments separated by n backbone bonds equals $r_{n,\mathrm{max,PC}} = 1.03n$ Å (for an even number of virtual bond vectors, i.e., if the number of backbone bonds n is a multiple of 24).

Fully-extended chain produced by simulations

To check these all-trans-based model calculations, MD simulations are applied for determining the maximal extension of the polymer chains. We realize this by adding a very weak spring between the first and the last atom of a single polymer chain, with an equilibrium distance which is somewhat larger than the maximally extended state of the chain. Then the force constant of this extension spring is increased to drive the chain to its extended state. As the covalent bonds in the chain are modelled by stiff harmonic springs, their lengths are not constant and the chain could in principle be infinitely extended. In order to still be able to define a reasonable maximally extended state, an extra criterion is added, namely that the length of the covalent backbone bond should not increase more than 1/3 of the average fluctuation around the equilibrium value.

To accomplish this a single chain is placed in a vacuum at $T = 300$ K. Then the new extension spring is added, which acts between the first and the last united atom of the chain. The accompanying interaction term is $U_l = \frac{k_l}{2}\left(l - l_0\right)^2$. Here l is the instant end-to-end distance of the chain and l_0 is set to a value somewhat larger than what is expected from the above calculations for the maximal extension of the chain. Hereafter MD simulations are carried out. During this process the force constant k_l is stepwise increased to 'slowly' force the chain in an extended conformation.

For the polystyrene chain this procedure is carried out using l_0 equal to $1.25n$ Å, as the real extended dimension is anticipated to be less than this. Subsequently the force constant of the extension spring is increased till $k_l = 17$ kJ mol^{-1} Å^{-2} (and equilibrated shortly afterwards for about 50 ps), as at this value the average length of the backbone bond is increased by 1%. This corresponds to about 1/3 of the relative fluctuation in the bond length $\frac{1}{\langle l \rangle}\sqrt{\langle \Delta l^2 \rangle}$ for the undeformed polymer chain in the glassy state at $T = 300$ K.

For the 10-monomer polycarbonate chain the same procedure is carried out. To achieve a similar relative extension of a similar backbone bond (the backbone bond between C and CT, see also chapter 2), the value of l_0 was set to 124 Å. Also for this chain the increase in the backbone bond (1%) is about 1/3 of the relative fluctuation of the same bond length for the isotropic case.

Conclusion

The end-to-end distance for the extended chain determined by the simulation method differs from the calculation by 2% for polycarbonate and less than 1% for polystyrene. This shows that despite the assumptions made in the calculations the final result is still reasonably accurate. Further on, however, the simulation result will be used, as for shorter distances larger deviations do occur between the two methods.

6.3.2 Intrachain length scales of vitrified polymer chains

The stiffness of a chain can be characterized by the characteristic ratio C_∞, the Kuhn length l_K or the persistence length l_p of a chain. The characteristic ratio is defined as

$$C_n = \frac{\langle |\mathbf{r}_n|^2 \rangle}{n l_b^2}. \tag{6.1}$$

Here $|\mathbf{r}_n|$ is the distance between two segments separated by n bonds, and l_b is the bond length [81]. Sometimes C_n is only defined for the end-to-end vector of a chain, so that $|\mathbf{r}_n|$ is equal to the distance between the first and the last segment. We will adopt the common extended definition in which it is applicable for two segments within the chain as well. The average is then also taken over all possible segment separations. For a freely-jointed chain, a random walk of n steps each of length l_b, C_n equals 1 for all n. The characteristic ratio can therefore be interpreted as a measure for the deviation from an ideal random walk.

The persistence length l_p can be defined as the integral of the the bond correlation function $K_b(\Delta l)$ [247]. That function is defined as the average of the inner product of the unit vector along the contour of the chain at a curvilinear distance l, $\mathbf{e}(l)$, with the unit vector a curvilinear distance Δl further, $\mathbf{e}(l + \Delta l)$, i.e., $K_b(\Delta l) = \langle \mathbf{e}(l) \cdot \mathbf{e}(l + \Delta l) \rangle$. So $l_p = \int_0^\infty K_b(\Delta l) d\Delta l$. In the limit of infinitely long chains the persistence length is related to the characteristic ratio of the chain as $l_p = \frac{1}{2}(C_\infty + 1) l_b$ [81]. In the current chapter we will adopt this last equality for determining l_p.

Another way to determine the stiffness of the chain is to measure the Kuhn length l_K. This length is defined as [56, 247]

$$l_K = \lim_{n \to \infty} \left(\frac{\langle |\mathbf{r}_n|^2 \rangle}{r_{n,\mathrm{max}}} \right), \tag{6.2}$$

where $r_{n,\mathrm{max}}$ is the maximum length of the end-to-end distance. The Kuhn length can be interpreted as the bond length of an equivalent freely-jointed chain, which has the same maximal extension $r_{n,\mathrm{max}}$ and the same root-mean-square (RMS) end-to-end distance $\langle |\mathbf{r}_n(\varepsilon_{\mathrm{eng}})|^2 \rangle^{1/2}$ as the real chain in the limit of $n \to \infty$ [81, 247].

We are dealing with relatively short chains, i.e., finite n, and some extrapolation method should be used to determine the long-chain limit. For determining the long-chain limit of the characteristic ratio, C_∞, we apply two fits. The first one is

$$C_n = C_\infty (1 - \alpha / n). \tag{6.3}$$

The functional form of this fit is based on the lowest-order correction ($\mathcal{O}(n^{-1})$) from C_∞, which is valid for model chains such as a chain with fixed bond angles and independent bond-rotational potentials [81] and is commonly used in other studies as well (see, e.g., Han and Boyd [109]). Recently Wittmer et al. [283] have shown that due to long-range interactions in dense polymer systems the first-order correction to the ideal-chain limit is of $\mathcal{O}(n^{-1/2})$ in the melt. We therefore also fit the internal distances by

$$C_n = C_\infty(1 - \alpha' n^{-1/2}). \tag{6.4}$$

In the determination of the Kuhn length deviations also occur for relatively short chains when using the definition of l_K [81]. Therefore, we will map the results on the worm-like chain (WLC), also known as the Porod-Kratky chain [56, 63, 81]. The mean square end-to-end distance for the Porod-Kratky chain with contour length L_c and stiffness length l_s is [56, 63, 81]

$$\langle|\mathbf{r}(L_c)|^2\rangle = l_s\left(L_c + \frac{l_s}{2}\left(\exp\left(-\frac{2L_c}{l_s}\right) - 1\right)\right). \tag{6.5}$$

In the limit of a very large contour length, i.e. $L_c/l_s \gg 1$ this equation reduces to $\langle|\mathbf{r}(L_c)|^2\rangle = l_s L_c\,(1 + \mathcal{O}(l_s/L_c))$ and the stiffness length is therefore equal to the Kuhn length, $l_s = l_K$. It can also be shown that the persistence length for the WLC obeys $l_p = l_K/2 = l_s/2$ [81]. The reason why we use the stiffness length as a parameter, instead of the Kuhn length becomes clear when we look at deformed chains later in this chapter. Note also that in principle eq. 6.5 would change if a melt of chains is considered instead of an ideal worm-like chain, just as the extrapolation formula for the characteristic ratio changes from eq. 6.3 to eq. 6.4. However, this is beyond the scope of the present chapter.

In the definition of the characteristic ratio a bond length l_b is needed. In case of polystyrene l_b is taken to be the equilibrium length of a backbone C-C bond, $l_{b,PS} = 1.53$ Å [290]. In the case of polycarbonate the monomer unit consists of different types of covalent backbone bonds, each with their own length. Nevertheless, for this polymer the monomer unit can be regarded as a rigid object. Hence instead of equalling l_b to an average covalent bond length, a longer virtual bond [81] is used. The length of the virtual bond is not unique and different conventions are in use: $l_{b,PC} = 12.63$ Å for one virtual bond per monomer [250], $l_{b,PC} = 8.65$ Å [4] or $l_{b,PC} = 7.0$ Å [280] for two virtual bonds per monomer. We will adopt $l_{b,PC} = 12.63$ Å. A property related to C_n for describing the extent of the polymer, but which has the additional benefit of not depending on the choice of the (virtual) bond length, is $\langle|\mathbf{r}_n|^2\rangle/M_n$, with M_n the molecular weight of n segments.

The quantity $\langle|\mathbf{r}_n|^2\rangle$ bears some analogy with the mean-square displacement $\langle|\mathbf{r}(t)|^2\rangle$ of a Brownian particle that still experiences inertial effects. Here $\mathbf{r}(t)$ is the particle displacement after a period of time t and it is in this analogy equivalent to the distance $\mathbf{r}_n$ between two segments separated by n bonds. In the case of a Brownian particle a ballistic regime is present at short time scales (in which the particle remembers its direction, and $\langle|\mathbf{r}(t)|^2\rangle \sim t^2$). At somewhat larger time scales there is a cross-over to the diffusive regime, $\langle|\mathbf{r}(t)|^2\rangle \sim t$. As C_n is equal to $\langle|\mathbf{r}_n|^2\rangle/l_b^2$ normalized by n this would correspond to a levelling-off of C_n for $n \to \infty$ and the characteristic ratio C_n of a chain has therefore analogy to the diffusion coefficient $D(t) = \frac{1}{6t}\langle|\mathbf{r}(t)|^2\rangle$ of a Brownian particle.

Characteristic ratio of polystyrene

The simulation results for the characteristic ratio for polystyrene together with the fits by eqs 6.3 and 6.4 are seen in fig. 6.1(a). The values for $\langle|\mathbf{r}_n|^2\rangle/M_n$ are calculated by using $M_n = \frac{n}{n_{\text{ch}}}M_{\text{ch}}$, where n_{ch} and M_{ch} are the total number of skeleton bonds and the total mass of a chain, respectively.

A few findings are apparent. The first observation to discuss is the long-chain limit. For our simulated polystyrene we get $C_\infty = 6.4$ at $T = 300$ K by using eq. 6.3 as a fit and $l_{b,PS} = 1.53$ Å. This value is comparable to, but lower than experimental values $C_\infty = 8.7$–9.6 from small-angle neutron scattering of a melt of polystyrene [29, $T = 390$–520 K] and $C_\infty = 9.9$–10.2, resulting from viscosity measurements around 308 K for various solvents [81]. Other simulation results for polystyrene are $C_\infty = 11.0$ [209], $C_\infty = 10.2$ [109], and $C_{80} = 6.5$ [249, $T = 450$ K]. However, when using eq. 6.4 for determining the long-chain limit we acquire $C_\infty = 8.2$, which is still lower but much closer to the experimental results.

The second observation is the functional behaviour of the characteristic ratio. For short separations (small n) the characteristic ratio rises with increasing n, implying that the internal distance increases more than what is expected for a freely-jointed chain of $l_b = l_{b,PS}$, meaning, in turn, that it is stiffer than such a chain. Near $n = 25$ the measured characteristic ratio C_n is found to be at its maximum. For larger n it seems to decrease again and we will discuss this in more detail later on.

We start with discussing in more detail the first observation. Several reasons could be at hand for the difference in C_∞ between the simulation and the experimental results. Firstly it could be the case that chains are not perfectly equilibrated at high temperatures. A more advanced equilibration method for PS is currently implemented in our group [190], which is based on the end-bridging Monte-Carlo technique. This equilibration technique has been successfully used before for other polymers [200].

A second reason could be that our chains are relatively short. We already saw that the exact extrapolation procedure has a large effect on determining C_∞. The ideal-chain extrapolation, eq. 6.3, discards excluded volume interactions present in the melt and leads to a different lowest-order correction in C_∞ than when these interactions are taken into account, e.g. by eq. 6.4. The difference between these extrapolation formulas is especially large for short chains. Moreover, our used extrapolation formulas (eqs 6.3 and 6.4) are only first-order approximations and could therefore lead to deviations for relatively short chains. It has also been shown theoretically that the stiffness near the ends of a chain can be much lower than in the middle of a chain [234].

A third reason could be that small deviations are present in the force field. An atactic-polystyrene chain used in experiments has more racemic dyads than meso dyads [138], leading to an increase in the characteristic ratio [290]. In our currently used model a 50%-50% division is present, as has been used before in other studies of atactic polystyrene

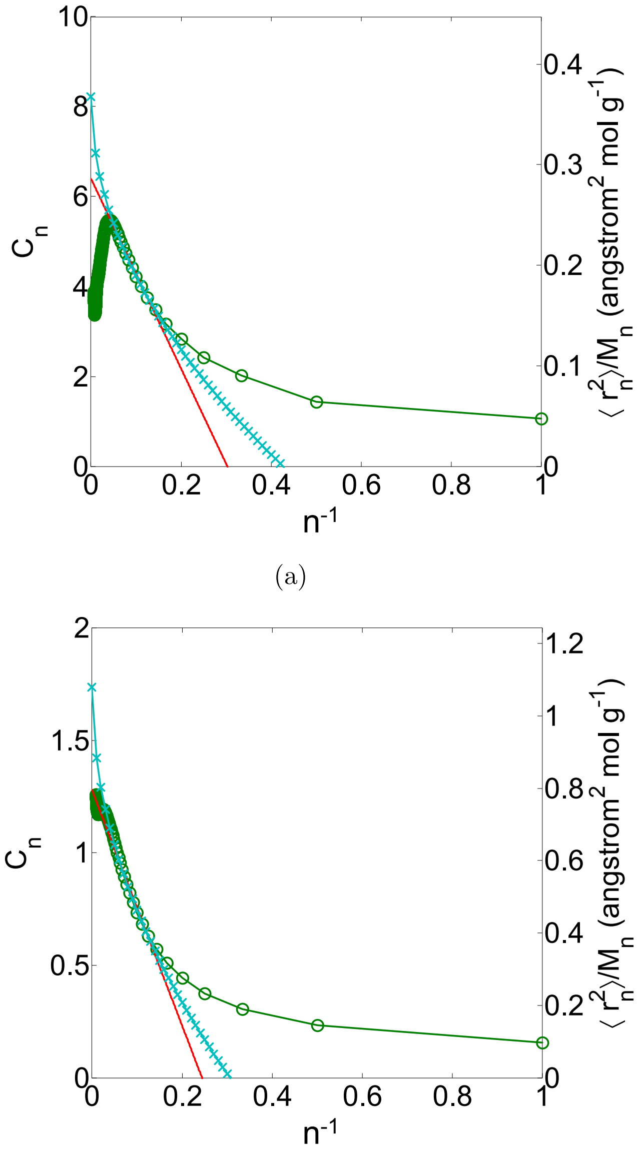

(a)

(b)

Figure 6.1: The characteristic ratio C_n at $T = 300$ K as a function of the inverse of the number of skeleton bonds for (a) PS and (b) PC. Circles are simulation results, solid line fit by eq. 6.3 and crosses fit by eq. 6.4. Ideal-chain fit results are for PS: $C_\infty = 6.4$ and $\langle |\mathbf{r}|^2 \rangle / M = 0.29$ Å^{2}g^{-1}mol; and for PC: $C_\infty = 1.3$ (for $l_{b,PC} = 12.63$ Å) and $\langle |\mathbf{r}|^2 \rangle / M = 0.80$ Å^{2}g^{-1}mol. Melt-chain fit results are for PS: $C_\infty = 8.2$ and $\langle |\mathbf{r}|^2 \rangle / M = 0.37$ Å^{2}g^{-1}mol; and for PC: $C_\infty = 1.7$ (again for $l_{b,PC} = 12.63$ Å) and $\langle |\mathbf{r}|^2 \rangle / M = 1.1$ Å^{2}g^{-1}mol.

[220]. Changing it to a 30%-70% division would lead to an increase of the characteristic ratio by about 20%, according to the two-state rotational scheme of Yoon et al. [290]. Calculations [281] imply that radically polymerized atactic polystyrene at 413 K contains about 43% of meso dyads, so that this effect would be somewhat smaller. The refinement of the force field, although an important task, is not the objective of the present study.

A fourth reason is that our samples are cooled down with a cooling rate that is higher than experimental ones. This causes a deviation from the experimentally observed characteristic ratio in two ways. The first one is related to the temperature dependence of the characteristic ratio; it is known that C_∞ increases with decreasing temperature [290]. It has been found experimentally that $\frac{d \ln C_\infty}{dT} = -0.1 \times 10^{-3}\ \mathrm{K}^{-1}$ [158], although a rotationally isomeric-state scheme gives a substantially larger temperature dependence, $\frac{d \ln C_\infty}{dT} = -1.6 \times 10^{-3}\ \mathrm{K}^{-1}$ [209]. If cooling is occurring fast, the end-to-end distance has not relaxed yet to the more extended state at lower temperature, leading to an underestimation of the characteristic ratio as compared to normal cooling rates. The second way enhances the deviation because of the temperature dependence of density. The inverse, the specific volume, decreases by about 10% when cooling from the initial high-temperature liquid state to the glassy state at $T = 300$ K [177]. If cooling happens fast enough, the end-to-end distance will transform approximately affinely and will therefore decrease simultaneously. As a consequence the value of C_∞ decreases accordingly for lower temperatures. If, on the other hand, the cooling rate is much lower, the polystyrene chains have more time to adjust to the equilibrium value. In experiments cooling velocities are typically about a Kelvin per second, so that the equilibrium value of C_∞ is approached more closely. Nevertheless, an out-of-equilibrium situation will ultimately occur also with experimental studies, because the huge chain-relaxation time will exceed experimental time scales below T_g.

The second observation, the decrease in characteristic ratio after $n = 25$ (fig. 6.1), is not to be expected for ideal chains. The cause of could be an incomplete relaxation. Next to non-perfect equilibration at high temperatures, chain retraction could play a role. As the characteristic ratio for polystyrene increases for lower temperature [290], the chain first extends on a local scale upon cooling down. As the contour length is constant, the local-scale extension happens at the expense of retracting at larger scales by means of reptation. Additional equilibration is then needed to also reach equilibrium at large scales. For long entangled chains the equilibration time is of the order of the disengagement time, i.e., the time needed for the chain to disengage from its initial confining tube [56]. Since the deformation will take place below the glass-transition temperature, where the disengagement time exceeds the time scale of the experiment, an out-of equilibrium situation will occur (also experimentally). Such a decline has been observed before in a similar situation, for a toy model polymer [122]. They observed that if the equilibration time of a polymer melt was on the order of the Rouse time, the short length-scale structure (i.e., for small values of n) C_n was equal to the equilibrium value, C_n^{eq}, but that for large n the observed C_n was smaller than the equilibrium value. Both theirs and ours observations could be explained by the same argument (i.e., equilibration of short scales at the expense of large scales).

Nevertheless, in other studies of relatively short chains [284] a non-monotonic increase in C_n was found in an equilibrated melt. The decline is therefore not always caused by non-equilibrium issues, but has some other physical origin. One reason could be the stiffness-variation along the chain in a polymer melt [234], as mentioned before.

To sum up, the characteristic ratio of the simulated polystyrene is slightly lower than experimental values at larger scales (mainly because of non-ideal equilibration at high temperatures and higher cooling rates in the simulations), but we think that the short length scales are not so affected as they have a shorter relaxation time.

Characteristic ratio of polycarbonate

The characteristic ratio is also calculated for the polycarbonate chains, see fig. 6.1(b). Adoption of the convention $l_{b,PC} = 12.63$ Å and extrapolation of n towards infinity (analogous to polystyrene) gives in case of the ideal-chain fit $C_\infty = 1.4$ and $\langle|\mathbf{r}|^2\rangle/M = 0.80$ Å^{2}g^{-1}mol and in case of the melt-chain fit $C_\infty = 1.7$ and $\langle|\mathbf{r}|^2\rangle/M = 1.1$ Å^{2}g^{-1}mol. The experimental value of polycarbonate in a θ-solvent in which the intrinsic viscosity was converted to $\langle|\mathbf{r}|^2\rangle/M$ [81, 280] is $\langle|\mathbf{r}|^2\rangle/M = 0.87$ Å^{2}g^{-1}mol. A configuration analysis gave $\langle|\mathbf{r}|^2\rangle/M = 0.85$ Å^{2}g^{-1}mol [280]. However, more recent results from small-angle neutron scattering experiments on polycarbonate melts gave $\langle|\mathbf{r}|^2\rangle/M$=1.2–1.3 Å^{2}g^{-1}mol [16, 95] and from other configurational analysis models gave $\langle|\mathbf{r}|^2\rangle/M = 1.1$ Å^{2}g^{-1}mol [162, 289] and $\langle|\mathbf{r}|^2\rangle/M = 1.0$ Å^{2}g^{-1}mol [128, 163]. These results show that by making use of the melt-chain fit the experimentally measured melt-chain dimensions are reproduced in the case of polycarbonate.

Kuhn lengths of PS and PC

Another way to compare the simulation results to the experimental values is to determine the stiffness length by mapping the results of $\langle|\mathbf{r}(L_c)|^2\rangle$ on the worm-like chain (eq. 6.5). For an infinity long worm-like chain the stiffness length would then equal the Kuhn length. In order to map the two studied polymers on the worm-like chain the contour length is needed. As a contour length we could take the length in the maximally extended state. To correct for any errors in this length we assume that $L_{c,n} = \alpha r_{n,\max}$ with α a free fit parameter. A fit of $\frac{\langle|\mathbf{r}_n|^2\rangle}{L_{c,n}}$ vs. $L_{c,n}$ for the two studied polymers onto the analogous expression for the worm-like chain (determined by eq. 6.5) renders correction factor values α of around 1.05, i.e., the fitted contour length is about 5% larger than the maximal extension. The fitted values of the so-determined stiffness lengths are $l_{s,PS} = 12$ Å and $l_{s,PC} = 21$ Å if we confine the fit to the range n =1–40.

Literature values for the Kuhn length are for polystyrene $l_K = 17$ Å and polycarbonate $l_K = 29$ Å [4]. In that reference these values were calculated by using the relation $l_K =$

$l_b(1+C_\infty)$. Upon interpreting our simulation values of the stiffness length as a Kuhn length we see that it is lower than these literature values. It is likely that the main reason for this is the relatively short chains we study. Also with the ideal-chain fit results of the characteristic ratio we found values lower than the literature values. Although we use the worm-like chain fit to have a better approximation for the Kuhn length, it still underestimates the real Kuhn length for relatively short chains. Other simulation results also demonstrate this, such as of some polyesters [139] and of the bond-fluctuation model [45]). However, the Kuhn length is just as the characteristic ratio a measure of chain stiffness. We indeed find very similar relative deviations from literature values, for both the characteristic ratio and the Kuhn length. Therefore, the discussion of the characteristic ratio could be applied here as well to explain the observed differences in Kuhn length between the simulation results and the experimental results. Although our measured stiffness lengths are lower, they are so in a persistent way. Therefore the worm-like-chain fit is still valuable in studying changes in the stiffness length. Later on we will apply the WLC method for determining the stiffness length of the chains in the deformed samples.

Conclusions

By means of MD simulations it is found that PC has a larger Kuhn length than PS, thereby confirming the same trend in literature data. This is primarily caused by the phenyl rings within the backbone and the rigid backbone carbon in the propane group of PC. In this respect PC can be considered to be stiffer than PS [16]. Nevertheless, PC is is often considered to be a very flexible polymer [23, 280]. This is because polycarbonate can be regarded as a nearly freely rotating chain albeit with a relatively large segment length. So with respect to the large virtual-bond length the chain is very flexible, as we found $C_\infty = 1.3$ (compared to PS, $C_\infty = 6.4$). With respect to a typical backbone-bond length, such as the length between two carbon atoms, the characteristic ratio is higher, making it a stiffer chain.

6.4 Deformation and strain hardening

During constant-velocity uniaxial-stress extension simulations of PS and PC at $T = 300$ K the von Mises equivalent true stress is measured as a function of engineering strain $\varepsilon_{\text{eng}} = \frac{L_\parallel(t_1)-L_\parallel(t_0)}{L_\parallel(t_0)}$. The result is shown in fig. 6.2 and is fitted by the Gaussian-based stress-strain relation

$$\sigma = \sigma_Y + G_h \left(\lambda^2 - \lambda^{-1}\right) \tag{6.6}$$

with the draw ratio $\lambda = 1 + \varepsilon_{\text{eng}}$. Here the two fit parameters G_h and σ_Y are the strain-hardening modulus and the offset yield value, respectively.

From the figure it can be seen that the strain-hardening modulus of PC is 19 MPa, almost twice the PS value, 11 MPa, while the offset yield values are very similar (PC: 88 MPa; PS: 86 MPa). Experimental strain-hardening moduli are relatively close to these results, G_h = 9–13 MPa for polystyrene [266, 267, 279] and G_h = 23–29 MPa for polycarbonate [102, 254, 267].

So what would be the reason for the high strain-hardening modulus of polycarbonate over polystyrene? The entanglement picture from rubber-elasticity theory predicts that the strain-hardening modulus equals $G_h = \rho k_B T/M_e$ [275]. Here ρ is the mass density, and M_e is the mean molecular mass of the chain segments between entanglement points. Although this formula gives for polystyrene an estimation which is smaller by a factor of about 100 compared to experimental results [155, 266], it does imply that the strain-hardening modulus of PS is lower than that of PC. This is primarily because the molecular weight between entanglements in polystyrene is higher than in polycarbonate (PS, T = 490 K: M_e = 18 kDa; PC, T = 298 K: M_e = 1.6 kDa [79]). Here we want to take a different route in shedding more light on the difference in strain-hardening moduli and look at non-affine responses.

6.5 The role of non-affinity

6.5.1 Principle of non-affine displacements

If a macroscopic sample is stretched in one direction ($\|$) by say 100%, the distance between the two ends of the sample is doubled. If the stretching occurs purely affinely, then this is also valid for every two points on the stretching axis. This means that the initial separation between any two points on this axis doubles. However, at a microscopic level this affine response breaks down due to particle-particle interactions such as connectivity and excluded-volume interactions. For example, it is highly improbable that a stiff covalent bond will be doubled in size. A more likely scenario is that the covalent bond retains its length and that particles tend to slip or slide along each other. Slippage causes friction and hence energy dissipation. One of the causes of friction is that Lennard-Jones bonds are broken and reformed. Another source are conformational transitions. These, however, will be discarded in this chapter. A further study could also take into account such a friction effect. As long as the sample deforms approximately homogeneously, the deviations from the affine response are a measure for the friction and therefore a rough estimate of the dissipated energy, and a measure of the plastic response and experienced stress of the material.

The assumption of homogeneous deformation can be made if no localization takes place. In our simulation method we are capable of applying an affine rescaling deformation (with possible non-affine response), so that localization is tempered and it is possible to measure the intrinsic stress-strain relation. However, at large strains localization does happen,

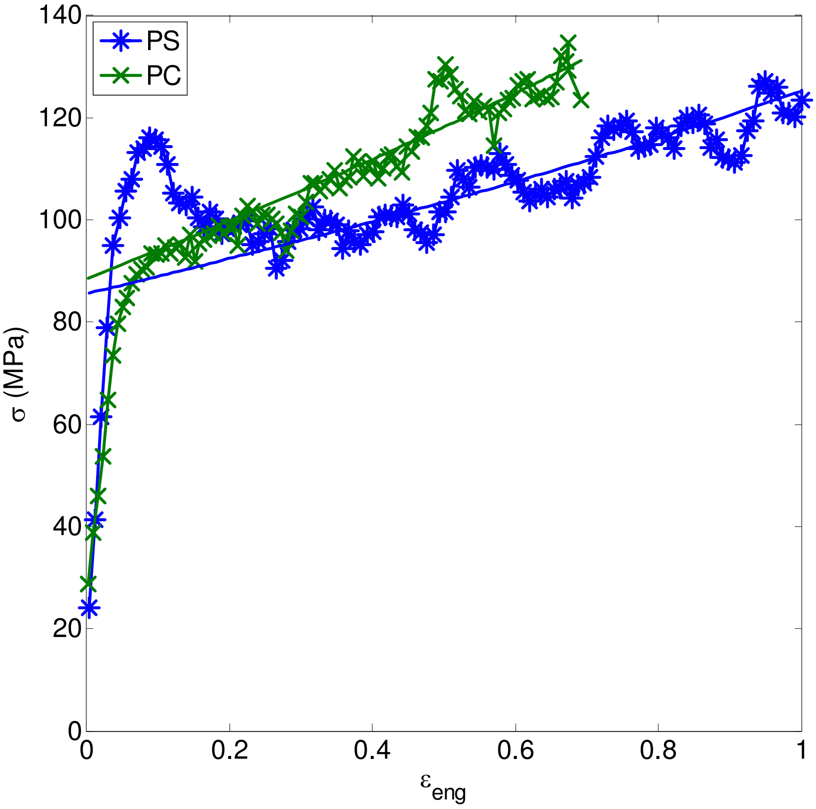

Figure 6.2: The von Mises equivalent true stress σ vs. strain $\varepsilon_{\mathrm{eng}}$ for PS and PC. Solid lines are fits to eq. 6.6. Fit range is $\varepsilon_{\mathrm{eng}} = 0.3$–$0.8$. Note that the strain-hardening modulus G_h for PC (19 MPa) is almost twice that of PS (11 MPa), while their extrapolated offset yield values σ_Y are about the same (PC: 88 MPa; PS: 86 MPa).

because of fracture. Nevertheless, the first fractured sample for the studied polystyrene glasses does not occur for $\varepsilon_{\mathrm{eng}} < 0.8$. Also for polycarbonate large cavities start to form only after this strain value. Therefore, we assume that the deformation is approximately homogeneous till $\varepsilon_{\mathrm{eng}} = 0.8$.

In view of the suggested connection between the plastic stress and the non-affine displacement we will calculate this non-affine displacement. This is realized by subtracting the local convective velocity arising from the global stretch. As the perpendicular directions ($\perp_1$ and $\perp_2$) are also affected by the deformation we do this for all three axes. Denote the component along one axis by μ, for $\mu = x,\ y,\ z$. Upon fixing the origin, the convective velocity at a certain position r^{μ} at time t is (without applying the Einstein summation convention)

$$v^{\mu}_{\mathrm{conv}}(t) = \frac{r^{\mu}(t)}{L^{\mu}(t)}\left(\frac{L^{\mu}(t+\Delta t) - L^{\mu}(t)}{\Delta t}\right) \tag{6.7}$$

in the limit of $\Delta t \to 0$. Here $L^{\mu}(t)$ is the time-dependent length of the box along one axis represented by μ. The affine part is removed by constructing a 'corrected' particle trajectory $\mathbf{r}_c(t)$ from the original one $\mathbf{r}_o(t)$ by subtracting the convective velocity $\mathbf{v}_{\mathrm{conv}}(t)$ at the position $\mathbf{r}_o(t)$

$$\Delta\mathbf{r}_c(t) = \Delta\mathbf{r}_o(t) - \mathbf{v}_{\mathrm{conv}}(t)\Delta t. \tag{6.8}$$

Here $\Delta\mathbf{r}(t) = \mathbf{r}(t+\Delta t) - \mathbf{r}(t)$. The initial condition $\mathbf{r}_c(t_0)$ is irrelevant for the resulting mean-square displacement, but can be taken to be equal to $\mathbf{r}_o(t_0)$, if you like. The calculation of the non-affine part of the particle's trajectory is carried out on the stored trajectory file, in which snapshots are saved every 8 ps. In principle eq. 6.8 is valid for $\Delta t \to 0$. However, artificially increasing the timestep between frames by only processing the odd frames does not lead to any significant difference in the final acquired corrected trajectory. Note that the result of this method, apart from a constant term, is independent of the choice of the origin t_0. Note also that in case of a constant-volume simulation without deformation the convective velocity equals zero making the corrected particle trajectory equal to the original particle trajectory. In this situation the mean-square non-affine displacement $\langle\Delta\mathbf{r}(t)^2\rangle = \langle(\mathbf{r}_c(t_0+t) - \mathbf{r}_c(t_0))^2\rangle$ obviously equals the normal mean-square displacement.

The just described method is also used in our previous work [177] and other simulation studies [253]. Other methods of measuring the non-affine displacement include the comparison of the actual coordinate $\mathbf{r}(t_0+t)$ with the affinely transformed coordinate at some initial time t_0 at zero strain, $\bar{\bar{F}}_{\mathrm{aff}} \cdot \mathbf{r}(t_0)$ [123]. Here $\bar{\bar{F}}_{\mathrm{aff}}$ is the macroscopic deformation tensor [179]. Then one can construct a different non-affine displacement $D_{na}(t)^2 = \langle\Big(\mathbf{r}(t_0+t) - \bar{\bar{F}}_{\mathrm{aff}} \cdot \mathbf{r}(t_0)\Big)^2\rangle$. The reason that we prefer the method as just described is illustrated by the following example. Assume that a particle is initially situated in the origin at t_0 and that afterwards uniaxial extension starts. Assume further that it makes only one non-affine jump from the origin to a new position in the extension direction, say at t_1, and moves affinely afterwards. The non-affine displacement of this particle therefore only takes place at t_1. Nevertheless, $D_{na}(t)^2$ keeps increasing for this particle

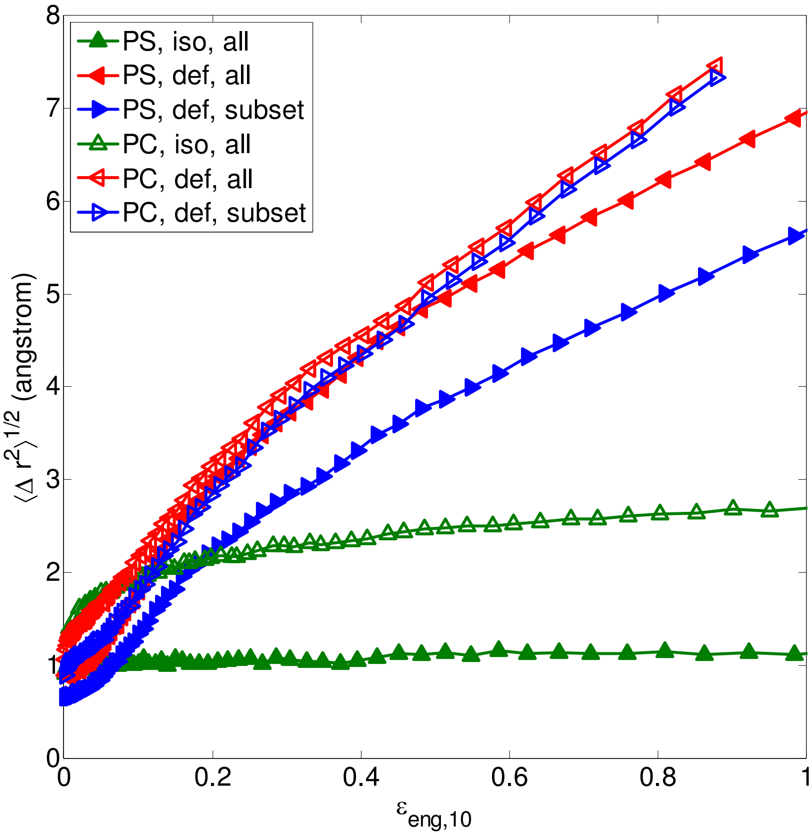

Figure 6.3: The root-mean-square non-affine united-atom displacement as a function of strain for polystyrene (filled markers) and polycarbonate (open markers) under the influence of active deformation. For comparison, the isotropic root-mean-square displacement at equal time separation ($t_1 - t_0 = \tau_{\text{def}}\varepsilon_{\text{eng},10}$) is also shown. See main text for details.

even for times larger than t_1. The reason is that the non-affine displacement is enlarged affinely after the jump at t_1 due to the ongoing extension of the sample. In the method currently in use, the mean-square non-affine displacement $\langle(\mathbf{r}_c(t_0+t) - \mathbf{r}_c(t_0))^2\rangle$ will not increase further and therefore plastic events occurring in the initial stages of deformation will not be blown up.

6.5.2 Isotropic vs. deformed non-affine bead displacements

The root-mean-square non-affine displacement will be calculated between two states, strained at $\varepsilon_{\text{eng},2}$ and $\varepsilon_{\text{eng},1}$

$$\langle \Delta\mathbf{r}(\varepsilon_{\text{eng},21})^2\rangle^{1/2} = \langle(\mathbf{r}_c(\varepsilon_{\text{eng},2}) - \mathbf{r}_c(\varepsilon_{\text{eng},1}))^2\rangle^{1/2}. \tag{6.9}$$

First we focus on the situation in which one state is the unstrained state, i.e.

$$\langle \Delta \mathbf{r}(\varepsilon_{\text{eng},10})^2 \rangle^{1/2} = \langle (\mathbf{r}_c(\varepsilon_{\text{eng}}) - \mathbf{r}_c(0))^2 \rangle^{1/2}. \tag{6.10}$$

Here $\varepsilon_{\text{eng},10} = \varepsilon_{\text{eng},1} - \varepsilon_{\text{eng},0} = \varepsilon_{\text{eng}} - 0 = \varepsilon_{\text{eng}}$. The subscript zero is included explicitly to indicate that $\langle \Delta \mathbf{r}(\varepsilon_{\text{eng},10})^2 \rangle^{1/2}$ also depends on the unstrained state. The result of both polymers during uniaxial extension is shown in fig. 6.3. Also shown in fig. 6.3 is the root-mean-square translational displacement for the undeformed case at the same temperature (denoted by 'iso'), by plotting the data at equal time separation $t_1 - t_0 = t_{10} = \tau_{\text{def}} \varepsilon_{\text{eng},10}$. Here τ_{def} is the time it takes to deform the material to a 100% strain increment. Notice that after initial yield the deformed samples have a large increase in non-affine displacement as compared to the isotropic case. The mean-square displacement for the isotropic case hardly rises in this region, a consequence of the caging of the particles deep in the glassy state (see also chapters 3 and 5).

When comparing polycarbonate to polystyrene the following is visible. Up to about 40% deformation the non-affine displacement of all (united) atoms of polystyrene is about equal to that of polycarbonate. Afterwards the non-affine displacement of polystyrene diminishes as compared to polycarbonate. Also apparent is the difference between the movement of all atoms and the movement of only a subset of atoms (the less mobile backbone atoms). For polycarbonate the difference is small; the average displacement of all atoms does not differ much from the average non-affine displacement of only the $\text{C}_{\text{C=O}}$ and the CT atoms (the two least mobile backbone atoms in the isotropic state, with $\text{C}_{\text{C=O}}$ in the carbonate group and CT the middle carbon of the propane part, see fig. 2.4). For polystyrene, however, a huge difference is present between the movement of all atoms and that of the subset (the backbone united atoms CH, CH_2 and CH_3, see fig. 2.2). An interpretation of this is that the side-group phenyl rings in polystyrene dominate the generation of initial plastic flow. However, these side-group phenyl rings can relatively easily turn in the plane perpendicular to the backbone vector pointing from one monomer to its neighbour, without disturbing the conformation of the backbone too much; therefore the phenyl rings will not drag along the backbone for all non-affine displacements. This could also explain the relatively large difference between the non-affine displacement of all atoms and the non-affine displacement of the backbone in PS. As we will see later on in this chapter, it is just the backbone that causes the strain-hardening effect. As the contribution of the backbone to the total non-affine displacement is only minor in PS, the resulting overall plasticity is less affected by the backbone. In polycarbonate, in contrast, no real side groups are present, and the available phenyl rings are within the backbone; therefore any motion of those rings (apart from rotation around their own axes) will lead to backbone motion and any increase in the backbone plasticity will also lead to a large increase in the overal plasticity.

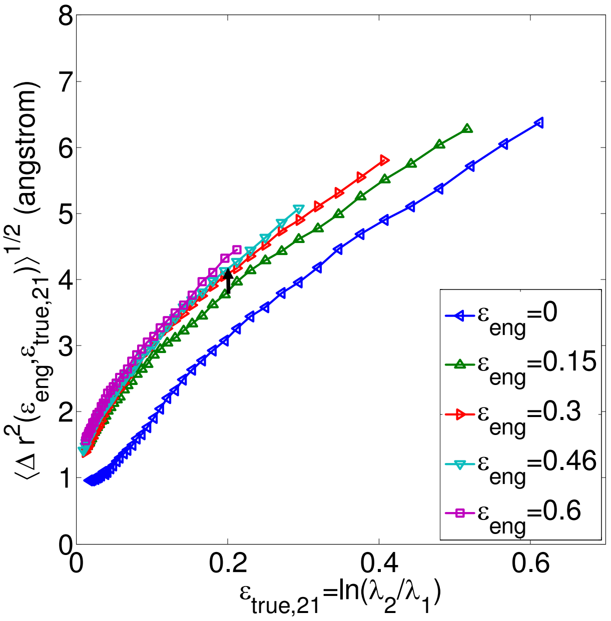

(a)

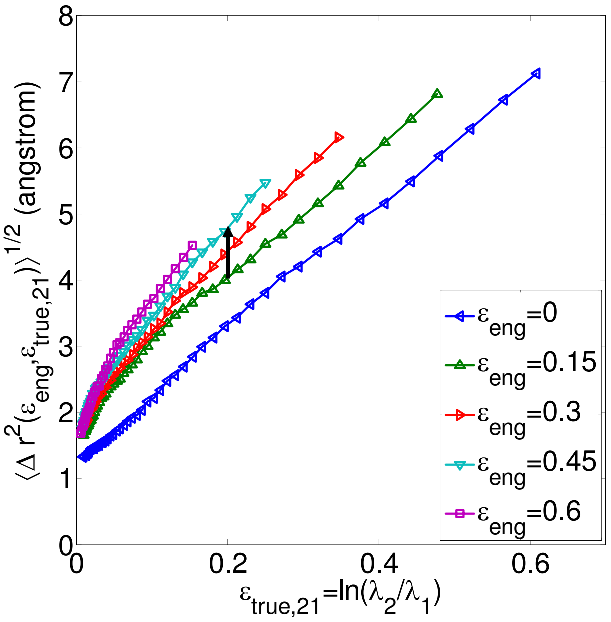

(b)

Figure 6.4: The RMS non-affine displacement as a function of relative extension (true-strain difference $\varepsilon_{\text{true},21}$) for various values of the origin ε_{eng} for (a) PS and (b) PC. At a later stage more non-affine displacement is necessary to deform the material. This effect is stronger for polycarbonate, being illustrated by the length of the arrows pointing from $\varepsilon_{\text{eng}} \approx 0.15$ to $\varepsilon_{\text{eng}} \approx 0.45$.

6.5.3 Non-affine bead displacements for various strains

The non-affine displacement as shown in fig. 6.3 and just discussed is calculated by comparing a sample at a strained state with respect to the state at zero strain. This non-affine displacement is increasing with increasing strain. However, for a non-polymeric glassy material this is also what one would expect, despite the absence of any polymeric strain hardening. See, e.g., Tanguy et al. [253], where the non-affine displacement for an atomic LJ glass increases in a diffusion-like matter under the influence of shear.

Yet another effect is that of thermal motion. As the deformation is at a constant strain velocity, strain differences correspond to time differences. Non-affine displacements can therefore also be regarded as being a function of time. In the undeformed, isotropic case the convective velocity is zero so that the non-affine RMS displacement is equal to the normal RMS displacement. And this normal RMS displacement simply increases due to thermally activated motion. So even for the undeformed, isotropic case the root-mean-square non-affine displacement is increasing with time.

To see evidence for a connection between the rate of energy dissipation and non-affine displacement, we need to look instead at the plasticity rate (i.e., the rate of non-affine displacement). So how can we see if this rate increases with increasing strain?

The solution for this is to compare the non-affine displacement at different origins, in which each origin corresponds to a different strained state rather than only the undeformed state. The non-affine displacement is then a function of both the origin $\varepsilon_{\text{eng}} = \lambda_1 - 1$ and the relative separation $\varepsilon_{\text{true},21} = \varepsilon_{\text{true},2} - \varepsilon_{\text{true},1} = \ln(\lambda_2/\lambda_1)$

$$\langle \Delta\mathbf{r}(\varepsilon_{\text{eng}}, \varepsilon_{\text{true},21})^2\rangle^{1/2} = \langle(\mathbf{r}_c(\lambda_2) - \mathbf{r}_c(\lambda_1))^2\rangle^{1/2}. \tag{6.11}$$

The non-affine displacement is taken as a function of the relative increase in strain $\varepsilon_{\text{true},21} = \ln(\lambda_2/\lambda_1) = \ln\left(\frac{L_{\parallel}(t_2)}{L_{\parallel}(t_1)}\right)$ instead of a function of the difference in engineering strain $\varepsilon_{\text{eng},21} = \varepsilon_{\text{eng},2} - \varepsilon_{\text{eng},1} = \lambda_2 - \lambda_1 = \frac{L_{\parallel}(t_2) - L_{\parallel}(t_1)}{L_{\parallel}(t_0)}$, to compare relative extensions instead of absolute ones at an equal footing.

Eq. 6.11 also corresponds to looking at the non-affine MSD for various time origins, because, again, differences in strain correspond to differences in time. In the equilibrium isotropic case the normal RMS displacement (and hence the RMS non-affine displacement) would be independent of the time origin, so that by looking at different origins any possible increase would be solely due to the increase in plasticity, and not an effect of thermal motion.

The RMS non-affine displacement $\mathbf{r}(\varepsilon_{\text{eng}}, \varepsilon_{\text{true},21})^2\rangle^{1/2}$ is a two-dimensional function. We therefore plot it both as a function of the relative extension $\varepsilon_{\text{true},21}$ for various values of the origin ε_{eng} (fig. 6.4) and as a function of ε_{eng} for various values of $\varepsilon_{\text{true},21}$ (fig. 6.5). The motive is that some observations turn out to be more clearly visible in one of the two representations. However, in plotting the RMS non-affine displacement as a function of ε_{eng} for various values of $\varepsilon_{\text{true},21}$ one point should be addressed. The saved trajectory file has a finite time step between frames, so that there is not always a pair of two frames available for a given value of $\varepsilon_{\mathrm{true},21}$. As the first frame is already determined by $\varepsilon_{\mathrm{eng}}$, the second frame is chosen as that which renders the closest value of the required $\varepsilon_{\mathrm{true},21}$. If the $\varepsilon_{\mathrm{true},21}$ from this pair of frames deviates by more than 5% from the requested $\varepsilon_{\mathrm{true},21}$ the point is discarded.

A few observations are visible when looking at the non-affine displacement as a function of $\varepsilon_{\mathrm{true},21}$ and $\varepsilon_{\mathrm{eng}}$ for both polymers in figs 6.4 and 6.5. We first focus on the initial yield regime. It clearly has a large effect on the increase in non-affine displacement. The non-affine displacement at small relative strains $\varepsilon_{\mathrm{true},21}$ increases a lot as a function of $\varepsilon_{\mathrm{eng}}$ during the first few percents of deformation, i.e., up to the initial yield point. For $\varepsilon_{\mathrm{eng}}$ beyond the initial yield region the relative increase is much lower. Also the increase in the non-affine displacement as a function of $\varepsilon_{\mathrm{true},21}$ for values of $\varepsilon_{\mathrm{true},21}$ smaller than about 0.05 is more steep for larger $\varepsilon_{\mathrm{eng}}$.

These observations near yield can be understood by the following picture. Straining the unstrained sample is initially mostly elastic. This is supported by the observation in chapter 5 that most of the initial applied work is converted into internal energy. This elastic response causes only a small deviation from the affine response as no significant structural rearrangements occur. After initial yielding rearrangements do occur and the mobility of atoms is at an enhanced level; the fluctuations around the affine trajectory are in this case larger than in the undeformed case. As the average RMS difference between two very fluctuating signals (i.e., between two strained samples) is larger than the average RMS difference between a very fluctuating signal and a less fluctuating signal (i.e., between the unstrained and the strained sample), the non-affine displacement for small values of $\varepsilon_{\mathrm{true},21}$ is expected to be larger after yield.

The second focus is on the strain-hardening regime. Here the first and most important observation is that at larger values of $\varepsilon_{\mathrm{eng}}$ more non-affine displacement is indeed needed to establish the same relative extension. As an example, consider the data of polystyrene in fig. 6.4. In order to stretch the sample by 22% ($\ln(\lambda_2/\lambda_1) = 0.2$) about 3.2 Å of non-affine displacement is necessary if the initial state is the unstrained one. However, if the initial state equals $\varepsilon_{\mathrm{eng}} = 0.15$, then about 3.8 Å of non-affine displacement is needed to increase the sample in the extension direction by the same relative amount. This value of non-affine displacement keeps on increasing in the strain-hardening region. The particles are moving more non-affinely at larger strains, implying that larger detours or deviations around the affine response are unavoidable at larger strains. This relative increase in non-affine displacement with increasing strain is larger for polycarbonate than for polystyrene. This can be judged by the difference in magnitude of the arrows present in fig. 6.4, showing the increase in non-affine displacement from $\varepsilon_{\mathrm{eng}} = 0.15$ to $\varepsilon_{\mathrm{eng}} = 0.45$ and by the difference in slope of the curves in fig. 6.5. The polymer structure apparently imposes the magnitude of detours from affinity.

Another observation in the strain-hardening regime is that the slope of the curves in fig. 6.5

increases with $\varepsilon_{\mathrm{true},21}$. Apart from the absolute value, the slope of the curve normalized by the RMS non-affine displacement at a fixed value of $\varepsilon_{\mathrm{eng}}$ is also increasing (not shown). The origin could be the influence of thermal motion. Small strain differences correspond to small time scales. However, for these small time scales non-affine displacements in the stressed state are comparable to the normal thermally activated displacements in the undeformed case. In this case the pure non-affine increase is somewhat overshadowed by thermal motion. At larger strain differences $\varepsilon_{\mathrm{true},21}$ the relative contribution of the thermal motion is smaller, resulting in a more pure non-affine increase. A similar situation is present when one considers a vector in space. If one component of the vector is increasing and other components are constant and nonzero, the relative increase in the length of that vector is less than the increase in the component. If, on the other hand, other components are negligible, the relative increase in the length of the vector is equal to that of the component. Therefore, one expects that for larger strain differences of $\varepsilon_{\mathrm{true},21}$, in which the relative contribution of the thermal motion is smaller, the resulting slope is higher.

The current results regarding the increase in the rate of non-affine displacement for the two polymers in the strain-hardening regime are in accordance with two previous studies on polymers where also an increase in a mobility-related rate is observed during deformation. In a polyethylene-like model polymer [38, 39] a steady increase in the torsion transition rate can be seen in the post-yield regime (the strain-hardening region). A study on a toy-polymer model at zero temperature [124, 125] revealed that the rate of changes in LJ binding is also increasing in the strain-hardening regime and, moreover, that it is directly correlated with the dissipative stress. These observations suggest that such rate increase during deformation is quite universal in polymer glasses.

6.5.4 Non-affine deformation of polymer-chain shape

So why is there an increase in the rate of non-affine displacement for the polymer glass? One reason for the non-affine displacement is that covalent bonds prevent the separation of the bonded particles. If particles would displace affinely, then the equilibrium value of this chemical bond would be excessively disturbed. To circumvent this bond stretch, the particles forming the covalent bond will rather move non-affinely at these small scales. The largest scale of the polymer chain, the end-to-end distance, is much less disturbed. For a long chain the internal conformation can be adjusted, while still having an affine displacement of the end-to-end distance. The affine displacement at large scales is a result of the glassy state of the polymer samples. As mentioned in §6.1 the relaxation time of spontaneous rearrangements at the scale of the whole chain greatly exceeds experimental and simulation time scales in the glassy state. Therefore, the end-to-end distance cannot adjust back towards the equilibrium value by means of spontaneous relaxations.

To see this in a more quantitative way we study the evolution of the internal distances of the polymer chain during deformation. It is compared both to the undeformed case and

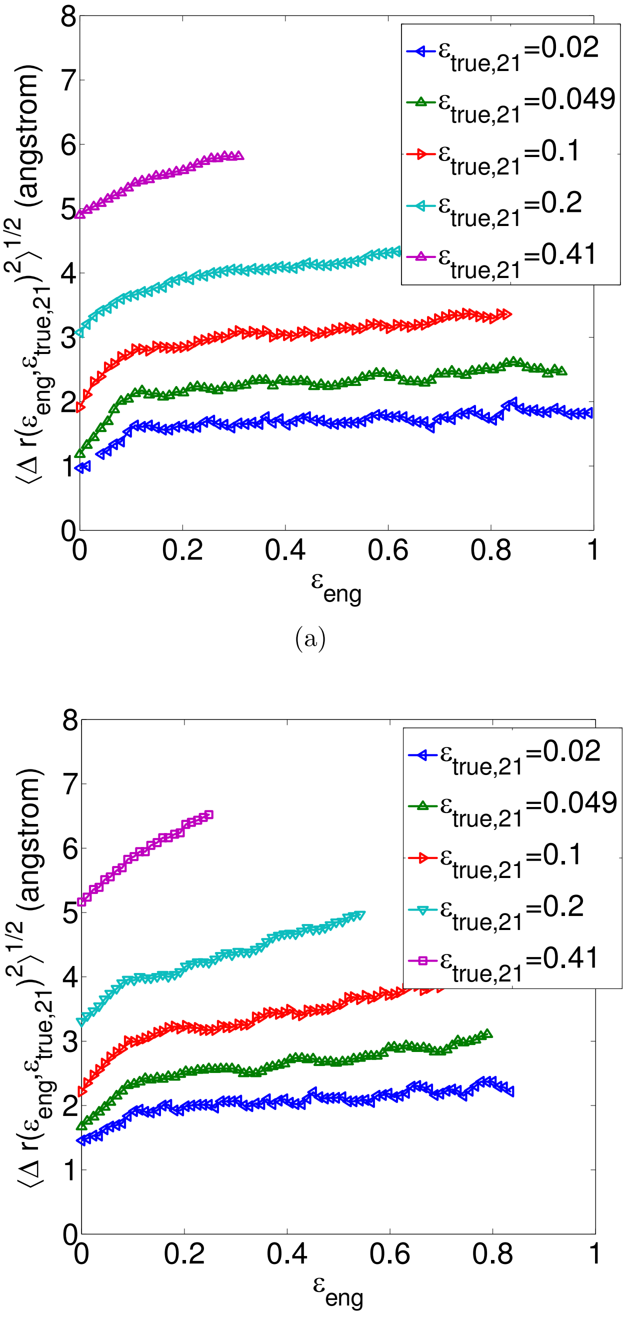

(a)

(b)

Figure 6.5: The non-affine displacement as a function of strain ε_{eng} at various separation strains $\varepsilon_{\text{true},21}$ for (a) polystyrene and (b) polycarbonate.

to the evolution if the response would be purely affine. This is realized by examining the evolution of the characteristic ratio during deformation normalized by the isotropic case

$$C'_n(\varepsilon_{\text{eng}}) = C_n(\varepsilon_{\text{eng}})/C_n(0) = \langle|\mathbf{r}_n(\varepsilon_{\text{eng}})|^2\rangle/\langle|\mathbf{r}_n(0)|^2\rangle. \tag{6.12}$$

Here the dependence of C'_n on the unstrained state is not shown in the argument for the sake of a shorter notation.

Results for polystyrene and polycarbonate are plotted as a function of ε_{eng} in fig. 6.6, closed symbols.

To see the deviations of the stretching at various scales from the affine response, this response is also included in the figure. The affine response is calculated in two ways. The first way is to affinely transform the coordinates of all particles at $\varepsilon_{\text{eng}} = 0$ according to the relative change in box sizes, meaning that for the x-components of the coordinates

$$x_{n,\text{aff}}(\varepsilon_{\text{eng}}) = \lambda_x x_n(0), \tag{6.13}$$

with $\lambda_x = L_x(t)/L_x(0)$. The coordinates in the direction of the two other axes (y and z) are rescaled likewise. Afterwards, the characteristic ratio of the affine coordinates is calculated, see open symbols in fig. 6.6. The second way assumes that the initial sample is isotropic in the sense that $\frac{1}{3}\langle|\mathbf{r}_n|^2\rangle = \langle|x_n|^2\rangle = \langle|y_n|^2\rangle = \langle|z_n|^2\rangle$. The affine response for the squared intrachain length scales including this isotropy condition equals

$$\langle|\mathbf{r}_{n,\text{aff}}(\varepsilon_{\text{eng}})|^2\rangle = \frac{1}{3}\left(\lambda_x^2 + \lambda_y^2 + \lambda_z^2\right)\langle|\mathbf{r}_n(0)|^2\rangle. \tag{6.14}$$

Hence $C'_{\text{aff}}(\varepsilon_{\text{eng}}) = \frac{1}{3}\left(\lambda_x^2 + \lambda_y^2 + \lambda_z^2\right)$. This affine response is shown as a solid line in fig. 6.6. Note that the two ways of calculating the affine response are close to each other, meaning that the samples can be regarded as being isotropic (in this sense). For large n less data points are available (poorer statistics) and the two ways of calculating the affine response deviate more from each other.

The following observations are apparent from fig. 6.6. As is expected, C_1 is almost unchanged with increasing extension, for polystyrene as well as for polycarbonate. This is due to the very rigid covalent bond. For somewhat larger separations the internal distance is able to increase, although the response is sub-affine, see, e.g., the evolution of C'_{30}. For even larger separations an almost affine response is present, see, e.g., C'_{100}. This internal distance responds affinely up to about 15% for both polystyrene and polycarbonate. However, for larger strains the relative deviation from affinity for C'_{100} becomes larger.

We can conclude that upon deforming further, larger and larger segments move in a non-affine way. This is in accordance with what was found in §6.5.3 for the increase in non-affine displacement of beads upon straining. As discussed earlier, the non-affine bead displacement at a fixed relative strain is also at a higher level at larger strain origins. It is therefore plausible that the increase in the relative non-affine bead displacement at larger strains is caused by the fact that at larger strains larger chain segments move non-affinely.

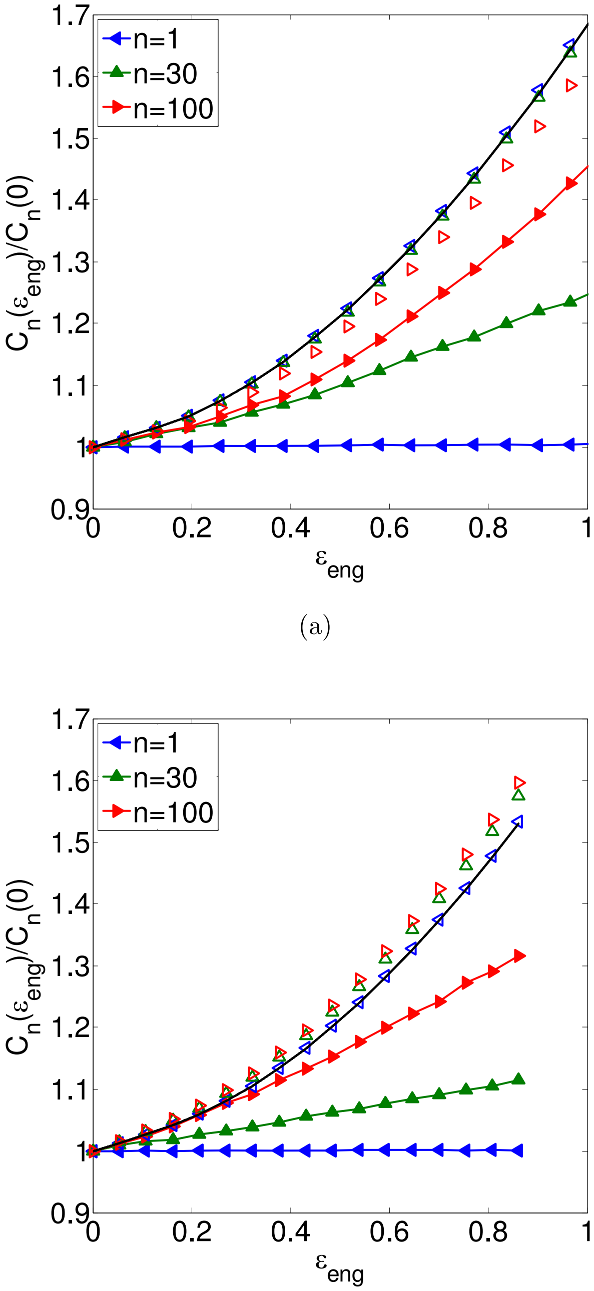

(a)

(b)

Figure 6.6: The normalized characteristic ratio $C'_n(\varepsilon_{\text{eng}}) = C_n(\varepsilon_{\text{eng}})/C_n(0)$ as a function of strain for (a) PS and (b) PC. Solid lines with filled symbols are simulation results, while open symbols are results as if the sample would deform in an affine way. The black curve is the affine approximation, eq. 6.14.

So a connection can be made between strain hardening, non-affine displacement of particles, and non-affine stretching of intrachain distances. If larger chain parts reshape non-affinely, then the accompanying beads of the chain parts move more non-affinely as well. A larger force is needed to move particles more non-affinely, so that this leads to an increase in the stress. So strain hardening is caused by the more non-affine reshaping of the internal distances of a chain.

Differences between PS and PC

For both PS and PC larger segments move non-affinely at larger inner length scales. However, a difference between PS and PC is the magnitude of the effect. This is exemplified by the stretch of the internal distance corresponding to $n = 30$ at $\varepsilon_{\text{eng}} = 0.5$. For polycarbonate $C'_{30}(0.5)$ is almost 30% of the affine value, $C'_{\text{aff}}(0.5)$, see fig. 6.6(b). For polystyrene the response is more affine for $n = 30$; in this case 50% of the affine value is reached at $\varepsilon_{\text{eng}} = 0.5$, fig. 6.6(a).

One could argue that the deviation from affine response should be compared at equal contour lengths instead of equal number of backbone bonds. Nevertheless, this does not change the conclusion if we define the contour length as the total length via covalent backbone bonds. This is justified by the fact that the RMS backbone bond length $\langle l_{bb,i}^2 \rangle^{1/2}$ is in fact very similar for both polymers. For PS $\langle l_{bb,i}^2 \rangle^{1/2} = 1.53$ Å. To determine the backbone bonds for PC we take one of the shortest pathways via covalent bonds from the start of one monomer to the start of the subsequent monomer. In this way we encounter $2l_{\text{O-CB}}$, $2l_{\text{CG-CG}}$, $2l_{\text{O-C}}$, $2l_{\text{CG-CT}}$ and $4l_{\text{CB-CG}}$ (see the force-field details in chapter 2), making $\langle l_{bb,i}^2 \rangle^{1/2} = 1.42$ Å. The difference between the PS and PC RMS backbone bond lengths is thus less than 10%, so that also for equal contour lengths the non-affine response is larger for PC.

This behaviour of a more non-affine chain-shape response for polycarbonate as opposed to polystyrene can be connected to the previous finding regarding the root-mean-square non-affine bead displacement. Also in terms of the bead displacements PC behaves more non-affinely than PS: the non-affine displacement at a certain value of $\varepsilon_{\text{true},21}$ increases more with increasing strain for PC than for PS (compare fig. 6.4(a) with 6.4(b)).

6.5.5 Effective chain stiffness during deformation

So what would be the reason for the difference in increase in the non-affine response of the inner chain dimensions between polystyrene and polycarbonate? To answer this question we again take a closer look at the internal distances of the chain. As was discussed, a huge force is needed to increase the bond length significantly upon straining. A more probable reaction path is therefore that the bond will slip. For very large scales the behaviour is

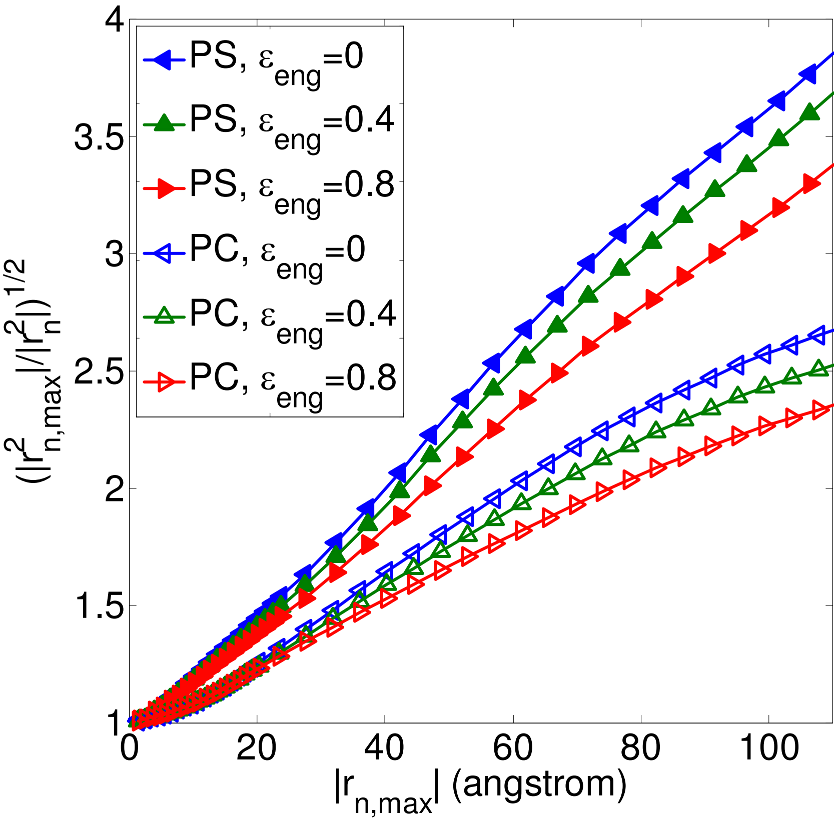

Figure 6.7: Simulation results of the maximal extensibility $\lambda_{n,\max}$ for PS (filled symbols) and PC (open symbols) as a function of the maximal extension $r_{n,\max}$ for different values of strain ε_{eng}.

also evident: if the maximal extensibility of the chain is much higher than the draw ratio and the relaxation time exceeds the time scale of deformation (as is the case for the glassy state), the displacement at these scales will be approximately affine. For particles within a chain which are separated by several bonds the situation is within these two limits, i.e., between pure affine deformation and pure slip and depends on the maximal extensibility of the chain.

At the scale of the Kuhn length the chain cannot be extended any further and a non-affine stretching of this length cannot be circumvented. The maximal (reasonable) extensibility at any internal distance n as a function of strain is the ratio of the end-to-end distance of the fully extended chain to the random-coil conformation of the chain

$$\lambda_{n,\max}(\varepsilon_{\text{eng}}) = \sqrt{C_{n,\max}/C_n(\varepsilon_{\text{eng}})} = \frac{r_{n,\max}}{\langle|\mathbf{r}_n(\varepsilon_{\text{eng}})|^2\rangle^{1/2}}. \tag{6.15}$$

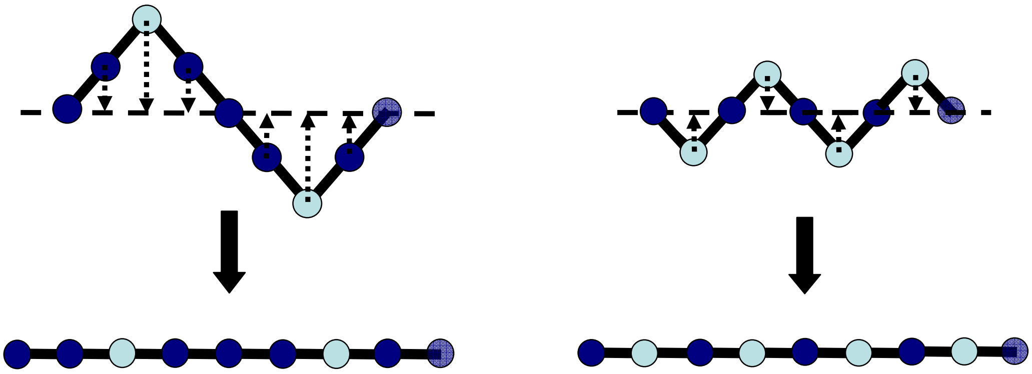

Figure 6.8: Illustration showing that a chain which has a larger Kuhn length (upper left chain, which has a pivoting point every fourth particle, indicated by the lighter particle) needs more non-affine displacement to stretch further than a chain with a smaller Kuhn length (upper right chain, which has a pivoting point every second particle). The dotted arrows indicate the amount of vertical non-affine displacement necessary for each particle in the two upper chains if the two end atoms of each chain are displaced from each other by the same amount in the horizontal direction, i.e., horizontal extension. So the total vertical non-affine displacement per particle of the stiffer chain on the left side is twice that of the more flexible chain on the right side.

For the two simulated polymers the maximal draw ratio $\lambda_{n,\max}$ is plotted in fig. 6.7 as a function of the maximal extension $r_{n,\max}$ for a certain number of backbone bonds n and for various values of ε_{eng}. If we do not use $r_{n,\max}$ for the horizontal axis, but the number of backbone atoms n, or the average backbone length times the number of backbone atoms $\langle l_{bb,i}^2 \rangle^{1/2} n$, then still fig. 6.7 hardly changes.

In fig. 6.7 we observe that an atactic polystyrene chain is able to extend much more than a polycarbonate chain for a certain fixed distance along the chain, reminiscent of the observation that the Kuhn length of PS is much lower than that of PC. This implies that during a uniaxial-stress extension experiment, the polystyrene chain is able to move more affinely, as is illustrated in fig. 6.8.

Also noticeable in fig. 6.7 is that during deformation the maximal extensibility $\lambda_{n,\max}(\varepsilon_{\text{eng}})$ decreases for larger scales. This has direct consequences for the non-affine displacement. More and more segments are moving non-affinely upon straining, thereby generating more plastic flow. It is therefore reasonable to assume that this also causes the hardening in the stress upon straining. Obviously the decrease of the maximal extensibility is caused by the stretching of the chains. Can we understand in which way this extensibility, and accompanied with it the intrachain distances, change upon straining?

The decrease in maximal extensibility during deformation can easily be seen by mapping the strained chain on an effective worm-like chain or on a freely-jointed chain (as both models have the same limit). The large-scale internal-chain distances deform nearly affinely, in a way given by eq. 6.14. In this case, however, the effective stiffness of the chain increases, as can be concluded from the following discussion.

First we consider an ideal unperturbed chain $C(0)$ in a one dimensional space. If such a chain would be stretched, so that the end points transform affinely by a factor $\lambda = 1 + \varepsilon_{\text{eng}}$ (but do not exceed the contour length L_c), then one can map the resulting deformed chain $C(\varepsilon_{\text{eng}})$ on an effective isotropic, undeformed freely-jointed chain C_{eff} but with the same contour length and average end-to-end distance as the deformed chain $C(\varepsilon_{\text{eng}})$. This effective FJC C_{eff} has a Kuhn length which is different from the Kuhn length of the unperturbed one-dimensional chain prior to deformation $C(0)$, as the end-to-end distance of the effective chain C_{eff} is larger than the end-to-end distance of the unperturbed chain $C(0)$. We will now define the effective Kuhn length of the deformed chain $C(\varepsilon_{\text{eng}})$ as being equal to the Kuhn length of the effective chain C_{eff}. To avoid any confusion with the intrinsic Kuhn length of the unperturbed chain $C(0)$, we will call the effective Kuhn length of a deformed chain $C(\varepsilon_{\text{eng}})$ the effective stiffness length $l_s(\varepsilon_{\text{eng}})$. In this one-dimensional case the effective stiffness length during deformation would be equal to $l_{s,\text{aff}}(\varepsilon_{\text{eng}}) = \lambda^2 l_s(0)$. So upon stretching the chain, the effective perturbed-chain stiffness length starts to deviate from the unperturbed-chain stiffness length.

In three dimensions we can do a similar calculation. Now we will map the deformed chain on an effective worm-like chain, as the intrachain distances of our polymers under study are better described by the WLC. Another point to mention is that now the chain shape will deform in an anisotropic way. Therefore it is expected that the internal distances of the effective chain C_{eff} will deviate from the internal distances of the deformed chain. Nevertheless, we can still define an effective stiffness length of the deformed chain. If the end points of the deformed chain transform affinely, the effective stiffness length as a function of strain equals

$$l_{s,\text{aff}}(\varepsilon_{\text{eng}}) = l_s(0)\frac{1}{3}\left(\lambda_x^2 + \lambda_y^2 + \lambda_z^2\right). \qquad (6.16)$$

So during deformation the effective stiffness length increases. As the non-affine particle displacements during deformation increase with increasing stiffness length (or Kuhn length, see fig. 6.8 where this is illustrated) it is natural to expect that the rate of non-affine displacement of the backbone increases with strain in a way similar to the increase in effective stiffness length.

As our chain lengths are rather limited, we can not determine the long-chain stiffness length by using eq. 6.2. Instead, we want to use the worm-like chain expression, eq. 6.5 for determining the effective stiffness length. However, the deformed chains are in generally anisotropic and therefore it is likely that the functional dependence of the intrachain distances would deviate from the WLC result. A possible direction of improvement would be to replace the WLC model by a distribution of internal distances that has more parameters and that takes the anisotropy of the deformed chain explicitly into account.

Nevertheless, on the basis of our simulation data we can conclude that mapping the deformed chain back onto an isotropic WLC albeit with an increase in the effective stiffness length does suffice. This evidence is presented in fig. 6.9, where the normalized squared intrachain length scales $\langle|\mathbf{r}|^2\rangle/(L_c l_s)$ as a function of the normalized chain contour length L_c/l_s is displayed. If the normalization is carried out by using the stiffness length of the unperturbed chain the intrachain lengths increase with strain, as expected. If, on the other hand, we fit the deformed intrachain lengths as a function of contour length by the intrachain lengths according to the isotropic WLC model, eq. 6.5, to determine the effective stiffness length and use this effective stiffness length to normalize the intrachain and the contour lengths, we see that the intrachain lengths do remain approximately invariant under the influence of deformation (both for PS and PC, see fig. 6.9). As we did also with the fit for the characteristic ratio, the fit for determining the effective stiffness length is confined to contour lengths smaller than 3 stiffness lengths, because the chains under consideration are not perfectly ideal for large scales (the decline in the characteristic ratio, fig. 6.1, as we saw before). To sum up, the effect of deformation on the intrachain distances can be interpreted simply as an increase in the effective stiffness length of an equivalent WLC.

What are the consequences of this interpretation for the resulting stress-strain relation? In a simple glassy system consisting of small molecules no polymeric strain hardening takes place, but straining occurs at an approximately constant yield stress (apart from yield-peak effects at small strains), also seen in simulations [253]. Hence, if the stiffness length of the unperturbed polymer chain is of the order of the scale of the small molecules, then the increase in the effective stiffness length has not much effect on the total stress as this effect is overwhelmed by the background yield stress of the equivalent small-molecule system. As the stiffness length of unperturbed polystyrene is relatively small, it is plausible that this mechanism is at hand with polystyrene. The dominant initial non-affine displacement is due to the phenyl ring side groups (conform fig. 6.3); the non-affine displacement of the backbone is much less. The increase in the effective stiffness length of the backbone will therefore not directly lead to much increase in total non-affine displacement; consequently a small strain-hardening effect would be present.

If the stiffness length for the undeformed chain is, on the other hand, much larger, and the non-affine displacements of the backbone atoms form a substantial part of the total non-affine displacement, then the increase in the effective stiffness length does have an effect on the total non-affine displacement. As a result, the stress will significantly increase at larger strains. If the stiffness length of the undeformed chain is so large that it is not much smaller than the entanglement length, the additional constraint from the entanglements could lead to an enhanced stiffening, an enhanced increase in non-affine displacements and therefore to a larger strain-hardening modulus. However, it is not likely that this enhanced increase is applicable for PS, since the contour length between entanglements is about 400 Å for this polymer [60], substantially larger than the Kuhn length.

The picture of stiffening for a higher effective stiffness length is in accordance with some

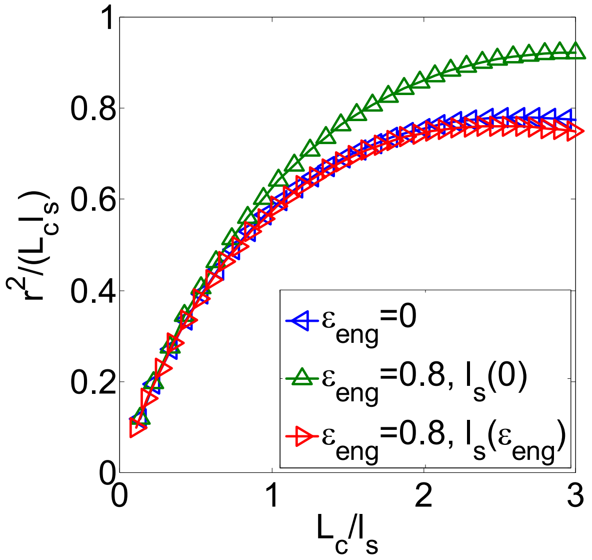

(a)

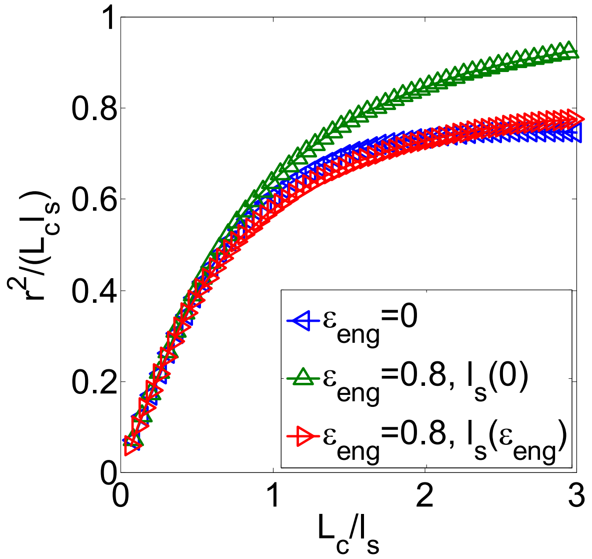

(b)

Figure 6.9: The normalized squared intrachain length $\langle|\mathbf{r}|^2\rangle/(L_c l_s)$ as a function of the normalized chain contour length L_c/l_s for (a) PS and (b) PC. When normalized by the effective stiffness length $l_s(\varepsilon_{\text{eng}})$ during deformation instead of the stiffness length of the unperturbed chain $l_s(0)$, the curve at a strained state turns out to be almost superimposable on the unstrained curve.

findings from literature. Stress-strain relations of preoriented samples [117, §5.2.7] show a higher slope after initial yield than unoriented samples. Also in this case the maximal remaining extensibility is lower for the preoriented samples. It was also observed experimentally that polymers with a high Kuhn length tend to have a high value of G_h [114].

6.6 Conclusions

For polycarbonate there is a pronounced increase in stress for large strains (strain hardening). For polystyrene, on the other hand, this effect is much less prominent; the strain-hardening modulus of PS as simulated by the molecular-dynamics method is about half the value of that of polycarbonate. Our simulations thereby support the experimental results in which also a huge difference in the strain-hardening moduli is present. It is shown that an increase in the amount of non-affine displacement is needed to strain the material further. It was demonstrated earlier by Hoy and Robbins [124] that the rate of changes in Lennard-Jones binding was linearly correlated with the stress. If one assumes that the amount of non-affine displacement needed to strain the sample further increases if the rate of changes in LJ binding is higher (as a larger detour around the affine particle trajectory and thus more non-affine displacement implies that more LJ bonds need to be broken to be able to make this detour), the conclusion must be that strain hardening is due to this increase in non-affine displacement. This increase occurs because upon stretching the sample local chain parts (like covalent bonds and longer distances) approach their maximal reasonable extensibility, requiring that larger length scales need to move non-affinely for larger strains. It is shown that the non-affine response of the intrachain length scales can be understood in the picture that the effective stiffness length (here the stiffness length is determined by fitting the internal distances of the chain by the worm-like chain results; in the limit of an infinite chain the stiffness length coincides with the Kuhn length) of the perturbed chain increases with increasing strain. As the Kuhn length of polycarbonate is already larger than that of PS and the total non-affine displacement of PC is to a large extent determined by the backbone atoms, the increase in the effective stiffness length leads to an increase in non-affine displacement, more energy dissipation and hence a higher strain-hardening effect. For polystyrene the Kuhn length is small and the major part of non-affine displacement is not caused by the backbone. Hence the expected increase in the effective stiffness length during deformation does not lead to a substantial increase in plastic flow, so that at moderate strains PS behaves more like a simple glass without strain hardening, as opposed to polycarbonate.

Chapter 7

Conclusions and outlook

One of the most striking features of glass-forming liquids, either simple or polymeric liquids, is the slowing down of their dynamics and a rapid increase in their viscosity. Understanding the mechanisms at work on a molecular scale is one of the most important challenges of condensed-matter physics. The dynamical properties of glasses are very heterogeneous; the displacement of the constituent particles shows strong non-Gaussian effects. Both of these phenomena are poorly understood theoretically. A strained polymer glass shows typical mechanical characteristics which can vary greatly between different types of polymers, but of which the origin is still unclear.

Our main goals are to acquire a better understanding at the molecular scale of heterogeneous and non-Gaussian dynamics and mechanical deformation of glassy polymers and to differentiate chemistry-specific from more physical universal properties hereof. By means of molecular-dynamics simulations in combination with analytical tools we study these subjects. In the next sections a short description will be given of the problems addressed together with the most important conclusions that have followed from the research.

Non-Gaussian displacements, chapter 3

Non-Gaussian particle displacements are often observed in glassy systems. They are usually interpreted as the sign of heterogeneous dynamics and many models incorporate heterogeneity to explain non-Gaussian dynamics. We have shown that even a simple model can be employed, which already shows non-Gaussian dynamics, but has no built-in heterogeneity. The model shows more communalities with simulation and experimental results:

- The global behaviour of the non-Gaussian parameter in vitrified systems (the maximum value and the time at which this maximum value occurs) is not a result of heterogeneous dynamics, but merely the signature of hopping processes.

- Heterogeneity reveals itself only in finer details, such as the time dependence of the non-Gaussian parameter.
- By means of the model quantitative statements, within fair detail, can be made about the maximum value of the non-Gaussian parameter and the position of this maximum as a function of time — in particular this is demonstrated for systems with widely different topologies: a quasi-two-dimensional colloidlike system, a glass of linear polystyrene, and a glass of branched dendrimers.
- The effective particle jump length as a function of density in a colloidlike system shows a maximum, which is situated just above the freezing density.

Heterogeneous dynamics, chapter 4

To acquire more evidence for heterogeneity in glassy polymer systems the motion of the side group of polystyrene, the phenyl ring, has been investigated by means of MD simulations. Heterogeneity is clearly observed in this study.

- The presence or non-presence of heterogeneous dynamics with the flipping motion of the phenyl ring depends on the following. If the relaxation time of a backbone vector is faster than the typical inverse short-time transition rate of a flip of the phenyl ring, no heterogeneous dynamics is present (in the sense that the relaxation is nearly exponential). In case the backbone relaxation is much slower, the phenyl ring is trapped in a local conformation. As the energy barrier of a flip is conformation-dependent and the time to change conformation is larger than the transition time for the most ideal conformation (i.e., the conformation that leads to the lowest energy barrier), then within the time of a conformational change the phenyl rings cannot reach this ideal conformation. Hence heterogeneous dynamics is present.
- There is a direct connection between the conformation and the dynamics of the phenyl ring, even in the presence of heterogeneity: within statistical error the enthalpy barrier as determined by the temperature dependence of the probability density function of the phenyl-ring conformation and the activation enthalpy determined by the temperature dependence of the short-time behaviour of the flipping motion of the phenyl ring are equal.
- The following can be concluded about the length scale of the heterogeneity associated with the flipping motion of the phenyl ring. As the local conformation is different for every phenyl ring, neighbouring phenyl rings are trapped differently and therefore the length scale of this heterogeneity (in the sense of clusters of very mobile ring flips) is restricted to one phenyl ring. The heterogeneity of other motions could act at larger length scales.

- Only based on the energy barrier associated with the phenyl-ring flip one cannot conclude that the experimentally observed γ relaxation in atactic polystyrene should be ascribed to the phenyl-ring flip. From the present MD simulations it follows that also the value of some torsion-energy barriers are approximately equal to the experimentally measured activation energy for what is termed the γ relaxation in the dynamic mechanical analysis of polystyrene.

Stress-strain behaviour of polystyrene, chapter 5

The mechanical behaviour of polymer glasses is still poorly understood. Especially the origin of the yield tooth and strain hardening is unclear. By means of MD simulations of polystyrene the interactions responsible for these phenomena have been identified and analyzed.

- The main difference in energy between a computationally annealed and a quenched polystyrene sample lies in the interchain interactions. During uniaxial extension this difference decreases up to just after the yield tooth. Near the yield tooth more interchain LJ bonds need to be broken for the more aged sample, which causes the higher yield tooth for the aged sample.
- The difference in interchain LJ energy between the two samples of different thermal history does not vanish after yielding, showing that mechanical deformation does not lead to complete erasure of this thermal history. One cause for this effect is that the large-scale structure of the chain (measured by the characteristic ratio) is temperature dependent and this structure is not rejuvenated by up to at least 100% strain.
- The strain-hardening modulus increases with pressure in a way similar to the yield value.
- The stress contribution to the strain-hardening modulus in the simulated polystyrene glass is mainly of intrachain nature.
- In the strain-hardening regime it is observed that only a small portion of the applied work is converted into internal energy. Most of the remaining part is dissipated.

Strain-hardening mechanisms, chapter 6

Although it has been observed that the strain hardening is mainly associated with an increase in dissipation, the reason for this increase is not clear. A comparison of polystyrene and polycarbonate in terms of deviations from affine deformation has been performed to give more insight in this matter.

- For both polymers the rate of non-affine displacement increases in the strain-hardening regime, likely to be the main cause for the increase in the rate of energy dissipation.
- Accompanied with this there is a non-affine chain stretch, occurring at larger scales for larger strains.
- This implies that the main mechanism behind strain hardening observed in polymer glasses is the following. On the scale of the Kuhn length (the stiffness length in case of a worm-like chain) chain parts cannot locally displace affinely, due to the connectivity constraint. Upon straining in the strain-hardening regime there is an increase in the stiffness length of the chain, so that larger segments need to move non-affinely at larger strains, causing an increase in the non-affine displacement rate and hence an increase in the dissipation rate.
- In polystyrene the side groups can move to some extent independently of the backbone. From the simulations it follows that the initial post-yield plasticity of polystyrene (in terms of non-affine displacements) is mainly caused by these side groups. Therefore the effective stiffening of the backbone does not immediately lead to a large increase in plasticity. In polycarbonate the backbone atoms do have a substantial contribution to the plasticity, so that the effective stiffening of the backbone does have a large effect on the stress-strain relation. Related to this is that the effective stiffness length (which equals the Kuhn length in case of a worm-like chain in the long chain limit) increase of PS occurs at too small scales as compared to PC. These effects are likely contributing to the observed difference in strain-hardening modulus between the two polymers.

Outlook

In this section we want to propose research directions for future studies. As can be judged from the conclusions, more insight is gained by means of molecular-dynamics simulations in combination with analytical modelling. The model employed for the study of non-Gaussian displacements is able to describe some features of the non-Gaussian parameter. To describe the width of the peak observed in the non-Gaussian parameter of glassy systems more realistically, one could extend the model by incorporating a fluctuating energy minimum or maximum or both. A fluctuating energy maximum will lead to correlations around the cage escape, and to more sub-diffusive motion, although it will probably be harder to get analytical results. The same description including the extension can also be used to model yielding and thermal-history effects observed in a simple glass.

Most of the correlation functions studied in this thesis are one- or two-point correlations. In order to see more evidence of cooperative motion near the glass transition temperature for the two studied polymers, as predicted by glass-transition theories such as that of

Adam and Gibbs, one could study multiple-point correlation functions. In this way the behaviour of clusters of particles can be measured and one can test theories that describe the glass transition by percolation of immobile domains, or study the yield and flow from the perspective of self-organized criticality [180, 292].

Polystyrene has a relatively high yield peak. From the uniaxial-extension simulations it seems that this is mainly the result of interchain interactions, as the main increase in energy is of interchain nature. A deeper analysis can be carried out by looking which pairwise interchain interactions are mainly responsible; for example, one can test if the energetic contributions from phenyl-phenyl interactions dominate near the yield peak.

Regarding the strain-hardening effect, it is proposed that not entanglements dominate this effect, but that it is mainly caused by chain stretching at a local scale; hence the effective stiffness length increases and therefore more dragging motion occurs. This will lead to an increase in friction and an increase in stress. However, only relatively short chains have been used in this study. Systems of longer chains should be equilibrated (to be checked with the characteristic ratio) and deformed afterwards. Then one can verify if the affine rescaling limit for long chains is visible for these systems. One is then also able to test if the strain-hardening modulus increases due to chain entanglements.

Bibliography

[1] *Science*, 309(5731), 2005. Special 125th anniversary issue.

[2] Y. Abe, A. E. Tonelli, and P. J. Flory. Optical anisotropy of vinyl polymer chains. 1. Strain birefringence of polypropylene and polystyrene. *Macromolecules*, 3(3):294–303, 1970.

[3] G. Adam and J. H. Gibbs. On the temperature dependence of cooperative relaxation properties in glass-forming liquids. *J. Chem. Phys.*, 43:139–146, 1965.

[4] S. M. Aharoni. On entanglements of flexible and rodlike polymers. *Macromolecules*, 16(11):1722–1728, 1983.

[5] M. Aichele, Y. Gebremichael, F. W. Starr, J. Baschnagel, and S. C. Glotzer. Polymer-specific effects of bulk relaxation and stringlike correlated motion in the dynamics of a supercooled polymer melt. *J. Chem. Phys.*, 119:5290–5304, 2003.

[6] M. P. Allen and D. J. Tildesley. *Computer simulation of liquids*. Clarendon Press, Oxford, UK, 1987.

[7] C. A. Angell. Formation of glasses from liquids and biopolymers. *Science*, 267(5206): 1924–1935, 1995.

[8] C. A. Angell. Perspective on the glass-transition. *J. Phys. Chem. Solids*, 49(8): 863–871, 1988.

[9] C. A. Angell. Relaxation in liquids, polymers and plastic crystals - strong/fragile patterns and problems. *J. Non-Crystalline Solids*, 131:13–31, 1991.

[10] C. A. Angell. Why $C_1 = 16$–17 in the WLF equation is physical - and the fragility of polymers. *Polymer*, 38(26):6261–6266, 1997.

[11] A. Arbe, J. Colmenero, F. Alvarez, M. Monkenbusch, D. Richter, B. Farago, and B. Frick. Experimental evidence by neutron scattering of a crossover from Gaussian to non-Gaussian behavior in the alpha relaxation of polyisoprene. *Phys. Rev. E*, 67 (5):051802, 2003.

[12] A. S. Argon, P. H. Mott, and U. W. Suter. Simulation of plastic deformation in a flexible chain glassy polymer. *Phys. Status Solidi B*, 172(1):193–204, 1992.

[13] A. S. Argon, V. V. Bulatov, P. H. Mott, and U. W. Suter. Plastic deformation in glassy polymers by atomistic and mesoscopic simulations. *J. Rheol.*, 39(2):377–399, 1995.

[14] C. Ayyagari, D. Bedrov, and G. D. Smith. Structure of atactic polystyrene: a molecular dynamics simulation study. *Macromolecules*, 33(16):6194–6199, 2000.

[15] N. K. Balabaev. Private communication, 2007.

[16] D. G. H. Ballard, A. N. Burgess, P. Cheshire, E. W. Janke, A. Nevin, and J. Schelten. Small-angle neutron-scattering study of amorphous polycarbonate. *Polymer*, 22(10): 1353–1354, 1981.

[17] U. Balucani and M. Zoppi. *Dynamics of the liquid state.* Oxford series on neutron scattering in condensed matter; 10. Clarendon Press; Oxford University Press, Oxford, New York, 1994.

[18] J. L. Barrat and J. P. Hansen. *Basic concepts for simple and complex liquids.* Cambridge University Press, Cambridge, England, 2003.

[19] J. Baschnagel, K. Binder, P. Doruker, A. A. Gusev, O. Hahn, K. Kremer, W. L. Mattice, F. Muller-Plathe, M. Murat, W. Paul, S. Santos, U. W. Suter, and V. Tries. Bridging the gap between atomistic and coarse-grained models of polymers: status and perspectives. *Adv. Polym. Sci.*, 152:41–156, 2000.

[20] C. L. Beatty and J. L. Weaver. Effect of temperature on compressive stress-strain properties of polystyrene. *Polym. Eng. Sci.*, 18(14):1109–1116, 1978.

[21] C. Bennemann, C. Donati, J. Baschnagel, and S. C. Glotzer. Growing range of correlated motion in a polymer melt on cooling towards the glass transition. *Nature*, 399:246–249, 1999.

[22] H. J. C. Berendsen, J. P. M. Postma, W. F. van Gunsteren, A. Dinola, and J. R. Haak. Molecular dynamics with coupling to an external bath. *J. Chem. Phys.*, 81 (8):3684–3690, 1984.

[23] G. C. Berry, H. Nomura, and K. G. Mayhan. Dilute solution studies on a polycarbonate in good and poor solvents. *J. Polym. Sci.: Polym. Phys.*, 5(1PA2):1–21, 1967.

[24] J. C. Berthet, C. Saelee, T. N. Liang, T. M. Nicholson, and G. R. Davies. Simulation of glassy state relaxations in polymers: a static analysis of methyl group and methoxy group rotation in poly(vinyl methyl ether). *Macromolecules*, 39(23):8186–8192, 2006.

[25] J. Bicerano. A model for dynamic relaxations in amorphous polymers. 2. Extensions and generalizations of formalism and application to poly(methacrylates). *J. Polym. Sci.: Polym. Phys.*, 29(11):1345–1359, 1991.

[26] K. Binder and W. Kob. *Glassy materials and disordered solids - An introduction to their statistical mechanics*. World Scientific, Singapore, 2005.

[27] K. Binder, J. Baschnagel, C. Bennemann, and W. Paul. Monte Carlo and molecular dynamics simulation of the glass transition of polymers. *J. Phys.: Condens. Matter*, 11(10A):A47–A55, 1999.

[28] R. Böhmer and C. A. Angell. Correlations of the nonexponentiality and state dependence of mechanical relaxations with bond connectivity in Ge-As-Se supercooled liquids. *Phys. Rev. B*, 45:10091–10094, 1992.

[29] A. T. Boothroyd, A. R. Rennie, and G. D. Wignall. Temperature coefficients for the chain dimensions of polystyrene and polymethylmethacrylate. *J. Chem. Phys.*, 99 (11):9135–9144, 1993.

[30] J. P. Bouchaud. Weak ergodicity breaking and aging in disordered systems. *J. Phys. I*, 2(9):1705–1713, 1992.

[31] R. K. Bowles and R. J. Speedy. Five discs in a box. *Physica A*, 262(1-2):76–87, 1999.

[32] M. C. Boyce and E. M. Arruda. An experimental and analytical investigation of the large strain compressive and tensile response of glassy polymers. *Polym. Eng. Sci.*, 30(20):1288–1298, 1990.

[33] D. Brown and J. H. R. Clarke. A direct method of studying reaction rates by equilibrium molecular dynamics - application to the kinetics of isomerization in liquid *n*-butane. *J. Chem. Phys.*, 92(5):3062–3073, 1990.

[34] D. Brown and J. H. R. Clarke. Molecular-dynamics simulation of an amorphous polymer under tension. 1. Phenomenology. *Macromolecules*, 24(8):2075–2082, 1991.

[35] H. R. Brown, A. S. Argon, R. E. Cohen, O. S. Gebizlioglu, and E. J. Kramer. New mechanism for craze toughening of glassy-polymers. *Macromolecules*, 22(2):1002–1004, 1989.

[36] W. D. Callister, Jr. *Materials science and engineering: an introduction*. John Wiley & Sons, Inc., New York, USA, fourth edition, 1997.

[37] D. Cangialosi, M. Wübbenhorst, H. Schut, A. van Veen, and S. J. Picken. Amorphous-amorphous transition in glassy polymers subjected to cold rolling studied by means of positron annihilation lifetime spectroscopy. *J. Chem. Phys.*, 122(6): 064702, 2005.

[38] F. M. Capaldi, M. C. Boyce, and G. C. Rutledge. Enhanced mobility accompanies the active deformation of a glassy amorphous polymer. *Phys. Rev. Lett.*, 89(17): 175505, 2002.

[39] F. M. Capaldi, M. C. Boyce, and G. C. Rutledge. Molecular response of a glassy polymer to active deformation. *Polymer*, 45(4):1391–1399, 2004.

[40] I. Carmesin and K. Kremer. The bond fluctuation method - a new effective algorithm for the dynamics of polymers in all spatial dimensions. *Macromolecules*, 21(9):2819–2823, 1988.

[41] R. Casalini and C. M. Roland. Why liquids are fragile. *Phys. Rev. E*, 72(3):031503, 2005.

[42] D. Chandler. *Introduction to modern statistical mechanics*. Oxford University Press, Oxford, Great Britain, 1987.

[43] S. H. Chong and M. Fuchs. Mode-coupling theory for structural and conformational dynamics of polymer melts. *Phys. Rev. Lett.*, 88(18):185702, 2002.

[44] C. Chui and M. C. Boyce. Monte Carlo modeling of amorphous polymer deformation: evolution of stress with strain. *Macromolecules*, 32(11):3795–3808, 1999.

[45] P. Cifra. Differences and limits in estimates of persistence length for semi-flexible macromolecules. *Polymer*, 45(17):5995–6002, 2004.

[46] J. H. R. Clarke and D. Brown. Molecular dynamics modelling of polymer materials. *Mol. Sim.*, 3:27–47, 1989.

[47] J. Colmenero, A. J. Moreno, and A. Alegria. Neutron scattering investigations on methyl group dynamics in polymers. *Prog. Polym. Sci.*, 30(12):1147–1184, 2005.

[48] H. Z. Cummins. The liquid-glass transition: a mode-coupling perspective. *J. Phys.: Condens. Matter*, 11(10A):A95–A117, 1999.

[49] A. A. Darinskii, Y. Y. Gotlib, A. V. Lyulin, L. I. Klushin, and I. M. Neelov. Brownian dynamics of the polymer-chain having rigid side groups. *Vysokomol. Soedin. Ser. A*, 32(11):2289–2295, 1990.

[50] S. P. Das. Mode-coupling theory and the glass transition in supercooled liquids. *Rev. Mod. Phys.*, 76(3):785–851, 2004.

[51] A. De la Rosa, L. Heux, J. Y. Cavaille, and K. Mazeau. Molecular modeling of the mobility of poly(allyl alcohol), PAA, and poly(vinyl alcohol), PVA. *Polymer*, 43(21): 5665–5677, 2002.

[52] P. G. Debenedetti. *Metastable liquids - concepts and principles*. Princeton University Press, Princeton, New Jersey, USA, 1996.

[53] P. G. Debenedetti and F. H. Stillinger. Supercooled liquids and the glass transition. *Nature*, 410(6825):259–267, 2001.

[54] R. C. Desai. Non-Gaussian corrections to van Hove's $G_s(r,t)$ for a monatomic gas. *J. Chem. Phys.*, 44:77–86, 1966.

[55] M. Doi. *Introduction to polymer physics.* Oxford University Press, Oxford, Great Britain, 1995.

[56] M. Doi and S. F. Edwards. *The theory of polymer dynamics.* Clarendon Press, New York, USA, 1986.

[57] B. Doliwa and A. Heuer. Cage effect, local anisotropies, and dynamic heterogeneities at the glass transition: A computer study of hard spheres. *Phys. Rev. Lett.*, 80: 4915–4918, 1998.

[58] B. Doliwa and A. Heuer. The origin of anomalous diffusion and non-Gaussian effects for hard spheres: analysis of three-time correlations. *J. Phys.: Condens. Matter*, 11 (10A):A277–A283, 1999.

[59] A. M. Donald. The effect of temperature on crazing mechanisms in polystyrene. *J. Mater. Sci.*, 20(7):2630–2638, 1985.

[60] A. M. Donald and E. J. Kramer. Deformation zones and entanglements in glassy-polymers. *Polymer*, 23(8):1183–1188, 1982.

[61] A. M. Donald and E. J. Kramer. Effect of molecular entanglements on craze microstructure in glassy-polymers. *J. Polym. Sci.: Polym. Phys.*, 20(5):899–909, 1982.

[62] C. Donati, J. F. Douglas, W. Kob, S. J. Plimpton, P. H. Poole, and S. C. Glotzer. Stringlike cooperative motion in a supercooled liquid. *Phys. Rev. Lett.*, 80(11):2338–2341, 1998.

[63] J. R. Dutcher and A. G. Marangoni. *Soft materials: structure and dynamics.* Marcel Dekker, New York, 2005.

[64] J. C. Dyre. Colloquium: the glass transition and elastic models of glass-forming liquids. *Rev. Mod. Phys.*, 78(3):953–972, 2006.

[65] J. C. Dyre. Master-Equation approach to the glass transition. *Phys. Rev. Lett.*, 58: 792–795, 1987.

[66] T. Eckert and E. Bartsch. Re-entrant glass transition in a colloid-polymer mixture with depletion attractions. *Phys. Rev. Lett.*, 89(12):125701, 2002.

[67] M. D. Ediger. Spatially heterogeneous dynamics in supercooled liquids. *Ann. Rev. Phys. Chem.*, 51:99–128, 2000.

[68] M. D. Ediger, C. A. Angell, and S. R. Nagel. Supercooled liquids and glasses. *J. Phys. Chem.*, 100:13200–13212, 1996.

[69] S. N. Ege. *Organic chemistry: structure and reactivity.* D.C. Heath, Lexington, Mass., 3rd edition, 1994.

[70] T. A. P. Engels, L. E. Govaert, G. W. M. Peters, and H. E. H. Meijer. Processing-induced properties in glassy polymers: application of structural relaxation to yield stress development. *J. Polym. Sci.: Polym. Phys.*, 44(8):1212–1225, 2006.

[71] P. Espanol and P. Warren. Statistical mechanics of dissipative particle dynamics. *Europhys. Lett.*, 30(4):191–196, 1995.

[72] U. Essmann, L. Perera, M. L. Berkowitz, T. Darden, H. Lee, and L. G. Pedersen. A smooth particle mesh Ewald method. *J. Chem. Phys.*, 103(19):8577–8593, 1995.

[73] R. Faller. Correlation of static and dynamic inhomogeneities in polymer mixtures: a computer simulation of polyisoprene and polystyrene. *Macromolecules*, 37(3):1095–1101, 2004.

[74] C. F. Fan. Yielding of a model glassy polycarbonate under tension - a molecular mechanics simulation. *Macromolecules*, 28(15):5215–5224, 1995.

[75] C. F. Fan, T. Cagin, Z. M. Chen, and K. A. Smith. Molecular modeling of polycarbonate. 1. Force-field, static structure, and mechanical-properties. *Macromolecules*, 27(9):2383–2391, 1994.

[76] J. D. Ferry. *Viscoelastic properties of polymers.* Wiley, New York, 3d edition, 1980.

[77] J. D. Ferry, L. D. Grandine, and E. R. Fitzgerald. The temperature dependence of relaxation mechanisms in amorphous polymers and other glass-forming liquids. *J. Appl. Phys.*, 24:911–916, 1953.

[78] L. J. Fetters, D. J. Lohse, D. Richter, T. A. Witten, and A. Zirkel. Connection between polymer molecular-weight, density, chain dimensions, and melt viscoelastic properties. *Macromolecules*, 27(17):4639–4647, 1994.

[79] L. J. Fetters, D. J. Lohse, S. T. Milner, and W. W. Graessley. Packing length influence in linear polymer melts on the entanglement, critical, and reptation molecular weights. *Macromolecules*, 32(20):6847–6851, 1999.

[80] E. Flenner and G. Szamel. Relaxation in a glassy binary mixture: comparison of the mode-coupling theory to a Brownian dynamics simulation. *Phys. Rev. E*, 72(3): 031508, 2005.

[81] P. J. Flory. *Statistical mechanics of chain molecules.* Hanser Publishers, Munich, Germany, 1989.

[82] A. Fortunelli, C. Geloni, and A. Lazzeri. Simulation of the plastic behavior of amorphous glassy bis-phenol-A-polycarbonate. *J. Chem. Phys.*, 121(10):4941–4950, 2004.

[83] D. Frenkel and B. Smit. *Understanding molecular simulation: from algorithms to applications*. Academic Press, San Diego, 2nd edition, 2002.

[84] K. Frobose, F. Kolbe, and J. Jackle. Size dependence of self-diffusion in a dense hard-disc liquid. *J. Phys.: Condens. Matter*, 12(29):6563–6573, 2000.

[85] K. Fuchizaki and K. Kawasaki. Dynamical density functional theory for glassy behaviour. *J. Phys.: Condens. Matter*, 14(46):12203–12222, 2002.

[86] K. Fuchizaki and K. Kawasaki. Dynamical density functional approach to supercooled liquid and glass transition. *Physica A*, 266(1-4):400–412, 1999.

[87] M. Fuchs, W. Götze, and M. R. Mayr. Asymptotic laws for tagged-particle motion in glassy systems. *Phys. Rev. E*, 58:3384–3399, 1998.

[88] H. Furuya, M. Mondello, H. J. Yang, R. J. Roe, R. W. Erwin, C. C. Han, and S. D. Smith. Molecular-dynamics simulation of atactic polystyrene. 2. Comparison with neutron-scattering data. *Macromolecules*, 27(20):5674–5680, 1994.

[89] M. M. Fuson, K. H. Hanser, and M. D. Ediger. Local dynamics of poly(ethylene oxide) in solution. 2. Vector autocorrelation functions and motional anisotropy. *Macromolecules*, 30(19):5714–5720, 1997.

[90] J. Gao and J. H. Weiner. Stress-relaxation in a polymer melt of freely-rotating chains. *J. Chem. Phys.*, 97(11):8698–8704, 1992.

[91] J. Gao and J. H. Weiner. Computer-simulation of viscoelasticity in polymer melts. *Macromolecules*, 25(4):1348–1356, 1992.

[92] J. Gao and J. H. Weiner. Simulated polymer melt stress-relaxation. 1. Plateau behavior. *J. Chem. Phys.*, 103(4):1614–1620, 1995.

[93] J. Gao and J. H. Weiner. Simulated polymer melt stress-relaxation. 2. Search for entanglements. *J. Chem. Phys.*, 103(4):1621–1626, 1995.

[94] J. P. Gao and J. H. Weiner. Bond orientation decay and stress relaxation in a model polymer melt. *Macromolecules*, 29(18):6048–6055, 1996.

[95] W. Gawrisch, M. G. Brereton, and E. W. Fischer. A new method for data evaluation of small-angle neutron-scattering experiments and its application to amorphous polycarbonate. *Polym. Bull.*, 4(12):687–691, 1981.

[96] O. S. Gebizlioglu, H. W. Beckham, A. S. Argon, R. E. Cohen, and H. R. Brown. A new mechanism of toughening glassy polymers. 1. Experimental procedures. *Macromolecules*, 23(17):3968–3974, 1990.

[97] U. W. Gedde. *Polymer physics.* Chapman & Hall, New York, 1995.

[98] B. R. Gelin and M. Karplus. Side-chain torsional potentials - effect of dipeptide, protein, and solvent environment. *Biochemistry*, 18(7):1256–1268, 1979.

[99] Goldstein. Viscous liquids and glass transition - a potential energy barrier picture. *J. Chem. Phys.*, 51(9):3728–3739, 1969.

[100] W. Götze. Aspects of structural glass transitions. In J. P. Hansen, D. Levesque, and J. Zinn-Justin, editors, *Liquides, cristallisation et transition vitreuse = Liquids, freezing and glass transition: Les Houches, session LI, 3-28 juillet 1989*, Amsterdam; New York, USA, 1991. North Holland; Sole distributors for the U.S.A. and Canada, Elsevier Science Pub. Co.

[101] W. Götze and L. Sjögren. Relaxation processes in supercooled liquids. *Rep. Prog. Phys.*, 52:241–376, 1992.

[102] L. E. Govaert and T. A. Tervoort. Strain hardening of polycarbonate in the glassy state: influence of temperature and molecular weight. *J. Polym. Sci.: Polym. Phys.*, 42(11):2041–2049, 2004.

[103] L. E. Govaert, H. G. H. van Melick, and H. E. H. Meijer. Temporary toughening of polystyrene through mechanical pre-conditioning. *Polymer*, 42(3):1271–1274, 2001.

[104] S. N. Goyanes. Dynamic mechanical behavior of atactic and high-impact polystyrene. *J. Appl. Polym. Sci.*, 75(7):865–873, 2000.

[105] A. L. Greer. Metallic glasses. *Science*, 267(5206):1947–1953, 1995.

[106] W. Grellmann and R. Lach. Toughness and relaxation behaviour of poly(methyl methacrylate), polystyrene, and polycarbonate. *Angew. Makromolek. Chemie*, 253: 27–49, 1997.

[107] P. C. Hagele and L. Beck. Calculation of phenyl group rotation in polystyrene by means of semiempirical potentials. *Macromolecules*, 10(1):213–215, 1977.

[108] J. M. Haile. *Molecular dynamics simulation: elementary methods.* Wiley, New York, 1992.

[109] J. Han and R. H. Boyd. Molecular packing and small-penetrant diffusion in polystyrene: a molecular dynamics simulation study. *Polymer*, 37:1797–1804, 1996.

[110] J. P. Hansen and I. R. McDonald. *Theory of simple liquids.* Acedemic Press, London, England, second edition, 1986.

[111] V. A. Harmandaris, N. P. Adhikari, N. F. A. van der Vegt, and K. Kremer. Hierarchical modeling of polystyrene: From atomistic to coarse-grained simulations. *Macromolecules*, 39(19):6708–6719, 2006.

[112] O. A. Hasan and M. C. Boyce. Energy-storage during inelastic deformation of glassy-polymers. *Polymer*, 34(24):5085–5092, 1993.

[113] R. N. Haward. The application of a simplified model for the stress-strain curves of polymers. *Polymer*, 28(9):1485–1488, 1987.

[114] R. N. Haward. Strain hardening of thermoplastics. *Macromolecules*, 26(22):5860–5869, 1993.

[115] R. N. Haward. The derivation of a strain-hardening modulus from true stress-strain curves for thermoplastics. *Polymer*, 35(18):3858–3862, 1994.

[116] R. N. Haward. Heating effects in the deformation of thermoplastics. *Thermochim. Acta*, 247(1):87–109, 1994.

[117] R. N. Haward and R. J. Young. *The physics of glassy polymers.* Chapman & Hall, London, second edition, 1997.

[118] Y. Y. He, T. R. Lutz, M. D. Ediger, C. Ayyagari, D. Bedrov, and G. D. Smith. NMR experiments and molecular dynamics simulations of the segmental dynamics of polystyrene. *Macromolecules*, 37(13):5032–5039, 2004.

[119] E. Helfand, Z. R. Wasserman, T. A. Weber, J. Skolnick, and J. H. Runnels. The kinetics of conformational transitions - effect of variation of bond angle bending and bond stretching force constants. *J. Chem. Phys.*, 75(9):4441–4445, 1981.

[120] P. J. Hoogerbrugge and J. M. V. A. Koelman. Simulating microscopic hydrodynamic phenomena with dissipative particle dynamics. *Europhys. Lett.*, 19(3):155–160, 1992.

[121] J. Horbach, W. Kob, and K. Binder. Molecular dynamics simulation of the dynamics of supercooled silica. *Philos. Mag. B*, 77:297–303, 1998.

[122] R. S. Hoy and M. O. Robbins. Effect of equilibration on primitive path analyses of entangled polymers. *Phys. Rev. E*, 72(6):061802, 2005.

[123] R. S. Hoy and M. O. Robbins. Strain hardening of polymer glasses: effect of entanglement density, temperature, and rate. *J. Polym. Sci.: Polym. Phys.*, 44(24):3487–3500, 2006.

[124] R. S. Hoy and M. O. Robbins. Strain hardening in polymer glasses: limitations of network models. *Phys. Rev. Lett.*, 99(11):117801, 2007.

[125] R. S. Hoy and M. O. Robbins. Strain hardening of polymer glasses: entanglements, energetics, and plasticity. *Phys. Rev. E*, 2008. accepted.

[126] B. D. Hughes. *Random walks and random environments.* Clarendon Press; Oxford University Press, Oxford New York, 1995.

[127] M. M. Hurley and P. Harrowell. Non-Gaussian behavior and the dynamical complexity of particle motion in a dense two-dimensional liquid. *J. Chem. Phys.*, 105: 10521–10526, 1996.

[128] M. Hutnik, A. S. Argon, and U. W. Suter. Conformational characteristics of the polycarbonate of 4,4'-isopropylidenediphenol. *Macromolecules*, 24(22):5956–5961, 1991.

[129] M. Hutnik, A. S. Argon, and U. W. Suter. Quasi-static modeling of chain dynamics in the amorphous glassy polycarbonate of 4,4'-isopropylidenediphenol. *Macromolecules*, 24(22):5970–5979, 1991.

[130] M. Hutnik, A. S. Argon, and U. W. Suter. Simulation of elastic and plastic response in the glassy polycarbonate of 4,4'-isopropylidenediphenol. *Macromolecules*, 26(5): 1097–1108, 1993.

[131] B. A. Isner and D. J. Lacks. Generic rugged landscapes under strain and the possibility of rejuvenation in glasses. *Phys. Rev. Lett.*, 96(2):025506, 2006.

[132] S. Itoh, Y. Hiwatari, and H. Miyagawa. Dynamic singularity of the glass-transition in molten lithium iodide. *J. Non-Crystalline Solids*, 156:559–563, 1993.

[133] J. Jackle and S. Eisinger. A hierarchically constrained kinetic Ising model. *Z. Phys. B Con. Mat.*, 84(1):115–124, 1991.

[134] S. S. Jang and W. H. Jo. Yielding and plastic behaviour of amorphous atactic poly(oxypropylene) under uniaxial compression: an atomistic modeling approach. *Polymer*, 40(4):919–925, 1999.

[135] C. Janot. *Quasicrystals – a primer.* Clarendon Press, Oxford, UK, second edition, 1994.

[136] W. Z. Jin and R. H. Boyd. Time evolution of dynamic heterogeneity in a polymeric glass: a molecular dynamics simulation study. *Polymer*, 43(2):503–507, 2002.

[137] Y. Jin and R. H. Boyd. Subglass chain dynamics and relaxation in polyethylene: a molecular dynamics simulation study. *J. Chem. Phys.*, 108(23):9912–9923, 1998.

[138] L. F. Johnson, F. Heatley, and F. A. Bovey. Polymer nuclear magnetic resonance spectroscopy. 19. Carbon-13 resonance observations of stereochemical configuration. *Macromolecules*, 3(2):175–177, 1970.

[139] B. Jung and B. L. Schurmann. Calculation of the persistence length of some polyesters on the basis of computer-simulations. *Makromol. Chem-Rapid Comm.*, 10(8):419–425, 1989.

[140] T. Kanaya and K. Kaji. Dynamics in the glassy state and near the glass transition of amorphous polymers as studied by neutron scattering. *Adv. Polym. Sci.*, 154:87–141, 2001.

[141] K. Karatasos. Static and dynamic behavior in model dendrimer melts: toward the glass transition. *Macromolecules*, 38(10):4472–4483, 2005.

[142] K. Karatasos, J. P. Ryckaert, R. Ricciardi, and F. Laupretre. Methyl dynamics and beta-relaxation in polyisobutylene: comparison between experiment and molecular dynamics simulations. *Macromolecules*, 35(4):1451–1462, 2002.

[143] C. Kaur and S. P. Das. Dynamic heterogeneities in a simple liquid over different time scales. *Phys. Rev. Lett.*, 89:085701, 2002.

[144] R. Khare and M. E. Paulaitis. Molecular simulations of cooperative ring flip motions in single chains of polystyrene. *Chem. Eng. Sci.*, 49(17):2867–2879, 1994.

[145] R. Khare and M. E. Paulaitis. A study of cooperative phenyl ring flip motions in glassy polystyrene by molecular simulations. *Macromolecules*, 28(13):4495–4504, 1995.

[146] K. Kim and T. Munakata. Glass transition of hard sphere systems: molecular dynamics and density functional theory. *Phys. Rev. E*, 68(2):021502, 2003.

[147] E. T. J. Klompen and L. E. Govaert. Nonlinear viscoelastic behaviour of thermorheologically complex materials. *Mech. Time-dep. Mater.*, 3(1):49–69, 99.

[148] E. T. J. Klompen, T. A. P. Engels, L. C. A. van Breemen, P. J. G. Schreurs, L. E. Govaert, and H. E. H. Meijer. Quantitative prediction of long-term failure of polycarbonate. *Macromolecules*, 38(16):7009–7017, 2005.

[149] M. Kluge and H. R. Schober. Diffusion and jump-length distribution in liquid and amorphous $Cu_{33}Zr_{67}$. *Phys. Rev. B*, 70(22):224209, 2004.

[150] W. Kob. Computer simulations of supercooled liquids and glasses. *J. Phys.: Condens. Matter*, 11(10):R85–R115, 1999.

[151] W. Kob and H. C. Andersen. Testing mode-coupling theory for a supercooled binary Lennard-Jones mixture - the Van Hove correlation function. *Phys. Rev. E*, 51(5): 4626–4641, 1995.

[152] F. Kolbe. *Molekulardynamische Studien der Teilchendiffusion in dichten binären Mischungen harter Scheiben.* PhD thesis, Universität Konstanz – Fakultät für Physik, Konstanz, Germany, 1998. `www.uni-konstanz.de/FuF/Physik/Jaeckle/papers/diploma-thesis-kolbe/`.

[153] M. Kotelyanskii, N. J. Wagner, and M. E. Paulaitis. Building large amorphous polymer structures: atomistic simulation of glassy polystyrene. *Macromolecules*, 29 (26):8497–8506, 1996.

[154] A. J. Kovacs, J. J. Aklonis, J. M. Hutchinson, and A. R. Ramos. Isobaric volume and enthalpy recovery of glasses. II. A transparent multiparameter theory. *J. Polym. Sci.: Polym. Phys.*, 17(7):1097–1162, 1979.

[155] E. J. Kramer. Open questions in the physics of deformation of polymer glasses. *J. Polym. Sci.: Polym. Phys.*, 43(23):3369–3371, 2005.

[156] A. S. Krausz and H. Eyring. *Deformation kinetics.* Wiley, New York, 1975.

[157] R. Kubo, N. Hashitsume, and M. Toda. *Statistical physics II: nonequilibrium statistical mechanics.* Springer series in solid-state sciences; 31. Springer, Berlin; London, 2nd edition, 1995.

[158] N. Kuwahara, S. Saeki, S. Konno, and M. Kaneko. Temperature-dependence of polymer-chain dimensions in polystyrene-cyclopentane system. *Polymer*, 15(2):66–68, 1974.

[159] R. Lach, W. Grellmann, K. Schroter, and E. Donth. Temperature dependence of dynamic yield stress in amorphous polymers as indicator for the dynamic glass transition at negative pressure. *Polymer*, 40(6):1481–1485, 1999.

[160] R. Lach, L. A. Gyurova, and W. Grellmann. Application of indentation fracture mechanics approach for determination of fracture toughness of brittle polymer systems. *Polymer Testing*, 26(1):51–59, 2007.

[161] L. D. Landau and E. M. Lifshitz. *Theory of elasticity.* Pergamon, Oxford, 3rd. English edition, 1986.

[162] B. C. Laskowski, D. Y. Yoon, D. Mclean, and R. L. Jaffe. Chain conformations of polycarbonate from abinitio calculations. *Macromolecules*, 21(6):1629–1633, 1988.

[163] S. Lee, H. Y. Jeong, and H. Lee. Conformational properties of the bisphenol-A polycarbonate using the RMMC method. *Comput. Theoret. Polym. Sci.*, 11(3):219–226, 2001.

[164] J. Lemaitre and J.-L. Chaboche. *Mechanics of solid materials.* Cambridge University Press, Cambridge, 1990.

[165] A. S. Lemak and N. K. Balabaev. Molecular dynamics simulation of a polymer chain in solution by collisional dynamics method. *J. Comput. Chem.*, 17(15):1685–1695, 1996.

[166] S. Leon, N. van der Vegt, L. Delle Site, and K. Kremer. Bisphenol A polycarbonate: entanglement analysis from coarse-grained MD simulations. *Macromolecules*, 38(19): 8078–8092, 2005.

[167] L. J. Lewis and G. Wahnstrom. Molecular-dynamics study of supercooled ortho-terphenyl. *Phys. Rev. E*, 50(5):3865–3877, 1994.

[168] J. Li, T. Mulder, B. Vorselaars, A. V. Lyulin, and M. A. J. Michels. Monte Carlo simulation of uniaxial tension of an amorphous polyethylene-like polymer glass. *Macromolecules*, 39(22):7774–7782, 2006.

[169] C. P. Lindsey and G. D. Patterson. Detailed comparison of the Williams-Watts and Cole-Davidson functions. *J. Chem. Phys.*, 73(7):3348–3357, 1980.

[170] D. Long and F. Lequeux. Heterogeneous dynamics at the glass transition in Van der Waals liquids, in the bulk and in thin films. *Eur. Phys. J. E*, 4:371–387, 2001.

[171] A. V. Lyulin and M. A. J. Michels. Molecular dynamics simulation of bulk atactic polystyrene in the vicinity of T_g. *Macromolecules*, 35(4):1463–1472, 2002.

[172] A. V. Lyulin and M. A. J. Michels. Simulation of polymer glasses: from segmental dynamics to bulk mechanics. *J. Non-Crystalline Solids*, 352(42-49):5008–5012, 2006.

[173] A. V. Lyulin and M. A. J. Michels. Time scales and mechanisms of relaxation in the energy landscape of polymer glass under deformation: direct atomistic modeling. *Phys. Rev. Lett.*, 99(8):085504, 2007.

[174] A. V. Lyulin, N. K. Balabaev, and M. A. J. Michels. Correlated segmental dynamics in amorphous atactic polystyrene: a molecular dynamics simulation study. *Macromolecules*, 35:9595–9604, 2002.

[175] A. V. Lyulin, N. K. Balabaev, and M. A. J. Michels. Molecular-weight and cooling-rate dependence of simulated T_g for amorphous polystyrene. *Macromolecules*, 36: 8574–8575, 2003.

[176] A. V. Lyulin, N. K. Balabaev, M. A. Mazo, and M. A. J. Michels. Molecular dynamics simulation of uniaxial deformation of glassy amorphous atactic polystyrene. *Macromolecules*, 37(23):8785–8793, 2004.

[177] A. V. Lyulin, B. Vorselaars, M. A. Mazo, N. K. Balabaev, and M. A. J. Michels. Strain softening and hardening of amorphous polymers: atomistic simulation of bulk mechanics and local dynamics. *Europhys. Lett.*, 71(4):618–624, 2005.

[178] W. J. Ma and S. K. Lai. Dynamics of supercooled Lennard-Jones system. *Physica B*, 233:221–229, 1997.

[179] C. W. Macosko. *Rheology: principles, measurements, and applications.* Advances in interfacial engineering series. VCH, New York, 1994.

[180] I. Malakhovski. *Pattern formation and fracture in brittle and polymer-like failure of disordered materials.* PhD thesis, Eindhoven, University of Technology, Eindhoven, The Netherlands, 2007.

[181] J. E. Mark, editor. *Polymer data handbook.* Oxford University Press, Inc., Oxford, 1999.

[182] T. G. Mason and D. A. Weitz. Optical measurements of frequency-dependent linear viscoelastic moduli of complex fluids. *Phys. Rev. Lett.*, 74(7):1250–1253, 1995.

[183] M. A. Mazo. Private communication, 2006.

[184] J. I. McKechnie, R. N. Haward, D. Brown, and J. H. R. Clarke. Effects of chain configurational properties on the stress-strain behavior of glassy linear-polymers. *Macromolecules*, 26(1):198–202, 1993.

[185] O. Mishima and H. E. Stanley. The relationship between liquid, supercooled and glassy water. *Nature*, 396:329–335, 1998.

[186] G. R. Mitchell and A. H. Windle. Structure of polystyrene glasses. *Polymer*, 25(7): 906–920, 1984.

[187] M. Mondello, H. J. Yang, H. Furuya, and R. J. Roe. Molecular-dynamics simulation of atactic polystyrene. 1. Comparison with X-ray-scattering data. *Macromolecules*, 27(13):3566–3574, 1994.

[188] B. Movaghar and W. Schirmacher. On the theory of hopping conductivity in disordered systems. *J. Phys. C: Solid State Phys.*, 14:859–880, 1981.

[189] C. T. Moynihan, P. B. Macedo, C. J. Montrose, P. K. Gupta, M. A. Debolt, J. F. Dill, B. E. Dom, P. W. Drake, A. J. Easteal, P. B. Elterman, R. P. Moeller, H. Sasabe, and J. A. Wilder. Structural relaxation in vitreous materials. *Ann. N.Y. Acad. Sci.*, 279(OCT15):15–35, 1976.

[190] T. Mulder. *Equilibration and deformation of glass-forming polymers: molecular simulation via connectivity-altering Monte Carlo and scale-jumping methods.* PhD thesis, Eindhoven, University of Technology, Eindhoven, The Netherlands, 2008.

[191] T. Mulder, J. Li, A. V. Lyulin, and M. A. J. Michels. Monte Carlo simulation of uniaxial deformation of polyethylene-like polymer glass: role of constraints and deformation protocol. *Macromol. Theor. Simul.*, 16(4):348–358, 2007.

[192] A. D. Mulliken and M. C. Boyce. Mechanics of the rate-dependent elastic-plastic deformation of glassy polymers from low to high strain rates. *Int. J. Solids Structures*, 43(5):1331–1356, 2006.

[193] O. S. Narayanaswamy. Model of structural relaxation in glass. *J. Am. Ceram. Soc.*, 54(10):491–498, 1971.

[194] T. M. Nicholson and G. R. Davies. Modeling of methyl group rotations in PMMA. *Macromolecules*, 30(18):5501–5505, 1997.

[195] S. Nosé and F. Yonezawa. Isobaric-isothermal molecular dynamics study on the glass transition of a Lennard-Jones system. *Solid State Commun.*, 56:1005–1008, 1985.

[196] V. N. Novikov and A. P. Sokolov. Poisson's ratio and the fragility of glass-forming liquids. *Nature*, 431(7011):961–963, 2004.

[197] M. R. Nyden, T. R. Coley, and S. Mumby. Applications of molecular dynamics to the study of thermal degradation in aromatic polymers. 1. Polystyrene. *Polym. Eng. Sci.*, 37:1496–1500, 1997.

[198] T. Odagaki and Y. Hiwatari. Gaussian-to-non-Gaussian transition in supercooled fluids. *Phys. Rev. A*, 43(2):1103–1106, 1991.

[199] E. F. Oleinik, S. N. Rudnev, O. B. Salamatina, S. V. Shenogin, M. I. Kotelyanskii, T. V. Paramzina, and S. I. Nazarenko. Energy storage in cold non-elastic deformation of glassy polymers. *E-Polymers*, art. 29, 2006.

[200] P. V. K. Pant and D. N. Theodorou. Variable connectivity method for the atomistic monte-carlo simulation of polydisperse polymer melts. *Macromolecules*, 28(21):7224–7234, 1995.

[201] K. N. Pham, A. M. Puertas, J. Bergenholtz, S. U. Egelhaaf, A. Moussaid, P. N. Pusey, A. B. Schofield, M. E. Cates, M. Fuchs, and W. C. K. Poon. Multiple glassy states in a simple model system. *Science*, 296(5565):104–106, 2002.

[202] D. J. Plazek, E. Riande, H. Markovitz, and N. Raghupathi. Concentration-dependence of the viscoelastic properties of polystyrene-tricresyl phosphate solutions. *J. Polym. Sci.: Polym. Phys.*, 17(12):2189–2213, 1979.

[203] R. Quinson, J. Perez, M. Rink, and A. Pavan. Components of non-elastic deformation in amorphous glassy polymers. *J. Mater. Sci.*, 31(16):4387–4394, 1996.

[204] R. Quinson, J. Perez, M. Rink, and A. Pavan. Yield criteria for amorphous glassy polymers. *J. Mater. Sci.*, 32(5):1371–1379, 1997.

[205] A. L. Rabinovich, P. O. Ripatti, N. K. Balabaev, and F. A. M. Leermakers. Molecular dynamics simulations of hydrated unsaturated lipid bilayers in the liquid-crystal phase and comparison to self-consistent field modeling. *Phys. Rev. E*, 67(1):011909, 2003.

[206] A.-R. A. F. Ragab and S. E. A. Bayoumi. *Engineering solid mechanics: fundamentals and applications.* CRC Press, Boca Raton, Fl., 1999.

[207] A. Rahman. Correlations in the motion of atoms in liquid Argon. *Phys. Rev.*, 136: A405–A411, 1964.

[208] D. C. Rapaport. *The art of molecular dynamics simulation.* Cambridge University Press, Cambridge, UK, 2nd edition, 2004.

[209] R. F. Rapold and U. W. Suter. Conformational characteristics of polystyrene. *Macromol. Theor. Simul.*, 3(1):1–17, 1994.

[210] R. F. Rapold, U. W. Suter, and D. N. Theodorou. Static atomistic modeling of the structure and ring dynamics of bulk amorphous polystyrene. *Macromol. Theor. Simul.*, 3(1):19–43, 1994.

[211] S. Reich and A. Eisenber. Theoretical approach to assignment of molecular mechanisms for cryogenic loss peaks in polymers. *J. Polym. Sci.: Polym. Phys.*, 10(7): 1397–1400, 1972.

[212] D. R. Reichman and P. Charbonneau. Mode-coupling theory. *J. Stat. Mech. - Theory Exp.*, art. 05013, 2005.

[213] M. Reiner. The Deborah number. *Physics Today*, 17:62, 1964.

[214] P. M. Richards. Theory of one-dimensional hopping conductivity and diffusion. *Phys. Rev. B*, 16(4):1393–1409, 1977.

[215] R. Richert. Heterogeneous dynamics in liquids: fluctuations in space and time. *J. Phys.: Condens. Matter*, 14(23):R703–R738, 2002.

[216] M. D. Rintoul and S. Torquato. Metastability and crystallization in hard-sphere systems. *Phys. Rev. Lett.*, 77:4198–4201, 1996.

[217] H. Risken. *The Fokker-Planck equation – Methods of solution and applications.* Springer-Verlag, Berlin, Germany, second edition, 1989.

[218] F. Ritort and P. Sollich. Glassy dynamics of kinetically constrained models. *Acedemic Press*, 52(4):219–342, 2003.

[219] P. Robyr, Z. Gan, and U. W. Suter. Conformation of racemo and meso dyads in glassy polystyrenes from ^{13}C polarization-transfer NMR. *Macromolecules*, 31(25): 8918–8923, 1998.

[220] P. Robyr, M. Müller, and U. W. Suter. Atomistic simulations of glassy polystyrenes with realistic chain conformations. *Macromolecules*, 32(25):8681–8684, 1999.

[221] R. J. Roe. Short time dynamics of polymer liquids and glass studied by molecular dynamics simulation. *J. Chem. Phys.*, 100:1610–1619, 1994.

[222] R. J. Roe. Molecular dynamics simulation study of short time dynamics in polystyrene. *J. Non-Crystalline Solids*, 235–237:308–313, 1998.

[223] R. J. Roe, M. Mondello, H. Furuya, and H. J. Yang. Molecular-dynamics simulation of atactic polystyrene. 3. Short-range order. *Macromolecules*, 28(8):2807–2818, 1995.

[224] C. M. Roland and R. Casalini. Temperature dependence of local segmental motion in polystyrene and its variation with molecular weight. *J. Chem. Phys.*, 119(3): 1838–1842, 2003.

[225] C. M. Roland, S. Hensel-Bielowka, M. Paluch, and R. Casalini. Supercooled dynamics of glass-forming liquids and polymers under hydrostatic pressure. *Rep. Prog. Phys.*, 68(6):1405–1478, 2005.

[226] J. Rottler and M. O. Robbins. Yield conditions for deformation of amorphous polymer glasses. *Phys. Rev. E*, 64(5):051801, 2001.

[227] J. Rottler and M. O. Robbins. Shear yielding of amorphous glassy solids: effect of temperature and strain rate. *Phys. Rev. E*, 68(1):011507, 2003.

[228] J. Rottler and M. O. Robbins. Unified description of aging and rate effects in yield of glassy solids. *Phys. Rev. Lett.*, 95(22):225504, 2005.

[229] J. Rottler and M. O. Robbins. Macroscopic friction laws and shear yielding of glassy solids. *Comput. Phys. Commun.*, 169(1-3):177–182, 2005.

[230] C. Saelee, T. M. Nicholson, and G. R. Davies. A molecular dynamics study of methyl group rotation in poly(vinyl methyl ether). *Macromolecules*, 33(6):2258–2265, 2000.

[231] O. B. Salamatina, S. I. Nazarenko, S. N. Rudnev, and E. F. Oleinik. Heat-effects and the mechanism of inelastic deformation of organic glassy-polymers. *Mech. Compos. Mater.*, 24(6):721–725, 1988.

[232] P. G. Santangelo and C. M. Roland. Molecular weight dependence of fragility in polystyrene. *Macromolecules*, 31(14):4581–4585, 1998.

[233] S. S. Sarva, S. Deschanel, M. C. Boyce, and W. N. Chen. Stress-strain behavior of a polyurea and a polyurethane from low to high strain rates. *Polymer*, 48(8): 2208–2213, 2007.

[234] L. Schafer and K. Elsner. Calculation of the persistence length of a flexible polymer chain with short-range self-repulsion. *Eur. Phys. J. E*, 13(3):225–237, 2004.

[235] F. Sciortino. One liquid, two glasses. *Nature Materials*, 1:145–146, 2002.

[236] F. Sciortino, P. Gallo, P. Tartaglia, and S. H. Chen. Supercooled water and the kinetic glass transition. *Phys. Rev. E*, 54(6):6331–6343, 1996.

[237] S. Shenogin and R. Ozisik. Deformation of glassy polycarbonate and polystyrene: the influence of chemical structure and local environment. *Polymer*, 46(12):4397–4404, 2005.

[238] S. V. Shenogin, G. W. H. Hohne, and E. F. Oleinik. Thermodynamics of the pre-yield deformation behavior of glassy polymers: measurements with new deformation calorimeter. *Thermochim. Acta*, 391(1-2):13–23, 2002.

[239] H. Sillescu. Heterogeneity at the glass transition: a review. *J. Non-Crystalline Solids*, 243(2-3):81–108, 1999.

[240] S. D. Sjoerdsma and D. Heikens. A model for the stress-strain behaviour of toughened polystyrene. *J. Materials Science*, 17:747–752, 1982.

[241] G. D. Smith, D. Bedrov, and W. Paul. A molecular dynamics simulation study of the alpha-relaxation in a 1,4-polybutadiene melt as probed by the coherent dynamic structure factor. *J. Chem. Phys.*, 121(10):4961–4967, 2004.

[242] P. Sotta and D. Long. The crossover from 2D to 3D percolation: theory and numerical simulations. *Eur. Phys. J. E*, 11:375–388, 2003.

[243] R. J. Speedy. 2 disks in a box. *Physica A*, 210(3-4):341–351, 1994.

[244] H. W. Spiess. Molecular-dynamics of solid polymers as revealed by deuteron NMR. *Colloid Polym. Sci.*, 261(3):193–209, 1983.

[245] F. H. Stillinger. A topographic view of supercooled liquids and glass-formation. *Science*, 267(5206):1935–1939, 1995.

[246] F. H. Stillinger and T. A. Weber. Hidden structure in liquids. *Phys. Rev. A*, 25(2): 978–989, 1982.

[247] G. R. Strobl. *The physics of polymers: concepts for understanding their structures and behavior.* Springer, Berlin ; New York, 2nd corr. edition, 1997.

[248] L. C. E. Struik. *Physical aging in amorphous polymers and other materials.* Elsevier, Amsterdam, the Netherlands, second edition, 1980.

[249] Q. Sun and R. Faller. Crossover from unentangled to entangled dynamics in a systematically coarse-grained polystyrene melt. *Macromolecules*, 39(2):812–820, 2006.

[250] P. R. Sundararajan. Possible helical shapes of the polycarbonate chain and their influence on the unperturbed dimensions. *Macromolecules*, 20(7):1534–1539, 1987.

[251] G. Sutmann. Classical molecular dynamics. In J. Grotendorst, D. Marx, and A. Muramatsu, editors, *Quantum simulations of complex many-body systems: from theory to algorithms*, volume 10, pages 211–254, Jülich, Germany, 2002. John von Neumann Institute for Computing.

[252] Y. Tanabe. Phenyl-group rotation in polystyrene. *J. Polym. Sci.: Polym. Phys.*, 23 (3):601–606, 1985.

[253] A. Tanguy, F. Leonforte, and J. L. Barrat. Plastic response of a 2D Lennard-Jones amorphous solid: detailed analysis of the local rearrangements at very slow strain rate. *Eur. Phys. J. E*, 20(3):355–364, 2006.

[254] T. A. Tervoort and L. E. Govaert. Strain-hardening behavior of polycarbonate in the glassy state. *J. Rheol.*, 44(6):1263–1277, 2000.

[255] D. N. Theodorou, T. D. Boone, L. R. Dodd, and K. F. Mansfield. Stress tensor in model polymer systems with periodic boundaries. *Makromol. Chem.-Theor.*, 2(2): 191–238, 1993.

[256] M. Tomaselli, M. M. Zehnder, P. Robyr, C. Grob-Pisano, R. R. Ernst, and U. W. Suter. Local conformations in the glassy polycarbonate of 2,2-bis(4-hydroxyphenyl)propane (bisphenol-A). *Macromolecules*, 30(12):3579–3583, 1997.

[257] A. E. Tonelli. Phenyl group rotation in polystyrene. *Macromolecules*, 6(5):682–683, 1973.

[258] A. Q. Tool. Relation between inelastic deformability and thermal expansion of glass in its annealing range. *J. Am. Ceram. Soc.*, 29(9):240–253, 1946.

[259] L. R. G. Treloar. *The physics of rubber elasticity.* Clarendon Press; Oxford University Press, Oxford New York, 3rd edition, 2005.

[260] L. R. G. Treloar. *Introduction to polymer science.* The Wykeham science series for schools and universities; 9. Wykeham Publications; Springer-Verlag, London, New York, 1970.

[261] M. Utz, P. G. Debenedetti, and F. H. Stillinger. Atomistic simulation of aging and rejuvenation in glasses. *Phys. Rev. Lett.*, 84(7):1471–1474, 2000.

[262] L. Van Hove. Correlations in space and time and Born approximation scattering in systems of interacting particles. *Phys. Rev.*, 95:249–262, 1954.

[263] N. G. van Kampen. *Stochastic processes in physics and chemistry.* North-Holland, Amsterdam, 1981.

[264] W. van Ketel, C. Das, and D. Frenkel. Structural arrest in an ideal gas. *Phys. Rev. Lett.*, 94(13):135703, 2005.

[265] D. W. van Krevelen. *Properties of polymers - their correlation with chemical structure; their numerical estimation and prediction from additive group contributions.* Elsevier Science B.V., Amsterdam, The Netherlands, third edition, 1997.

[266] H. G. H. van Melick, L. E. Govaert, and H. E. H. Meijer. On the origin of strain hardening in glassy polymers. *Polymer*, 44(8):2493–2502, 2003.

[267] H. G. H. van Melick, L. E. Govaert, and H. E. H. Meijer. Localisation phenomena in glassy polymers: influence of thermal and mechanical history. *Polymer*, 44(12): 3579–3591, 2003.

[268] H. G. H. van Melick, L. E. Govaert, B. Raas, W. J. Nauta, and H. E. H. Meijer. Kinetics of ageing and re-embrittlement of mechanically rejuvenated polystyrene. *Polymer*, 44(4):1171–1179, 2003.

[269] M. P. J. van Staveren, H. B. Brom, and L. J. de Jongh. Metal-cluster compounds and universal features of the hopping conductivity of solids. *Phys. Rep.*, 208(1):1–96, 1991.

[270] A. van Zon and S. W. de Leeuw. Self-motion in glass-forming polymers: a molecular dynamics study. *Phys. Rev. E*, 60(6):6942–6950, 1999.

[271] B. Vorselaars, A. V. Lyulin, and M. A. J. Michels. Development of heterogeneity near the glass transition: Phenyl-ring-flip motions in polystyrene. *Macromolecules*, 40(16):6001–6011, 2007.

[272] S. Vyazovkin and I. Dranca. A DSC study of alpha and beta-relaxations in a PS-clay system. *J. Phys. Chem. B*, 108(32):11981–11987, 2004.

[273] D. J. Wales. *Energy landscapes.* Cambridge University Press, Cambridge, UK, 2003.

[274] M. L. Wallace and B. Joos. Shear-induced overaging in a polymer glass. *Phys. Rev. Lett.*, 96(2):025501, 2006.

[275] I. M. Ward and J. Sweeney. *An introduction to the mechanical properties of solid polymers.* John Wiley & Sons Ltd, West Sussex, England, second edition, 2004.

[276] E. R. Weeks and D. A. Weitz. Properties of cage rearrangements observed near the colloidal glass transition. *Phys. Rev. Lett.*, 89(9):095704, 2002.

[277] M. Wehrle, G. P. Hellmann, and H. W. Spiess. Phenylene motion in polycarbonate and polycarbonate/additive mixtures. *Colloid Polym. Sci.*, 265(9):815–822, 1987.

[278] S. J. Weiner, P. A. Kollman, D. A. Case, U. C. Singh, C. Ghio, G. Alagona, S. Profeta, and P. Weiner. A new force-field for molecular mechanical simulation of nucleic-acids and proteins. *J. Am. Chem. Soc.*, 106(3):765–784, 1984.

[279] M. Wendlandt, T. A. Tervoort, and U. W. Suter. Non-linear, rate-dependent strain-hardening behavior of polymer glasses. *Polymer*, 46(25):11786–11797, 2005.

[280] A. D. Williams and P. J. Flory. Analysis of random configuration of polycarbonate of diphenylol-2,2'-propane. *J. Polym. Sci.: Polym. Phys.*, 6(12PA):1945–1952, 1968.

[281] A. D. Williams and P. J. Flory. Stereochemical equilibrium and configurational statistics in polystyrene and its oligomers. *J. Am. Chem. Soc.*, 91(12):3111–3118, 1969.

[282] T. Witten and P. A. Pincus. *Structured fluids: polymers, colloids, surfactants.* Oxford University Press, Oxford; New York, 2004.

[283] J. P. Wittmer, H. Meyer, J. Baschnagel, A. Johner, S. Obukhov, L. Mattioni, M. Müller, and A. N. Semenov. Long range bond-bond correlations in dense polymer solutions. *Phys. Rev. Lett.*, 93(14):147801, 2004.

[284] J. P. Wittmer, P. Beckrich, H. Meyer, A. Cavallo, A. Johner, and J. Baschnagel. Intramolecular long-range correlations in polymer melts: the segmental size distribution and its moments. *Phys. Rev. E*, 76(1):011803, 2007.

[285] J. J. Wu and C. P. Buckley. Plastic deformation of glassy polystyrene: a unified model of yield and the role of chain length. *J. Polym. Sci.: Polym. Phys.*, 42(11): 2027–2040, 2004.

[286] L. Yang, D. J. Srolovitz, and A. F. Yee. Extended ensemble molecular dynamics method for constant strain rate uniaxial deformation of polymer systems. *J. Chem. Phys.*, 107(11):4396–4407, 1997.

[287] O. Yano and Y. Wada. Dynamic mechanical and dielectric relaxations of polystyrene below the glass temperature. *J. Polym. Sci. A-2*, 9:669–686, 1971.

[288] K. Yashiro, T. Ito, and Y. Tomita. Molecular dynamics simulation of deformation behavior in amorphous polymer: nucleation of chain entanglements and network structure under uniaxial tension. *Int. J. Mech. Sci.*, 45(11):1863–1876, 2003.

[289] D. Y. Yoon and P. J. Flory. Intermediate angle scattering functions and local chain configurations of semi-crystalline and amorphous polymers. *Polym. Bull.*, 4(12): 693–698, 1981.

[290] D. Y. Yoon, P. R. Sundararajan, and P. J. Flory. Conformational characteristics of polystyrene. *Macromolecules*, 8:776–783, 1975.

[291] R. Zangi and S. A. Rice. Cooperative dynamics in two dimensions. *Phys. Rev. Lett.*, 92(3):035502, 2004.

[292] S. Zapperi, A. Vespignani, and H. E. Stanley. Plasticity and avalanche behaviour in microfracturing phenomena. *Nature*, 388(6643):658–660, 1997.

[293] P. Zoller and D. J. Walsh. *Standard pressure-volume-temperature data for polymers.* Technomic Pub. Co., Lancaster, PA, 1995.

[294] R. Zorn. Deviation from Gaussian behavior in the self-correlation function of the proton motion in polybutadiene. *Phys. Rev. B*, 55(10):6249–6259, 1997.

Author index

Abe et al. [2], 59, 157
Adam and Gibbs [3], 13, 157
Aharoni [4], 125, 129, 157
Aichele et al. [5], 7, 157
Allen and Tildesley [6], 29, 30, 33, 34, 59, 73, 86, 157
Angell [10], 120, 157
Angell [7], 4, 157
Angell [8], 11, 14, 157
Angell [9], 11, 157
Arbe et al. [11], 43, 157
Argon et al. [12], 85, 157
Argon et al. [13], 85, 158
Ayyagari et al. [14], 58, 158
Böhmer and Angell [28], 11, 159
Balabaev [15], 85, 158
Ballard et al. [16], 129, 130, 158
Balucani and Zoppi [17], 7, 9, 12, 158
Barrat and Hansen [18], 3, 13, 158
Baschnagel et al. [19], 25, 158
Beatty and Weaver [20], 84, 158
Bennemann et al. [21], 7, 158
Berendsen et al. [22], 30, 158
Berry et al. [23], 130, 158
Berthet et al. [24], 58, 61, 158
Bicerano [25], 72, 158
Binder and Kob [26], 6, 9, 10, 12–14, 159
Binder et al. [27], 15, 159
Boothroyd et al. [29], 126, 159
Bouchaud [30], 15, 159
Bowles and Speedy [31], 5, 159
Boyce and Arruda [32], 119, 159
Brown and Clarke [33], 74, 159
Brown and Clarke [34], 85, 103, 159
Brown et al. [35], 84, 159
Callister, Jr. [36], 19, 103, 159
Cangialosi et al. [37], 24, 84, 107, 159
Capaldi et al. [38], 85, 139, 159
Capaldi et al. [39], 85, 139, 160
Carmesin and Kremer [40], 25, 160
Casalini and Roland [41], 11, 160
Chandler [42], 61, 160
Chong and Fuchs [43], 14, 160
Chui and Boyce [44], 85, 99, 109, 160
Cifra [45], 130, 160
Clarke and Brown [46], 85, 160
Colmenero et al. [47], 69, 160
Cummins [48], 14, 160
Darinskii et al. [49], 67, 160
Das [50], 14, 160
Debenedetti and Stillinger [53], 15, 160
Debenedetti [52], 4, 9–11, 13–15, 43, 57, 64, 68, 160
Desai [54], 42, 161
De la Rosa et al. [51], 25, 160
Doi and Edwards [56], 10, 12, 23, 75, 124, 125, 128, 161
Doi [55], 23, 47, 49, 69, 161
Doliwa and Heuer [57], 5, 161
Doliwa and Heuer [58], 42, 43, 53, 161
Donald and Kramer [60], 147, 161
Donald and Kramer [61], 84, 161
Donald [59], 84, 161
Donati et al. [62], 7, 44, 161
Dutcher and Marangoni [63], 125, 161
Dyre [64], 11, 161

Dyre [65], 15, 161
Eckert and Bartsch [66], 4, 161
Ediger et al. [68], 3, 42, 161
Ediger [67], 10, 77, 161
Engels et al. [70], 21, 162
Espanol and Warren [71], 25, 162
Essmann et al. [72], 34, 162
Ege [69], 34, 35, 162
Faller [73], 58, 162
Fan et al. [75], 85, 162
Fan [74], 85, 162
Ferry et al. [77], 10, 162
Ferry [76], 16, 162
Fetters et al. [78], 87, 119, 162
Fetters et al. [79], 87, 119, 131, 162
Flenner and Szamel [80], 15, 42, 43, 53, 162
Flory [81], 32, 124–126, 129, 162
Fortunelli et al. [82], 85, 162
Frenkel and Smit [83], 25, 29, 163
Frobose et al. [84], 5, 163
Fuchizaki and Kawasaki [85], 15, 163
Fuchizaki and Kawasaki [86], 15, 163
Fuchs et al. [87], 43, 163
Furuya et al. [88], 58, 163
Fuson et al. [89], 67, 69, 163
Götze and Sjögren [101], 14, 164
Götze [100], 5, 164
Gao and Weiner [90], 85, 163
Gao and Weiner [91], 85, 163
Gao and Weiner [92], 85, 110, 163
Gao and Weiner [93], 85, 163
Gao and Weiner [94], 85, 163
Gawrisch et al. [95], 129, 163
Gebizlioglu et al. [96], 84, 163
Gedde [97], 15, 163
Gelin and Karplus [98], 38, 164
Goldstein [99], 15, 164
Govaert and Tervoort [102], 21, 84, 119, 131, 164
Govaert et al. [103], 20, 84, 88, 164
Goyanes [104], 57, 164
Greer [105], 5, 164
Grellmann and Lach [106], 84, 164
Hagele and Beck [107], 57, 72, 164
Haile [108], 29, 164
Han and Boyd [109], 35, 37, 58, 124, 126, 164
Hansen and McDonald [110], 8, 9, 12, 72, 164
Harmandaris et al. [111], 58, 164
Hasan and Boyce [112], 20, 84, 88, 90–92, 164
Haward and Young [117], 90, 92, 93, 97, 100, 118, 149, 165
Haward [113], 90, 165
Haward [114], 20, 84, 93, 95, 119, 149, 165
Haward [115], 90, 165
Haward [116], 97, 165
He et al. [118], 58, 64, 69, 165
Helfand et al. [119], 37, 165
Hoogerbrugge and Koelman [120], 25, 165
Horbach et al. [121], 42, 53, 165
Hoy and Robbins [122], 128, 165
Hoy and Robbins [123], 85, 93, 95, 119, 133, 165
Hoy and Robbins [124], 85, 87, 97, 118, 119, 139, 149, 165
Hoy and Robbins [125], 85, 118, 139, 165
Hughes [126], 54, 165
Hurley and Harrowell [127], 5, 42, 43, 53, 165
Hutnik et al. [128], 37–39, 129, 166
Hutnik et al. [129], 29, 166
Hutnik et al. [130], 36, 85, 166
Isner and Lacks [131], 24, 107, 166
Itoh et al. [132], 42, 53, 166
Jackle and Eisinger [133], 6, 166
Jang and Jo [134], 85, 88, 99, 166
Janot [135], 3, 166
Jin and Boyd [136], 58, 166
Jin and Boyd [137], 69, 166
Johnson et al. [138], 126, 166
Jung and Schurmann [139], 130, 166
Kanaya and Kaji [140], 9, 166
Karatasos et al. [142], 58, 67, 72, 167
Karatasos [141], 52, 166

Kaur and Das [143], 43, 167
Khare and Paulaitis [144], 57, 68, 167
Khare and Paulaitis [145], 58, 63, 68, 167
Kim and Munakata [146], 15, 167
Klompen and Govaert [147], 84, 167
Klompen et al. [148], 26, 167
Kluge and Schober [149], 42, 53, 167
Kob and Andersen [151], 42, 53, 167
Kob [150], 5, 167
Kolbe [152], 5, 167
Kotelyanskii et al. [153], 58, 167
Kovacs et al. [154], 15, 107, 167
Kramer [155], 84, 118, 131, 168
Krausz and Eyring [156], 16, 168
Kubo et al. [157], 16, 168
Kuwahara et al. [158], 128, 168
Lach et al. [159], 84, 168
Lach et al. [160], 84, 168
Landau and Lifshitz [161], 96, 168
Laskowski et al. [162], 129, 168
Lee et al. [163], 129, 168
Lemak and Balabaev [165], 30, 59, 85, 86, 168
Lemaitre and Chaboche [164], 19, 88, 94, 168
Leon et al. [166], 39, 40, 168
Lewis and Wahnstrom [167], 64, 168
Li et al. [168], 85, 169
Lindsey and Patterson [169], 64, 169
Long and Lequeux [170], 15, 169
Lyulin and Michels [171], 40, 58, 59, 69, 169
Lyulin and Michels [172], 58, 169
Lyulin and Michels [173], 85, 102, 169
Lyulin et al. [174], 51, 58, 169
Lyulin et al. [175], 58, 59, 169
Lyulin et al. [176], 24, 35, 85, 103, 120, 169
Lyulin et al. [177], 14, 37, 58, 85, 87, 105, 119–121, 128, 133, 169
Ma and Lai [178], 5, 169
Macosko [179], 133, 169
Malakhovski [180], 155, 169
Mark [181], 31, 86, 120, 169
Mason and Weitz [182], 12, 170
Mazo [183], 85, 170
McKechnie et al. [184], 24, 85, 119, 170
Mishima and Stanley [185], 5, 170
Mitchell and Windle [186], 84, 170
Mondello et al. [187], 29, 34, 35, 58, 122, 170
Movaghar and Schirmacher [188], 44, 170
Moynihan et al. [189], 15, 21, 170
Mulder et al. [191], 85, 170
Mulder [190], 126, 170
Mulliken and Boyce [192], 90, 170
Narayanaswamy [193], 15, 21, 170
Nicholson and Davies [194], 58, 170
Nosé and Yonezawa [195], 5, 170
Novikov and Sokolov [196], 11, 171
Nyden et al. [197], 58, 171
Odagaki and Hiwatari [198], 43, 46, 171
Oleinik et al. [199], 84, 118, 171
Pant and Theodorou [200], 126, 171
Pham et al. [201], 4, 171
Plazek et al. [202], 84, 171
Quinson et al. [203], 84, 171
Quinson et al. [204], 84, 94, 171
Rabinovich et al. [205], 33, 171
Ragab and Bayoumi [206], 96, 171
Rahman [207], 42, 171
Rapaport [208], 29, 171
Rapold and Suter [209], 107, 126, 128, 172
Rapold et al. [210], 58, 68, 172
Reich and Eisenber [211], 57, 172
Reichman and Charbonneau [212], 15, 172
Reiner [213], 12, 172
Richards [214], 10, 52, 172
Richert [215], 9, 42, 172
Rintoul and Torquato [216], 5, 172
Risken [217], 45, 47, 74, 172
Ritort and Sollich [218], 6, 172
Robyr et al. [219], 59, 172
Robyr et al. [220], 128, 172
Roe et al. [223], 58, 172
Roe [221], 42, 53, 172
Roe [222], 58, 172
Roland and Casalini [224], 11, 173
Roland et al. [225], 13, 173
Rottler and Robbins [226], 19, 85, 94, 173

Rottler and Robbins [227], 85, 173
Rottler and Robbins [228], 100, 173
Rottler and Robbins [229], 85, 173
Saelee et al. [230], 58, 74, 79, 173
Salamatina et al. [231], 118, 173
Santangelo and Roland [232], 57, 59, 173
Sarva et al. [233], 90, 119, 173
Schafer and Elsner [234], 126, 129, 173
Sciortino et al. [236], 42, 53, 173
Sciortino [235], 4, 173
Sci [1], 2, 157
Shenogin and Ozisik [237], 85, 173
Shenogin et al. [238], 84, 97, 173
Sillescu [239], 10, 58, 174
Sjoerdsma and Heikens [240], 84, 85, 174
Smith et al. [241], 64, 174
Sotta and Long [242], 15, 174
Speedy [243], 5, 174
Spiess [244], 79, 174
Stillinger and Weber [246], 15, 174
Stillinger [245], 15, 174
Strobl [247], 124, 174
Struik [248], 15, 174
Sun and Faller [249], 58, 87, 126, 174
Sundararajan [250], 122, 125, 174
Sutmann [251], 29, 174
Tanabe [252], 57, 68, 72, 174
Tanguy et al. [253], 133, 137, 147, 174
Tervoort and Govaert [254], 20, 23, 93, 131, 175
Theodorou et al. [255], 31, 175
Tomaselli et al. [256], 36, 175
Tonelli [257], 57, 67, 72, 175
Tool [258], 15, 21, 175
Treloar [259], 92, 175
Treloar [260], 22, 175
Utz et al. [261], 24, 107, 175
Van Hove [262], 7, 42, 175
Vorselaars et al. [271], 85, 176
Vyazovkin and Dranca [272], 57, 176
Wales [273], 9, 10, 13–15, 100, 176
Wallace and Joos [274], 85, 176
Ward and Sweeney [275], 19–23, 88, 92, 93, 112, 131, 176
Weeks and Weitz [276], 42, 53, 176
Wehrle et al. [277], 81, 176
Weiner et al. [278], 37, 38, 176
Wendlandt et al. [279], 84, 85, 90, 131, 176
Williams and Flory [280], 125, 129, 130, 176
Williams and Flory [281], 128, 176
Witten and Pincus [282], 10, 63, 68, 177
Wittmer et al. [283], 124, 177
Wittmer et al. [284], 129, 177
Wu and Buckley [285], 84, 85, 90, 177
Yang et al. [286], 85, 177
Yano and Wada [287], 57, 68, 177
Yashiro et al. [288], 99, 177
Yoon and Flory [289], 129, 177
Yoon et al. [290], 107, 125, 126, 128, 177
Zangi and Rice [291], 42, 48, 51, 53, 177
Zapperi et al. [292], 155, 177
Zoller and Walsh [293], 40, 59, 86, 177
Zorn [294], 42, 53, 177
van Kampen [263], 45, 175
van Ketel et al. [264], 5, 175
van Krevelen [265], 103, 175
van Melick et al. [266], 20, 23, 36, 84, 85, 90, 118, 119, 131, 175
van Melick et al. [267], 20, 84, 85, 88, 90, 93, 94, 103, 120, 131, 175
van Melick et al. [268], 20, 84, 85, 176
van Staveren et al. [269], 44, 176
van Zon and de Leeuw [270], 14, 176

Summary

Local dynamics and deformation of glass-forming polymers: modelling and atomistic simulations

The research described in the present thesis is about glassy phenomena and mechanical properties in vitrifiable polymer materials. Glasses are solid materials, but, in contrast to crystals, the structure is disordered. Polymers are macromolecular chains formed by covalently linking a very large number of repeating molecular building blocks or monomers. Polymeric materials are easy to reshape and reuse. Also they are lightweight and often transparent. These characteristics make them ideal materials for commodity products such as compact discs, safety helmets, or vandal-proof glazing. Some glassy polymers are also biocompatible, so that they can be used in medical applications.

For a successful usage of polymer glasses it is necessary to understand and predict their behaviour under various circumstances. Although many new insights have been acquired over the last decades still a lot of questions remain open. Upon vitrifying a polymer melt the relaxation times and the viscosity increase dramatically. Accompanied with this increase various glassy phenomena are observed — in particular dynamical heterogeneities and non-Gaussian displacements of particles. The comprehension of the striking viscosity increase and the two phenomena mentioned above is still far from complete.

During the straining of a polymer glass typical mechanical characteristics are observed, of which the magnitude can vary enormously between different types of polymers. A well-known example of a polymer glass is atactic polystyrene. In its glassy state polystyrene is usually found to be very brittle. Within a few percent of elongation the material breaks. This behaviour is caused by a relatively high yield tooth in combination with a relatively low strain-hardening modulus. Other polymers, such as bisphenol-A polycarbonate, show a tough response; a test bar can easily be extended to twice its original length. In spite of much study, the physical (molecular) origin of this difference in mechanical behaviour is still not clear. Below the glass transition rubber-elasticity theory appears to be invalid, as it fails to explain the observation that the strain-hardening modulus of polystyrene in its glassy phase is about two orders of magnitude higher than its modulus in the rubbery state.

Our main goals are to acquire a better understanding at the molecular scale of heterogeneous and non-Gaussian dynamics and mechanical deformation of glassy polymers and to differentiate chemistry-specific from more universal physical properties. These goals are achieved by carrying out molecular-dynamics simulations on glass-forming systems. In addition, the results are elucidated by the usage of simple physical models.

The simulations consist of solving the equations of Newton, a coupled set of differential equations with a given force field and initial conditions. The force field describes the interactions between the various particles. As the main interest is in glassy polymers, most simulations are done for a united-atom model of polystyrene.

In the simulation run several characteristics of the glass transition are identified. As is typical for other vitreous systems as well, anomalous, non-Gaussian displacements play an important role near the glass transition for polystyrene; the same observation has been made for a dendritic melt and a colloid-like system. For all these systems of different architecture we have described some essential features of this non-Gaussian behaviour with a simple one-particle model in an effective field. The non-Gaussian behaviour is mainly caused by the cage-to-cage motion of the constituent particles, whereby the cage is formed by interactions with neighbouring particles. By means of the model the height of the so-called non-Gaussian parameter can be interpreted as a measure for the ratio of the root-mean-square displacement within the cage and the effective jump length between cages, without the assumption of any heterogeneity of glassy dynamics in the sense of site-specific relaxation times. The maximum of the non-Gaussian parameter occurs in each case at the crossover from the cage regime to the (sub)diffusive regime and is connected to the cage-escape time. For the colloid-like system also the shape of the time-dependent non-Gaussian parameter is described well by the model (chapter 3).

Dynamical heterogeneity, a phenomenon observed in many experiments on glasses, is also found in the simulation result of the polystyrene phenyl-ring-flip movement (to which the mechanical gamma relaxation is ascribed). This means that some phenyl rings behave very differently than others within a typical simulation run. Different relaxation times and activation enthalpies associated with the flip are determined using various methods. A particular result of the study of the phenyl flip is that an enthalpy barrier determined solely from structural properties is in accordance with an activation enthalpy acquired by analyzing the dynamics of the phenyl rings, even in the presence of dynamical heterogeneity. The heterogeneity arises because of the following mechanism. The conformation of the backbone determines to a large extent the barrier of the phenyl-ring flip. Eventually the relaxation of the backbone is becoming so slow upon cooling down that the phenyl ring is unable to access the conformation-dependent state with the lowest flip barrier within the corresponding barrier-jump time. The phenyl rings are trapped instead in various other states with accompanying different energy barriers. These states are available because of the disordered nature of the material. The mechanism just described for the heterogeneous dynamics in the phenyl-ring flip movement becomes stronger upon cooling down towards the glass transition; eventually the relaxation becomes more Arrhenius-like below the glass-transition temperature because only the fastest phenyl flips occur within the accessible observation time (chapter 4).

By doing uniaxial-stress extension and compression simulations the stress-strain relation of polystyrene has been measured under various conditions. Although the cooling and deformation velocities in the simulations differ many orders of magnitude from their values in usual experiments, the characteristic features of the experimental stress-strain relation are well reproduced, which allows one to study the origin of the yield tooth and strain hardening. It is observed that the strain-hardening modulus increases with increasing pressure, an effect not described by rubber-elasticity theory. Also it is observed that the thermal history is not completely erased by the mechanical deformation. The picture arising from this study is that the yield peak in polystyrene is mostly mediated by interchain energetic interactions. A net debonding of these interactions is likely causing this yield peak and the subsequent strain softening. The positiveness of the strain-hardening modulus in polystyrene is mainly due to intrachain interactions (chapter 5).

From our comparative study of polystyrene and polycarbonate it can be concluded that strain hardening in polymer glasses such as these two polymers is likely caused mainly by the following mechanism. During uniaxial extension a glassy chain adopts a more stretched and hence more inflexible state, also at a local scale. Due to interactions with other particles non-affine displacements take place. The non-affine response is stronger at shorter length scales, but as the deformation proceeds and the effective flexibility decreases also longer length scales are affected. This is accompanied with more bond-altering processes and implies an increase in the rate of energy dissipation, causing in turn an increase in stress upon straining the polymer material further (chapter 6).

All these results show that simple physical models supported and tested by results of molecular-dynamics simulations (in which typical physical phenomena observed in real experiments can be reproduced) provide a fruitful approach in understanding glassy materials.

Samenvatting

Moleculaire dynamica en vervorming van verglaasbare polymeren: modellering en atomistische simulaties

Het onderzoek dat in dit proefschrift is beschreven betreft de studie van glasachtige fenomenen en mechanische eigenschappen van verglaasbare polymeren. Een glas is een vaste stof, maar in tegenstelling tot een kristal is de structuur ervan ongeordend. Polymeren zijn macromoleculaire ketens, gevormd door het aan elkaar koppelen van een groot aantal moleculaire bouwstenen of monomeren. Het voordeel van polymere materialen is dat ze gemakkelijk zijn om te vormen. Ook zijn ze licht en vaak transparant. Hierdoor zijn polymere materialen geschikt voor producten zoals CD's, veiligheidshelmen of vandalisme-ongevoelig glaswerk. Een aantal glasachtige polymeren hebben ook een uitstekende biocompatibiliteit en kunnen daarom gebruikt worden in medische toepassingen.

Het begrijpen en het voorspellen van het gedrag van polymeerglazen zal bijdragen tot een beter gebruik van deze materialen. Hoewel tijdens de laatste decennia er veel nieuwe inzichten zijn verworven, zijn er ook nog steeds veel open vragen. De relaxatietijden en de viscositeit van een polymeersmelt nemen drastisch toe tijdens de verglazing. Dit gaat gepaard met verscheidene glasachtige fenomenen — in het bijzonder dynamische heterogeniteiten en niet-Gaussische deeltjesverplaatsingen. Het begrip van de uitermate snelle viscositeitstoename en deze twee fenomenen is verre van volledig.

Tijdens het rekken van een polymeerglas zijn mechanische karakteristieken te zien, waarvan de grootte sterk kan variëren tussen verschillende type polymeren. Een bekend polymeerglas is atactisch polystyreen, dat normaal erg bros is. Als dit materiaal uitgerekt wordt, zal het binnen een paar procent al breken. Dit gedrag wordt veroorzaakt door een relatief hoge vloeigrens in combinatie met substantiële rekverzwakking. Polymeren zoals polycarbonaat vertonen taai gedrag; een trekstaafje kan makkelijk worden uitgerekt tot twee maal zijn oorspronkelijke lengte. Ondanks vele studies is de oorzaak van dit gedrag nog niet helemaal begrepen. In de glastoestand kan rubber-elasticiteitstheorie niet worden toegepast. Een voorbeeld hiervan is polystyreen; in de glasfase is de mate van rekversteviging een factor 100 groter dan men zou verwachten op de mate van rekversteviging in de rubberfase.

Ons doel is om een beter microscopisch begrip te verkrijgen van heterogene en niet-

Gaussische dynamica, van het mechanisch vervormen van glasachtige polymeren en om de universele eigenschappen te kunnen scheiden van chemische details. Met behulp van moleculaire-dynamica simulaties van verglaasbare polymeren en het ontwikkelen en gebruik van fysische modellen proberen we dit doel te bereiken.

In de simulaties zien we verscheidene fenomenen van de glasovergang terug. Nabij de glasovergang spelen niet-Gaussische, anomale, verplaatsingen van deeltjes een belangrijke rol, zo ook voor polystyreen. We zien hetzelfde gedrag bij een smelt van dendrimeren en een colloïdaal systeem. Een model van een deeltje in een effectieve potentiaal is opgesteld, dat essentiële kenmerken van dit niet-Gaussisch gedrag kan beschrijven. Dit niet-Gaussisch gedrag wordt voornamelijk veroorzaakt door de kooi-naar-kooi–beweging van de deeltjes. Deze kooi wordt gevormd door interacties met omliggende deeltjes. M.b.v. het model kan de hoogte van de zogenoemde niet-Gaussische parameter geïnterpreteerd worden als een maat voor de verhouding van de effectieve kwadratische spronglengte tussen kooien en de gemiddelde kwadratische verplaatsing binnen een kooi. Hierbij hoeft men niet aan te nemen dat er dynamische heterogeniteiten in de zin van plaatsafhankelijke relaxatietijden zijn. Voor alle drie systemen ligt het maximum van de niet-Gaussische parameter op de grens tussen het gebied waar het deeltje gekooid is en het gebied waar (sub)diffusie optreedt. De tijd waarbij dit optreedt is een maat voor de ontsnappingstijd uit de kooi. Het model is bijzonder goed in het beschrijven van de tijdafhankelijkheid van de niet-Gaussische parameter van het colloïdale systeem (hoofdstuk 3).

Ook zien we dynamische heterogeniteiten in onze simulaties van polystyreen voorkomen, in het bijzonder bij de omdraaiing van de fenylzijgroep. De mechanische gamma-relaxatie wordt toegeschreven aan deze rotatie. De heterogeniteiten houden in dat tijdens een simulatie sommige fenylgroepen zich veel anders dan andere gedragen. Dit komt door het volgende mechanisme. De omgeving van de fenylgroep en in het bijzonder de chemische conformatie van de hoofdketen bepalen de omdraaiingsenergiebarrière van de fenylgroep. Bij een hoge temperatuur zal de relaxatie van de hoofdketen voldoende snel zijn, zodat de ketenconformatie met de laagste omdraaiingsbarrière binnen de typische omdraaiingstijd behorende bij deze barrière kan worden gevonden. In dit geval zullen alle fenylgroepen ongeveer dezelfde omdraaiingstijd hebben. Als men de glasovergang nadert vanuit de vloeistoffase, zal de relaxatie van de hoofdketen zeer traag worden en zullen conformatieveranderingen niet meer zo snel optreden. Uiteindelijk worden deze veranderingen zelfs langzamer dan de omdraaiingstijd van de fenylgroep in de meest gunstige ketenconformatie. Hierdoor worden de fenylgroepen gevangen in verschillende ketenconformaties met bijbehorende energiebarrières, met als gevolg dat de omdraaiing dynamisch heterogeen wordt. Sommige barrières zijn zo hoog, dat de bijbehorende fenylgroepen niet meer roteren binnen de tijd van een typisch experiment. Onder de glasovergang zal de relaxatie dan ook meer Arrheniusachtig gedrag vertonen, daar alleen de fenylgroepen met een gunstige ketenconformatie binnen de observatietijd kunnen draaien (hoofdstuk 4).

Het spannings-rek gedrag van polystyreen is m.b.v. moleculaire-dynamica simulaties bepaald, zowel onder extensie als onder compressie en onder verschillende condities. Hoewel de koel- en vervormingssnelheid van de simulaties veel hoger liggen dan in typische experimenten, kunnen de mechanische karakteristieken zoals ze in experimenten te zien zijn toch kwalitatief gereproduceerd worden. Hiermee kunnen we de piek nabij de vloeigrens en de rekversteviging nader onderzoeken. Het blijkt dat de mate van rekversteviging toeneemt met toenemende druk, een effect dat niet verklaard kan worden met rubberelasticiteitstheorie. We zien ook dat de thermische geschiedenis van ons polymeersysteem niet geheel verdwijnt tijdens mechanische vervorming. De dominerende energetische interactie bij de piek rond de vloeispanning in polystyreen is die van de interketen (Lennard-Jones) interactie. Deze piek (vloeispanning gevolgd door rekverzwakking) wordt waarschijnlijk veroorzaakt doordat er netto meer interketenbindingen worden verbroken dan worden gevormd tijdens de initiële rek. Dat er positieve rekversteviging is, komt voornamelijk door intraketen interacties (hoofdstuk 5).

Onze vergelijkende simulatiestudie van polystyreen en polycarbonaat laat zien dat het plausibel is dat rekversteviging bij polymeerglazen zoals bij deze twee polymeren mede veroorzaakt vooral door het volgende mechanisme. Tijdens het uitrekken zal een glasachtige keten een meer gestrekte toestand verkrijgen, in het bijzonder op lokaal nivo. Hierdoor zal de effectieve ketenflexibiliteit afnemen. Door restricties zoals covalente bindingen en verhinderingen met andere deeltjes zullen de verplaatsingen van de deeltjes niet affien met de vervorming van het polymeersysteem meebewegen. Deze niet-affine verplaatsingen vinden initieel vooral op korte ketenlengteschalen plaats. Maar omdat de effectieve flexibiliteit van de keten afneemt, zal de beweging ook op grotere lengteschalen meer niet-affien zijn. Dit impliceert een toename van het Lennard-Jones-bindingsveranderingstempo en daarom een toename van de energiedissipatiesnelheid. Dit heeft als gevolg dat de spanning toeneemt tijdens verdere rek (hoofdstuk 6).

List of Publications

Molecular-dynamics simulation of amorphous polymers in the isotropic state and under uniaxial deformation
Alexey V. Lyulin, Bart Vorselaars and M.A.J. Michels
Proceedings of the 3rd international conference on "Computational modeling and simulation of materials", part A. Editors: P. Vincenzini and A. Lami, Sicily, Italy, **42**, 743 (2004)

Strain softening and hardening of amorphous polymers: atomistic simulation of bulk mechanics and local dynamics
Alexey V. Lyulin, Bart Vorselaars, M.A. Mazo, N.K. Balabaev and M.A.J. Michels
Europhys. Lett. **71**, 618 (2005)

Atomistic simulation of bulk mechanics and local dynamics of amorphous polymers
Alexey V. Lyulin, Jing Li, Tim Mulder, Bart Vorselaars and M.A.J. Michels
Macromol. Symp. **237**, 108 (2006)

Monte Carlo simulation of uniaxial tension of an amorphous polyethylene-like polymer glass
Jing Li, Tim Mulder, Bart Vorselaars, Alexey V. Lyulin, and M.A.J. Michels
Macromolecules **39**, 7774 (2006)

Non-Gaussian nature of glassy dynamics by cage to cage motion
Bart Vorselaars, Alexey V. Lyulin, K. Karatasos and M.A.J. Michels
Phys. Rev. E **75**, 011504 (2007)

also listed in:

Virtual J. Biological Phys. Research **13**, issue 3 (2007)

Development of heterogeneity near the glass transition: phenyl-ring-flip motions in polystyrene
Bart Vorselaars, Alexey V. Lyulin, and M.A.J. Michels
Macromolecules **40**, 6001 (2007)

Deformation of polystyrene: atomistic simulations
Bart Vorselaars, Alexey V. Lyulin, and M.A.J. Michels
In preparation

Microscopic mechanisms of strain hardening in glassy polymers
Bart Vorselaars, Alexey V. Lyulin, and M.A.J. Michels
In preparation

Dankwoord

Bij deze wil ik een aantal mensen opnoemen, die direct of indirect hebben bijgedragen aan de totstandkoming van dit proefschrift. Allereerst mijn begeleiders Alexey Lyulin en Thijs Michels. Alexey, je stond altijd klaar om me bij een probleem te helpen. Je bent een prettig persoon om samen mee te werken en we hebben vele vruchtbare discussies gevoerd. Ook waardeer ik de enorme gastvrijheid. Ter illustratie kan ik het bezoek aan Sint Petersburg aanhalen, waar ik een zeer vorstelijk behandeling van jou en je familie kreeg, спасибо. Thijs, je ondersteuning op de meer theoretische kant van het proefschrift is erg waardevol geweest, en je daagde me uit om scherp te zijn.

For the support regarding the molecular dynamics simulation code *puma* and the force fields I would like to thank Mikhail Mazo and Nikolai Balabaev. For the help in visualizing the dynamics of the polymer chains the help of Travis DePuy with his visit from the USA is acknowledged. Arieh Tal, bedankt voor de ondersteuning m.b.t. de lokale SGI computer. Jing Li, it was a pleasure to work together with you on the MC project and to learn more about the Chinese culture. Also thanks to Kostas Karatasos and Ronen Zangi for providing their simulation results. Leon Govaert wil ik bedanken voor het delen van zijn kennis in de huidige stand van zaken op het gebied van de mechanische eigenschappen van polymeren. I am grateful to the members of my commission, Herman Clercx, Michael Wübbenhorst and in particular Joerg Baschnagel for his valuable comments.

Tim Mulder, mijn kamer- en lotgenoot gedurende het hele project, we hebben een leuke en enerverende tijd gehad, ook tijdens de nodige ontspanningsmomenten, proppentennis niet te vergeten! Daarnaast wil Clazien Saris en Helmi van Lieshout bedanken voor hun ondersteuning. Ook wil ik ik m'n andere kamergenoten, de vaste medewerkers, postdocs, promovenda en studenten van de polymeerfysica groep bedanken voor de gezellige en inspirerende tijd.

Mijn vrienden hebben voor 'n welkome afleiding gezorgd. Mijn familie en met name mijn ouders en mijn vriendin Sybille, ze hebben altijd liefdevol achter me gestaan en vertrouwen in me gehad.

Curriculum Vitæ

Bart Vorselaars is geboren te Goirle op 22 maart 1978. In 1996 heeft hij aan het Durendael college te Oisterwijk met goed gevolg het VWO-examen afgelegd. In deze periode heeft hij ook deelgenomen aan een internationale wiskundeweek-bijeenkomst n.a.v. de Nederlandse wiskunde-olympiade. Na de middelbare school is hij begonnen met de ingenieursopleiding Technische natuurkunde aan de Technische Universiteit van Eindhoven (TU/e). Tijdens deze opleiding heeft hij een interne stage gelopen bij de vakgroep Evenwicht en Transport in Plasma's, onder de supervisie van Jan van Dijk en Joost van der Mullen, met als onderwerp het ontwikkelen van een botsings-stralingsmodel van Neon. De externe stage is uitgevoerd aan de University of Newcastle in Newcastle, Australië. Het onderwerp betrof hier de controle van de grenslaag van een ronde turbulente straal m.b.v. piezo-electrische actuatoren, onder de supervisie van R. Parker en Prof. R.A. Antonia. Ter afronding van de opleiding is er een afstudeeronderzoek verricht. Dit besloeg de studie van anisotrope afwijkingen van een turbulente stroming, opgewekt in een windtunnel. Deze afwijkingen zijn gekwantificeerd door de irreduceerbare representatie van de SO(3) groep te gebruiken. Dit project werd begeleid door Prof. dr. ir. W. van de Water van de groep transportfysica. In november 2003 is Bart Vorselaars begonnen met het promotieonderzoek onder begeleiding van dr. Alexey V. Lyulin en prof. dr. M.A.J. Michels in de groep Polymeerfysica van de faculteit Technische natuurkunde aan de TU/e. De belangrijkste resultaten zijn vermeld in dit proefschrift.